Patient derived lymphoma spheroids (PDLS) as preclinical follicular lymphoma models for personalized medicine : identification of CD39 as a potential new therapeutic target

Carla Faria

Université Fédérale
Toulouse Midi-Pyrénées

THÈSE

En vue de l'obtention du
DOCTORAT DE L'UNIVERSITÉ DE TOULOUSE

Délivré par l'Université Toulouse 3 - Paul Sabatier

Présentée et soutenue par

Carla FARIA

Le 30 juin 2022

Patient derived lymphoma spheroids (PDLS), un modèle préclinique du lymphome folliculaire: identification de CD39 comme une nouvelle cible thérapeutique potentielle

---

Ecole doctorale : **BSB - Biologie, Santé, Biotechnologies**

Spécialité : **CANCEROLOGIE**

Unité de recherche :
CRCT - Centre de Recherche en Cancérologie de Toulouse

Thèse dirigée par
Christine BEZOMBES et Patricia Perez-Galan

Jury

M. Daniel OLIVE, Rapporteur
M. Emmanuel DONNADIEU, Rapporteur
Mme Nathalie BONNEFOY, Examinatrice
M. Cédric ROSSI, Examinateur
Mme Christine BEZOMBES, Directrice de thèse
Mme Patricia PéREZ-GàLAN, Co-directrice de thèse
Mme Camille LAURENT, Présidente

REMERCIEMENTS

Mes premiers remerciements vont auprès des membres de mon jury, mes rapporteurs, le Pr Daniel Olive et le Dr Emmanuel Donnadieu, qui m'ont faits l'honneur d'évaluer mon manuscrit et le Pr Nathalie Bonnefoy et le Dr Cédric Rossi d'avoir accepté d'examiner mes travaux. Merci à tous d'avoir apporté vos expertises respectives et pour votre bienveillance.

Un immense merci à ma directrice de thèse, le Dr Christine Bezombes, de m'avoir confié ce projet de thèse qui m'a passionné dès le premier jour. Merci d'avoir cru en moi plus que je n'ai jamais cru en moi-même et de m'avoir donné l'opportunité de faire mes premiers pas dans le monde fantastique de la recherche académique. Tes qualités humaines m'ont toujours beaucoup touché et m'ont permis de passer chaque étape de ma thèse dans la bonne humeur et la sérénité.

Merci également à ma co-directrice, le Dr Patricia Pérez-Galàn, pour avoir guidé ces travaux avec bienveillance et pour tous ses encouragements. Merci également à toute l'équipe d'IBIDAPS (Célia, Ferran, Juan, Heribert, Laia, Neus, Dolores) avec qui j'ai eu la chance d'échanger à l'aide de nos nombreuses réunions à Barcelone, Toulouse ou Girone. Le projet IMLINFO a été très enrichissant tant sur le plan humain que scientifique. Muchas gracias ! Je remercie également les autres partenaires du projet IMLINFO. Tout d'abord, toute l'équipe d'IMACTIV 3D, Jean-Michel, Renaud, Pascale, Aurélie, Marine, Victoria, merci pour vos conseils et votre soutien pendant ce projet. Merci également à Nahomi et Alina de Palobiofarma pour avoir participé à l'avancer de ce projet à travers nos nombreuses discussions.

Je remercie chaleureusement, tout d'abord le Dr Jean-Jacques Fournié, ancien directeur de l'équipe 9 du CRCT, pour tous ses enseignements et ses récits d'aventures toujours plus fous les uns que les autres. Tu es une source d'inspiration pour toute une génération, merci pour tes contributions humaines et scientifiques tout au long de ces bons et loyaux services au sein de la communauté scientifique. Je te souhaite une belle retraite pleine d'aventures. Mes remerciements vont également au Pr Camille Laurent, qui a pris brillamment le lead de l'équipe NoLYmIT. Merci d'être toujours à l'écoute de nos demandes, de t'interessé à chacun des projets de l'équipe malgré ton emploi du temps surchargé. Je ne pouvais pas rêver meilleure présidente de jury ! Je te souhaite de continuer à mener cette équipe NoLYmIT, qui porte bien son nom, vers de belles aventures scientifiques et humaines.

On dit que les amis sont la famille que l'on a choisie, les membres de l'équipe 9 sont devenus au fil des années bien plus que des collègues. Merci d'avoir faits de chacune de mes journées au sein du CRCT et en dehors, des souvenirs indélébiles incluant : des soirées endiablées, des randonnés de

l'extrême, de pénible mais régulière course à pied pendant l'heure du déjeuner (merci à mon acolyte Julie !), et des séances d'escalade incroyable (merci Benoît et Marcin pour votre motivation à toute épreuve, promis après la thèse je serai plus présente !). A cette team diadème, ou qui change de nom à chaque soirée, Sarah, Olivia, Julie, Pauline, Marcin, Nicolas, Benoît, Don-Marc, Chloé, Fabien, un grand merci pour tous ces bons moments passés ensemble, j'attends avec impatience nos prochaines aventures. Merci à Anne également pour ta bienveillance et tes conseils tout au long de ces années pendant les salvatrices pauses café ! J'ai toujours admiré ta passion pour la science qui s'est traduit par une belle carrière. Quelques belles années de science se profilent encore mais je te souhaite une retraite, qui s'approche, pleine de bonne lecture et d'aventures. Merci à Mary pour ton enthousiasme et tes conseils sur le projet IMLINFO, je te souhaite une belle suite de carrière. L'équipe 9 a évolué au cours des années pour devenir l'équipe NoLYmIT, incluant de nouveaux membres tous aussi exceptionnels les uns que les autres. L'une des premières nouvelles arrivantes, plus si nouvelle maintenant, Léa, j'espère que tu as appris autant que moi j'ai appris en t'encadrant du mieux que je pouvais pendant ces années de M1, M2 et début de thèse. Je te souhaite le meilleur pour la suite, je ne doute pas de ton succès ! Amandine, quel bonheur d'avoir pu travailler avec toi, merci pour ta bonne humeur, ton enthousiasme et ta gentillesse. A très vite pour une séance d'apprentissage d'amigurumi ! Aux autres nouveaux arrivants avec qui j'ai moins eu l'occasion d'échanger, Jerko, Chloé, Marion, Nicolas.G, je vous souhaite une bonne continuation pour la suite et je compte sur vous pour maintenir les bonnes vibes de l'équipe comme vous le faites si bien !

Merci à l'ensemble du personnel du plateau technique du CRCT pour votre aide, bienveillance et bonne humeur qui m'ont permis d'acquérir des compétences tant en cytométrie en flux (merci Manon d'avoir géré avec moi les caprices du Fortessa et du LSRII), en microscopie (Laetitia, merci pour la mise en place du workshop 3D, l'aventure MiFoBio et la mise en place du groupe 3D au sein du CRCT qui je l'espère va perdurer), et en bio-informatique (Marie, Frédéric, Marion et Juan merci de votre aide précieuse).

Je remercie également tout le personnel hospitalier de l'IUCT-O et plus particulièrement les cliniciens de notre équipe, le Pr Camille Laurent et Loïc Ysebaert pour leur aide dans la collecte des échantillons et leur soutien dans l'ensemble des projets de recherche translationnels.

Merci à mes proches, amis et famille d'ici et du portugal, pour leur soutien indéfectible tout au long de ces années. Un immense merci à mes parents pour les valeurs d'humilité, d'amour du travail et de générosité qu'ils ont toujours su m'inculquer. Pour finir je tiens à remercier mon mari, pour l'amour et la complicité qu'il m'apporte au quotidien.

RÉSUMÉ

Le lymphome folliculaire (LF) est le 2ème type de lymphomes non Hodgkiniens (LNH) le plus fréquent, dont le traitement a largement bénéficié de l'introduction de l'anticorps monoclonal anti-CD20, le rituximab, en combinaison avec une polychimiothérapie. Malgré ces progrès thérapeutiques considérables, de nombreux patients rechutent et certains patients ne répondent pas aux traitements standards. Ainsi, il est primordial d'identifier de nouvelles cibles thérapeutiques à l'aide de modèles d'études pertinents. Ces dernières années ont vu émerger de nouveaux traitements anti-cancéreux « chemo-free ». Dans ce contexte, l'immunothérapie a bénéficié d'un puissant développement permettant ainsi, par différentes approches, de stimuler le système immunitaire afin qu'il puisse reconnaître les cellules tumorales et les éradiquer. Le microenvironnement ou la cellule tumorale elle-même sont donc devenus des cibles privilégiées de molécules thérapeutiques.

Parmi celles-ci, les molécules ciblant à la fois des récepteurs à l'adénosine ou la génération de son métabolite sont prometteuses. Les modèles 3D représentent un outil d'étude clé dans ce projet car ils reflètent la pathologie en terme : i) d'architecture tridimensionnelle, ii) de profils transcriptomique et protéique et enfin iii) de réponse aux traitements. Les objectifs spécifiques de ma thèse ont été de: (i) Mettre au point la culture en 3D à partir de lignées cellulaires (MALC, *multicellular aggregates of lymphoma cells*) et de cellules de patients atteints de LF (PDLS, *patient-derived lymphoma spheroids*), (ii) Caractériser les PDLS sur le plan transcriptomique et phénotypique (composition cellulaire, expression des récepteurs à l'adénosine et ses métabolites, récepteurs d'*immune checkpoint*…), (iii) tester l'efficacité d'immunothérapies sur les PDLS et (iv) Identifier de nouvelle(s) cible(s) thérapeutique(s).

Ainsi, ce travail a permis d'identifier CD39, une endoectonucléotidase impliquée dans la voie adénosinergique, comme nouvelle cible thérapeutique dans le LF, une pathologie qui reste à l'heure actuelle considérée comme incurable.

ABSTRACT

Follicular lymphoma (FL) is the second most frequent non-Hodgkin's lymphoma (NHL), which benefited greatly from anti-CD20 monoclonal antibody (rituximab) introduction in combination with chemotherapy in first-line therapy. Despite this huge therapeutic progress, numerous patients relapse and some are refractory to first-line treatments. Thus, it is essential to identify new therapeutic targets using relevant models.

Recently, new anti-cancer treatments called "chemo-free" has emerged. In this context, immunotherapy has benefited from a powerful development allowing, by different approaches, to stimulate the immune system in order to recognize tumoral cells and eradicate them. Tumor microenvironment or even tumor cells themselves have become key targets for these therapeutic approaches.

Among them, molecules targeting adenosine receptors or its metabolites generation are promising. 3D models represent a key element in this project as they reflect the pathology in term of: (i) spatial architecture, (ii) transcriptomic and protein profiles and (iii) treatment responses. The specific objectives of my PhD were to: (i) establish 3D cultures from FL cell lines (MALC, multicellular aggregates of lymphoma cells) and FL patient samples (PDLS, patient-derived lymphoma spheroids), (ii) characterize the transcriptomic and phenotypic profiles of PDLS (including: immune cell, adenosinergic pathway, immune checkpoint receptors), (iii) test efficacy of immunotherapies on PDLS and (iv) identify new therapeutic targets.

Thus, this work allowed the identification of CD39, an endoectonucleotidase implicated in adenosine generation, as a new therapeutic target in FL, a pathology that still remains incurable.

TABLE OF CONTENTS

FIGURES LIST

TABLES LIST

ABBREVIATIONS LIST

ADCC	antibody-dependent cell-mediated cytotoxicity
ADCP	antibody-dependent cellular phagocytosis
AID	activation-induced cytidine deaminase
APC	antigen-presenting cells
ATP	Adenosine-triphosphate
BCR	B-cell receptor
BiTe	Bi-specific T-cell engager
BL	Burkitt lymphoma
BM	bone marrow
CAF	Cancer associated fibroblast
CAR-T cells	Chimeric antigen receptors expressing T cell
CDC	complement-dependent cell cytotoxicity
CLP	common lymphoid progenitor
CR	Complete response
CTL	cytotoxic T cells
CXCL12	CXC-chemokine ligand 12
DC	dendritic cells
DLBCL	diffuse large B cell lymphoma
DOTs	delta one T cells
DZ	dark zone
ECM	Extracellular matrix
ETP	early T-cell-lineage progenitor
FDC	follicular dendritic cells
FL	follicular lymphoma
FRC	fibroblastic reticular cell
GC	germinal center
GEMM	Genetically engineered mouse model
HL	Hodgkin lymphoma
HSCs	hematopoietic stem cells
ICP	Immune checkpoint
IE	immune escape
IEGS	Immune escape gene set
Ig	immunoglobulin
IHC	immunohistochemistry
IT	immunotherapy
LMPP	lymphoid-primed multipotent progenitors
LN	lymph node
mAbs	monoclonal antibodies
MALC	Multicellular aggregate of lymphoma cells
MALTs	mucosa-associated lymphoid tissues
MCL	Mantle cell lymphoma
MCTS	Multicellular tumor spheroid
MDSC	myeloid-derived suppressor cells
MHC	major histocompatibility complex
MMP	common myeloid progenitor
MSC	mesenchymal stromal cell
MZL	Marginal zone lymphoma

NHL	non-Hodgkin lymphoma
NK cells	Natural killer cells
ORR	Overall response rate
OS	overall survival
PAgs	phosphoantigens
PBMC	peripheral blood mononuclear cells
PDLS	Patient-derived lymphoma spheroids
PDMS	polydimethylsiloxane
PDTX	Patient derived tumor xenograft
PFS	Progression free survival
R/R	Relapse/Refractory
RAG1 and RAG2	Recombination-activating gene 1 and 2
R-CHOP	rituximab-cyclophosphamide, hydroxydaunorubicine, oncovin, prednisone
R-CVP	rituximab, cyclophosphamide, vincristine sulfateand prednisone
RSS	recombination signal sequences
SLOs	secondary lymphoid organs
TAM	tumor associated macrophage
TCR	T-cell receptor
TEGs	T cells engineered with defined γδ TCR
TFh	T follicular helper cell
TFr	T follicular reticular cell
TME	tumor microenvironment
Treg	T regulator cell
ULA	Ultra low attachment
WHO	world human organization
γδ T cells	gamma delta T cells

I. INTRODUCTION

1. Lymphopoiesis and lymphomagenesis: from order to anarchy

In vertebrates, genesis of lymphocytes starts in the bone marrow (BM) from multipotent hematopoietic stem cells (HSCs). Differentiation of lymphocyte (B or T) from HSCs, requires tightly orchestrated steps, which constitute a branch of hematopoiesis system[1]. This system allows the formation of all types of blood cellular components starting from two main progenitors: the common myeloid progenitor (MMP) that gives rise to megakaryocytes (thrombocytes), erythrocytes, mast cells, myeloblasts (basophils, neutrophils, eosinophils, monocytes and then macrophages) and the common lymphoid progenitor (CLP) that gives rise to natural killer cells (NK cells) and small lymphocytes (T cells and B cells differentiating in plasma cells) (Figure1). We will focus the rest of this first introductory part on the CLP and the genesis of B and T lymphocytes. These cell types differentiate and proliferate in specialized structures. Their precursors express a large repertoire of random receptors deriving from somatic recombination and must follow steps of positive and negative selection to select the appropriate amount of affinity to ensure self-tolerance and sufficient immune response. These steps occur mainly in primary lymphoid organs (bone marrow and thymus) and then B and T cells are matured in secondary lymphoid organs (SLOs) (lymph nodes(LN) , spleen, or mucosa-associated lymphoid tissues MALTs) [2].

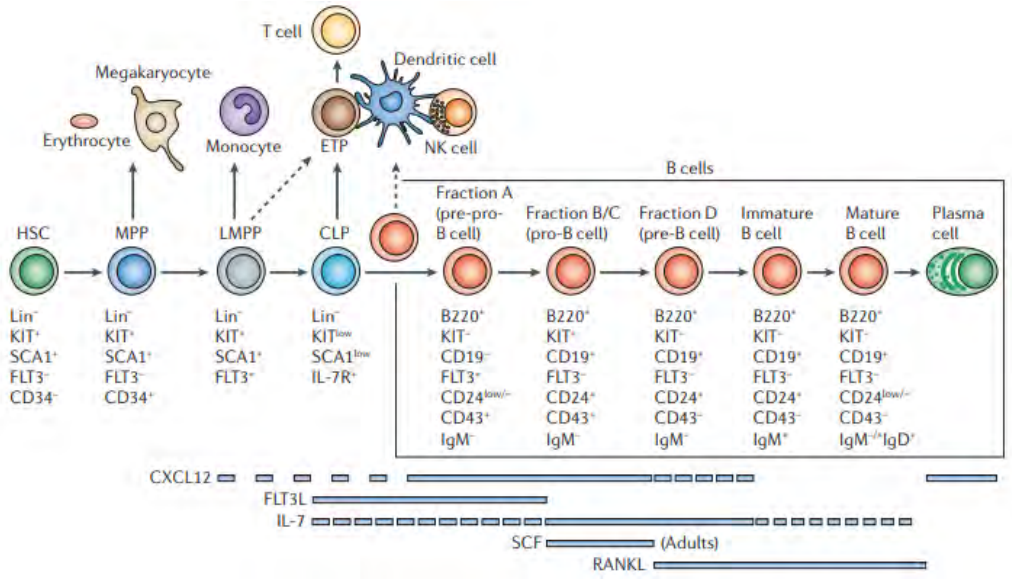

Figure 1 : Hematopoiesis and detailed B cell differentiation with associated markers and genetic features
HSC, multipotent hematopoietic stem cells; MPP, common myeloid progenitor; LMPP, lymphoid-primed multipotent progenitors; CLP, common lymphoid progenitor; ETP, early T-cell-lineage progenitor; NK, natural killer. From Nagasawa, Nature immunolology reviews, 2006 [2].

1.1 B cell differentiation: from HSC to plasma and memory cells

B cells are responsible for specific immune humoral response through the production of antibodies. They also play the role of antigen-presenting cells (APC). To obtain functional B cells, many genetic and epigenetic mechanisms must occured and specific microenvironment interactions are needed (Figures 2 and 3). Lymphopoiesis is a gradual and hierarchical process in which cells progressively lose their stem cell differentiation capacity to gain more specialized features. Several subtypes of B cells can be distinguished in this process also according to their locations. First in the BM, HCS differentiate in pro-B cell. These pro-B cells enter the blood circulation to differentiate into pre-B cell, then immature and naïve B cells. Subsequently, in the germinal center (GC) B cells undergo their ultimate differentitation steps (first centroblast and then centrocyte) to give birth to memory B cells and plasma cells in the blood circulation again (Figure 2).

Various soluble factors are necessary for orchestrating B-cell differentiation and trafficking. For instance, CXC-chemokine ligand 12 (CXCL12) is an important chemokine for differentiation of B-cell progenitor's subtypes and afterwards for homing of plasma cells to the BM. FLT3 ligand (FLT3L) allows differentiation of CLP and pre-pro-B cells. Interleukin 7 (IL-7) is required for generation of pro-B and pre-B cells. Stem-cell factor (SCF) is essential in adults for differentiation of pro-B-cells. Receptor activator of nuclear factor- κB ligand (RANKL) is important at late stage of differentiation: from pre-B cell to mature B cell (Figure 1).

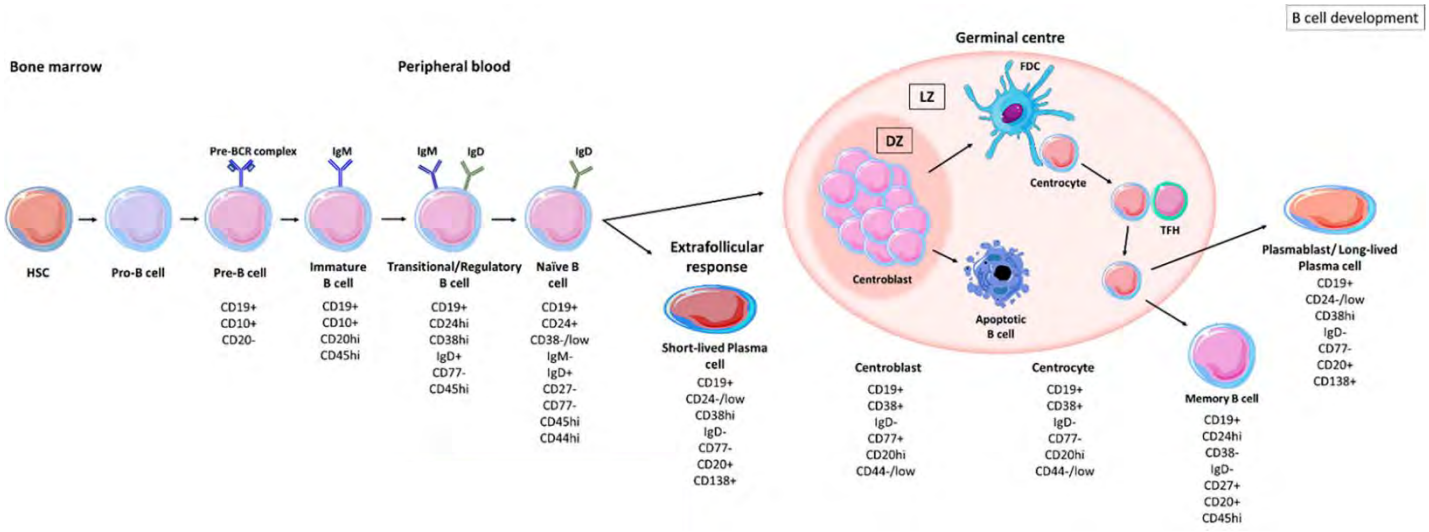

Figure 2 : Detailled markers and subtypes upon B cell differentiation
First steps occur in the bone marrow (HSCs) then progress to circulation and finally to germinal center to reenter the circulation and the bone marrow once fully differentiated into plasma cells or memory B cells. During their transit in the germinal center, they undergo clonal expansion and somatic hypermutation (SMH) in the dark zones (DZ). Inefficient B cells undergo apoptosis whereas B-cell with efficient BCR (B-cell receptor) receive survival signals to differentiate into plasma cells or memory B cells. From Patel et al, frontiers in immunology, 2021[3].

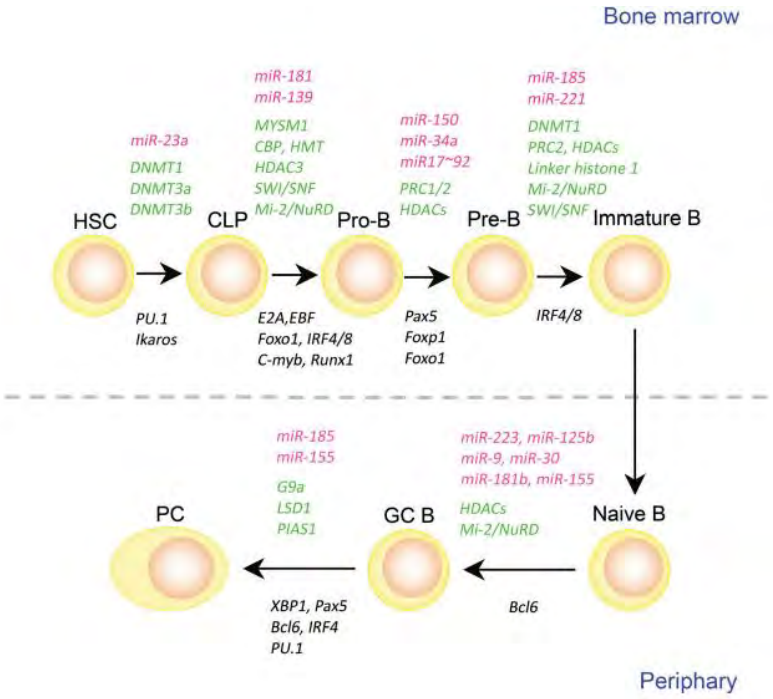

Figure 3: Principal known transcriptional factors, epigenetic regulator of B cell development

At each step of B cell differentiation key transcriptional factors, epigenetic modulators and miRNAs are involved in this process. In green is indicated epigenetic enzymes and chromatin remodeling complex; in red miRNAs and in black transcriptional factors. From Bao et al, Clin Rev Allergy Immunol, 2016 [4].

1.1.1. From HSC to Pro-B cell: V(D)J happens

HSCs cells are present in the BM, more accuretly in the central BM cavity, and posses the capacity of self-renewal. Differentiation of HCS into lymphoid-primed multipotent progenitors (LMPPs) and then into CLPs leads to B and T cell generation. B cell precursors rise from CLPs [5]. These different progenitors are categorized in 4 distinct subpopulations named (fraction A,B,C,D) or alternatively pre-pro B, pro-B and pre-B cells (Figure 1). These subpopulations can be distinguished by their differential expression of specific surface markers. By extension, pre-pro B cells are B220+, KIT-, CD19-, FLT3+, CD24-, CD43+, IgM-; pro-B cells express in addition KIT+, CD19+, CD24+ and lose FLT3 and finally, pre-B cells lose KIT and CD43 (Figure 1) [6].

The BM microenvironment and cell interaction are essential for B cell differentiation process. Indeed, intercellular contacts, growth factors and cytokines are necessary for triggering and regulate the activity of transcription factors responsible for the expression of the immunoglobulin (Ig) and other surface molecules by B cells. For example, CXCL12 and IL-7 secreted by stromal cells in the BM niche are key in early B cell differentiation steps by participating to B cell trafficking and antigenic presentation (Figure 4) [2].

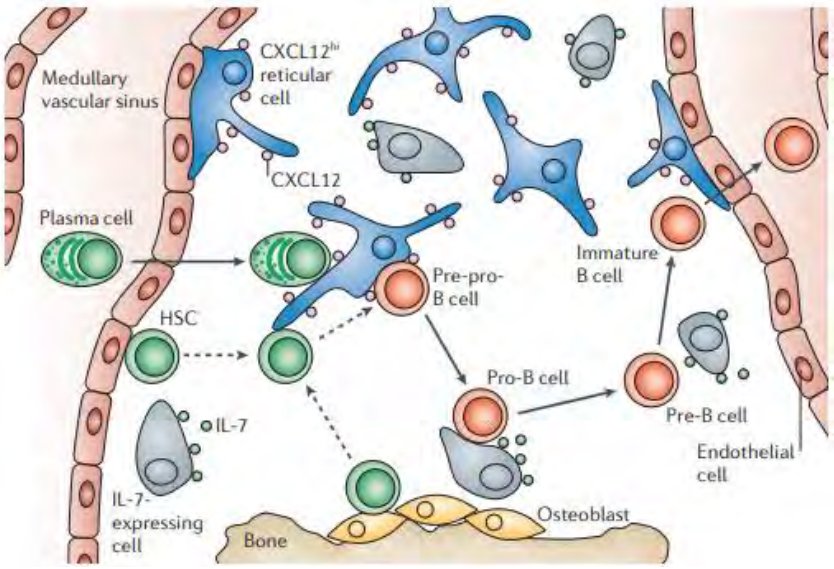

Figure 4 : Illustration of bone marrow cell niche and B cell movement upon B cell differentiation
In this model, pre-pro B cells are attracted by CXCL12hi secretion by reticular cells. Pro-B cells first join IL-7 expessing cells and pre-B cells leave them. Finally, immature B cells expressing IgM at their surface, exit the bone marrow to mature into the periphery. Once fully differentiated into plasma cell, B cell are attracted again by CXCL12hi reticular cells in the bone marrow. From Nagasawa, Nature immunolology reviews, 2006 [2].

V(D)J recombination is one of the most important steps in early B cell development leading to Ig expression at their surface and allows antibody diversity. This discovery of this process by Tonegawa et al was rewarded by a Nobel price in 1987 [7]. VDJ stands for Variable (Diversity) Joining and consists of the assembling of gene segments V, D and J (Figure 5). Thanks to the specific sites called recombination signal sequences (RSS), recombination sites are defined. Recombination-activating gene 1 and 2 (RAG1 and RAG2) are encoding key proteins for recombination initiation. Indeed, they induce double strand breaks in DNA between gene segments and RSS sequences [8–10]. These breaks, are further ligated by non-homologous end-joining, a repair mechanism. This event first occurs on the immunoglobulin heavy chain (IgH) of the CLP leading to the pro-B cell. It is important to notice that recombination occurs in a controlled step-by-step manner. Indeed, in pro-B cells, the heavy-chain (H) gene domain that includes the DH, JH, constant-μ (Cμ) and Cδ segments is accessible for rearrangement, thereby allowing D-to-J recombination to occur before V-to-DJ recombination. At the pro-B cell step, the light-chain (L) gene segments are not accessible for rearrangement. This is allowed at the pre-B cell stage where the germline VH gene segments are activated for rearrangement of the DJ junctions. Nevertheless, the κ-locus remains inaccessible for rearrangement. This occurs at the late stage of pre-B cell differentiation where the Ig heavy chain is produced [11].

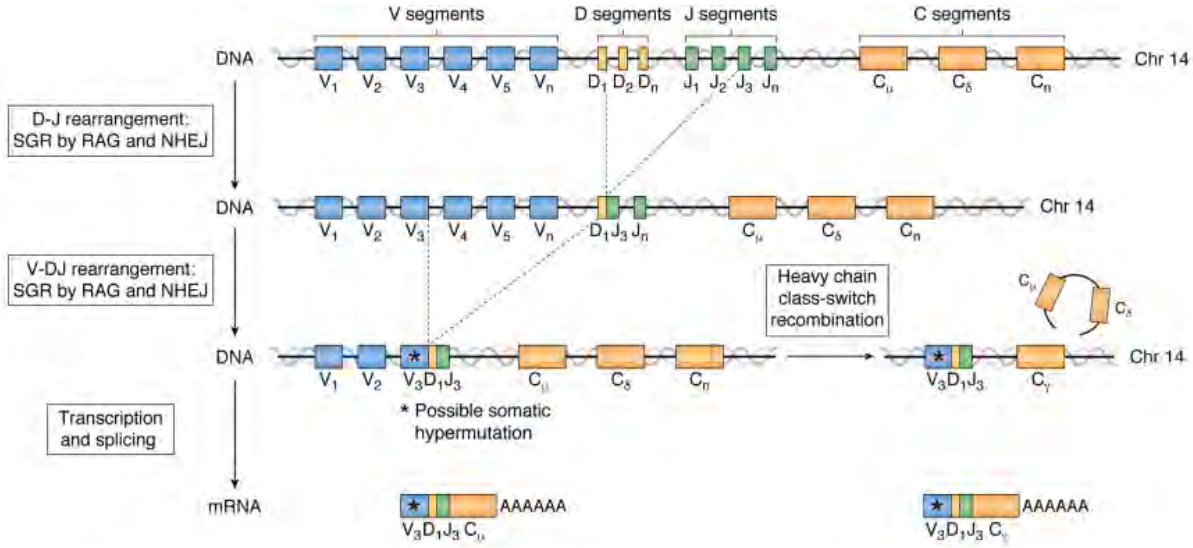

Figure 5 : Multistep VDJ recombination in the immune system.
This process requires several steps starting with RAG enzymes to create breaks in the DNA allowing reassembling of each gene segments followed by NHEJ DNA repair mechanism to reassemble new arrangement gene. From Kaeser and Chun, JBC review, 2020 [12].

This V(D)J recombination is also finely regulated by epigenetic changes allowing the accessibility in a stepwise manner (Figure 6). Indeed, in B cell progenitor K-alleles are positioned away from heterochromatin domains. Then in pro-B cell, they are joining the center, still away from heterochromatic regions. In early pre-B cells, one κ-allele is getting closer to the heterochromatin where histone hyperacetylation occurs. In late pre-B cells, this hyperacetylated allele undergoes a demethylation process allowing rearrangement.

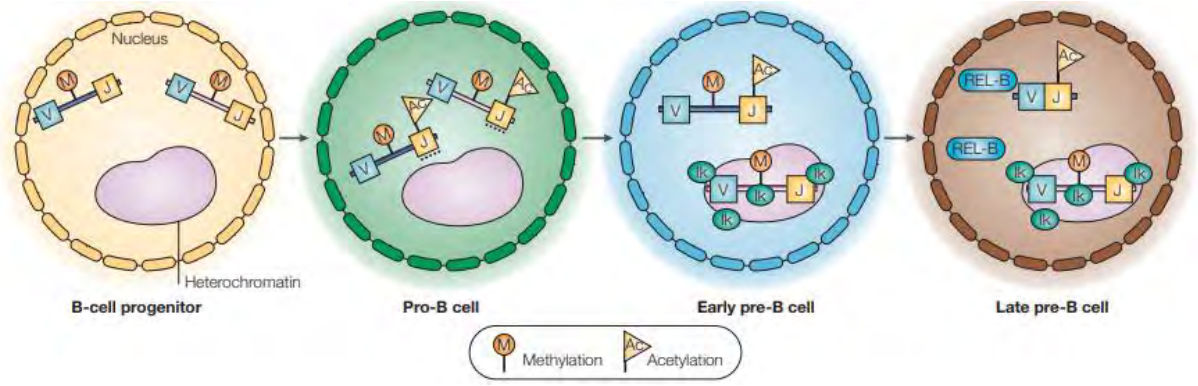

Figure 6 : Epigenetic modulation upon B cell differentiation.
Representation of an epigenetic modulation possible model allowing k-chain gene rearrangement. At the progenitor stage, two alleles are unarranged, methylathed and away from the heterochromatin. Step by step, alleles are acetylated and get closer to the heterochromatin to undergo recombination. From Bergman and Cedar, nature immunology reviews, 2004 [11].

1.1.2. From pro to pre-B cell and immature B cells: allelic exclusion happens

Once the V(D)J recombination is accomplished, the Igμ chains are generated allowing pre-BCR complexes assembly and expression by pre-B cells. During the pre-B cell phase of differentiation, one

of the main event is the occurrence of allelic exclusion [13]. This event occurs when only one allele of a gene is expressed while the other is silenced. To prevent more rearrangement, RAG proteins are downregulated. This process allows the generation of a specific B-cell receptor (BCR). After rearrangement, B cells express a BCR with recombined heavy and light chains characteristic of immature B cells. If rearrangement induces an autoreactive receptor, another V(D)J is stimulated to eliminate and replace it. If needed, the second allele become accessible and undergoes further editing, in order to reach a productive rearrangement (Figure 7).

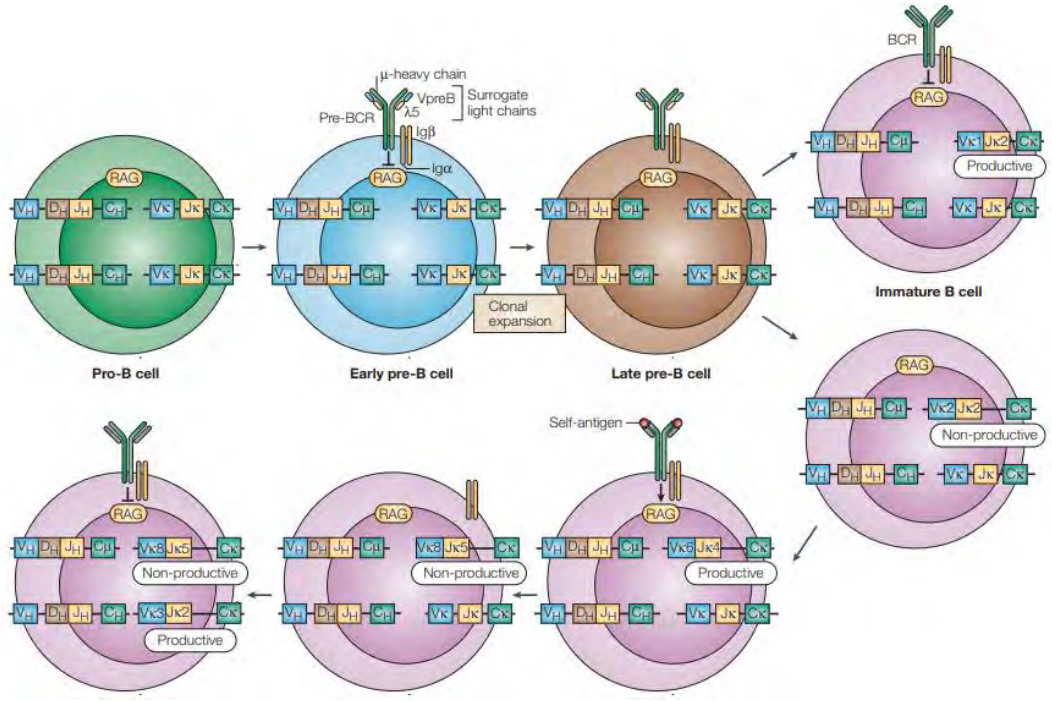

Figure 7 : B- cell receptor editing during B cell differentiation.
During early pre-B cell stage only one heavy chain alleles follow V-to-DJ rearrangement. Next, during late pre-B cell stage, μ-chain pairs with surrogate light chains and with Iga and Igb, form a complex. If the first rearrangement is non-productive, another rearrangement occurs leading to a productive one. From Bergman and Cedar, nature immunology reviews, 2004[11].

1.1.3. From immature B cells to naïve B cells

Before migrating to SLOs such as LN, immature B cells undergo negative selection to suppress by apoptosis cells with self-reactive BCR (Figure 8). Other cells receive prosurvival signals to continue their differentiation.

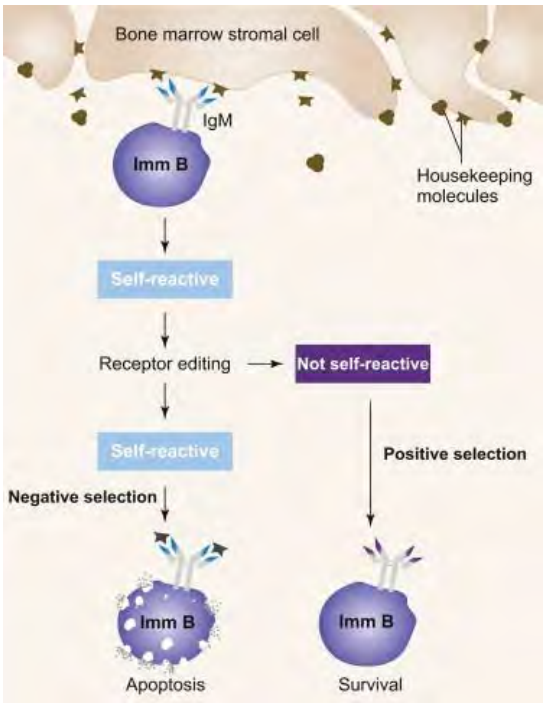

Figure 8 : Negative selection of reactive B-cells
From Tak W. Mak, Mary E. Saunders and Bradley D. Jett, Book Primer to the Immune Response 2014

Then, alternative splicing occurs during the transition from BM to SLOs allowing the expression of IgD and IgM at the cell surface [14] (Figure 9). These cells are called B mature naïve cells and are ready to migrate to SLOs.

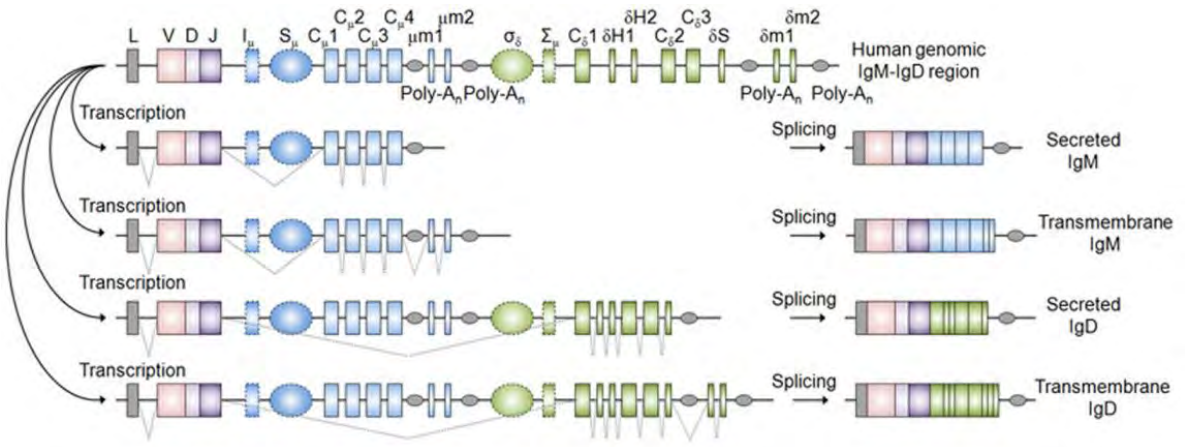

Figure 9 : Alternative splicing in immature B cells.
Depending on the splicing it can lead to either secreted or transmembrane IgM or IgD. From Chen and Cerutti, Immunol Rev, 2010 [15]

1.1.4. From naive B cell to GC B cells

Further B cell maturation occurs once the cells reach the LN. In contrast to the previous stages of differentiation, this phase is antigen dependent. CD40+ naive B cells are attracted in the paracortex of LN called T cell zone by cytokines secretion where they can interact with helper T cells expressing

CD40L. T cells and B cells interaction leads to their proliferation and GC formation with centroblasts forming the dark zone (DZ) and the light zone composed by centrocytes, follicular dendritic cells (FDC), T cells and macrophages (Figure 10). FDC act as antigen-presenting cells (APC) for B cells. This step is crucial for the B cell affinity selection. Only B cells with high affinity BCR receive prosurvival signals, while the others undergo apoptosis and are eliminated by macrophages to avoid auto-immune reactions [16,17].

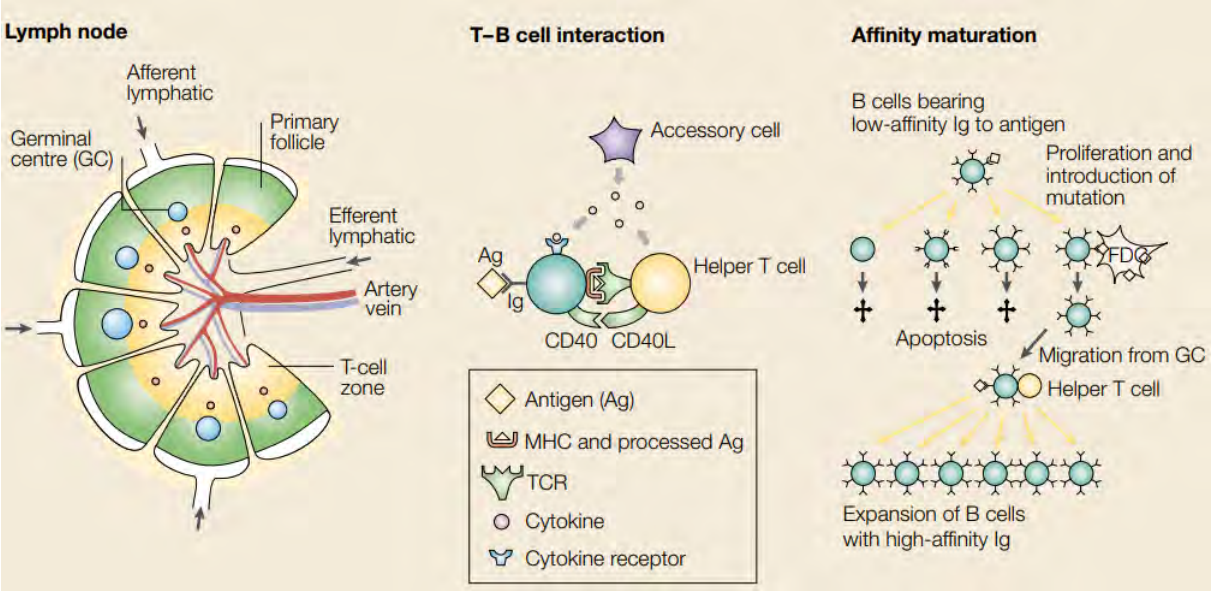

Figure 10 : Germinal center interactions implicated in B cell differentiation.
Lymph nodes are important sites in proliferation and selection of B cells. After contact with antigens, B cells are activated and proliferate to form germinal centers.

After B cell selection and activation, additional modifications to increase Igs diversity occur and are gathered in two main mechanisms: the hypersomatic mutation and class switching (Figure 11). The hypersomatic mutation is a process where point mutations are introduced in the variable regions of heavy and light BCR chains. This mechanism leads to the maturation and diversification of antibody repertoire. This step occurs in the DZ of GC by the action of centroblasts, that express activation-induced cytidine deaminase (AID), an enzyme important for DNA damage repair after substitution, deletion, insertion due to V(D)J rearrangement [18,19]. Moreover, during the DNA repair process, the additional point mutations are introduced into DNA coding variable regions of Ig, thus further increasing diversity of antibody repertoire [20]. Altogether, hypersomatic mutation allows B cell selection based on their BCR increasing affinity to antigens.

The other mechanism, class switching, uses AID enzyme to induce an irreversible DNA rearrangement. During this process, the type of cytokines and co-stimulatory receptors will guide Ig

isotype. Indeed, through this step, switch sequences upstream each gene led to bring closer IgM and IgD. This step is also under the control of IRF4 capable of regulating indirectly AID expression [20].

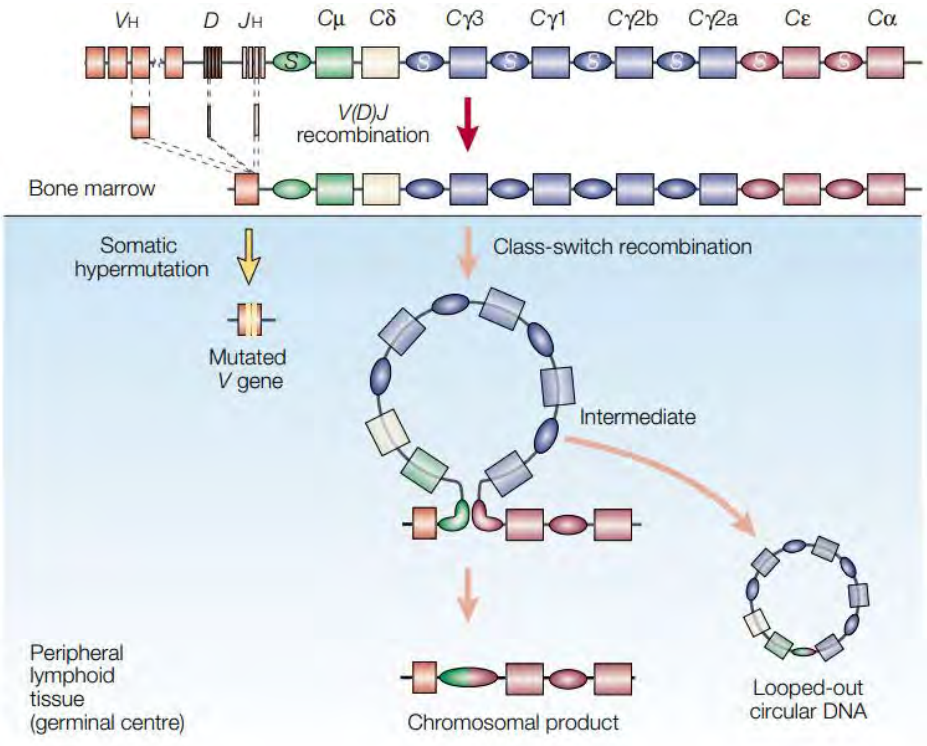

Figure 11 : Remodeling of Immunoglobulin during somatic hypermutation and class-switch recombination. V(D)J occurs in bone marrow when somatic hypermutation and class-switch recombination occurs in germinal centers. Somatic hypermutation promote mutations in the rearranged V exon to provide diversity in B cell antigen specificity. Class-switch recombination induces a deletion between Su and another S region to bring closer constant C region exon and V exon.

1.1.5. What do you want to be when you grow up? Plasma cell or memory B cells

The final step in B cell differentiation is to guide to become either a plasma cell or a memory B cell. This mechanism is not well known, nonetheless some genes have been identified. One of the example is paired box 5 (PAX5) gene, which inactivation is important for the differentiation step into plasmocytes cells. This is followed by BCL-6 inhibition, leading to the formation of plasmocytes capable of secreting antibodies with high affinity. Plasmocytes localization define their life expectancy. Indeed, short living plasmocytes stay in the LN where long living plasmocytes transit to the blood circulation and then to the BM where they can remain for years. B memory cells present a high life expectancy both in the blood circulation and in various tissues, where they act as immune guardians. If needed, they are able to detect specific antigens and be the first cells on the site to provide a response through massive differenciation into plasmocytes (Figure 12).

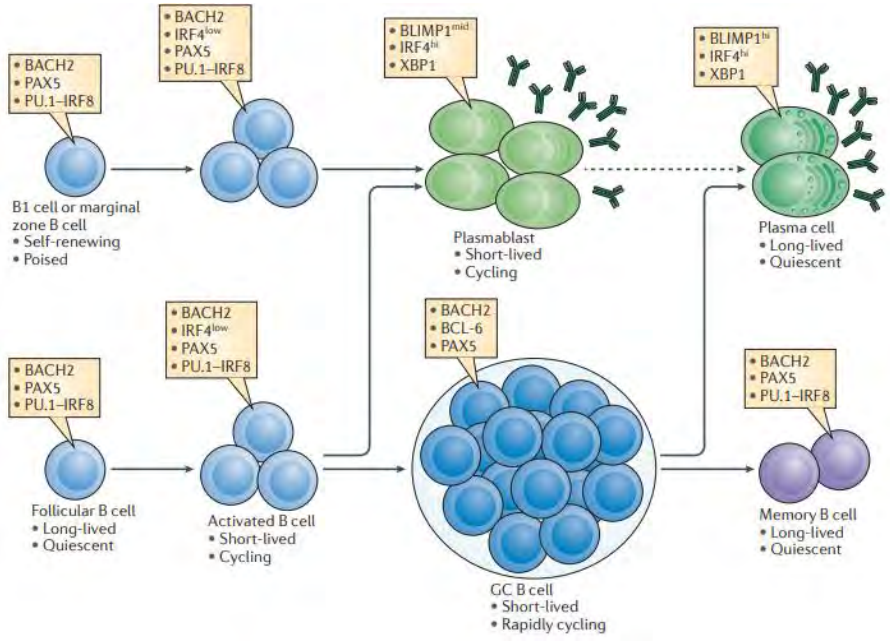

Figure 12 : The fate of mature B cells: Plasma cells or memory B cells.
Mature B cells are located in follicles characterized by expression of paired box protein 5 (PAX5), interferon-regulatory factor 8 (IRF8) and BTB and CNC homologue 2 (BACH2). Upon activation, B cell proliferate and can differentiate into short-lived plasmablasts expressing IRF4 and X-box binding protein 1 (XBP1). Follicular B cells during the GC reaction can upregulate BCL-6 and IRF4. After selection of high affinity receptors mature B cell exit the GC to become memory B cells or plasma cells expressing high level of BLIMP1, IRF4 and XBP1 and are able to produce numerous antibodies. From Nutt et al nature review 2015 [21].

1.2 Immune effectors differentiation and mechanism of action: the example of γδ T cells

In addition to B cells differentiation, CLP cells give rise to T cells. These two components of the immune system belong to the adaptive immunity that trigger a low but specific and efficient response toward threats. On the opposite, the innate immunity, composed mainly by myeloid cells, allows a rapid but less specific response. In between, two classes of T cells, NK cells and gamma delta T cells (γδ T cells) are at the frontier of innate and adaptive immunity (Figure13).

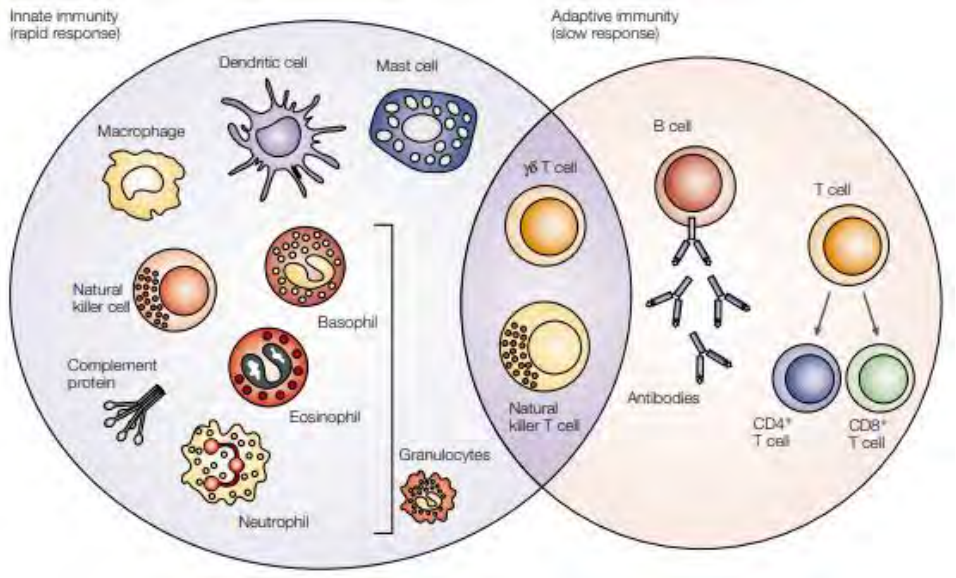

Figure 13 : Immune cell composing innate and adaptive immunity
From Dranoff, Nature Cancer Review, 2004 [22].

1.2.1. Innate and adaptive immunity: two interconnected systems

Our body is systematically under the attack from exogenous (micro-organisms, macromolecules) or endogenous threats (cancer). In order to protect from these aggressions, our immune system is in charge of monitoring, recognizing and eliminating these exogenous agents, pathogens or damaged cells. There are two types of immunity responsible for maintainence of homeostasis: innate immunity able to provide a fast response but not specific without memory and adaptive immunity, that takes much longer to act but is very specific and provide memory against future attacks. Even if these mechanisms are described separately, they are interconnected all along the span of immune response, in order to maximize its efficiency (Figure 14).

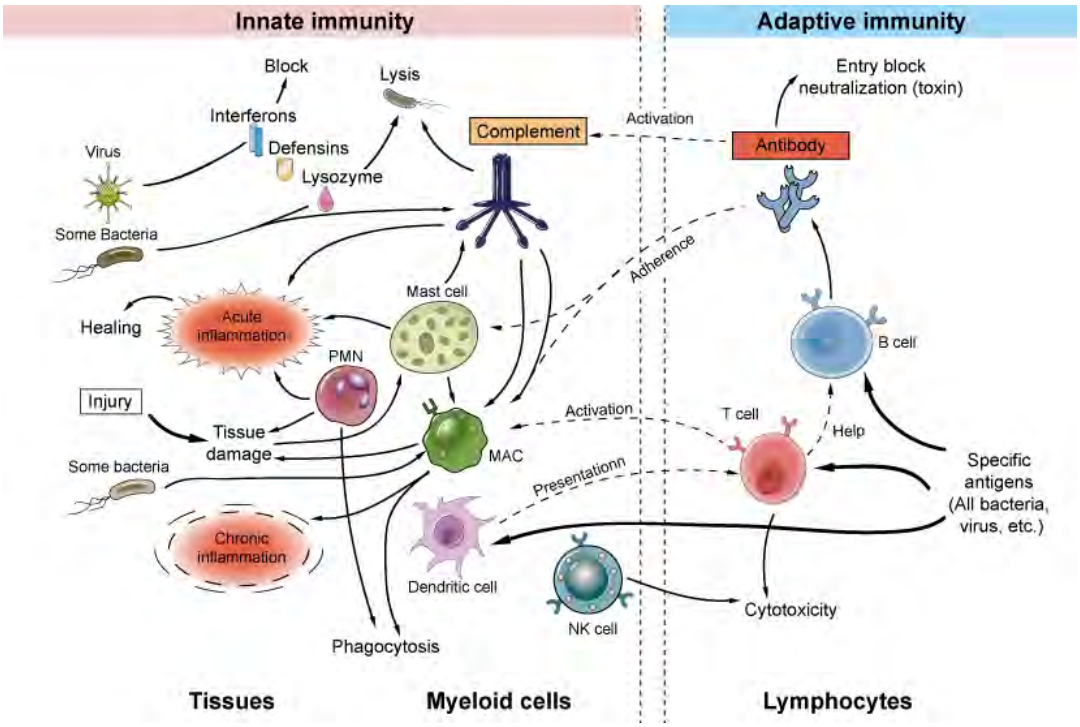

Figure 14 : Innate and adaptive immunity, actors and interactions
From https://www.creative-diagnostics.com/innate-and-adaptive-immunity.htm

Innate immunity is known as the first line of defense. Its main actors are myeloid cells, γδ T cells and NK cells. The innate immunity response is activated by the detection of danger signal, including pathogen-associated microbial patterns (PAMP) or damage-associated molecular patterns (DAMP). These signals can be sensed by so-called pattern recognition receptors (PRR) present on the surface of various immune cells. For instance, the PRR family is composed of TLR toll-like receptor (TLR), C-type lectin receptor (CTLR) and nucleotide binding oligomerization domain – like receptor (NLR). After the binding of danger signal to PRR, an inflammatory environment composed of a ballet of secreted cytokines appears. If TLRs are activated, MyD88 or TRIFF pathways are triggered, leading to secretion of IL-12, that in turn can activate NK cells. In the next step, NK cells can secrete IFNγ, that

among others leads to recruitment and polarization of macrophages. In turn, activated macrophages produces IL-8, that induces chemotaxis of neutrophils.

On the other hand, NLR stimulation can lead to inflammasome establishment, activation of caspase 1, and further secretion of pro-inflammatory cytokines, including IL-1b and IL-18 by macrophages[23]. Attraction of macrophages then induces phagocytosis of bacteria, cell debris which are internalize in an internal compartment called phagosome, where they are degraded.

Another mechanism that can be used during innate immunity is dependent on the complement. It involves the sequential proteolysis of proteins to generate enzyme complexes with proteolytic activity [24]. Three different pathways can trigger this system: classical (activated by certain antibodies bound to antigens), lectines (activated by plasma lectin that binds to mannose residues on microbes) or alternative (activated on microbial cell surfaces without antibodies). Once the complement system is triggered, the cascade of subsequent cleavages of proteins begins, leading to membrane attack complexes formation in the targeted pathogen, resulting in lysis. The remaining cellular debri is further phagocyted by specialized cells. These innate immune mechanisms can be active within the span of minutes and then last for days (Figure 14).

Adaptive immunity, in opposition to the innate immunity, requires time to recruit all the necessary actors (mainly B and T cells) in order to develop a specific response. This specific response can be further preserved by specific memory cells, allowing a quick response in case of subsequent encounter of the same antigen. Innate and adaptive immunity are linked as the chemokines and cytokines secreted by cells from the innate compartment trigger and attract cells from the adaptive compartment. T cell activation goes through a process of different steps: first, antigen presentation by APC *via* the interaction with major histocompatibility complex (MHC)/peptide/T-cell receptor (TCR); second, the co-stimulation of CD28 and finally, cytokine-induced signals. Depending on the cytokine signal received, CD4+ naïve T cells can differentiate into different actors of the immune system: Th1 (cellular response), Th2 (humoral response), Th9 (tissue inflammation), Th17 (extracellular pathogens), Th22 (skin infections) and iTreg (self tolerance) [25].

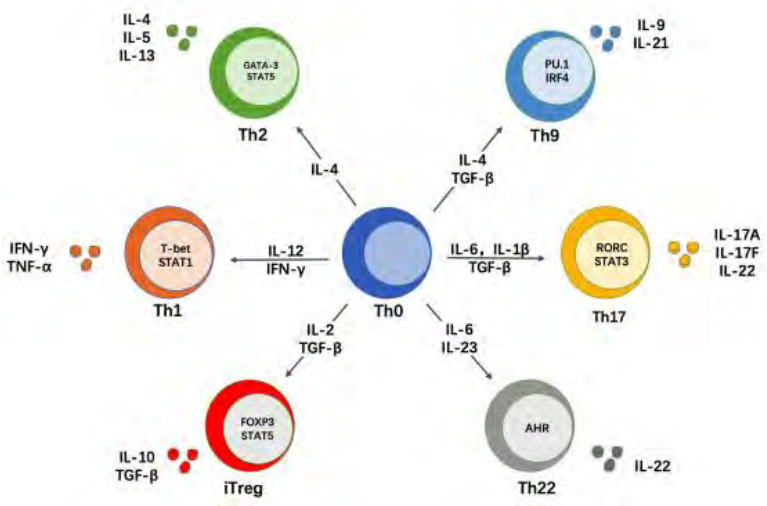

Figure 15 : Polarization of naive T cells upon cytokines exposure.

From Lee et al, Front Immunol, 2021 [25].

In cancer, immune cell effectors are the main actors in elimination of malignant cells. These effector immune cells belong to the branch of Th1 cellular response which involves for example APC, CD4+ and CD8+ T lymphocytes. Indeed, Th1 cells produce IFNγ, IL-2 and TNFβ, which activate macrophages and are responsible for cell-mediated immunity and phagocyte-dependent protective responses. After binding of MHCII, expressed on naïve CD4+ T cells, to APC through antigen and in presence of IL-12, differentiation into effector Th1 CD4+ T cells able to secrete IFNγ, TNFα and IL-2 occurs. This secretion helps in the differentiation of CD8+ naive T cells into activated CD8+ T cells. Indeed, besides the interaction of MHCI/antigen/APC, they need cytokines secreted by Th1 to finalize their maturation process and become CTLs. CTLs exhibit the capacity to eradicate target cells through the action of granzymes and perforins. A fraction of CD8+ T cells constitute a pool of memory cells, ready for any second exposure to the same threat thus triggering a more efficient response [25].

As represented in figure 13, NK cells and γδ T cells are particular cell types as they are at the frontier of innate and adaptive immunity. These cells can be recruited at the first sign of danger and do not require MHCI or II interaction with TCR to trigger their cytotoxic action. Although the role of NK cells is important in cancer immune response [26], γδ T cells are no less important and their function in tumor immune escape (IE) in B-NHL is particularly important [27,28]. Thus, we will focus the next part of this introduction on this cell population.

1.2.2. αβ/γδ T cells lymphopoiesis and focus on γδ T cells plasticity

In the BM, HCS cells will differentiate into lymphoid precursors that transit from the thymic cortex to the thymic medulla to process to further T cell differentiation. The first steps of differentiation are

common between αβ and γδ T cells. At the stage of double negative (DN) progenitor, these cells do not express TCR, CD4 or CD8, but do express CD117, CD44, CD25 and CD24. Separation between αβ T cells and γδ T cells happens during the phase DN3a characterized by a loss of CD44 and CD117 markers (Figure 16) [29]. Melichar et al demonstrated that an inhibition of the transcription factor SOX13 leads to γδ T cell differentiation [30]. Another important actor involved is Notch receptor that when highly expressed, directs into γδ T cell lineage, whereas when weakly expressed, induces a αβ T cell differentiation [31].

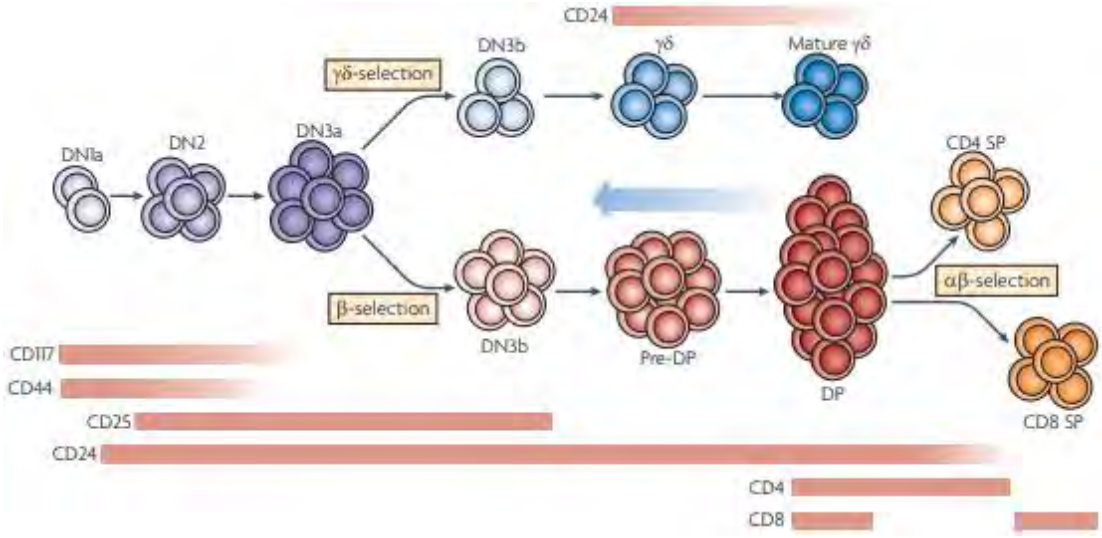

Figure 16 : Differentiation step of T cells, αβ and γδ selection.
From Ciofani et al, Nat Rev Immunol [29]

TCR diversity for αβ and γδ T cells depends on the somatic recombination V(D)J of different segments composing αβ or γδ chains. This mechanism has been described before in BCR rearrangement (Figure 17). Gene coding for γ chain is constituted of segments V and J and for δ chain is constituted of V, D and J.

This recombination leads to different subtypes of γδ T cells which vary in proportion, function and localization in the body. Indeed, three main classes of γδ T cells are described in human and two in mouse (Figure 18). In humans, Vγ1 T cells are located in musocal epithelial tissues, Vγ2 T cells are preferentially in peripheral blood and Vδ3 T cells mainly in the liver [33–35].

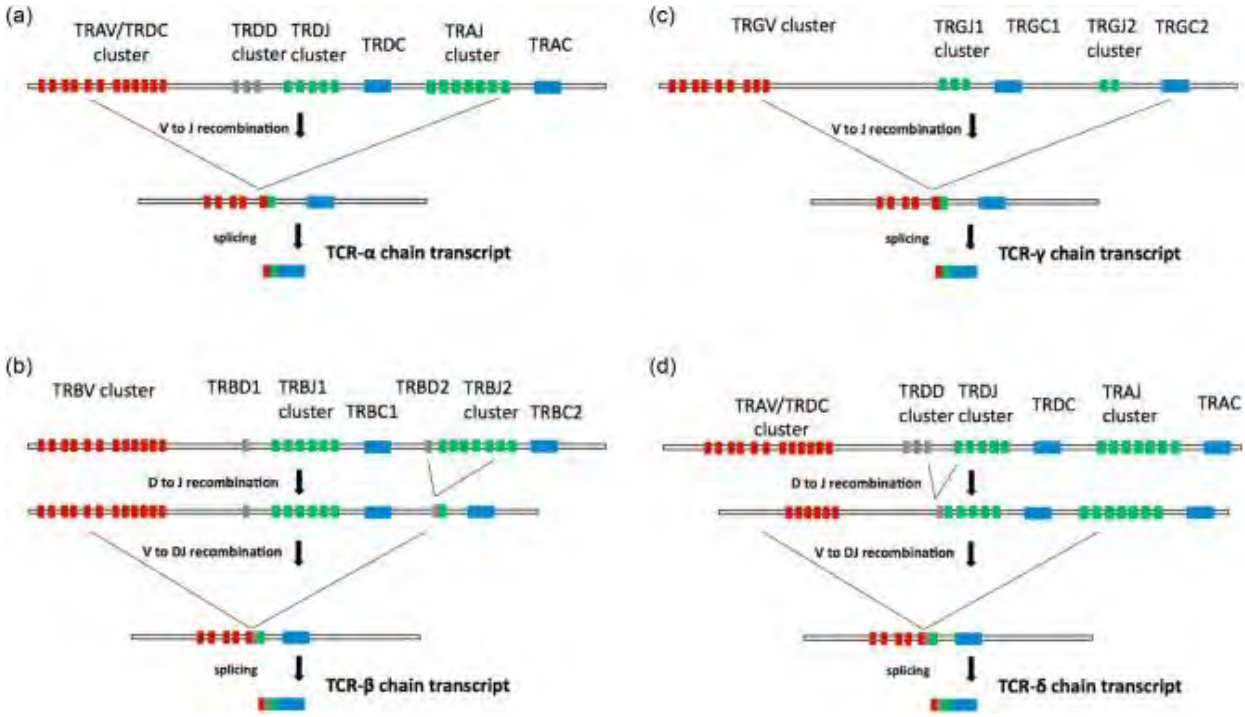

Figure 17 : Somatic recombination of TCR
(a) TCR-alpha chain, (b) TCR-beta chain (c) TCR-gamma chain, (d) TCR-delta chain. From Attaf et al, Clin Exp Immunol, 2015 [32].

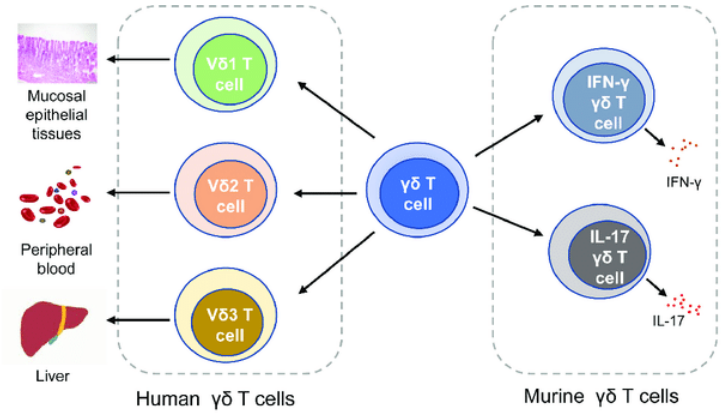

Figure 18 : γδ T cells subtypes localization in human and mouse.
From Ma et al, Front Immunol, 2020[36]

In human, the subpopulation TCR Vγ9Vδ2 represents only 1 to 5% of total PBMC (peripheral blood mononuclear cells), whereas Vδ1 γδ T cell can represent up to 50% of lymphocytes in the intestines [37].

In addition to their different subpopulation's types and localization in the body, γδ T cell display an impressive phenotypic plasticity depending on the signals they receive. For example, by the action of IL-12 and IL-18, Vγ9Vδ2 T cells can be polarized into Th1 types of cells, able to secrete IFNγ and TNFα. On the other hand, IL-1b, IL-6 or IL-23 will orient these cells into Th17 side [38,39] (Figure 19).

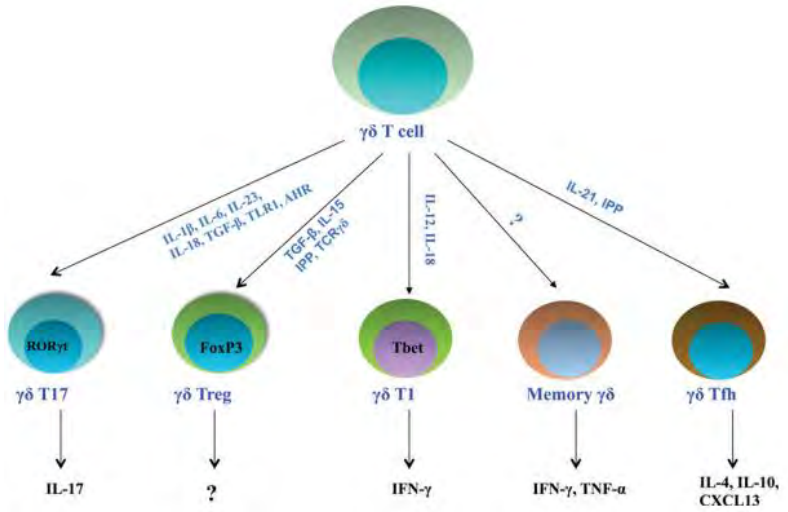

Figure 19 : γδ T cell plasticity.
From Paul et al, International reviews of immunology, 2013.[39]

This ability to differentially respond to cytokines allowed γδ T to display diverse functions, from: lysis of infected or stressed cells, cytokine production, cooperation with B cells and help for IgE production, priming of αβ T cells *via* antigen presentation, dendritic cell (DC) maturation or regulation of stromal cell function *via* growth factor production [40]. Depending on their polarization, they can be involved in immune responses related to bacteria, virus and parasites, as well as in anti-tumoral actions through cytokines secretion (IFNγ, TNFα, IL-17, IL-13), chemokines secretion (MIP-1A, RANTES) and cytotoxic function (Fas ligand, TRAIL, granzyme, perforin,). Interestingly, they can also play the role of APC, just like mature DC, by recognizing soluble protein antigens, processing them and inducing proliferation of cells from the adaptive immunity branch, such as CD4 T cells [41]. Thus, γδ T cells are able to interact with many other cells type to provide an efficient immune response.

Among Vδ2 T cells, the ones co-expressing Vδ2 and Vγ9 chain, Vγ9Vδ2 T cells, are the most abundant. These cells mediate Th1 and cytolytic activities in response to stimulation by soluble phosphoantigens (PAgs) or cancer cells. They can be divided in the four subtypes, depending on their differentiation status following CD27 and CD45RA expression markers (Figure 20): naives (T_N) CD27+CD45RA+ presenting a potent proliferation but no capacity to secrete cytokines or lytic activity;

central memory (T_{CM}) CD27+CD45RA- that display high proliferation and low cytokine secretion capacity; effector memory (T_{EM}) CD27-CD45RA- presenting no proliferation but high cytokine secretion and low potential lytic and finally, effector memory re-expressing CD45RA (T_{EMRA}) CD27-CD45RA+ that are not able to proliferate but present a high lytic potential [42].

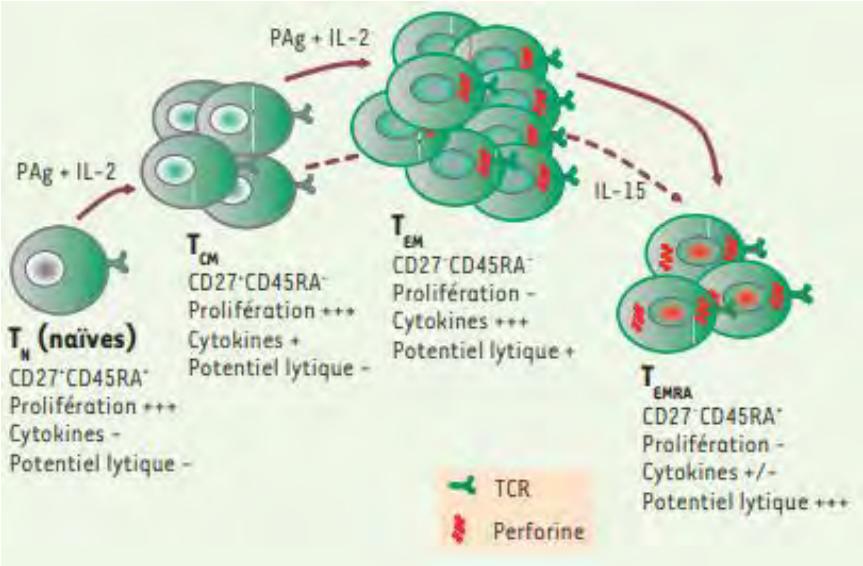

Figure 20 : γδ T cell differentiation from T_N to T_{EMRA}.
From Catros et al, Med Sci, 2010 [42]

Their activation and mechanisms of action, in particular in cancer, are developed in the next part.

1.2.3. γδ T cell pro and anti-tumoral activity: focus on Vγ9δ2 T cells activation and function

γδT cells present an unique role in the immune surveillance and also an advantage over αβ Tcells as they can directly recognize molecules that are expressed on cancer cells without needing antigen processing and presentation [43,44]. Moreover, many studies have demonstrated their capacity to infiltrate solide tumors [45], recognize and eliminate *in vitro* tumor cells from myeloma [46,47], non-hodgkin lymphoma [48], prostate cancer [49] and colon cancer [50] for instance. Interestingly, Catros et al showed that isolated autologous Vγ9Vδ2 T cells from hepatocarcinoma patients were able to kill tumor cells without affecting normal cells [51]. Thus, this γδ T cell subtype became of great interest in cancer therapy.

Circulating Vγ9Vδ2T cells are present in a small proportion in healthy PBMC (1 to 5%) but exhibit rapid proliferation, cytokine secretion and cytolytic action after activation *via* PAgs that are expressed by tumor cells or induced by amino bisphosphonates treatment [52–54]. PAgs are metabolites composed of an alkyl radical and a pyrophosphate. They are deriving either from the methyl erythritol phosphate pathway in microbial pathogens, or from eukaryotic mevalonate pathway in tumors cells [55,56]. On the basis of their structural conformation, synthetic PAg such as bromohydrine pyrophosphate (BrHPP)

have been generated, showing an efficient activation of γδ T cells *in vitro* and *in vivo* [57]. Other PAgs have been reported to activate γδ T cells such as natural ones (isopentenyl pyrophosphate IPP, dimethylallyl pyrophosphate DMAPP, hydroxyl dimethylallyl pyrophosphate HDMAPP) or synthetic ones (C-HDMAP and BrHPP) [58].

Even if γδ T cells do not need any MHC interaction to be activated, TCR is still essential following PAgs recognition, in order to initiate their activation (Figure 21). BTN3A butyrophilin-3 (BTN3A) is a key element in PAg recognition and its binding to TCR induces Vγ9Vδ2 T cell activation [59]. Indeed, Scotet et al discovered that BTN3A is capable of activating TCR to induce cytokines secretion and cytolytic function. RHOB has also been identified recently, as to be important for interaction with PAgs thus inducing conformation modification in the membrane bound BTN3A1 that in turn activates Vγ9Vδ2 TCR [59].

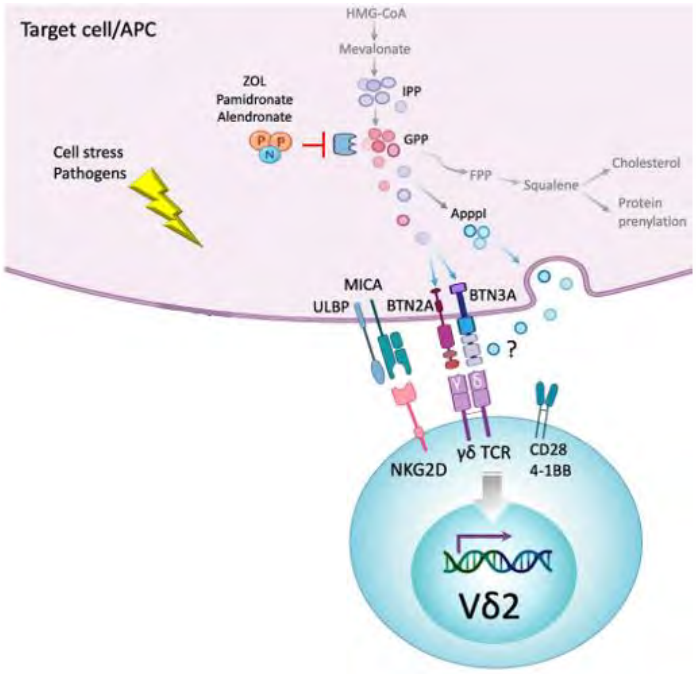

Figure 21 : Partners important for γδ T cells activation.
Adapted from Yazdanifar, Cells, 2020[57]

Natural killer cell receptors (NKRs) represent the important partners in Vγ9Vδ2 T cell activation. Among them, NKG2D, a lectine-C receptor binding MICA/MICB and ULBPs molecules, are a major co-stimulatory receptor for Vγ9Vδ2 T cells. This receptor is recruited after formation of the immunological synapse between Vγ9Vδ2 T cells and target cells and will trigger the cytotoxic signals towards target cells. Because Vγ9Vδ2 T cell activation does not depend on MHC interaction, they need other control mechanism to avoid self-immunity. To do so, there is an equilibrium between activator receptors (NKG2C/CD94) and inhibitor receptors (NKG2A/CD94).

In the tumoral context, γδ T and Vγ9Vδ2 T cell can provide an anti-tumoral or a pro-tumoral effect (Figure 22) [37]. It is well-known that γδ T cells and in particular Vγ9Vδ2 T cell play an important role in immune response against several tumor types (lymphoma, myeloma, breast cancer, colon, lung…) through their cytotoxic activity and by stimulating other cell types such as DC and cytotoxic CD8+ T cells [51,60,61]. This process starts with the capacity of γδ T cell to recognize tumor cells through interaction with various molecules such as PAgs, BTN3A1, endothelial protein C receptor (EPCR), as presented in Figure 22 left A. Once γδ T cells recognize a malignant cell, they become activated and trigger their direct cytotoxic functions based on : perforin/granzyme secretion, death receptor in response to TRAIL or Fas-L expression and antibody-dependent cell-mediated cytotoxicity (ADCC) in the presence of tumor-specific antibodies. Moreover, they can have indirect effect on tumor cells by secreting TNFα and IFNγ and they promote DC maturation and T cell differentiation towards Th1 cells that will in turn display anti-tumor function (Figure 22 left B). Anti-tumor T cell response is also increased by the γδ T cell property to capture and express CD1b molecules able to promote iNKT cell activation. γδ T cells present also APC capacity through the expression of MHCI and II, CD40, CD83 and CD86 to activate T cells presenting cytotoxic activity against tumor cells (Figure 22 left C). With CD137L expression, γδ T cells provide a co-stimulatory signal to CD137+ NK cells and increase their cytotoxic effect (Figure 22 left D). γδ T cells are able to support B cell antibody production responsible for humoral anti-tumor response (Figure 22 left E). On cancer patient sample, Tosolini et al by using a deconvolution of human cancers microarrays, showed that CRC patients presenting a high infiltration of Vg9Vδ2 cells revealed a higher overall survival (OS) [62].

In contrast, some recent studies highlighted that the increased level of tumor infiltrating γδ T cells, was associated with poor prognosis in some cancers, such as breast and colon cancer [63]. These contradictory observations opened a new perspective for research on pro-tumoral function of γδ T cells. Thus, it has been shown that γδ Th17 and Treg-like cells producing IL-17 and TGFβ, can favor tumor cell proliferation and dissemination and are implicated in chemoresistance (Figure 22 right A). Moreover, γδ T cell can abort DC maturation, thus impairing their APC function and further T cell differentiation and activation [64] (Figure 22 right B). Recruitment of myeloid-derived suppressor cells (MDSC) and small peritoneal macrophages by γδ Th17 is another example of their pro-tumoral role (Figure 22 right C). Finally, γδ Treg produce immunosuppressive factors such as IL-4, IL-10 and TGF-β cytokines, which show broad immunosuppressive activity, impairment of cytotoxic activity of CD8 T and NK cells [65] (Figure 22 right D).

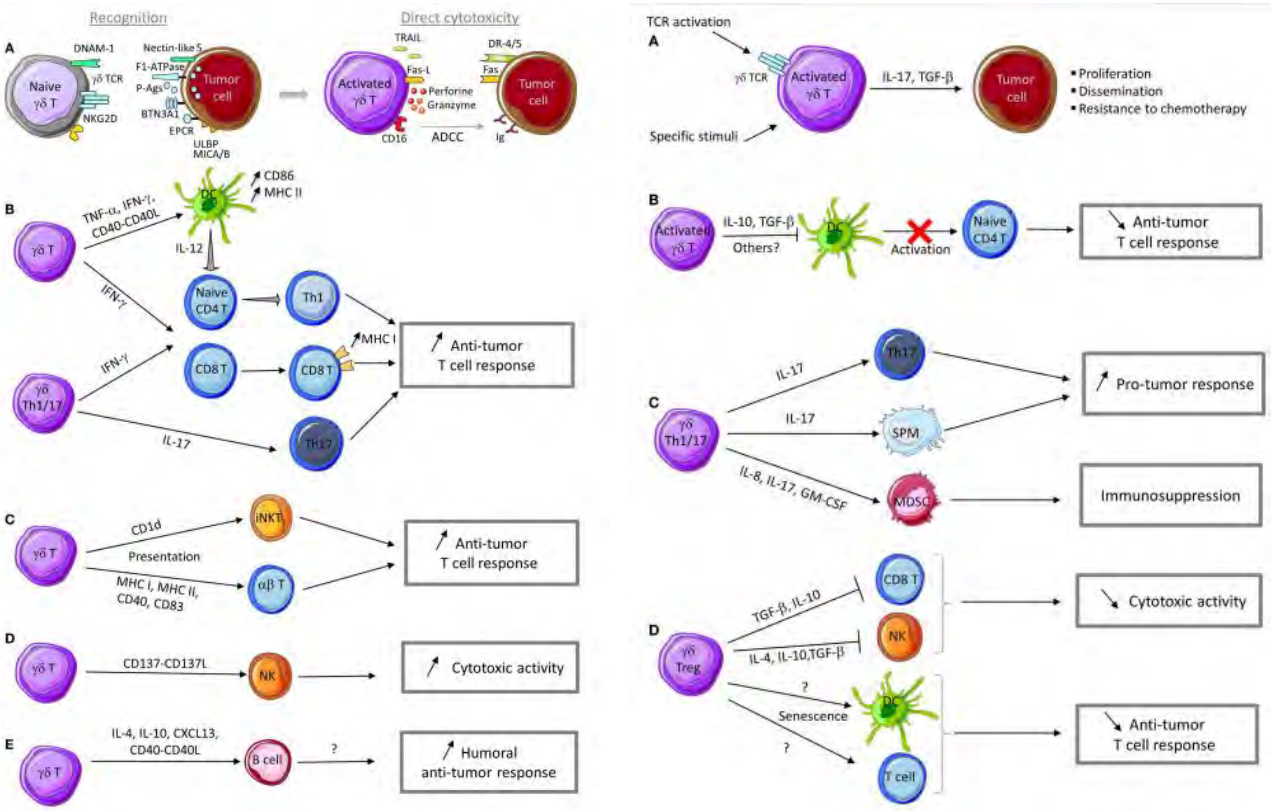

Figure 22 : anti and pro-tumoral activity of γδ T cells.
From Lafont et al, frontiers in immunology, 2014 [37].

The advantages conferred by the lack of MHC restriction, their capacity to recognize a large panel of antigens, trigger a rapid and efficient anti-tumor response drew the curiosity of researchers to use Vγ9Vδ2 T cells in therapeutic strategies, involving : monoclonal antibodies (mAbs), adoptive cell transfer, or treatment with cytokines and PAgs in order to stimulate their anti-tumoral action.

Adoptive cell transfer is an elegant strategy, in which cells from patient are cultivated *ex vivo* with the intent to amplify γδ T cells which are then reinjected to patient in order to excert their anti-tumoral effect [66]. Among them, new sophisticated immunotherapies using γδ T cells have seen the light of the day in these past few years, including : delta one T cells (DOT cells) consisting of δ1-oriented γδ T cell repertoire, characterized with a good migratory potential and high level of NKG2D and cytotoxic receptors, that are able to reach tumor cells and eliminate them [67]; Chimeric antigen receptors expressing T cell (CAR γδ T cells), consisting of Vγ9Vδ2 T cells genetically modified to force expression of CAR reactive against tumors [68] and finally T cells engineered with a defined γδ TCR (TEGs), for which the concept is to force genetical expression of TCR γδ into αβ T cells, in order to gain capacity of γδ reactivity against tumors combined with capacity to proliferate and acquire memory functions from αβ T cells [69] (Figure 23).

No clinical trials are using these approaches for now, but nonetheless they represent very interesting and promising new strategies.

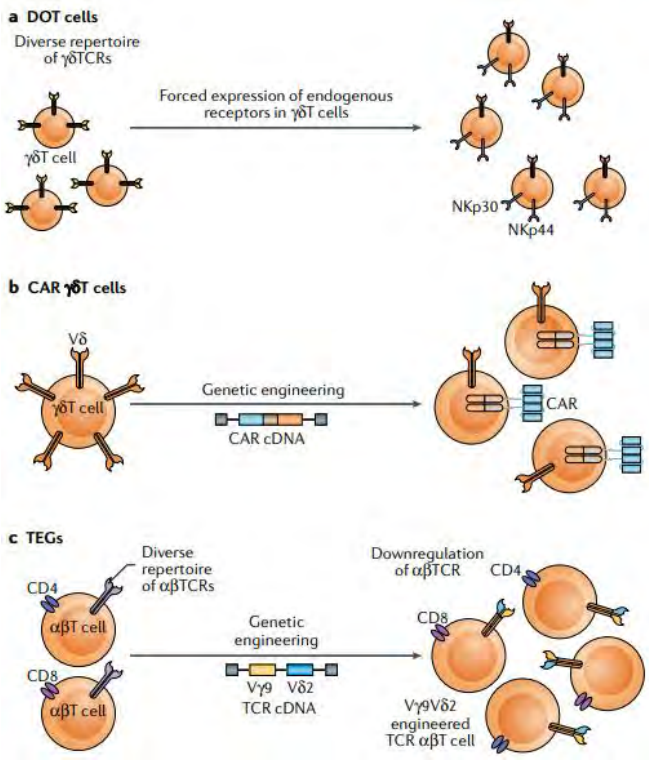

Figure 23 : New adoptive cell transfert concept using γδ T cells.
From Sebestyen, Nature drug discovery review 2020 [66]

Over the years, many evidences showed the interest in enhancing γδ T cell activity in lymphoma. In B-NHL, γδ T cells and more specifically Vγ9Vδ2 T cells have shown their potent capacity in elimating tumor cells. Braza et el conducted a study where they compared frequency and distribution of γδ T cell in 51 LN from patients with FL (FL-LNs) and 28 patients with inflammatory LN (I-LNs) and found that they were less abundant in FL-LNs than I-LNs [70]. In FL-LNs, most of γδ T cells were found outside of the tumor follicles and expressed CCR7 in contrast to peripheral blood γδ T cells. Interestingly, γδ T cells isolated from FL patients and healthy donors presented the same expansion capacity *in vitro*, opening perspectives for adoptive cell transfert in FL patients. Targeting γδ T cells capacity to infiltrate the tumor and kill cancer cells is an interesting therapeutic strategy. Moreover, anti-CD20 mAbs, a gold standard used in almost all B-NHL treatment strategies, is known to trigger ADCC by γδ T cells. Indeed, Braza et al, have demonstrated that GA101 (type II targeting CD20 mAb) is able to potentiate γδ T cell killing of tumor cells through ADCC[48]. This results were also demonstrated by my team who described a potentialization of γδ T cells ADCC activity upon anti-CD20 treatment by

blocking PD-1 in a 3D *in vitro* models of FL cell line co-cultured with γδ T cell primary cell line and *in vivo* in FL xenograft models [71].

Another interesting way to benefit from γδ T cells anti-tumoral action in therapeutic strategies, is to promote their proliferation and activation by PAgs and IL-2 [72]. This strategy was tested in hematological malignancies with a pilot study in 2003 associating low-dose of IL-2 in combination with pamidronate in nineteen patients with relapsed/refractory low-grade non-Hodgkin lymphoma (NHL) or multiple myeloma (MM) [73]. They demonstrated that response to treatment was obtained in patients exhibiting a proliferation of γδ T cells. This was the first clinical trial showing that γδ T cell mediated-immunotherapy was possible [73]. In FL, a study enrolling patients with low tumor burden were included in a treatment associating rituximab, IPH-1101 and IL-2. Unfortunately, the results were desapointing with only 26% complete response (CR) and 18% partial response (PR). This result could be explained by tumor IE mechanisms as described later [74].

Foregoing examples present, γδ T cells as an attractive tool in immunotherapy (IT) strategies for B-NHL. However, further investigations are needed to find new targets to unleash anti-tumoral potential and to improve their adoptive cell transfert therapy use.

1.3 Lymphomagenesis: B-NHL genesis

As presented in the previous part, lymphopoiesis is a strictly regulated process, where accumulation of dysregulation in epigenetic, genetic or B cell migration can leads to neoplastic cells and lymphoma genesis. Hematological malignancies can be divided into: leukemias, including acute lymphoblastic leukemia (ALL), acute myeloid leukemia (AML), chronic lymphocytic leukemia (CLL), chronic myeloid leukemia (CML); lymphomas, including Hodgkin and Non-Hodgkin lymphomas and myelomas represented for instance by multiple myeloma (MM).

In particular, B-lymphomas are characterized by an anarchic accumulation of B cells and differentiation blockage in LN. They represent the seventh most common types of cancer in occidental population, with a higher incidence rates in men than women, in adults than children and in industrialized countries compared to developed countries [75]. They are categorized into precursor or mature cell neoplasms by the world human organization (WHO) classification [75]. Mature cell neoplasms comprise of B cell lymphomas, T cell lymphomas and Hodgkin lymphoma (HL). Lymphomas are historically distinguished in Hodgkin and non-Hodgkin lymphoma in the behalf of the first lymphoma discovered by Thomas Hodgkin in 1832 [76]. HL are characterized by the presence of giant cells called Reed Sternberg cells. Lymphomas that lack these cells are, by opposition, called non-Hodgkin lymphoma (NHL). More than 35 subtypes of NHL have been identified so far, with follicular lymphoma

(FL) and diffuse large B cell lymphoma (DLBCL) representing the most frequent cases of B-NHL. B-NHL comprise of indolent (FL or Marginal zone lymphoma MZL, Mantle cell lymphoma MCL) or aggressive disease entities (DLBCL and Burkitt lymphoma BL) (Figure 24).

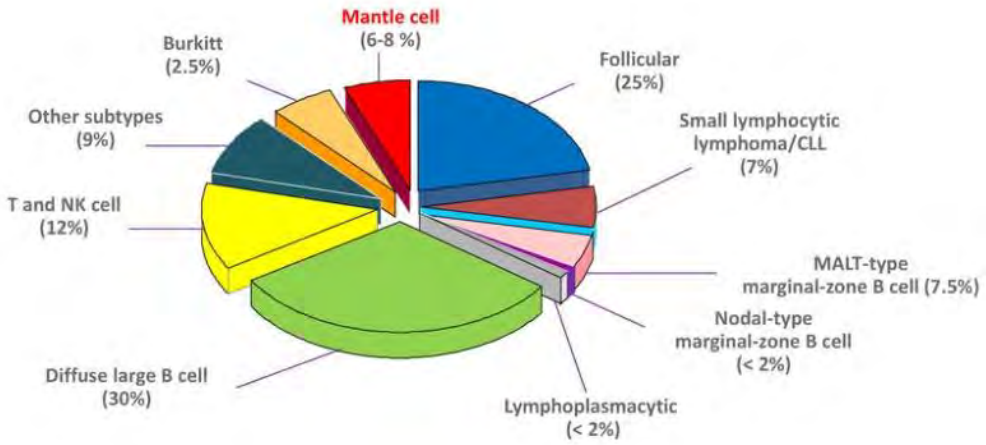

Figure 24 : Subtypes of NHL divided by incidence.
From https://slideplayer.com/slide/12844767/

Genetic alterations and TME modelling are two main features implicated in B-NHL genesis and progression.

1.3.1 Main oncogenic pathways described in B-NHL

Each B-NHL subtype can be assigned to a unique stage of B-cell differentiation and harbors a panel of genetic alterations sustaining specific transformation pathways and disease evolution (Figure 25). These specific features will be briefly described for two aggressive B-NHL (DLBCL and BL) and one indolent B-NHL (MCL). A specific part will be dedicated to FL.

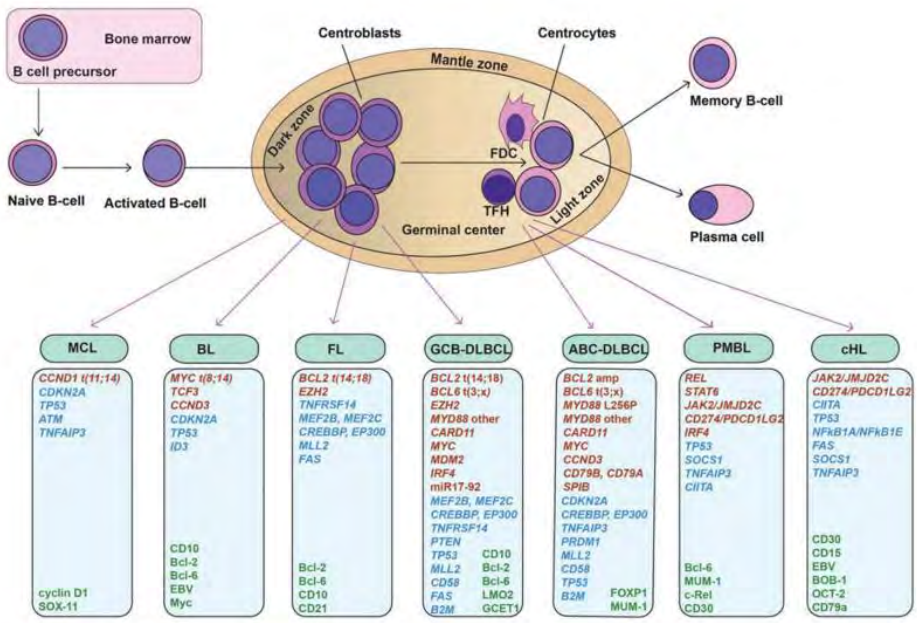

Figure 25 : Origin of B-NHL subtypes at various stages of ontogeny and their associated oncogenic hit.
Loss of function mutations are represented in blue, and gain of function mutations are represented in red.

Immunohistochemical biomarkers used for diagnosis are represented in green. From Sun et al, modern pathology, 2016.[77]

BL is classified as an aggressive B-NHL, and commonly contains genetic alterations leading to MYC overexpression and to the activation of PI3K signalling pathway [78]. MYC is a nuclear phosphoprotein controlling proliferation, cell growth, differentiation and apoptosis, all being involved in cancer genesis. All BL present translocation of the MYC oncogene into the Ig loci leading to constitutive expression of the MYC proto-oncogene, that in healthy B-cells is suppressed by BCL-6 [79]. The second most common mutations in BL is TCF3 mutation (encoding E2A transcription factor) impeding its regulation by ID3 leading to promotion of antigen-independent activation of BCR signalling. Moreover, this mutation leads to PI3K pathway dysregulation, that is also implicated in BCR signalling [80]. HIV-associated BL is a well-known disease that is characterized in part by AID aberrant expression, required for IgM class switching, and contributing to MYC translocation [79].

DLBCL is the most frequent B-NHL representing around 30% of all cases. This highly heterogenous lymphoma is characterized by a diffuse proliferation of B cells with a high mitotic rate. Additionnaly, it can be classified based of variable numbers of normal T cells in the biopsy [81]. Historically, Alizadeh et al used a gene expression profiling (GEP) to divide DLBCL in two disease entities called cell of origin (COO) [82]: the first subtype called GC B cell-like (GCB) presents an expression profile resembling to normal GC but exhibiting an intraclonal heterogeneity ongoing somatic hypermutation and presenting CD10, BCL6 high expression in B cells; the second type called activated B cell-like (ABC), presents gene expression profile of activated B cells with high expression and constitutive activity of *NF-κB* and expression of *IRF4* and *BCL2*. The rest of cases are named "unclassified group". This classification is important as prognostic is different depending on the subtypes. Indeed, ABC type represents a poorer prognosis [83,84]. However, with huge advances in transcriptomic technologies, the molecular classification of DLBCL evolved into a more complex subclassification proposed by several algorithm such as LymphGen which proposes eight subgroups [85]. The classical COO classification has evolved to separate subtypes with gene expression profiles resembling double-hit lymphoma (DHITsig+) or not (DHITsig-) and subtypes resembling BL (MHG).

MCL is characterized mutationally by a translocation between chromosomes 11 and 14 leading to cyclin D1 overexpression. Histologically, cancer cells in MCL express CD5 and in some cases overexpress SOX11 leading to a poorer prognosis [86]. Different subtypes of MCL are defined as follows: classical MCL located in LN, blastoid and pleomorphic MCL in the circulation and leukaemic non-nodal MCL in the spleen. This lymphoma is heterogeneous, with some patients presenting an aggressive disease and others having a more indolent course. Indeed, these malignancies are prone to acquisition of

additional abnormalities in the cell cycle dysregulation, DNA damage response, or cell survival pathways, leading to more aggressive disease. For instance, TP53 mutations, result in more aggressive disease associated with poor outcomes.

Interestingly all these phenotypic features are used in immunohistochemical (IHC) analysis by pathologist to confirm diagnosis as presented in figure 25 and 26.

From Hassler et al, epigenomics, 2013 [87]

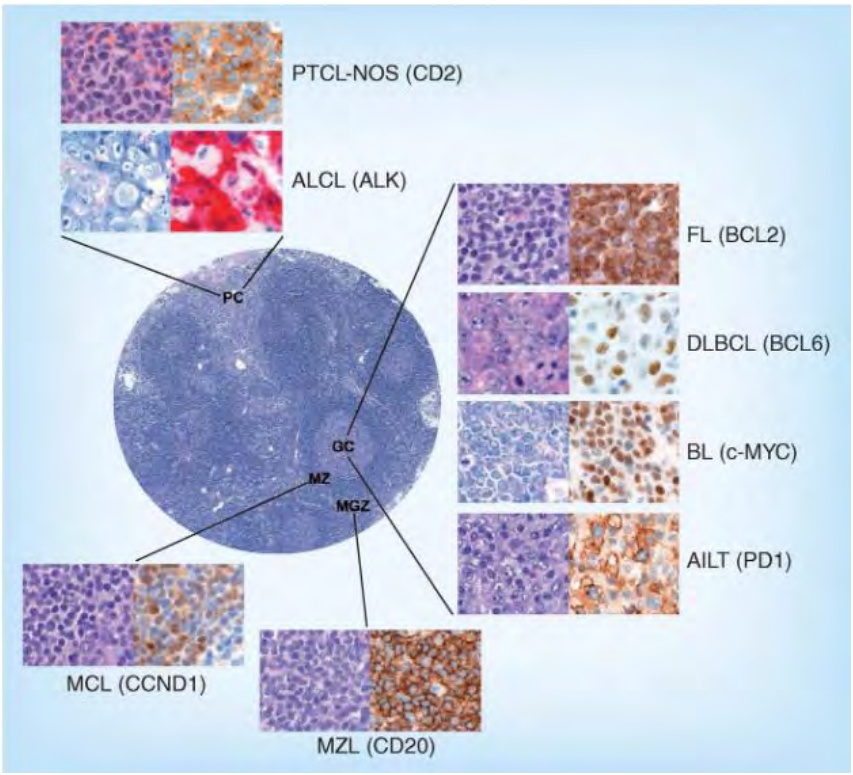

Figure 26 : immunohistochemistry from several B-NHL subtypes with their respective localization.

1.3.2. Lymph node organization and cell microenvironment: B-NHL's nest

LN are organized in three compartments: the cortex (outer region), paracortex and the medulla (inner region). Follicles containing GCs are located within the cortex (Figure 27) [88]. Different types of cells preferentially reside in the separate areas of these compartments. B cells are usually found in the follicles within the outer cortex, while T cells are mainly present within the paracortex and medulla.

After antigen stimulation mediated by APC, T and B cells undergo a clonal expansion. FDC are the main APC present in follicles and playing an important role for B-cell maturation. Indeed, after antigen stimulation, follicles develop to a GC phenotype where B cells differentiate to Ig-secreting plasma cells. Most T cells such as CD8+ T cells are present outside of the follicle, except for an important subtype of CD4+ T cells called follicular T helper (TFh) that are specialized in antigen-

dependent activation of B cells in the follicle. Diffuse macrophages are present in GC and their main function is to remove debris from apoptotic cells [88].

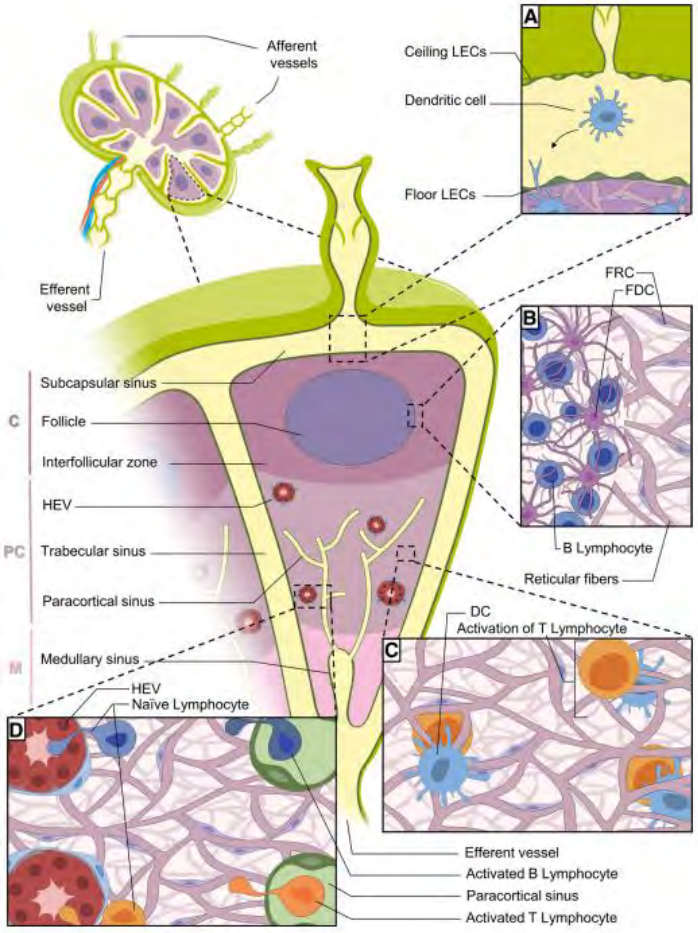

Figure 27 : Illustration of the lymph node different compartiments and cell population distribution.
C (Cortex), PC (Paracortex), M (Medulla). FDC (Follicular dendritic cells), FRC (follicular reticular cells). From Gillot et al, Cell Mol Life, 2021 [88]

In B-NHL, all these cellular actors are present but in a different proportion and a few changes in phenotype can also be observed. Scott and Gascoyne, proposed a classification in three categories of NHL depending on their dependency on the microenvironment: recruitment (HL), re-education (FL) and effacement (BL) (Figure 28) [89]. In the re-education model, cell composition and spatial arrangement are similar to the healthy LN. In addition, B cells are dependent on their microenvironment for survival and proliferation. The recruitment model is highly dependent on supportive non-malignant cells from the microenvironment and tumor cells are in minority. Finally, in the effacement model a majority of tumor cells show self-dependency, while the presence and role of TME is limited.

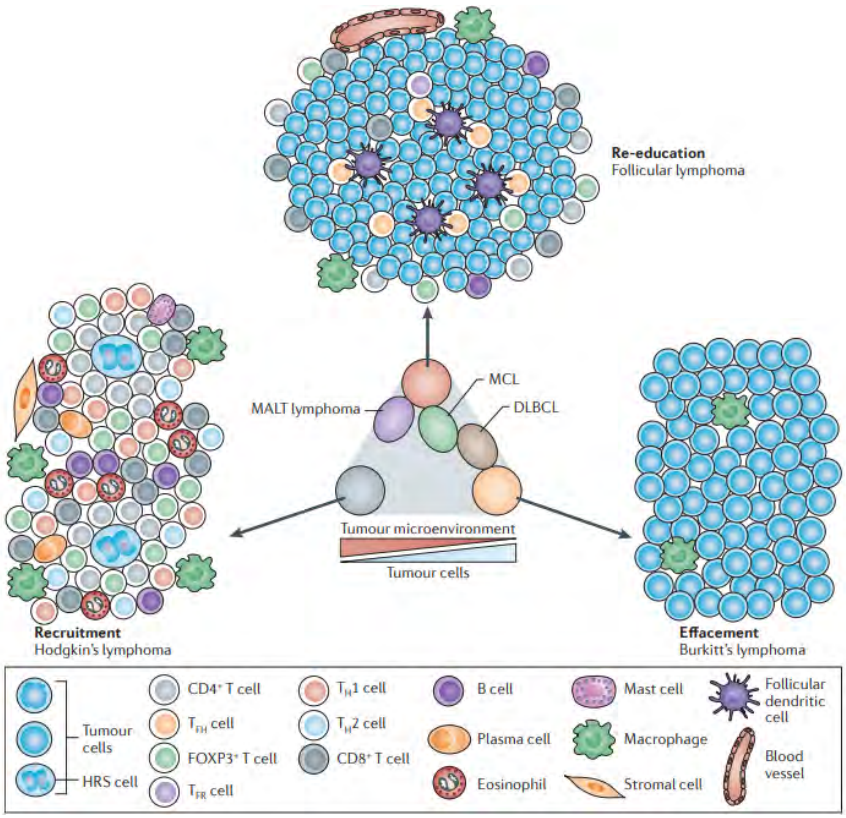

Figure 28 : B-cell lymphoma microenvironment differential composition among subtypes.
From Scott et al, nature review cancer, 2014 [89]

Summary lymphopoiesis and lymphomagenesis (1)

Hematopoiesis in general and lymphopoiesis in particular are very strictly regulated mechanisms giving rise to the numerous immune actors of innate and adaptive immunity. Any changes or dysregulation of lymphopoiesis can lead to abnormal proliferation of malignant cells or blockade at a certain stage of differentiation responsible for the genesis of lymphomas. Among hematological diseases, non-Hodgkin lymphomas are heterogenous tumors originated from T or B lymphocytes, mainly located in LN and circulating through the blood and lymphatic system. B-NHL are the most frequent and present, immunohistological, genetic landscape and microenvironment features specific to each subtype.

2. Focus on follicular lymphoma: indolent but not innocent

2.1. Incidence, epidemiology and diagnosis

Among lymphoid malignancies, the indolent B-NHL, FL, is the second most frequent subtype in Western Europe, representing 22% of all NHL. Incidence raised up from 2-3/100 000 in 1950 to 5/100 000 in recent years [90,91], which is attributed to, pesticides exposure and life style factors such as nutrition and alcohol consumption [92]. The EUROCARE-5 study evaluated the 5-year OS of FL patients in 20 European countries, and showed an increase from 64.1% in 2000-2002 to 69% in 2003-2005 and to 74.3% 2006-2008 [93]. This increase of OS is mostly due to introduction of rituximab in first-line treatment, as described by the Sweden study [94]. The tumors usually present a slow progression and the most of patients respond well to first-line therapy, leading to long-term survival [95]. However, approximately 45% of patients develop an aggressive form by transformation into DLBCL and the 5-year survival rate drop to 50% for these patients [96–98]. The median age at diagnosis is around 60 years old [99].

FL diagnosis is obtained after surgical excision of LN biopsy. IHC analysis of CD20, CD79b GC and CD10 tumoral markers on mature B cells, Bcl6, GCET1, LMO2, HGAL and BCL2 GC (overexpression in 85% of cases) and markers of FDC network CD21, CD23 and CD35 markers are needed to confirm the diagnosis (Figure 29).

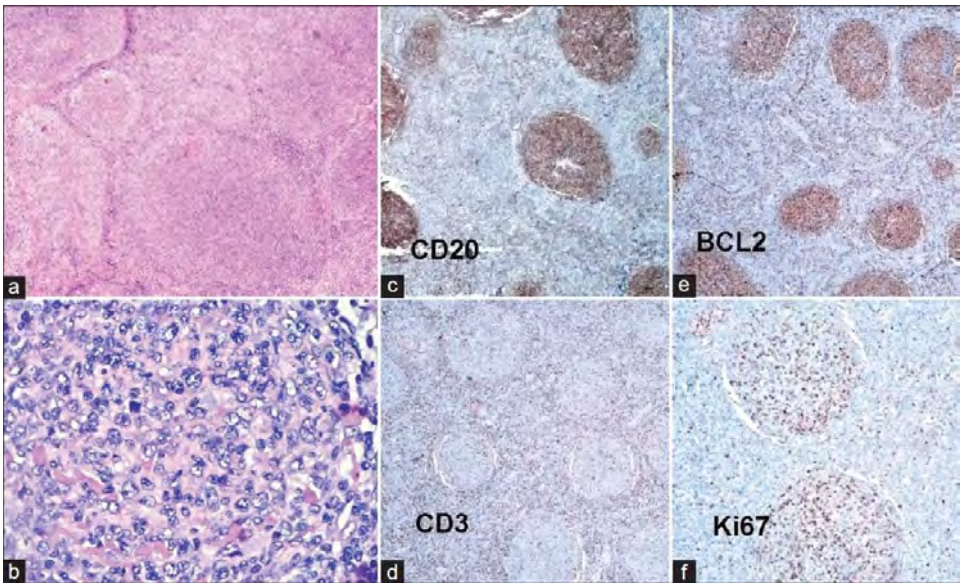

Figure 29 : FL biopsy immunohistochemistry of several important markers for diagnosis.

a. Lymph node biopsy showing cells arranged in follicular pattern with closely packed follicles (Hematoxylin and Eosin staining (H&E) x100). b. Higher magnification of the same picture showing centroblasts (6 -8/ HPF) (H&E x400). c. The neoplastic cells are positive for CD20 (IHC x100). d. CD3 has stained the reactive cells (IHC x100). e. BCL2 positivity in follicles (IHC x 100). f. High Ki67 index (60%) in neoplastic cells IHC x100. From Das et al, Indian J Pathol Microbiol 2012 [100].

According to the histological report following the WHO classification, grading is carried out by determining average number of centroblasts (Table 1 left): grade 1 corresponds to less than five blasts/ high power field (HPF, referring to the field of view in the microscope), grade 2 from six to fifteen blasts/HPF, grade 3A up to 15 blasts/HPF and centroblasts with intermingled centrocytes and finally grade 3B present up to fifteen blasts structured like sheets. Grades 1 to 3A are categorized as indolent diseases whereas grade 3B is classified as aggressive lymphoma. BM aspirate and computed tomography scan of neck, thorax and abdomen are also required to confirm the diagnosis [91]. Ann Arbor classification is also essential to determine the stage of the disease based on number of lymphoid structures affected and their localization (Table 1 right). Briefly, classification relies on the following criterias: stage I that presents no LN areas or extralymphatic site; stage II which displays two or more LN regions or at least, one and in addition extralymphatic site; stage III that exhibits LN regions on both sides of the diaphragm with possible localised extranodal site and finally, stage IV that corresponds to diffuse or disseminated extralymphatic organ involvement.

Grading of FL	
Grade	**Description**
1	≤5 blasts/HPF
2	6-15 blasts/HPF
3A	>15 blasts/HPF, centroblasts with intermingled centrocytes
3B	>15 blasts/HPF, pure sheets of blasts

Ann Arbor classification	
Stage	**Area of involvement**
I (I_E)	One LN region or extralymphatic site (I_E)
II (II_E)	Two or more LN regions or at least one LN region plus a localised extralymphatic site (II_E) on the same side of the diaphragm
III (III_E, III_S)	LN regions or lymphoid structures (e.g. thymus, Waldeyer's ring) on both sides of the diaphragm with optional localised extranodal site (III_E) or spleen (III_S)
IV	Diffuse or disseminated extralymphatic organ involvement

Table 1 : Grading of FL and Ann Arbor classification.
From Dreyling et al, Annals of oncology, 2021.[91]

2.2. FL genetic and epigenetic ground

2.2.1. BCL2 overexpression: first FL oncogenic hit

FL lymphomagenesis is a complex multistep process that occurs at stages of B cell differentiation, led by genetic and epigenetic alterations.

The t(14;18)(q32,q21) translocation in B cells, which occurs in the BM during the V(D)J recombination at the pre B-cell stage, is a genetic hallmark of FL (up to 85% of patients present this translocation) leading to BCL2-IGH fusion and constitutive expression of the anti-apoptotic protein

BCL2 [95]. This overexpression is responsible for the accumulation of abnormal B cells in the GC. Nevertheless, it is now well-established that this translocation is not sufficient to induce FL as it is also being found in healthy adults who will never develop FL (50 to 70%) [101]. However, the presence of this genetic characteristic is associated with a 23-fold higher risk of developing FL.

There are accumulating evidences, that other genetic hits are required for complete transformation into FL. With next generation sequencing technologies, the knowledge of the genetic landscape of FL has dramatically increased drawing a more precise picture. GC is a fertile ground for B lymphocytes differentiation and evolution but can provide also dangerous acquisition of oncogenic mutations leading to lymphomagenesis. Early pre-follicular lymphoma lesions arising from differentiation blockage of B cell in the GC, presenting normal GC B cell features, such as BCL-6 and a follicular structure with important interactions with the surrounding microenvironment [102]. At this stage, the cells are called follicular lymphoma-like cells (FLLCs) and they may undergo many re-entries into the GC where they potentially accumulate other genomic alterations to evolve as FL precursors. FL initiation has also been proposed to come from single-nucleotide polymorphisms in the genomic region encoding HLA I and II antigens, CXCR5 protein, *ETS1 LPP* transcription factor and BCL-2 protein [103]. FL genetic landscape comprises many other mechanisms such as epigenetic dysregulation, survival pathways overactivation and immune evasion which are going to be detailed in the following parts.

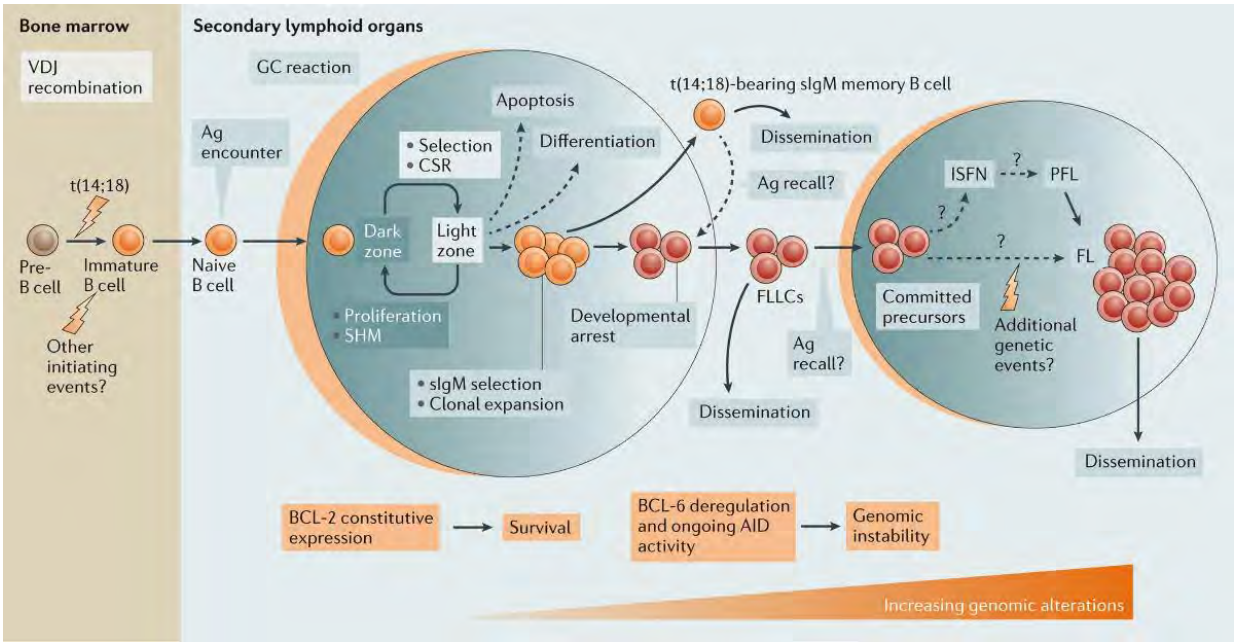

Figure 30 : Follicular lymphoma genesis and accumulation of genetic alterations, from bone marrow to GC center.

From Huet et al, nature reviews cancer, 2018 [104]

2.2.2. Epigenetic dysregulations

Epigenetic is the study of inheritable changes that do not involve alterations in the DNA sequence. Epigenetic alterations are at the heart of follicular lymphomagenesis. A dynamic equilibrium of chromatin conformation is determined by the introduction of activating and repressing histone modifications that in turn influence gene expression of given part of the genome under the influence of gene promoters and enhancers to control them. This dynamic is important in B cell differentiation [4]. Different types of epigenetic dysregulations have been depicted, such as alterations of chromatin-modifying genes and aberrant DNA methylation (Figure 31).

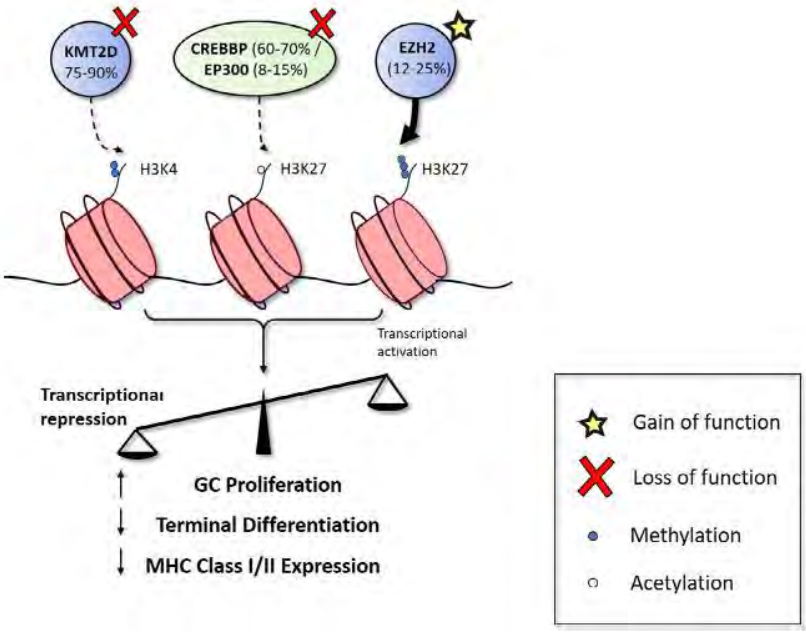

Figure 31 : Illustration of main epigenetic alterations consequences in proliferation, differentiation and MHC expression by FL cells.
From Kumar et al, Br J Haematol, 2021 [105]

Table 2 summarizes the main epigenetic alterations encountered in FL [104]. Among them, genes encoding histone-lysine N-methyltransferase 2D (KMT2D), KMT2C, the Polycomb-group catalytic protein histone-lysine N-methyltransferase EZH2 and the histone acetyltrans- ferases CREB-binding protein (CREBBP) and EP300 are the most frequent. Inactivation of KMT2D, CREBBP and EP300 after mutation causes a loss of function of transcription activating marks H3K4me and H3K27ac [106,107]. On the opposite, gain of function mutations in EZH2 leads to increase of repressive mark H3K27me3 [108]. Dysregulation in BCL-6, a transcriptional repressor is a key in the pathology progression. So far, severals alterations of this process have been described in FL [104]. For example, it can recruit HDAC3 that will inactivate B cell enhancers by H3K27 deacetylation, canceling the effect of CREBBP and EP300. BCL-6

can also cooperate with EZH2 to stop genes implicated in cell cycle checkpoints and plasma cell differentiation. MEF2B mutations are occurring in 15% of FL patients leading to increased expression of BCL-6 and MYC oncogene.

Thus, combination of BCL-2 overexpression and alterations in epigenetic regulation are necessary for FL genesis and progression. Moreover, in most of the cases, several mutations are observed suggesting a cooperation to build a regulation loops. For example, Béguelin et al showed that *EZH2* and *BCL6* genes can cooperate with *PRC1-BCOR-BCX8* complex to increase histone modifications [109]. DNA aberrant methylation is also an epigenetic mechanism involved in FL development [105]. It occurs at promoters of tumor suppressor genes and targets genes such as *BCL6* and *EZH2*. Thus, hypermethylation and chromatin modifiers cooperate to block GC B cells in their differentiation and favor malignant transformation. Consequently, the identification of such alterations encourages the development of epigenetic-targeted therapies for FL such as tazemetostat, an EZH2 inhibitor. These therapies have already presented promising results by reversing abnormal methylation profiles and increasing tumor cell sensitivity to chemotherapy [110].

Pathway	Gene	Function	Frequency (%)*	Oncogenic alteration
Epigenetic and transcriptional regulation	*KMT2D*	Histone H3K4 methyltransferase	70–90	Loss of function
	CREBBP	Histone H3K27 and H3K18 acetyltransferase	50–70	Loss of function
	Histone-encoding genes	Histone linkers and core histones	20–30	Unknown
	EZH2	Histone H3K27 methyltransferase	10–30	Gain of function
	EP300	Histone H3K27 and H3K18 acetyltransferase	10–20	Loss of function
	MEF2B	Transcription factor	10–20	Gain of function
	KMT2C	Histone methyltransferase	13	Loss of function
	BCL7A	SWI/SNF complex; nucleosome remodelling	~10	Unknown
	ARID1A	SWI/SNF complex; nucleosome remodelling	~10	Unknown
	ARID1B	SWI/SNF complex; nucleosome remodelling	~5	Unknown
	SMARCA4	SWI/SNF complex; nucleosome remodelling	~5	Unknown
	BCL6	Transcriptional inhibitor	Mutations, ~5; translocations, ~10	Gain of function

Table 2 : Recurrent epigenetic and transcriptional mutations in FL.

From Huet et al, nature reviews cancer, 2018 [104]

2.2.3. Signaling pathway dysregulation

Antigen-independent BCR signaling pathways dysregulation is also at the heart of FL pathogenesis [104] (Figure 32 and Table 3). Its constitutive activation leads to induction of many other pathways such as NF-κB, MAPK and PI3K-AKT, all of which are involved in proliferation and survival of malignant B cells [111]. Around 30% of patients present mutations in genes encoding proteins in BCR-NF-κB pathway such as BTK and CARD11 [112,113]. Other mechanisms leading to constitutive BCR signaling have been proposed such as mutation in variable regions of Ig heavy and lights chain genes responsible

for N-glycosylation site. This leads to increased interaction of B cells with TME such as stromal cells, DC and macrophages, all of which are further responsible for BCR signaling activation [114,115].

Other signaling pathways are involved in sustaining proliferation and survival of tumor cells such as JAK-STAT and NOTCH pathways [116,117]. 18% of patients with harbor mutations in *NOTCH coding gene* such as the mutation disrupting the C-t PEST domain of the NOTCH1 and NOTCH2 proteins [104] or mutation in DTX1 and SPEN regulators of the NOTCH pathways [118].

Another important pathway in FL is the mTORC1 pathway which is dysregulated in around 15% of FL patients [119]. mTORC1 is a master regulator of protein synthesis integrating the responses to growth factors and overall energetical level of the cell [120]. In FL we usually observe mutations leading to constitutive activation of this pathway leading to increased proliferation of the cancer cells, even in the unfavourable metabolic conditions. For example, active RAG GTPase hetero-dimers recruit mTORC1 to the lysosomal membrane. Thus, activating mutations targeting RRAGC activate mTORC1.

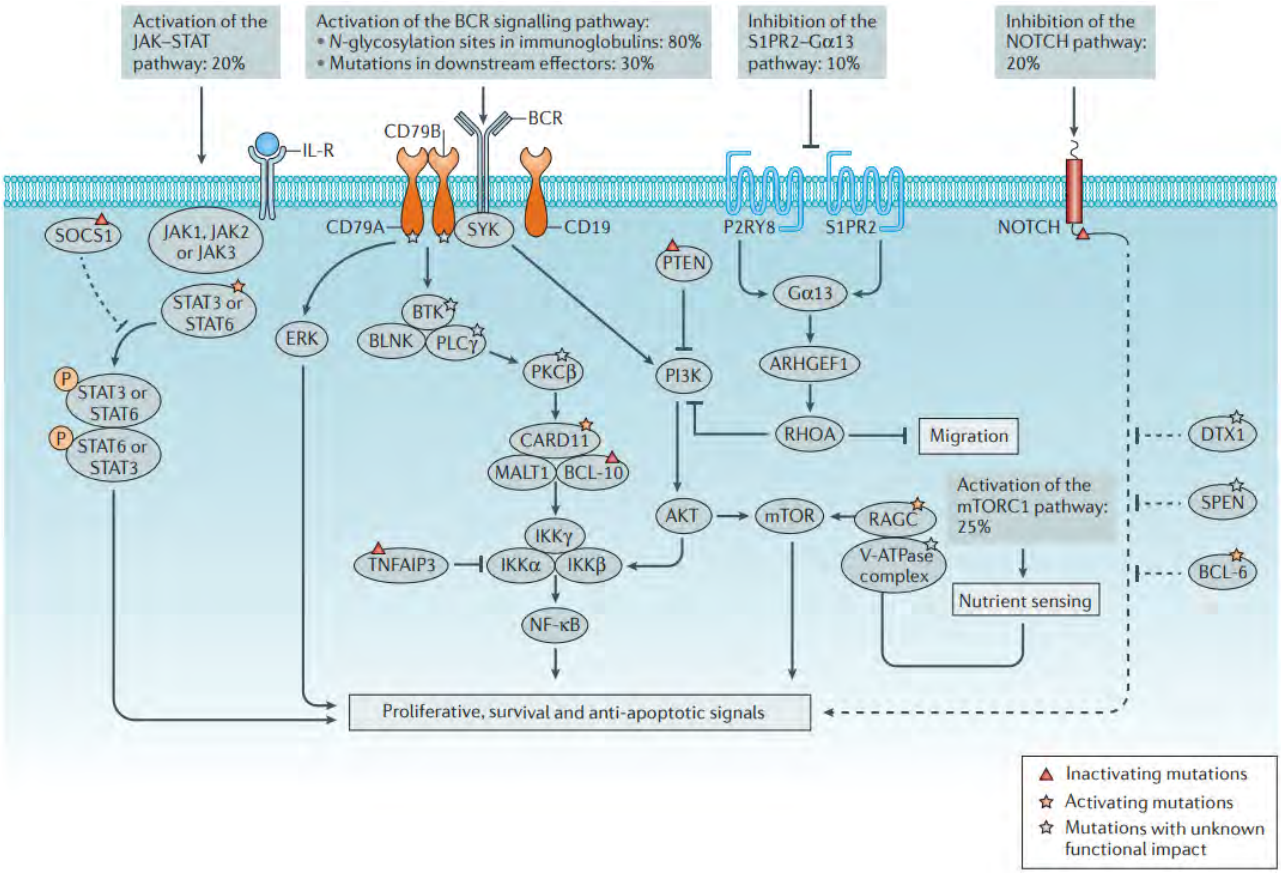

Figure 32 : Signalling pathway affected by genetic and epigenetic mutations in FL

From Huet et al, nature reviews cancer, 2018 [104]

Finally, one last pathway involved in GC B cells differentiation blockage, is the S1PR2-Gα13 pathways [104]. Indeed, S1P binds to S1PR2 on GC B cells and then downstream Gα13 effectors, ARHGEF1 and RHOA inhibit cell migration, favoring GC homeostasis.

BCR signalling	*IGH* and *IGL* variable domains	Promotes *N*-glycosylation	~80	Gain of function	94
	CARD11	BCR–NF-κB signalling pathway	10–15	Gain of function	42,44,46, 157
	BTK	BCR–NF-κB signalling pathway	5–10	Unknown	
	TNFAIP3	BCR–NF-κB signalling pathway	~5	Loss of function	
	FOXO1	Transcription factor activated downstream of BCR signalling	5–10	Gain of function	
mTORC1 signalling	*RRAGC*	Guanine nucleotide-binding protein	10–15	Gain of function	62,107,108
	ATP6V1B2	V-ATPase complex	~10	Unknown	
	ATP6AP1	V-ATPase complex	~10	Unknown	
	VMA21	V-ATPase complex	5	Unknown	
Migration	*GNA13*	Guanine nucleotide-binding G protein	5–10	Loss of function	46,62,157
	GNAI2	Guanine nucleotide-binding and inhibiting G protein	5	Unknown	
Survival	*BCL2*	Anti-apoptosis	Translocations, ~85	Gain of function	10
			Mutations, ~50	Unknown	169
	SOCS1, *STAT6* and *STAT3*	JAK–STAT signalling	20	Gain of function	44
	NOTCH1, *NOTCH2*, *NOTCH3*, *NOTCH4*, *DTX1* and *SPEN*	NOTCH pathway	18	Unknown	62,103

Table 3 : Recurrent mutations in FL inducing signalling pathway alterations.
From Huet et al, nature reviews cancer, 2018 [104]

2.2.4. Genes involved in immune evasion

Genetic alterations can also affect tumor cell interaction with their microenvironment. Tumor cells "use" these mutations to remodel the microenvironment to their advantages. Among these mechanisms, IE allows tumor cells to survive. Two main mutations impacting immune cell interaction with FL cells are well described: CREB-binding protein (CREBBP) and Herpesvirus entry mediator A (HVEM) [104] (Figure 33).

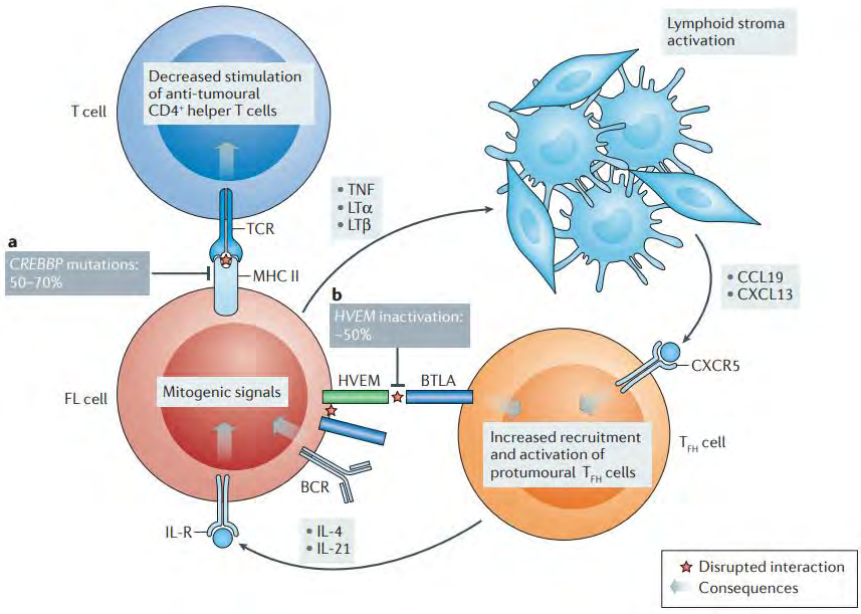

Figure 33 : Microenvironment diversion toward B cell survival through genetic alterations.
From Huet et al, nature reviews cancer, 2018 [104]

Around 50% of FL patients harbor a loss of function mutations in *CREBBP*. This mutation controls MHC expression by downregulating it [121], thus reducing the capacity to stimulate T cell proliferation and infiltration.

Cathepsin S (*CTSS*) mutation (activating point or amplification) appears in 20% of FL patients. This mutation has opposite effect of *CREBBP* mutations in terms of antigen presentation as it will increase MHC binding to antigenic peptides [122]. Indeed, an hyperactivation of cathepsin S leads to increase in substrate cleavage such as CD74, inducing an upregulation of MHC classe II genes and CD4+ T cell infiltration [123,124]. It has been shown that patients carrying *CTSS* mutations present high level of IFN-γ and IFN-γR1 and a better outcome following chemoimmunotherapy treatment [123]. Moreover, Dheilly et al, using *CTSS* KO mice model showed a modification in antigen repertoire towards CD8+ CTLs expansion and they also highlighted an inverse correlation between PD-1 and CTSS expression [124].

HVEM, presents at B cell surface, binds BTLA expressed in T cells surface leading to inhibitory signals to T cells and also to inhibit BCR signaling [104]. In up to 50% of FL patients a point mutation or 1p36 deletions in *HVEM* gene is detected. Deficiency in *HVEM,* increases the secretion of activating cytokines such as TNFα, LTα and LTβ creating a supportive tumor environment containing more TFh. In turn, TFh cells secrete IL-4 and IL-21 that bind to receptor expressed at the B cell surface thus inducing mitogenic signals and tumor cell survival.

Altogether, FL genetic landscape exhibits many cancer hallmarks in terms of genetics, epigenetics, cell signaling and microenvironment interactions. A better understanding of their implication in FL progression and transformation is a key element to develop new and efficient therapeutic strategies. Nevertheless, it is important to understand that each mutation induces a specific cellular effect that also depends on the molecular context of other existing alterations and surrounding cells. In consequence, combining therapeutic strategies targeting both tumoral cells and TME is an encouraging perspective to target FL genetic landscape in an efficient and global manner.

2.3. FL microenvironment: a heterogeneous and plastic microenvironment

First steps of FL development occur in the BM with the translocation t (14;18) in around 80% of patients. Nevertheless, the further disease progression occurs in the GC where B cells acquire other genetic alterations. The LN is the main organ in which lymphoma cells reside. Structurally and in terms of cell composition, LN microenvironment from healthy and FL patients are similar but display different features in terms of supportive niche and immunosuppressive cells.

2.3.1 FL microenvironment composition

As represented in figure 34, FL microenvironment is composed by numerous actors that support tumor, through a complex set of cytokines, receptors, immune modulators and pro-angiogenic factors: FDCs, fibroblastic reticular cells (FRCs), mesenchymal stromal cells (MSCs) and tumor-associated macrophages (TAMs), together with a rich T cell infiltrate composed of CD4+ T follicular helpers (TFh) cells, CD4+ T follicular regulatory cells (TFr), CD4+ T regulatory cells (Treg) and CD8+ cells. Here is a brief overview of their function and clinical impact. Their crosstalk and involvement in FL progression will be discuss in the next parts depicting the supportive niche and IE mechanisms.

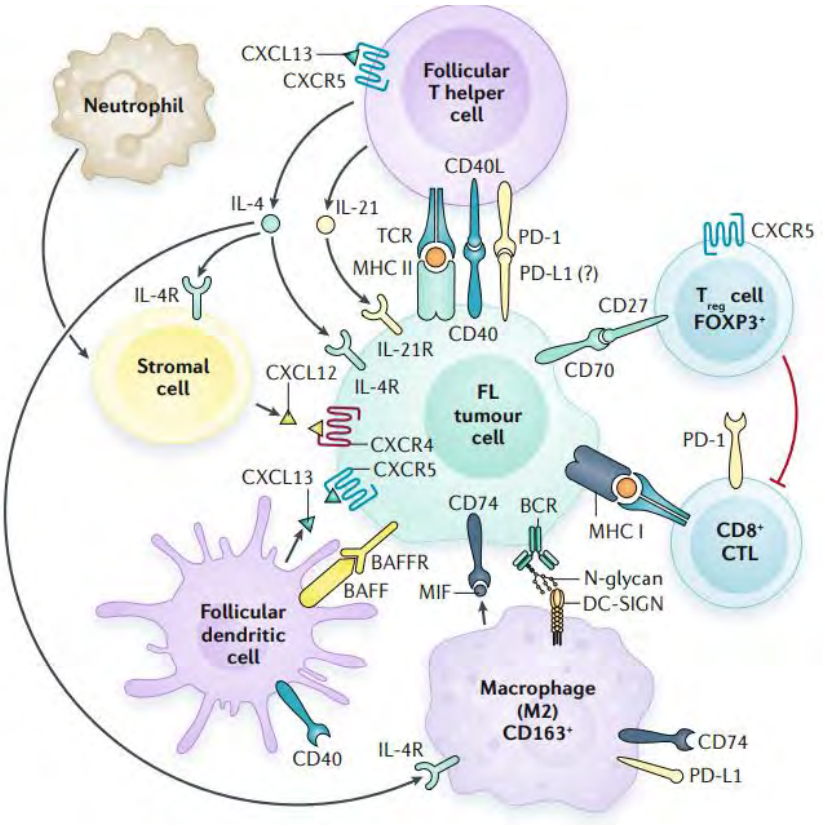

Figure 34 : FL microenvironment main actors
From Carbone et al, Nat Rev Dis Primers., 2019[125]

FDC are stromal cells specialized in presenting antigens to B cells in the GC [126]. Their main function is mediated through CD40L interaction and cytokines release such as IL-15, to ensure GC B-cell proliferation and survival. They are characterized by CD14+CD21+ and CD23+ markers and are localized in the intrafollicular zone. In clinic, patients with a predominance of mature FDC often show advanced clinical stages (III or IV) whereas patients with immature FDC predominance present with localized clinical stage (I or II) [127].

FRCs are stromal cells located in the T cell zone of the LN and their main action is to secrete components of the extracellular matrix (ECM), including laminin, fibronectin and collagen IV [128]. They are able to secrete cytokines such as CCL2 that were detected in high amount in LN and BM sample from FL patients [129].

MDSC represent an heterogenous group of immature myeloid cells that are characterized by their extreme immunosuppressive potential. These cells have been extensively investigated in the context of solid tumors and a few studies exists in hematologic malignancies. Nevertheless, Lin et al identified a CD14+ subtype presenting low HL human leukocyte antigen DR (HLA-DR) expression in peripheral blood of B-NHL patients. These cells are able to elicit T-cell anergy, promoting tumour IE *via* several mechanisms including depletion of tryptophan, arginine and cysteine due to the high

expression level respectively of 2,3 indoleamine dioxygenase and arginase, nytrosylation of TCR and increased production and release of reactive oxygen species. Moreover, increase in this cell frequency correlates with PFS (progression free survival) and OS [130] mainly due to their anergy action on T cells.

TAMs originate from the myeloid lineage and present highly plastic characteristics [131]. Depending on the signals present in their proximity macrophages can acquire a specific polarization state, fitting between, M1 (pro-inflammatory phenotype) and M2 (anti-inflammatory phenotype) extremes of the spectrum. M2 macrophages have a role in B cell survival through crosstalk with other cells from the microenvironment that will be discussed in the part 2.3.2. In a Spanish study, FL patients presenting high percent of CD68+ cells localized in the follicles exhibit a shorter OS [132]. M2 polarization of macrophages is associated with tumor dissemination, immunosuppression and angiogenesis [133]. Clear et al observed a positive correlation between macrophages infiltration and angiogenic sprouting, leading to a poorer outcome in FL [134]. Interestingly, prognostic impact of TAM infiltration depends on the applied treatment. Indeed, some studies showed that anthracyclines were able to modulate the differentiation and function of TAM towards a tumoricidal phenotype [135]. PFS was increased in rituximab maintenance arm displaying an elevated CD163 staining[136]. This could be explained by the antibody-dependent cellular phagocytosis (ADCP) mechanism of action displayed by rituximab, as macrophages are one of the main effector cells in this process. Moreover, Taskinen et al showed that elevated numbers of macrophages correlated with favorable PFS in patients treated with R-CHOP but not with CHOP alone [132].

Considering the T cell compartment, the main population is represented by TFh cells. TFh cells are a subpopulation of CD4+ T cells that specifically help GC B-cell maturation and differentiation [126]. In terms of phenotype, they express CD3+CD4+CXCR5+ICOS+CD25- and PD-1+ and are located in the follicles [137]. In the study of Ame-thomas et al, it was observed that FL patients exhibit high number of CD3+ CD4+CXCR5+ICOS+ TFh cells compared to DLBCL or reative LN. In this study, they also identified another population called Tfr expressing CD3+ CD4+ CXCR5+ ICOS+ CD25+ FoxP3+. Even if phenotype between TFh and Tfr is quite similar their functions are different. Indeed, TFh support FL B-cells avoiding their apoptosis whereas Tfr have a regulatory function towards CD4+CD25- cell proliferation leading to their inhibition thus participating in an immunosuppressive microenvironment. Treg are another subset of CD4+ T cells that harbor CD3+ CD4+ CXCR5- ICOS- FOXP3+ CD25+ phenotype. In FL, Treg are known as immunosuppressive cells, that inhibit CD8+ T cell proliferation and cytotoxic action by decreasing their granule production. For example, Yang et al demonstrated an abrogation of degranulation and cytotoxicity of CD8+ T cells towards B-NHL cells, that was mediated by Treg cells when the three cell types were co-cultured [138]. Moreover, in this study, they showed increased Treg infiltration in biopsy from B-NHL but so far, no clear conclusions were available on the OS or PFS

parameters. Nevertheless, some studies showed no impact of Treg on OS and PFS [139] and others presented positive impact depending on their localization[138]. Indeed, Farinha et al showed that patient with diffuse pattern of infiltrating FOXP3+ T cells have a more favorable OS than patients with infiltration in follicles.

Finally, in FL, infiltration of CD8+ T cells is associated with a higher OS. Indeed, Wahlin et al showed that patient with higher CD8+T cell number, as evaluated by IHC, presented a higher PFS [140] and this was confirmed by another group for OS [141]. Indeed, patients with more than 8% of CD8+ T cells presented a fivefold lower risk of death than patients with less than 4%. My group investigated CD8+ T cell infiltration by IHC and confocal microscopy on pretreated LN from FL patients [142]. This study revealed an important level of CD8+ granzyme B cells in the interfollicular spaces where they formed lytic synapse-like structures with FL B cells showing an *in situ* cytotoxic function of these cells [142]. Moreover, it has been observed that PFS was increased in patients presenting high CTLs expressing granzyme B. Altogether, these observations highlighted the anti-tumoral effect of CD8+ T cells in FL. Nevertheless, some studies demonstrated that TILs in FL were able to impair recruitment of signaling proteins important for immunologic synapse [143]. Global gene expression analysis performed by Kiaii et al allowed to explain this phenomenon by the impaired motility of FL purified CD8+ T cells compared to healthy CD8+ T cells [144]. By clustering gene expression dependently on CD8+ T cell localization (interfollicular or intrafollicular area), they were able to observe different OS. Thus, patients with high number of intrafollicular ETV1-expressing TILs presented a poor OS [144]. In contrast, patients with high number of interfollicular ETV1-expressing TILs exhibited a higher OS. These observations demonstrate that not only gene expression but also the localization of CD8+ T cell are important in FL progression.

The innate immune lymphoid compartment is also well-represented in the FL microenvironment mainly with NK cells and γδ T cells and it plays a major role in treatment efficacy [65,145,146]. Gibson et al analyzed NK cells and their subtypes in FL patients. They observed a cell number variation depending on tissue site and in peripheral blood of FL patients and that their number predicted the outcome [147]. Enqvist et al, published recently a study where they followed the dynamic of NK cell repertoire in LN and peripheral blood during rituximab therapy in FL patients. First, they observed that NK cells present a naive phenotype in LN with a slight increase in CD56dim NK cells compared to control tonsils. After rituximab therapy, this repertoire evolved to Ki67+ NK cells with an increase in CD16, CD57, granzyme A and perforin [148]. Braza et al compared γδ T cell infiltration in FL and reactive LN and found that these TILs were less abundant in FL. They were located outside the follicles, in the perifollicular zone [70]. The same team evaluated the cytotoxic activity of Vγ9Vδ2 T cells against FL cells by measurement of perforin/granzyme release and IFNγ secretion. They found that these immune cells efficiently kill primary FL cells and that their effect was potentiate by anti-CD20

mAbs therapy [48]. My team also observed the same result with 3D FL models in co-culture with primary Vγ9Vδ2 T cell lines [71].

As presented here, LN microenvironment and consequently FL microenvironment is a complex and well-organized structure where many partners interact together. Dave et al demonstrated by gene expression profiling, that FL patients' survival correlates with molecular features of non-malignant immune cells present in the tumor at diagnosis[149]. The most common cellular alterations in FL microenvironment are: Treg number increase, T cell effector decrease with an exhausted phenotype, immature immune-suppressive macrophages increase. All the recent studies highlight the influence of microenvironment towards two main directions: first, a supportive niche that promotes B cell survival and proliferation and second, evasion from immune antitumor signals.

Thus, understanding cell interaction and implication in FL progression is essential for the development of new therapeutic strategies.

2.3.2. A supportive niche for B cell survival and proliferation

FL progression is associated with an intensified crosstalk between cells from the FL microenvironment and FL B cells, which also involves activation of numerous signaling pathways (Figure 35). To survive in this microenvironment, tumor cells have to circumvent mechanisms able to eradicate them and receive protective mechanisms through survival and proliferative signals. FL microenvironment is composed by a rich compartment of lymphoid cells (CD8+ T cells, Treg, TFr, TFh, CD4+ T cells, TAM, M2 macrophages), stromal cells (FDC, FRC, mesenchymal stromal cells (MSCs)) and ECM resembling normal GC B cells microenvironment [150]. Work from K. Tarte's group, allows a deep understanding of FL microenvironment interactions.

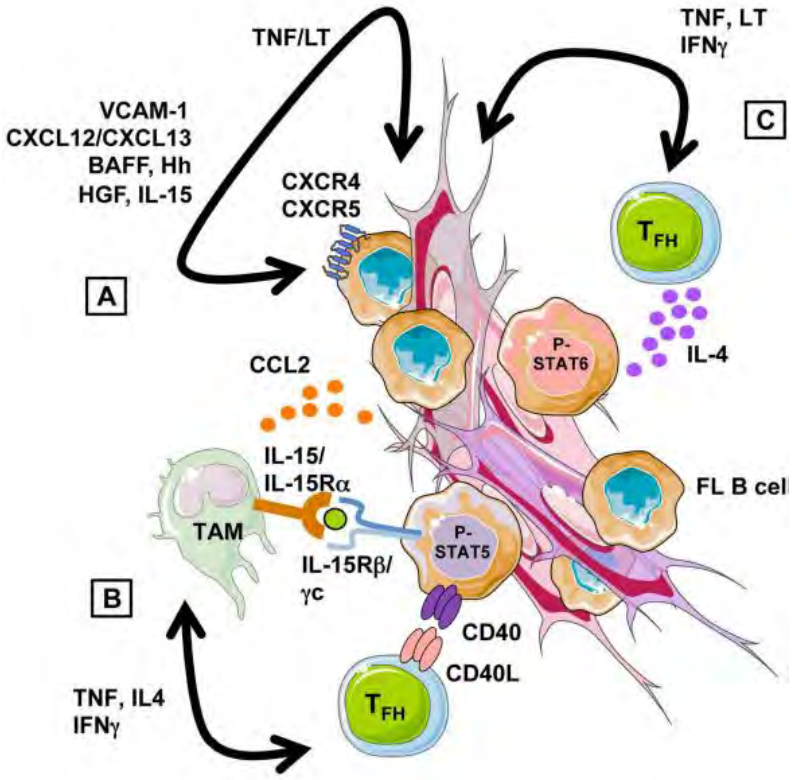

Figure 35 : Complex crosstalks between FL cells and their microenvironment.
From Mourcin et al, frontiers in immunology, 2012 [151]

One of the main crosstalk occurs between TFh, FDC and FL B cells. Indeed, FL B cells express CD40 receptor that binds to TFh expressing CD40L [152,153]. This binding increases secretion of IL-4 and IL-21 by TFh that in turns binds to dedicated receptors expressed by FL cells thus providing growth and survival signals. IL-4 is able to activate STAT-6 responsible for FL cell survival. Even if FL TFh resemble healthy TFh, they present differential gene expression profile with overexpression of *TNF*, *LTA*, *IL-4* and *CD40LG.* A study demonstrated that IL-4 and CD40L are able to protect B cells from rituximab-induced apoptosis [137]. Moreover, stromal cells and FDC secrete chemokines (CXCL12 and CXCL13) that bind TFh and FL cells. IL-4 has a role in stimulating stromal cells (FDC) to increase their CXCL12 secretion that in turns helps B cell trafficking between the GC dark and light zone. This is also a possible mechanism for FL cells to disseminate to other organs. An interesting study, from Haebe et al, demonstrated by single cell RNA seq that depending on patient, site-to-site heterogeneity and TFh abundance can be different [154]. FRC are also implicated in immune cell trafficking, differentiation and migration through IL-4/CXCL12 interaction with TFh [155]. They are implicated in B cell activation and survival by activating BAFF signaling [128]. MSCs, by secreting many factors such as BAFF, TNFα and lymphotoxin α (LTα) for example, support B cell survival [129]. In their study, Amé-thomas et al described an interaction between BM-MSCs and primary FL cells, that helps their migration and adhesion thanks to the secretion of

CXCL12 in combination with CCL2. Both chemokines were detected at high levels in LN and BM derived stromal cells [129].

TAM are also deeply involved in many crosstalks with other cell types. For example, TFh help in the polarization of FL TAM and FL CAF. Indeed, TFh CD40L+ stimulates crosstalk between B cells and TAM secreting IL-15 [156]. Moreover, TFh secreting IL-4 induce CAF CXCL12 expression. My PhD-co director group in Barcelona, have highlighted in FL patients that M2 macrophages are promoted after FDC secretion of CCL2 and CSF-1 [157]. This pro-tumoral phenotype favors angiogenesis, dissemination and immunosuppression [158]. For example, macrophages present IL-15 to B cells, to cooperate with T cells expressing CD40L such as TFh to increase B cell proliferation [156]. Moreover, binding of macrophages DC-SIGN (C-type lectin dendritic cell-specific intercellular adhesion molecule-3-grabbing non-integrin) to mannosylated BCR triggers B cell survival in a independent antigen manner [115,159,160].

2.3.3. Immune evasion

In order to survive, tumor cells apply a pressure on innate and adaptive immune response to downregulate its response through the establishment of IE mechanisms. IE relies on the concept of the 3E: elimination, where immune cells are able to take charge of tumor cells and eliminate them; equilibrium, where tumor cells gain capacity to escape immune cells recognition; and finally, escape where immune cells are not able to exercise their killing actions and tumor cells are taking the advantage over them (Figure 36).

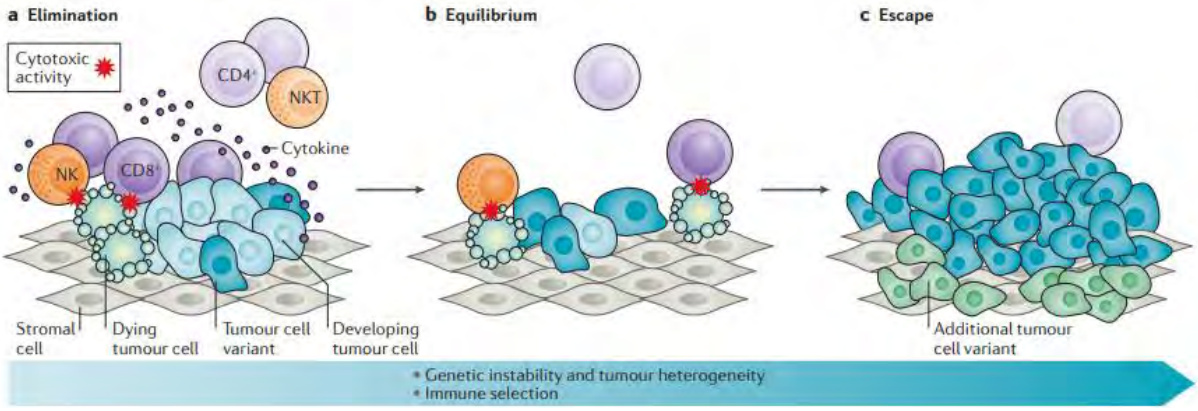

Figure 36 : Immune evasion 3E concept: elimination, equilibrium and escape.
From Sjoerd H van der Burg, et al Nat Rev Cancer 2016[161]

Classical T cell response requires several steps: immunogenic tumor antigens presentation by APC cells, recognition by MHC, effective co-stimulation signals and cytokine secretion. Any changes in these basic mechanism of T cell activation can lead to an immunosuppressive microenvironment. In B-NHL, the most frequent aberrations are lack of immunogenic tumor antigens, loss of MHC molecules expression, interruption of co-stimulatory signals and immunosuppression through overexpression of

immune checkpoint (ICP) [162]. All these features are known to regulate FL initiation, evolution and response to treatment. Even if innate and adaptive immune cells such as CD8 T cells, γδ T cells, NK cells and M1-like TAM are efficient in their effector functions, B cells are able to downregulate their action through several mechanisms. Indeed Andor et al, demonstrated at a single-cell level, that MHC class I expression was downregulated in FL [163] and MHC class II was known to be associated with loss-of-function *CREBBP* mutations as described before [121]. Downregulation of co-stimulatory receptors such as CD27 and CD28 have also been described in the literature [164]. Kiaii et al, demonstrated that T cells presented an impaired LFA-1 dependent motility [144] and Ramsay et al showed a disruption to mobilize F-actin to the immunological synapse with B cells [143]. Moreover, efficient effector cells such as CD8+ T cells are retained at the periphery of tumor follicles as demonstrated by my team [142].

Here we present an overview of ICPs present in FL microenvironment and their action [165](Figure 37). ICP are another important key element of FL IE. T cell activity homeostasis depends on an equilibrium between ICP activatory (CD40L, OX40, CD27, CD28 and CD137) and inhibitory (CTLA-4, PD-1, LAG-3, TIM-3 and TIGIT) receptors [166]. In particular, LAG-3, TIM-3 and TIGIT are CD4+ and CD8+ T cell exhaustion markers [167–171].

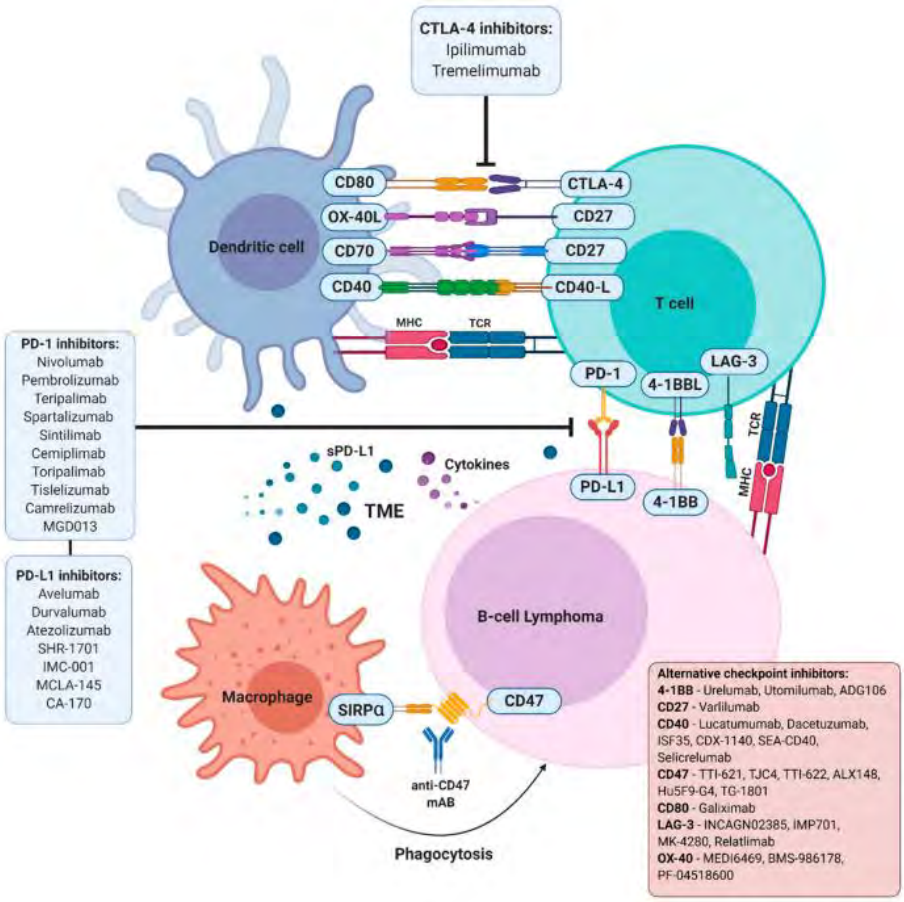

Figure 37 : ICP interaction with B-lymphoma microenvironment
From Armengol et al, Cancers, 2021 [165]

One of the most spectacular beackthrough of IT so far, was associated with targeting of ICP, more precisely the PD-1/PDL1 axis. Briefly, the main interactions between ICP and their ligands will be detailled. After binding to its ligands PDL1 or PDL2, expressed at the surface of B cells and macrophages, PD-1 intracellular signaling is activated leading to a reduction of T cell activation. CTLA-4 expressed by Treg binds to CD80/CD86 present at DC surface. LAG-3 is upregulated on CD4+ and CD8+ T cells and NK cells after binding to MHC class II leading to lymphocytes anergy [172]. Yang et al found a high proportion of T cells in FL biopsies displaying exhausted phenotype and functional characteristics such as TIM-3 overexpression [169]. TIM-3 is expressed on TFh, CTL and NK cells and represent the most exhausted stage of CD8+ T cells. Indeed, TIM-3 is often co-expressed with PD-1, LAG-3 and TIGIT [173]. TIGIT is expressed at the surface of APC, CTL and Treg and can be further upregulated by IL-10.

Thus, the interactions of ICP and their corresponding ligands confer a potent IE effect in FL. It is important to underline that some ICP interaction with their ligands are not always occurring between B cells and T cells. For instance, PD-1 and TIGIT are detected on TAM and FDC respectively, to exert their immunosuppressive function towards cells from the microenvironment [168,174]. In FL, CD4 and CD8+ T cells express PD-1 but at different level. Indeed, CD4+ T cells presenting a PD-1hi TIM3low phenotype are known as TFh in the follicles and have a B-cell supportive function whereas CD4+ PD-1low TIM3hi, in interfollicular areas, present an exhausted phenotype. CD8+ T cells are PD-1low and express a higher level of TIM-3 then CD4+ T cells. These studies indicate that PD-1 is not sufficient to distinguish exhausted or activated status. Thus, expression profiles of other ICP are needed to better understand FL microenvironment exhaustion. In this context, my team established a signature called immune escape gene set (IEGS) composed by genes involved in IE. By analysing of 38 FL samples, it was observed that this IEGS score was upregulated compared to normal tonsils [175]. Among these genes, *BTLA*, *CD80*, *CD86*, *CTLA4*, *LAG3*, *PDCD1*, *CD274*, *PDCD1LG2* and *TIGIT* are particularly interesting as they can be targeted by ICP blockers. Moreover, 1446 transcriptome microarrays were analyzed from public GEO datasets and an enrichment of 33 IE genes in DLBCL, FL and a few MCL and MZL samples was found [28]. A large-scale microarray profiling revealed four stages of IE in B-NHL: stage I represented by non-immunogenic tumors, stage II represented by immunogenic tumors without IE, stage III represented by immunogenic tumors with IE and stage IV represented by fully immune-edited tumors (Figure 38 left). 73% of FL exhibit a stage III or IV showing a strong level of IE mechanism in these tumors [28]. Tosolini et al also correlated each stage with OS and observed that stages I and IV presenting decreased T cell activation were associated with the poorest OS. On the opposite, stages II and III presenting T cell activation exhibited a higher OS (Figure 38 right).

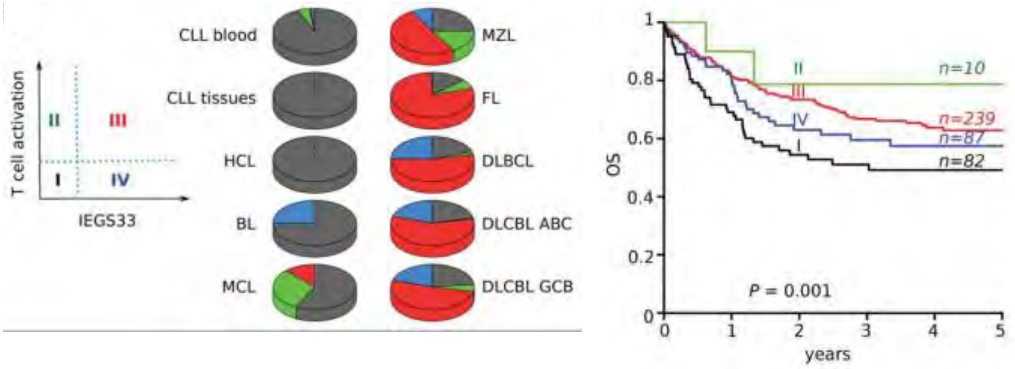

Figure 38 Immune escape stages in B-NHL based on T cell activation and IEGS33
From Tosolini et al, oncoimmunology, 2016[28]

IE mechanisms affect also innate immune cells such as γδ T cells and NK cells. For instance, FL B cells block γδ T cells proliferation through the inhibitory receptor BTLA-4 [176]. An action towards NK cells was also described, where overexpression of the inhibitory receptor CD161 and LLT1 (lectin-like transcript 1) led to downregulation of NK cytotoxic activity [177]. *In silico*, analysis of FL samples revealed that FL tumors are also characterized by an abundant infiltration of PD-1+ CD16+ γδ T cells. To study the IE mechanism, my team modeled PD-1+ γδ T cells and FL B cells interaction in presence of anti-CD20 mAbs and demonstrated potentialization of mAb efficacy against B cells by blocking PD-1 on γδ T cells [71].

Moreover, CD47 is a known ICP expressed at the surface of TAM, that reduce phagocytosis capacity implicated in efficiency of anti-CD20 mAbs leading to a "don't eat me" signal [178].

In addition to their T cell cytotoxic downregulation, B cells have another string in their bow. Indeed, they are able to recruit Treg cells displaying immunosuppressive actions towards cytotoxic cells such as CD8+ T cells. Indeed, overexpression of ICOS-L, CD70 and CCL22 on Treg leads to T cells polarization to a regulatory phenotype [179–181]. In clinic, Amé-Thomas et al and others observed an amplification of Treg CXCR5-CD25+cells and Tfr CXCR5+CD25+ in FL patients biopsies [137,182], thus, demonstrating their contribution in the FL immunosuppressive microenvironment.

2.3.4. CD39: a potential new target in FL immunosuppressive microenvironment

Physiologically, CD39 (ecto-nucleoside triphosphate diphosphohydrolase-1) encoded by *ENTPD-1* gene is an ectonucleotidase implicated in the equilibrium between ATP (adenosine-triphosphate) and adenosine accumulation in the extracellular compartment [183] (Figure 39). Indeed, to obtain a homeostasis between activated and resting immune cells, an equilibrium between these two

metabolites is necessary. ATP and adenosine are abundant intracellular metabolites but also important autocrine/paracrine messengers [184–186]. In the immune response homeostasis context, ATP, released after a cellular stress, acts as a danger signal able to activate immune cells through purinergic receptors such as P2Y2 and P2X7 whereas adenosine acts as an immunosuppressive metabolite able to limit immune cell activity after binding to adenosine receptors (A2aR and A2bR). CD39 catalyzes the degradation of ATP into adenosine di-phosphate (ADP) and then adenosine mono-phosphate (AMP) and CD73 hydrolyses AMP into adenosine [187]. This pathway is called adenosinergic pathway (Figure 39).

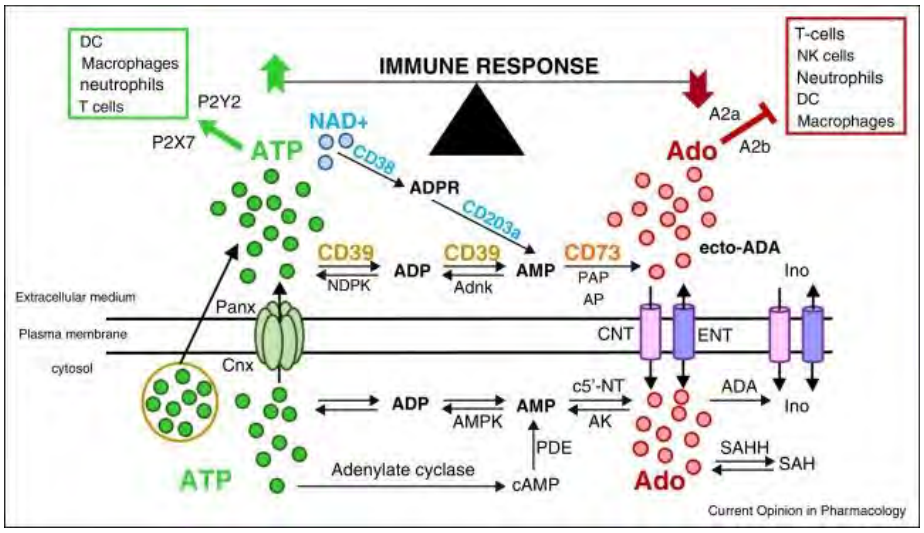

Figure 39 : Homeostasis of immune response by ATP and adenosine equilibrium
From Allard et al, Current Opinion in Pharmacology, 2016 [187]

CD39 and adenosine receptors are known to be upregulated after stress such as hypoxia, tissue damage or in chronic inflammation [188]. In a tumor context, cellular stress of hypoxic tumor core cause ATP accumulation. It is therefore processed by CD39 and CD73 thus inducing the accumulation of the immunosuppressive adenosine that can signals to other immune cells (Figure 40). In solid cancer, the impact of this accumulation is well-documented. Indeed, high levels of CD39 were measured in several cancers such as pancreatic cancer, lung cancer and sarcoma [187]. CD39 have been reported to be overexpressed on many cells of the microenvironment such as fibroblasts, myeloid cells, vascular endothelial cells, T regs and CTLs [189].

Adenosine mediates an immunosuppressive microenvironment through several mechanisms. For instance, on DC, activation of CD39 impairs DC antigen presentation leading to decreased T cell activation [190]. Generation of adenosine will signal through A2aR on CD4+ T cell to promote Treg phenotype by activating FOXP3 and LAG3 on these cells [191,192]. Treg present high level of CD39 and CD73 thus increasing the amount of immunosuppressive adenosine in the microenvironment. Expression of CD39 on B cells suppresses T effector function and induces secretion of IgA and IgG type

antibodies [193]. On cytotoxic cells such as CD8+ T cells and NK cells, A2aR activation impairs their killing capacity [194–196]. A2bR expressed on MDSCs can induce VEGF secretion, stimulating the angiogenesis [197]. Moreover, A2bR stimulation in TAMs favors their anti-inflammatory M2 polarization.

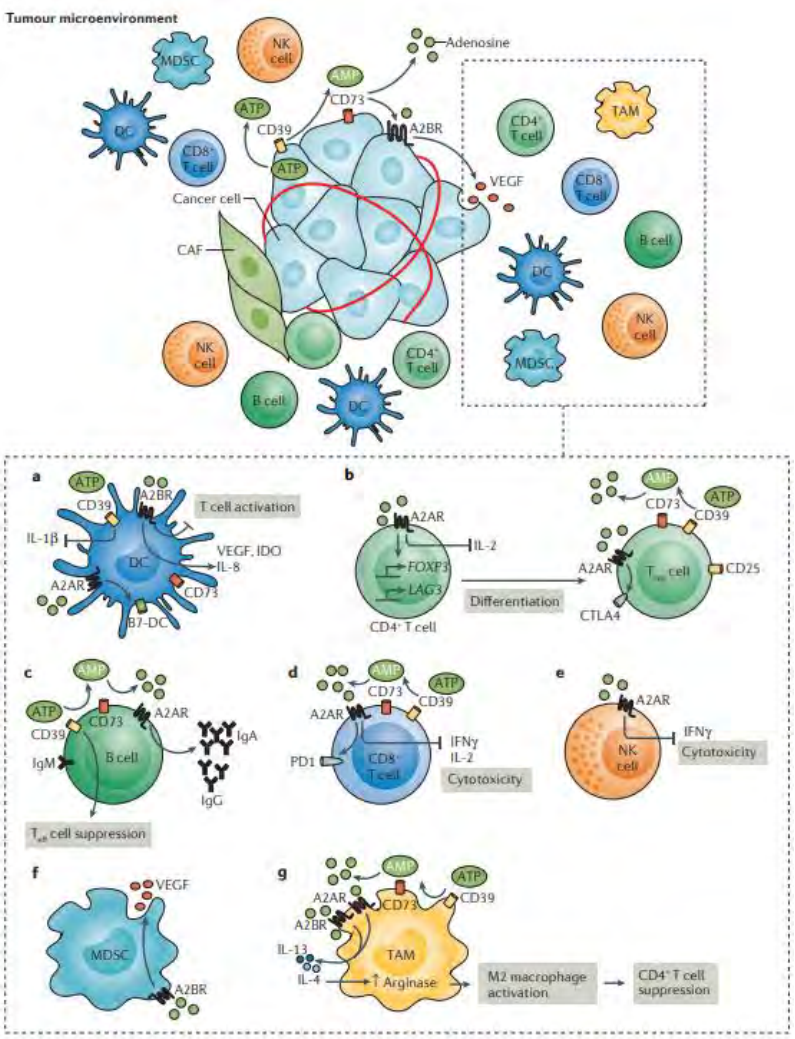

Figure 40 : Immunosuppressive microenvironment mediated by adenosine production
From Vijayan, nature cancer reviews, 2017 [198]

CD39 is implicated in all aspects of cancer-immunity cycle, including: restriction of leukocyte migration; enhancement of tumor angiogenesis; increase in fibroblast barrier function; inhibition of effector T cells and NK cells; enhancement of suppression by Tregs; B cells and macrophages; inhibition of NLRP3 inflammasome and pyroptosis; suppression of antigen presentation and inhibition of T cell activation (Figure 41). Thus, this ectonucleotidase appears from several years as a very interesting target for anti-cancer therapy [189,199,200].

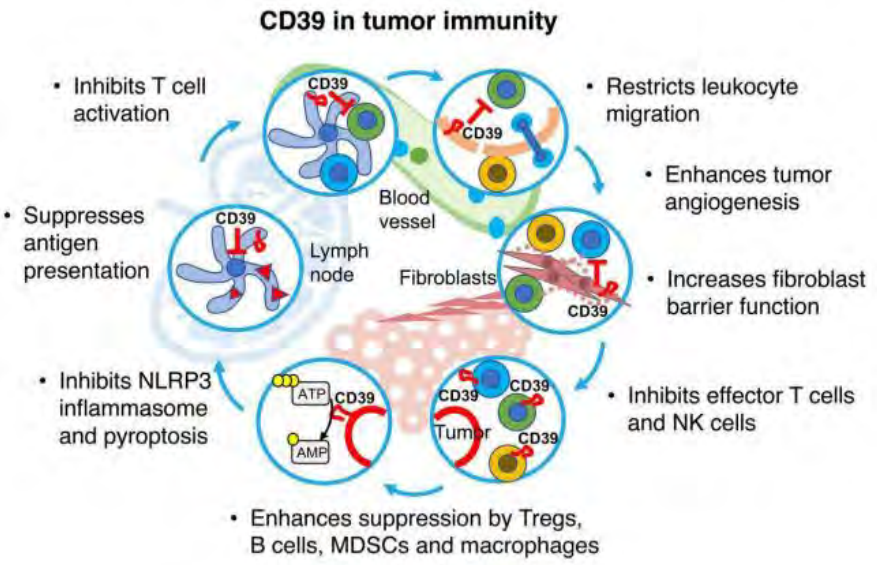

Figure 41 : Impact of CD39 in tumor immunity
From Allard et al, J Immunother Cancer, 2020 [199]

In B-NHL, only few studies have investigated the role of CD39. Cardoso et al using flow cytometry analyses determined a high expression of CD39 in eleven DLBCL (four GCB type and seven ABC type) and nine FL samples originating from LN biopsies or BM aspirates (Figure 42 A) [201]. Hilchey et al also found an increased expression of CD39 in CD3+ FL patient cells in comparison to normal LN, reactive LN and PBMC from healthy donors (Figure 42 B) [202]. Moreover, after blocking CD39 with a non-specific inhibitor (ARL67156), they succeeded to induce T cell IFNγ secretion in one patient (Figure 42 C) showing the possibility to reverse T cell anergy following CD39 blocking.

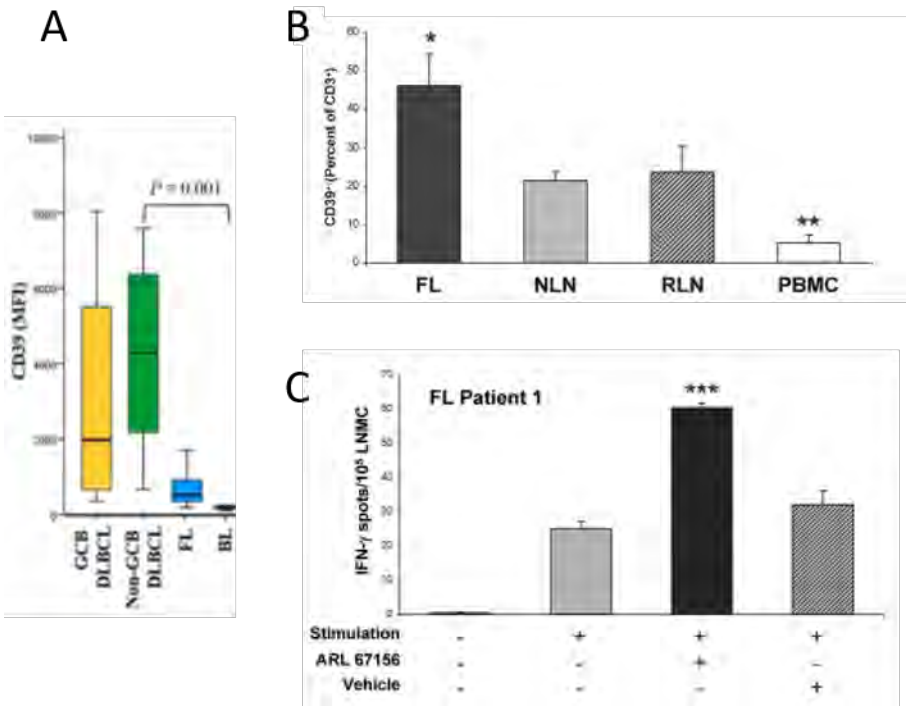

Figure 42 : Studies highlighting CD39 expression in B-NHL
A. Cardoso et al analyzed expression of CD39 (MFI mean fluorescence intensity) by flow cytometry in 4 GCB-DLBCL, 7 Non-GCB DLBCL, 9 FL and 7 BL patients samples (lymph node or bone marrow biopsies) [201] B. Hilchey et al analyzed by flow cytometry CD39 expression on CD3+ cells isolated from FL lymph nodes, normal lymph nodes (NLN), reactive lymph nodes (RLN) and PBMC from healthy donors. They also analyzed IFNγ expression after using ARL67156 CD39 inhibitor or not.[202]

Another interesting study showed that after stimulation with PAgs, γδ T cells express higher level of CD39. Moreover, Gruenbacher et al highlighted that CD39 can use PAgs as substrate to impede their action on γδ T cells activation thus underlying a new mechanism of γδ T cell activation homeostasis [203]. This was described in a physiological context but one could speculate that increased CD39 expression on γδ T cell surface could cause their anergy in a tumoral context. Nakamura et al investigated resistance to rituximab in a lymphoma mouse model expressing high level of CD39 leading to the accumulation of the immunosuppressive molecule adenosine [204]. Interestingly, using public data set from the European Genome-phenome Archive (EGA), they studied survival probability on the basis of *ENTPD-1* expression. Thus, they found that DLBCL patients expressing high level of *ENTPD-1* presented a lower survival than patients with low *ENTPD-1* (Figure 43 A). To investigate further the role of aberrant expression of *ENTPD-1*, Raji cells were transfected with a vector allowing overexpression of CD39. As control, they used Raji cells transfected with vector allowing overexpression of CD38, another enzyme responsible for adenosine generation through NAD+ catalyzation in contrast to CD39 that uses ATP (Figure 43 B). Transfected cells were then injected in NRG mice which were treated or not with rituximab. As shown in figure 43C, an increase of tumor growth after rituximab treatment was observed demonstrating the negative impact of CD39 overexpression on rituximab efficacy.

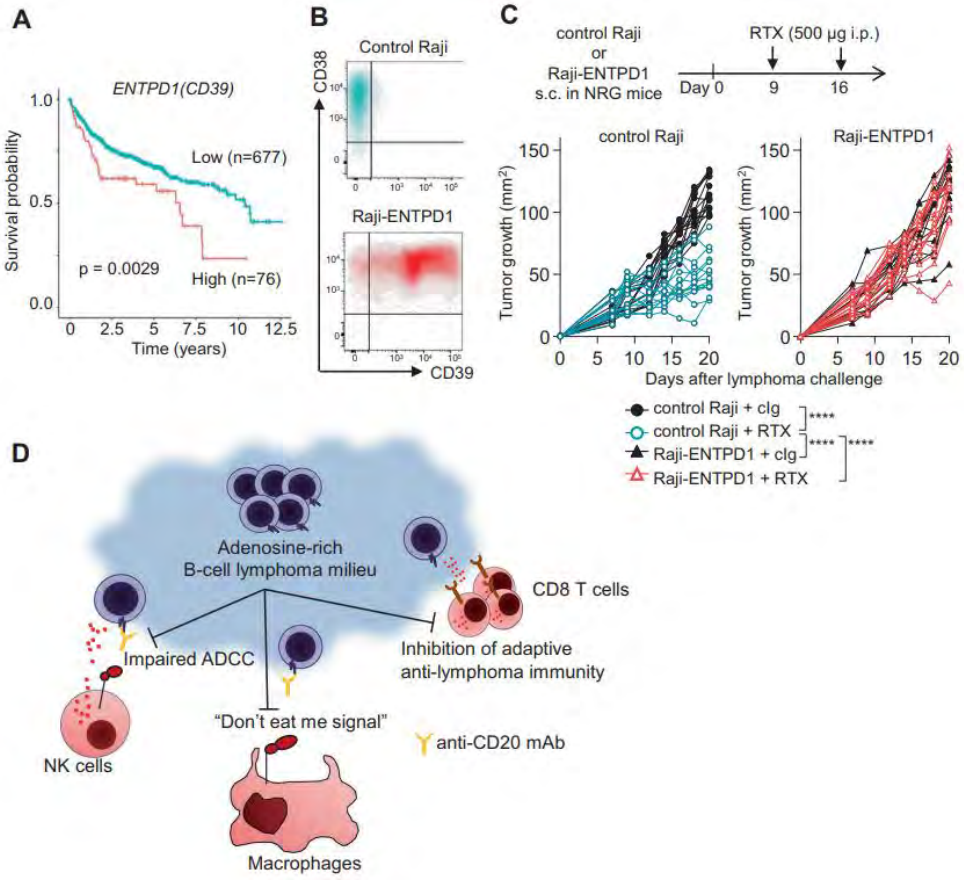

Figure 43 : Study of CD39 impact in rituximab resistance from Nakamura et al[204]

A. Kaplan–Meier survival curves showing overall survival in patients with DLBCL based on *ENTPD-1* (CD39) mRNA expression (n = 753). The stratification into low and high CD39 expression groups was based on an optimal threshold. B. FACS plots showing the expression levels of CD38 and CD39 in control Raji cells and Raji cells transfected with CD39 (Raji-*ENTPD-1* cells). C NRG mice were subcutaneously challenged with control Raji cells, left panel).

In this study, they also investigated the role of A2AR in the generation of adenosine responsible for the negative regulation of ADCC induced by NK cells and ADCP induced by macrophages, two key processes important in anti-lymphoma immunity. In KO Adora2a-/- mice, they demonstrated an increase of macrophages co-expressing MHC-II and B7-1, suggesting that the absence of adenosine signaling favored generation of macrophages with higher antigen presentation capacity. This result showed the negative role of adenosine in macrophages proliferation and function called the "don't eat me signal". Moreover, absence of A2AR in myeloid cells in mice demonstrated a better anti-lymphoma control.

All of these studies highlighted the important role of CD39 in IE of cancers in general but also in B-NHL. These last few years, interest in inhibiting this enzyme has grown as revealed by the recent development of CD39 antagonists [189]. In table 4 six antagonists currently used in preclinical or clinical stages of development are listed: TTX-030 antibody in phaseI/IIb clinical trial for solid tumors and lymphoma in combination with pembrolizumab, doxetaxel, gemtamicine, nab-paclitaxel; IPH5201 antibody in phase I clinical stage for solid tumors in association with duvalumab and/or oleclumab; SFR-617 antibody in phase I for advances solid tumors with gemcitabine/abraxane in pancreatic cancer and anti-PD-1 in gastric cancer; ES002 antibody in preclinical stage and one antibody called 9-8B and one antisense oligonucleotide under development. For now, no results from these clinical trials are available but for sure, they will bring new datas on the interest of targeting CD39 in cancer, giving a great promise.

Modality	Agent (sponsor)	Stage	Indications	Combination agents	Identifier
Antibody, hulgG4; enzymatic inhibitor	TTX-030 (Tizona Therapeutics)	Clinical, phase I/Ib	Solid tumour and lymphoma	Pembrolizumab, doxetaxel, gemcitabine, nab-paclitaxel	NCT03884556 (REF.[101])
Antibody, hulgG1 (mut)*; enzymatic inhibitor	IPH5201 (Innate Pharma/AstraZeneca)	Clinical, phase I	Solid tumours	Durvalumab with or without oleclumab	NCT04261075 (REF.[99])
Antibody, IgG4; enzymatic inhibitor	SRF-617 (Surface Oncology)	IND filed; phase I initiation anticipated in 2020	Advanced solid tumours, phase II planned in gastric and pancreatic cancer	Gemcitabine/abraxane in pancreatic cancer; anti-PD1 in gastric cancer	NCT04336098 (REF.[99])
Antibody, enzymatic inhibitor, depletion	ES002 (Elpisciences)	Preclinical	NA	NA	100
Antibody, mulgG2a; enzymatic inhibitor	9-8B (Igenica)	Unknown	NA	NA	17
Antisense oligonucleotide	(Secarna)	Unknown	NA	NA	92

Table 4 : CD39 antagonists in preclinical or clinical development
From Mosta et al, cancer review immunology, 2020 [189]

Summary focus on follicular lymphoma (2)

The understanding of FL genesis and progression by deciphering FL genetic landscape progressed these past few decades and highlighted the role and complexity of TME (Figure 44). High-content analysis at the genomic and cellular levels, allowed to draw a clearer picture of FL. FL progression clearly depends on epigenetic mutations and is influenced by immune and stromal populations present in FL TME. A better understanding of the TME crosstalk and kinetic of genetic aberrations during disease progression are still needed to improve the efficiency of treatment and to discover new therapeutic strategies which have to target both tumoral cells and cells composing FL microenvironment.

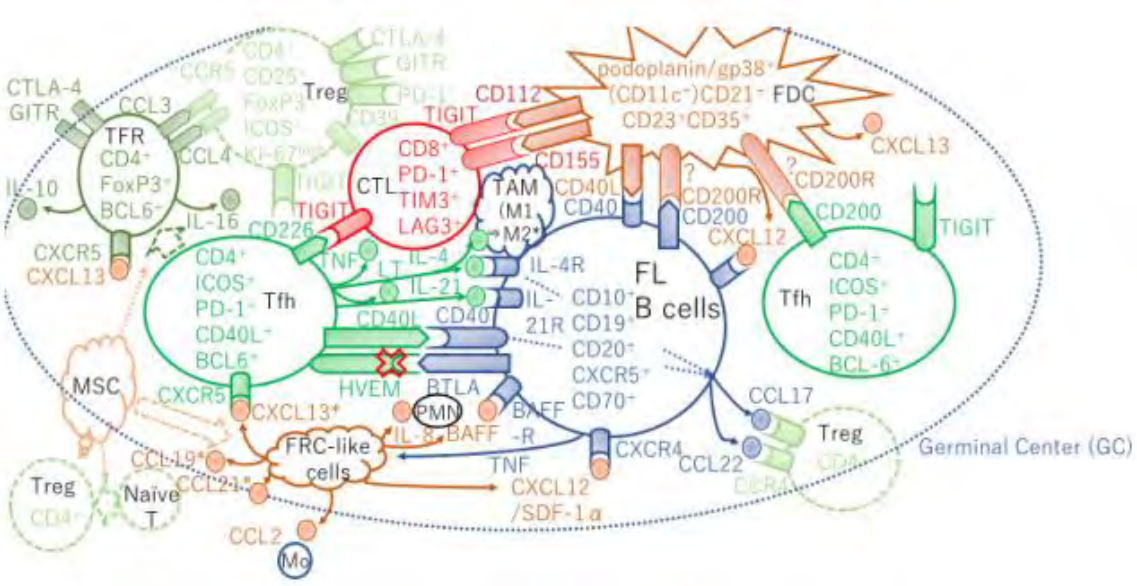

Figure 44 : FL microenvironment, a complex network

From Watanabe, Int J Mol Sci, 2020 [205]

3. Follicular lymphoma treatments: the more the better

3.1. Therapeutic standards: anti-CD20 mAb, FL treatment backbone

As treatment depends on the stage of the disease, initial classification is essential to better categorize patients. Staging is determined based on the Ann Arbor classification system (Table 5). Prognosis factors also has been established such as FLIPI, FLIPI2, GELF, BNLI and they present different criteria such as age, level of serum lactate dehydrogenase, hemoglobin level or beta-2 microglobulin level. These factors help to evaluate the responses of treatment but most of them are based on demographic and clinical informations, rather than molecular ones. Another index, which seems to be more powerful, is called m7-FLIPI which proposes in addition to FLIPI score, a mutation status of seven candidate genes (*EZH2*, *ARID1A*, *MEF2B*, *EP300*, *FOXO1*, *CREBBP* and *CARD11*). However, none of these indexes are used in clinical practice because of conflicting data.

FLIPI	• Age > 60 years • Elevated serum lactate dehydrogenase • Hemoglobin < 12 g/dL • Ann Arbor stage III or IV disease • > 4 involved nodal sites
FLIPI2	• Age > 60 years • Hemoglobin < 12 g/dL • Elevated beta-2 microglobulin • Any node > 6 cm • Bone marrow involvement
GELF criteria	• Any node > 7 cm • 3 or more nodes each > 3 cm • Splenomegaly (> 16 cm per imaging) • B symptoms • Increased lactate dehydrogenase or Beta-2 microglobulin • Leukemia (> 5×10^9/L malignant cells) • Compression syndrome (ureteral, gastrointestinal) • Effusions (pleural or peritoneal) • Cytopenias ○ Leukocytes < 1×10^9/L ○ Platelets < 100×10^9/L ○ Hemoglobin < 10 g/dL
BNLI criteria	• Rapid disease progression within 3 months • B symptoms • Life-endangering organ involvement (or impending involvement) • Osseous lesions • Renal infiltration • Cytopenias related to bone marrow involvement: ○ Leukocytes < 1.5×10^9/L ○ Platelets < 100×10^9/L ○ Hemoglobin < 10 g/dL

FLIPI, Follicular Lymphoma Involvement Prognostic Index; *GELF*, Groupe d'Etude des Lymphomes Folliculaires; *BNLI*, British National Lymphoma Investigation

Table 5 : Available prognostic scores for FL management
From Dreyling et al, Annals of oncology, 2021 [91].

Regarding the treatment, different options are possible depending on patients' stages. FL Patients exhibiting early stage FL associated with a good prognosis benefit from a "watch and wait" therapy which consists in an active monitoring without treatment until is needed. For the others, stages stratification determines the treatment regimen [206].

For localized stage I-II (around 5 to 15% of patients), different curative strategies can be proposed. Single therapy with a radiotherapy (RT) based treatment (ISRT), or rituximab single-agent can be considered. In some cases, combination strategies with RT and rituximab chemotherapy can be applied. Indeed, its efficacy has been demonstrated on PFS compared to rituximab alone [207]. Moreover, a study showed that a localized irradiation combined with rituximab as single agent represent a good side-effects/efficacy balance therapeutic strategy [208].

For advanced stages (III-IV) of FL, representing around 50 to 60% cases, different lines of treatment exist, but they are unfortunately not curative. As FL exhibits an indolent course, majority of patients do not require any treatment until symptom development. Before rituximab era, some studies showed that therapy in asymptomatic patients did not improved OS [209]. After rituximab introduction, early treatment initiation resulted in improved PFS but not OS. Nevertheless, many studied showed that rituximab combined with chemotherapy improved OS [210–214]. Rituximab can be combined with several poly-chemotherapies such as CHOP (cyclophosphamide, doxorubicin, vincristine and prednisone), bendamustine, CVP (cyclophosphamide, vincristine and prednisone). Another anti-CD20 antibody, Obinutuzumab, displays increased PFS in comparison to rituximab but no difference was observed for OS [215]. Interestingly, the combination of rituximab and lenalidomide showed similar efficacy compared to immunochemotherapy [216]. A rituximab maintenance treatment is recommended during 2 years and has shown improved PFS [217].

For relapsed disease, "watch and wait" approach can be considered in asymptomatic patients with a low tumor burden[91]. In other cases, the choice of treatment depends on efficacy and duration of response of the first line therapy and age of patients. Indeed, for high tumor burden category, different strategies are applied for patients under or over 65 years old (Figure 45) [91]. Briefly, different polychemotherapy approaches can be proposed in combination with rituximab (R-CHOP: rituximab-cyclophosphamide, hydroxydaunorubicine, oncovin, prednisone; R-CVP: rituximab, cyclophosphamide, vincristine sulfate and prednisone), or monotherapy with rituximab and in some selected cases, rituximab associated with lenalimodide, radioimmunotherapy or others.

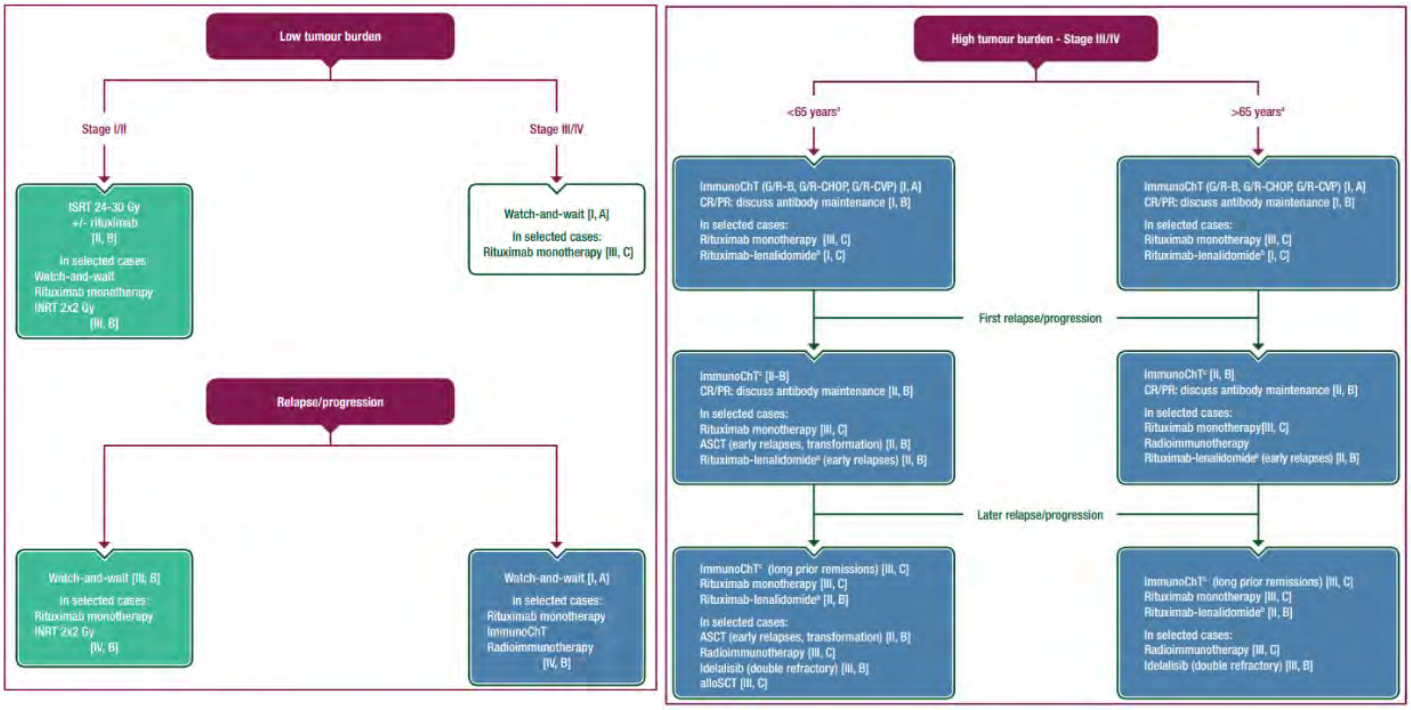

Figure 45 : Therapeutic management guidelines in FL

From Dreyling et al, Annals of oncology, 2021.[91]

3.1.1 Anti-CD20 mAbs mechanisms of action

As presented in the figure 45, mAbs targeting CD20 (GA101 or rituximab) are at the center of FL patients' treatment regimen. Indeed, since its development in the 1990s, rituximab has become rapidly a key therapy in FL treatment. The addition of rituximab to conventional polychemotherapy tremendously increased patient OS.

Even if its structure is well known, CD20 cellular function is poorly understood. Except its role in intracellular calcium signaling associated with BCR, no other evidence about its function has been clearly described [218,219]. Experiments on KO mice for CD20 encoding gene (*MS4A1*) did not show deficiency in B cell differentiation, maturation, localization and function [220]. Targeting CD20 with antibodies was one way to try to decipher its cellular function.

Targeting CD20 in B-cell malignancies appeared to be very encouraging as malignant B cells also express CD20. Nevertheless, expression of CD20 on cancer B cells is not the only reason making it an interesting therapeutic target. For example, first CD20 does not circulate in the plasma. Second, CD20 displays an elimination and finally an internalization limited after antibody binding prolonging its effect. Based on this rationale, the number of mAbs targeting CD20 has significantly grown in the last decade. It is important to keep in mind that each mAb responds to a specific nomenclature: -momab for murin, -ximab for chimeric, -zumab for humanized and -mumab for full humans mAb (Figure 46

left). Since rituximab revolution in 1997, various changes in the monoclonal antibody technologies were introduced. We can differentiate multiple: means of a new antibody generation (including: hybridoma, phage display, mRNA display); antibody formats with unique characteristics associated with their size, functionality and valency (monospecific antibodies, antibody fragments, multispecific antibodies); strategies to improve already generated antibodies, including: tailoring of Fc region, glycoengineering, affinity optimization and conjugation of specific molecules [221]. To measure up to this diversity of antibodies the INN (International Nonproprietary Names) revised the monoclonal antibody nomenclature (Figure 46 right).

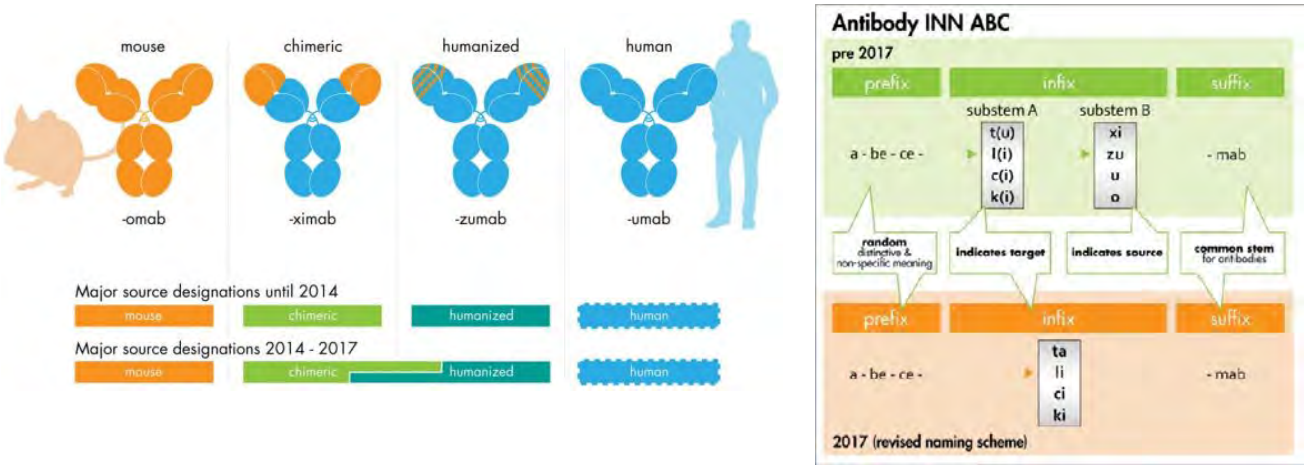

Figure 46 : Antibodies nomenclature before 2017 (left) and 2017 revised one (right)
From Parren et al, mAbs, 2017 [221]

Monoclonal antibodies targeting CD20 are divided into two types, I and II, according to different modes of action [222,223]. Both of these antibodies present direct and indirect effects against their target (Figure 47).

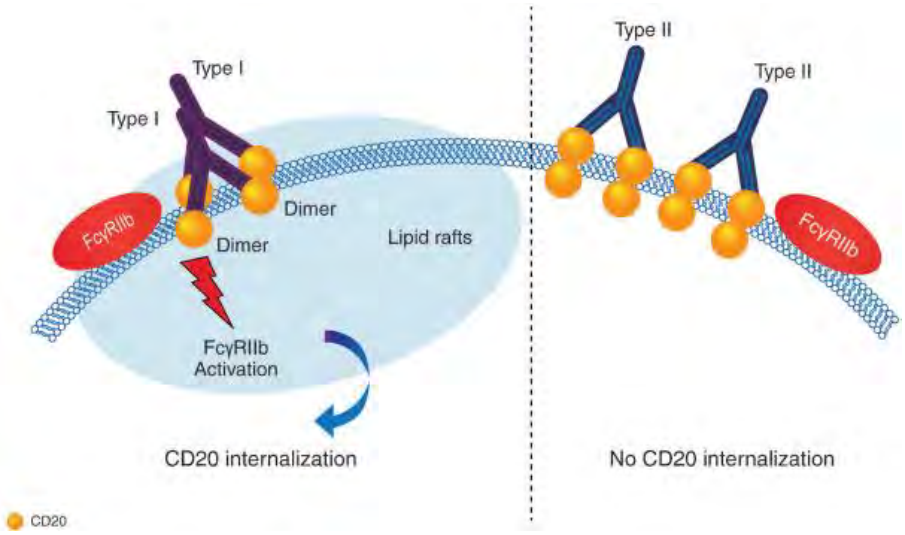

Figure 47 : Type I and type II anti-CD20 mAb and their mechanism of action
From Klein et al, Expert Opin Biol Ther 2021 [223]

Type I mAbs, such as rituximab and ofatumumab, attach to CD20 oligomers, creating inter-tetrameric complexes followed by a migration into lipid rafts. About their direct mechanisms of action, CD20-mAb complex favors co-localization with Cbp (or CREBBP) proteins and to induce a calcium signal leading to a caspase-dependent apoptosis of target cells. Another important effect of rituximab is the chemosensitization [224]. The p38MAPK, PI3K, RKIP and Ras pathway have been demonstrated in BL to be involved in this phenomenon. Chemosensitization induced by rituximab was also reported through BCL2 and BclXL dependently of NF-κB, AP1 and SP1 [224]. Rituximab also sensitized B-NHL cell lines to TRAIL and FasL through YY1 and NF-κB transcription factors [225,226]. Thus, the inhibition of NF-κB or YY1 by anti-CD20 mAb induced a sensitization to TRAIL-induced apoptosis. Beside direct mechanisms, rituximab is also able to induce indirect mechanisms of action such as complement-dependent cell cytotoxicity (CDC) and antibody-dependent cell cytotoxicity (ADCC) or phagocytosis (ACDP). First, due to its inter-tetrameric attachment to CD20 and the following migration into lipid raft, rituximab is able to link the C1q and to activate complement cascade. This mechanism called, CDC allies innate and adaptive immunity (Figure 48). Second, owing to the fact that most mAbs developed are IgG1, they can recruit FcγRIII expressing effector cells through their Fc portion and induce ADCC or ADCP when macrophages are recruited. Briefly, for ADCC, after binding of antibody Fc portion to FcγR present on effector cells, a lytic synapse is formed and triggers a degranulation leading to death of tumor cells. For ADCP the mechanism is quite similar, except that binding with the FcγRIIIa expressed on macrophages thus leading to phagocytosis and elimination of the tumor cell (Figure 48). Many studies pointed out that NK cells are the major effectors of ADCC [227] and in particular by the subpopulation CD56dim NK cells that express higher levels of FcγRIII receptor (CD16) [228]. As NK cells do not need priming to start a rapid immune response, they are key element in initiating anti-tumor response. Moreover, γδ T cells have been depicted in many studies as a great boost for anti-CD20 induced ADCC against tumor cells [229–232]. ADCC has been modeled *in vitro* on 3D culture and *in vivo* on xenograft models by my team with NK cells and γδ T cells [71,233]. Altogether, as ADCC represents one of the most potent mode of action of therapeutic mAbs, newly developed immunoglobulins, such as GA101, are usually characterized by an increased potential to induce ADCC.

Type II mAbs such as GA-101 (obinutuzumab) present an intra-tetrameric binding to CD20 and do not induce CD20 migration into lipid rafts induce CDC. Changes in the VH-CH1 angle of GA-101, confers a higher direct effect in terms of cytotoxicity by promoting cell-cell adhesion leading to a caspase-independant cell death and more protein phosphorylation downstream the BCR. Moreover, studies from my team and others have shown different types of cell death after GA-101 treatment such as lysosomal cell death, senescence and inhibition of signaling pathways including : AKT, ERK, Syk

and mTOR [234–239]. About indirect effect, GA-101 afucosylation in its Fc portion allows a higher affinity to FcγRIIIa, thus a higher ADCC capacity [234,240] (Figure 48).

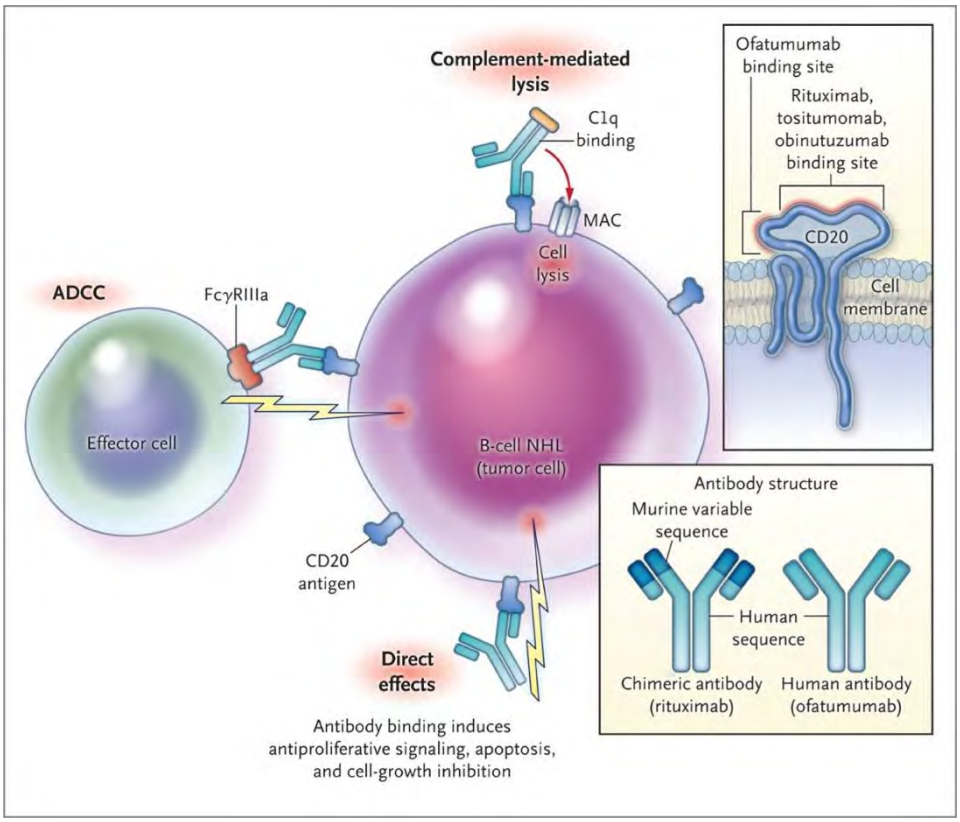

Figure 48 : anti-CD20 mAbs mechanism of action
From Maloney DG, NEJM 2012 [241]

3.1.2 mAb anti-CD20 mechanism of resistance

Despite, its undeniable efficacy, some patient remains refractory to rituximab leading to further relapse. Understanding the mechanism of resistance is one of the main challenges in FL research. Over the past few years, many mechanisms have been depicted such as FcR polymorphism [242], rituximab dosing [243], dose-density [244], loss of CD20 expression, antigenic modulation and survival pathway overactivation [224] impacting both direct and indirect effects of anti-CD20 mAbs.

For instance, rituximab resistant cell lines show an overactivation of survival pathways such as NF-κB leading to BCL2 anti-apoptotic protein overexpression. Thus, altered apoptotic effect of rituximab could explain resistance [245 246 247 248]. Another obvious mechanism of resistance to anti-CD20 is the loss of the target itself, which has been observed in patients. Moreover, loss of CD20 was observed in rituximab resistant cell lines and this was due to altered lipid rafts organization and altered signaling [249]. One mechanism that could explain this CD20 loss, is the shedding which is caused by an

effector cells such as macrophages [250]. This mechanism called shedding induces the elimination of extracellualar rituximab/CD20 complex on the target cells.

Indirect mechanism of action can also be affected. Resistance to CDC has been reported to be induced mainly due to the expression of the complement regulatory protein (mCRP) such as CD46, CD55, CD35 and CD59 by tumor cells. Preclinical studies showed that blocking these proteins could enhance rituximab efficacy [251]. Another explanation of this resistance is the long term use which can induce an exhaustion of complement resources [252]. For ADCC, one of resistance mechanism is the modulation of membrane conformation that confers a decreased efficacy of effector cell recognition. For example, inhibition of cholesterol synthesis which induces a modification of lipid raft composition, was shown to decrease rituximab induced ADCC *in vitro*. Another important mechanism of resistance is FcR polymorphism. Indeed, many *in vitro* and *in vivo* studies have been conducted to support this mechanism of action [242,253,254]. It has been shown that genotype homozygous for FgRIIIa-158V (VV) was associated with higher clinical response to rituximab [253].

Another mechanism of resistance can be attributed to the TME. Indeed, tumor cells are surrounded by other cells and components that can act on rituximab efficacy by affecting their signaling. For instance, galectin-1 expression in local microenvironment was showed to induce resistance through blocking macrophages activation leading to a reduced ADCP [255]. Tumoral volume is also important to consider as it may affect rituximab penetration into the tumor. This was shown in a mouse model [256] but also in FL patients using computed tomography [213] (ct scan) or positron emission tomography [257] (PET scan).

Altogether, numerous mechanisms of resistance can impede mAbs efficacy. Thus, discovering novel targets and establishing new therapeutical strategies are necessary.

3.2 Novel agents under clinical development

Even if anti-CD20 based therapy associated to chemotherapy represents an efficient therapeutic strategy, alternatives are needed to overcome resistance and to offer new perspectives to relapsed and refractory patients. Among myriads of newly developed therapeutic strategies, it was decided to review closer to following ones: BCL2 inhibitors, immunomodulatory molecules, inhibitors targeting BCR signaling, molecules targeting epigenetic alterations, antibody drug conjugates and cellular therapy.

3.2.1. BCL2 inhibitory molecules

The rationale of targeting BCL2 was quite evident with the presence of t (14;18) translocation in 80% of FL patients. Nevertheless, venetoclax (ABT-199), a BCL2 inhibitor, in monotherapy showed limited results in FL with 17% CR [258]. A long term follow-up of this study showed interesting maintenance in few patients treated during 5 years who presented stable disease [259]. Nevertheless, majority of patients did not respond sufficiently to the single agent, suggesting that combination with other therapies could enhance the effectiveness of response. Other clinical trials combining venetoclax with other agents such as rituximab or bendamustine were also tested, exhibiting promising results in phase I & II [260,261]. In the phase II study, a CR of 75% has been shown in the arm treated with bendamustine + rituximab + venetoclax and a CR of 17% for patients treated with venetoclax + rituximab [231].

3.2.2. Immunomodulatory molecule: Lenalidomide

Lenalidomide, is an immunomodulatory drug that exhibits two types of mechanisms of action. First, a direct cytotoxic effect against lymphoma cells by inducing degradation of IKZF1 and IKZF3 through its binding to E3 ligase Cereblon. After Cereblon degradation, p21 is increased, leading to IRF4 decrease and consequently to inhibition of proliferation [262]. Second, an indirect effect of lenalidomide consist in increase in proliferation and activation of NK cells, resulting in increased ADCC against tumor cells. This molecule is also able to act on T cell stimulation and cytotoxicity and dendritic cell presentation [262]. Lenalidomide has proven its efficacy in FL in different clinical trials. Indeed, a phase III study showed a synergy of combining rituximab with lenalidomide in comparison to rituximab alone (39.4 months versus 14.1 months) but unfortunately more side effects were observed [263]. In GALEN trial, phase I/II study showed that obinutuzumab and lenalidomide combination, led to an increased response rate from 38% with obinutuzumab alone to 79% with the combination [264]. As there are no randomized studies showing benefits of obitunutuzumab over rituximab in combination with lenalidomide, only the rituximab combined with lenalidomine obtained the FDA approval in May 2019.

3.2.3. Targeting BCR signaling with inhibitory molecules: PI3K and BTK inhibitors

PI3K signaling pathway is a well-known regulator of cell metabolism, growth and cell division [265]. Three classes of PI3K exist, class I (PI3K α, β, γ); II, III according to their regulation, structure and lipid substrates [266]. PI3K pathway plays an important role in BCR signaling and B cell activation [267]. Class I is most relevant for cell growth and survival and it has been the target of anti-cancer drug development. PI3Kδ and -γ expression is largely limited to leukocytes, while PI3K-α and -β are ubiquitously expressed [268]. PI3Kδ and -γ regulate leukocyte trafficking and cell proliferation [269]. There are several studied mechanisms of PI3K signaling upregulation in human cancers, including somatic mutations

and PI3K activation *via* the receptor tyrosine kinase and RAS pathways [270]. To date, a limited number of studies have investigated these events specifically in the context of FL. Among them Yahiaoui et al showed that PI3K-δ may also play a role in activating AKT in FL. Thus, therapies including PI3K inhibitors has been developed and approved in FL with four different molecules: idelalisib (PI3Kδ inhibitor), copanlisib (PI3Kα/δi), duvelisib (PI3Kδ/γi) and umbralisib (PI3Kδi). Idelalisib, a specific PI3Kδ inhibitor, was the first drug approved in FL therapy, and results from a phase II study showed a median PFS of 11 months [271]. Unfortunately, this therapy used in long term can confer a risk of auto-immune toxicity and infectious disease complications. In this context, novel PI3Ki are under development to lower the risk of these side effects. For example, parsaclisib, a selective PI3Kδ inhibitor is a promising new molecule exhibiting better specificity and less toxicities than other PI3Ki. This drug is still under phase II clinical trials but the phase I showed promising results in terms of monotherapy response [272].

Another class of molecules targeting the BCR signaling are BTK inhibitors. The most renowned one – Ibrutinib, showed already impressive results in CLL and MCL. This allowed to develop a clinical trial in FL called DAWN, which did not bring the expected results as seen in other diseases [273]. Nevertheless, pre-selection of patients on the basis of CARD11 mutation showed increased efficacy of BTKi in FL. Moreover, the combination of ibrutinib and rituximab showed promising results in a phase II study with efficient activity in first-line therapy in FL [274]. Another promising combination is the one associating ibrutinib with ABT-199 [275].

3.2.4. Targeting epigenetic alterations

FL cells epigenetic regulators are known to undergo mutation and dysregulation in GC. The main mutations are KMT2A (histone methyltransferase, lysine methyltransferase 2A) and CREBBP (acyltransferase). To restore epigenetic balance, many therapeutic strategies are ongoing such as EZH2 and HDAC inhibitors. As EZH2 is mutated in around 20% of FL, its targeting represents an interesting strategy to affect the main driver of FL pathogenesis and also to induce immune modulatory effects. In contrast to most epigenetic alterations of FL that present loss of function, *EZH2* mutation results in a gain of function of methyltransferase activity. Thus EZH2 inhibitors were developed and the first one, tazemetostat, showed promising results in phase I and II studies [276].

Taken into account the frequent acetyltransferase loss of function mutations in FL, targeting HDAC to restore epigenetic homeostasis is another potential therapeutic approach. Interestingly, Vorinostat in a phase II study showed a response of 49% [277]. In combination with rituximab, vorinostat showed a PFS of 41% [278].

3.2.5. Antibody drug conjugates (ADC)

The approach of ADC brings new insight in FL treatment. Indeed, the concept is to combine the target-specificity of monoclonal antibody which is chemically linked to a cytotoxic drug. In FL, inotuzumab ozoguamicin (INO), an mAb anti-CD22 conjugated to the cytotoxic antibiotic from the class of calicheamicin is under investigation. Phase I-II study showed promising results in association with rituximab with 87% response [279] with a 2 years PFS of 68%. Pinatuzumab vedotin is another example of CD22 targeting ADC. This ADC is linked to microtubule agent, monomethyl auristatin E (MMAE) and showed interesting results in a phase II study, with 62% monotherapy response [280]. Another target of ADC in FL is CD79b which can be targeted by the polatuzumab vedotin (POLA) associating an anti-CD79 and MMAE agent. In a phase I/II, combination of GA-101 and lenalidomide, showed potent effects with around 76% response but unfortunately, associated with severe toxicity (grade 3 and 4) in 63% of patients [281].

3.3.6. Immune checkpoint inhibitors

IE is one of the main mechanisms leading to NHL pathogenesis [282]. Overexpression of ICP such as PD-1, represents a key mechanism in the process of tumor induced-immunosuppression. Indeed, in a physiologic context, PD-1 links to PDL-1 to suppress T cell activity and restore T cell homeostasis. In a tumor context, this pathway is overactivated and T cells present an exhausted profile and consequently their cytotoxic activities are compromised. From this rationale, ICP blockade became a key strategy in cancer therapy armamentarium. Given the great results obtain in solid cancer and HL, clinical trials have been developed in FL as well [283–285]. Unfortunately, mitigated results were obtained. The first development aimed to target the PD-1/PDL1 axis as preclinical studies showed an upregulation of PD-1 expression in intratumoral TILs and that DP-1 blockade, enhanced T cell function [286]. Moreover, numerous PD-1+ infiltrating T-cells were shown in FL [287]. Nivolumab (anti-PD-1 antibody) was tested in monotherapy but showed disappointing results with only 4% ORR (overall response rate) [288]. Thus, combination with other immune stimulatory therapies were tested. Evaluation of pembrolizumab (anti-PD-1 antibody) and rituximab in a phase II showed an interesting ORR of 64% and 48% CR [289]. Other ICP targeting were also tested such as the promising combination of anti-PD-1/anti-CTLA4 which was successful in some malignancies. Unfortunately combination of nivolumab and ipilimumab did not exhibit efficiency in phase Ib [290]. PI3Ki combination with ICP is of interest because of the immunomodulatory effect of PI3Ki that could be potentially enhanced with ICP therapy. Many ongoing clinical trials are pointing towards this direction. Another interesting IT targeting is the protective “don’t eat me” signal. Indeed, Hu5F9-G4, an anti-CD47, stimulates tumor cell phagocytosis

and induces an antitumor T cell response. A phase I/II study that evaluates the combination of anti-CD47 / rituximab showed promising results with an ORR of 71% and 43% CR in FL associated with no severe adverse events [291]. Table 6 presents a list of some checkpoint inhibitor tested in B-NHL patients [162].

Name	Trade Name	Developed by	Structure	Target	First Approval by US FDA for the Treatment of Cancer	Number of Studies in Patients with NHL Registered at ClinicalTrials.gov
Ipilimumab	Yervoy	Bristol-Myers-Squibb	human IgG1	CTLA-4	2011	13
Tremelimumab	N/A	AstraZeneca	human IgG2	CTLA-4	N/A	3
Pembrolizumab	Keytruda	Merck	humanized IgG4	PD-1	2014	60
Nivolumab	Opdivo	Bristol-Myers-Squibb	human IgG4	PD-1	2014	41
Pidilizumab	N/A	Medivation	human IgG1	PD-1	N/A	3
Durvalumab	Imfinzi	AstraZeneca	human IgG1	PD-L1	2020	19
Avelumab	Bavencio	Merck, Pfizer	human IgG1	PD-L1	2017	9
Atezolizumab	Tenetriq	Roche	humanized IgG1	PD-L1	2016	20

Table 6 : Checkpoint inhibitors evaluated in clinic for patients with NHL
From Pytlik et al, Vaccines, 2020 [162]

3.3.7 Cellular therapy: CAR-T cell and BiTE

CAR-T cells are autologous T-cells transduced with a chimeric antigen receptor (CAR) which targets the modified T-cell against a specified cancer antigen. A CD19 CAR-T cells therapy is one of the main revolutions in the field since rituximab introduction. Indeed, this treatment has tremendously changed the management of relapsed lymphoid malignancies giving a chance of remission to patient that were impossible to cure. The first FDA approval was in 2017 for axicabtagene ciloleucel that exhibited an ORR of 83% in ZUMA-1 trial. Another CAR-T, tisagenlecleucel, was approved in 2018 after the JULIET trial showing an ORR of 52%. Now, these therapies are under investigation in FL. For axicabtagene ciloleucel, the ZUMA-5 trial showed an impressive 94% ORR and 60% CR. For tisagenlecleucel, the ELARA study presented an ORR of 82,7% and a CR of 65,4% in FL patients. Thus, both of these strategies seem to be extremely efficient for FL R/R (relapse/refractory) patients.

Another promising strategy called BiTE for Bi-specific T-cell engagers was developed in the last decade. Here, the concept is to bring closer tumor and effector cells to exercise their cytotoxic role. To do so, BiTEs antibodies are composed of two antibody chains, one to recognize an epitope present on T cells and the other one to target an epitope on the target cell of interest. Some of these compounds have shown promising results in FL. Mosunetuzumab is a CD20 directed BiTE that have been tested in phase I with a 68% ORR and 50% CR. Odronextamab a CD20/CD3 BiTE, have a phase II ongoing in FL but higher side effects seem to appeared with this compound. Epcoritamab, a CD20/CD3

BiTE, showed impressive results in phase I with 100% ORR and 25% CR with no severe side effects. To finish, glofitamab present a particular conformation with a bivalency for CD20 and monovalency for CD3. In a phase I study, this compound showed interesting results with 69% ORR and 58,6% CR in FL patients but some severe adverse events appeared.

Summary follicular lymphoma treatments (IV)

FL patients have benefited from immunochemotherapy treatments such as R-CHOP and have relatively good long-term outcomes. Nonetheless, there is no consensus in the protocol to follow in first-line therapy and even less in R/R FL patients. Moreover, 20% FL patients are refractory and need new therapeutic strategy to increase their life expectancy. For this purpose, the range of therapeutic strategies in FL has exploded from targeting the TME (Table 7), BCR signaling or the immune system (Table 8). With these approaches, some new promising agents emerged, such as: immune modulators, ICP inhibitors, BCR signaling inhibitors, CAR-T cell and BiTE. Another important point to take into account in FL treatment, is finding the right sequence of therapy in the R/R setting. Moreover, finding personalized approach that balances patient-specific factors such as preferences and comorbidities with treatment-related factors such as known response rates and toxicity profiles are needed. In conclusion, with so many promising novel treatment options offering a favorable toxicity profile and durable responses, the future of FL management seems hopeful (Figure 49).

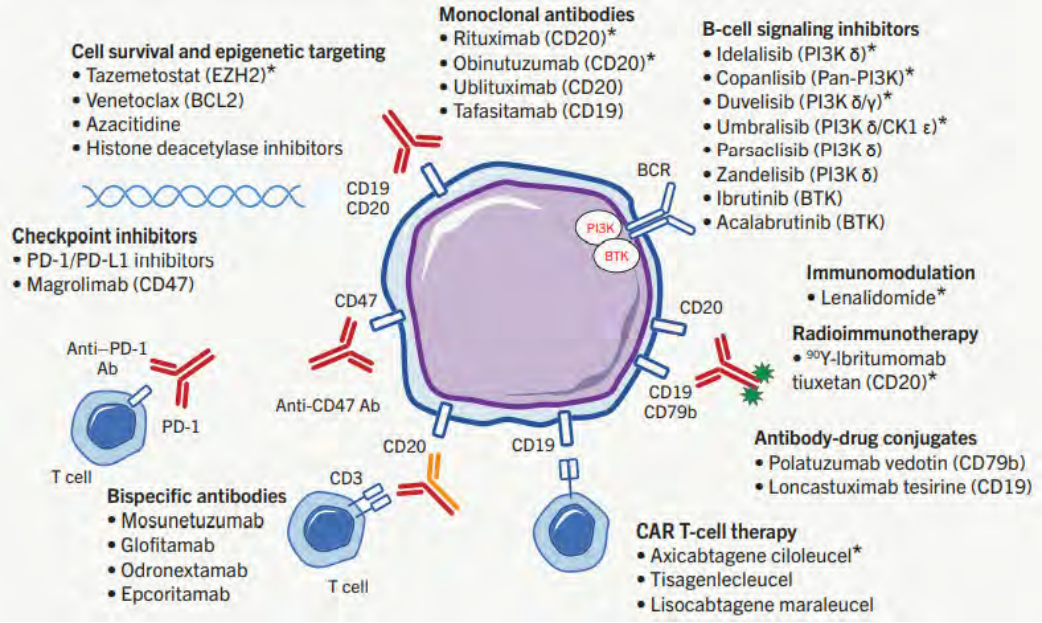

Figure 49 : Novel agents in FL overview
From Cahill et al, Oncology, 2022[292]

Drug Family	Target	Status [1]	Combination	Clinical Responses	
				ORR [2] (%)	PFS [3] (Months)
Epigenetic Regulators					
BRD3308	HDAC3i	PC	Anti-PDL1	NA	
Vorinostat	HDACi	C	None	47	15.6
			None	49	20
Abexinostat	HDACi	C	None	63	20.5
Tazemetostat	EZH2	C	None	*mutEZH2*: 69 *wtEZH2*: 35	*mutEZH2*: 13.8 *wtEZH2*: 11.1
Metabolic Regulators					
Temsirolimus	mTOR	C	None	53.8	12.7
			Bendamustine and rituximab	90	22
			Bortezomib	56	16.5
B-Cell Receptor Inhibitors					
Idelalisib	PI3Kδ	C	None	57	11
		PC	Venetoclax	NA	
Copanlisib	PI3Kαδ	C	None	58.7	11.2
		C	Nivolumab	NCT03884998	
		C	Rituximab	NCT03789240	
Duvelisib	PI3Kγδ	C	None	42	9.5
		C	Venetoclax	NCT03534323	
		C	Nivolumab	NCT03892044	
Ibrutinib	BTK	C	None	37.5	14
		C	Rituximab	85	41.9
Fostamatinib	SYK	C	None	10	4.2
Entospletinib	SYK	PC	Obinutuzumab	NCT03010358	
Cerdulatinib	SYK/JAK	C	None	>50%	NA
Immune Checkpoints Inhibitors					
CAR-T	HVEM	PC	None	NA	
Nivolumab	PD1	C	None	40	NR
Pidilizumab	PDL-1	C	Rituximab	66	18.8
Sym022	LAG-3	C	None	NCT03489369	
		C	Anti-PD1	NCT03311412	
Sym023	TIM-3	C	None	NCT03489343	
		C	Anti-PD1	NCT03311412	
Immune Checkpoint Activators					
Urelumab	CD317	C	Rituximab	21	4.5
Selicrelumab	CD40	C	Anti-PD-L1	NCT03892525	
Macrophage Checkpoint Inhibitors					
Pexidartinib	CSF1-R	PC	Rituximab	NA	
SIRPα-Fc	SIRPα	PC	Rituximab	NA	
Hu5F9-G4 (5F9)	CD47	C	Rituximab	71	NR

[1] C, Clinical, PC, Preclinical; [2] ORR, overall response rate; [3] PFS, progression free survival; [4] Ref, reference; NA, not availa
not reached.

Table 7 : Therapies in FL targeting TME crosstalk

From Dobaño-López et al, Cancers, 2021 [293]

Treatment	Targets	Patients	Phase	Trial number
Venetoclax + Oral AZA (CC-486) + Obinutuzumab	BCL2, epigenetic modulation, CD20	Frontline FL	1/2	NCT04722601
PrE0403: Venetoclax + Obinutuzumab + Bendamustine	BCL2, CD20, DNA damage	Frontline FL	2	NCT03113422
LEVERAGE: Lenalidomide + Venetoclax + Obinutuzumab	Immunomodulation, BCL2, CD20	Frontline FL	1/2	NCT03980171
Acalabrutinib + Obinutuzumab	BTK, CD20	Frontline FL	2	NCT04883437
SWOG S1608 (Randomized): 1: Obinutuzumab + Umbralisib 2. Obinutuzumab + Lenalidomide 3. BO or O-CHOP	CD20, PI3K δ, CK1 ε, immunomodulation, DNA damage	RR-FL (early relapse)	2	NCT03269669
Umbralisib + Ublituximab + Lenalidomide	PI3K δ, CK1 ε, CD20, immuno-modulation	RR-FL	1	NCT04635683
CITADEL-302 (Randomized): 1. Parsaclisib + Rituximab or Obinutuzumab 2. Placebo + Rituximab or Obinutuzumab	PI3K δ	RR-FL	3	NCT04796922
COASTAL (Randomized): 1. Zandelisib + Rituximab 2. BR or R-CHOP	PI3K δ, CD20, DNA damage	RR-FL	3	NCT04745832
Randomized: 1. Tazemetostat + Lenalidomide + Rituximab 2. Placebo + Lenalidomide + Rituximab	EZH2, immunomodulation, CD20	RR-FL	3	NCT04224493
SYMPHONY-2: Tazemetostat + Rituximab	EZH2, CD20	RR-FL	2	NCT04762160
InMIND (Randomized): 1. Tafasitamab + Rituximab + Lenalidomide 2. Placebo + Rituximab + Lenalidomide	CD19, CD20, immunomodulation	RR-FL	3	NCT04680052
LOTIS 6 (Randomized): 1. Loncastuximab tesirine 2. Idelalisib	CD19 ADC, PI3K δ	RR-FL	2	NCT04699461
Loncastuximab tesirine + Venetoclax	CD19 ADC, BCL2	RR-FL	1	NCT05053659
TRASNCEND FL: Lisocabtagene maraleucel	CD19 CAR T cell	RR-FL	2	NCT04245839
VENOM: Venetoclax + Obinutuzumab + Magrolimab	BCL2, CD20, CD47	RR-FL	1	NCT04599634
Magrolimab + Rituximab	CD47, CD20	RR-FL	2	NCT02953509
1. Rituximab + Pembrolizumab 2. Rituximab + Pembrolizumab + Lenalidomide	CD20, PD-1, immunomodulation	RR-FL	2	NCT02446457
Pembrolizumab + Rituximab or Obinutuzumab	PD-1, CD20	RR-FL	2	NCT03401853
Ibrutinib + Nivolumab	BTK, PD-1	RR-FL	1/2	NCT02329847

Table 8 : Ongoing clinical trials with novel therapeutic approaches in FL

From Anastasia et al, Mediterr J Hematol Infect Dis, 2016[294]

4. Goodbye Flat *Lymphoma* Biology

4.1. Models' evolution in cancer research

The classical research pattern in oncology starts with *in vitro* studies followed by *in vivo* confirmations studies which can be transferred into clinical trials, the so called from "bench to bedside". However, many factors led to reconsider this model, such as ethics, the 3Rs principle (replacement, reduction and refinement), costs, complexity and laborious techniques requiring dedicated technicians and engineers[295]. In this context, 3D models appeared to fill the gap between easy to handle but less relevant *in vitro* models and relevant but time consuming and costly *in vivo* models.

4.1.1. In vitro studies: HeLa legacy

In vitro studies are one of the gold standards models in biology to understand cancer progression and/or identify new therapeutics targets. Cell lines cultured in 2D are largely used in cancer research for their straightforward use and well-established cultivation conditions. Thanks to advances defining the best conditions for growing transformed cells by Dr. George Otto Gey at Johns Hopkins Hospital in Baltimore, the first famous human cell line derived from cervical carcinoma cell was born in 1951: HeLa. "HeLa" is an acronym for Henrietta Lacks, a woman affected by cervical carcinoma [296]. Her incredible destiny was written by Rebecca Skloot in *The immortal life of Henrietta Lacks*. Since this milestone event in cell biology history, many other cell lines were developed. Establishing a new cell line is not an easy task as some cell type need their microenvironment and cell interaction to be kept *in vitro*. To help in this process, guidelines for establishment and characterization of new cell lines have been proposed in 1999 by Drexler and Matsuo[297]. In these guidelines, many features are recommended to be confirmed such as cell culture immortality, proof of neoplasticity, authentication of the true origin of the cells, scientific significance and availability for the community.

In hematology, the first cell line RAJI, was established in 1963 from BL patient's cells [298]. A few decades after, the use of recombinant growth factors and conditioned media allowed during the 80s and 90s, the establishment of other cancer cell lines of FL, such as RL or DOHH-2. These scientific advancements helped in deciphering molecular mechanisms of key events such as tumor growth, metastasis, drug resistance and aspects of immune evasion. They were also used for anti-cancer drug development and screening. For example, K562 leukemic cell line establishment was a key element in BCR-ABL fusion protein study. Indeed, this model was crucial in imatinib development, the first tyrosine kinase inhibitor [299]. Another important development using cell lines is the NCI60 screening project that

used 60 different human tumor cell lines to screen up to 3000 small molecules for potential anti-cancer activity [300]. Thanks to this project, many important anti-cancer drugs were discovered such as paclitaxel, cisplatin, fludarabine and more. It would be wrong to say that cell lines are not part of modern cancer research anymore. Indeed, based on advances performed in omics and highthroughput data generation, recent studies allowed a more in depth cell lines characterization. In particular, the work of two groups, Barretina et al and Garnett et al, provided a large scale genetic and pharmacological characterization of around 900 cell lines to the community, which was brought together in a public collection called Cancer Cell Line Encyclopedia (CCLE). Some important events of cancer cell line generation from 1907 to 2019 are summarized in figure 50 [301].

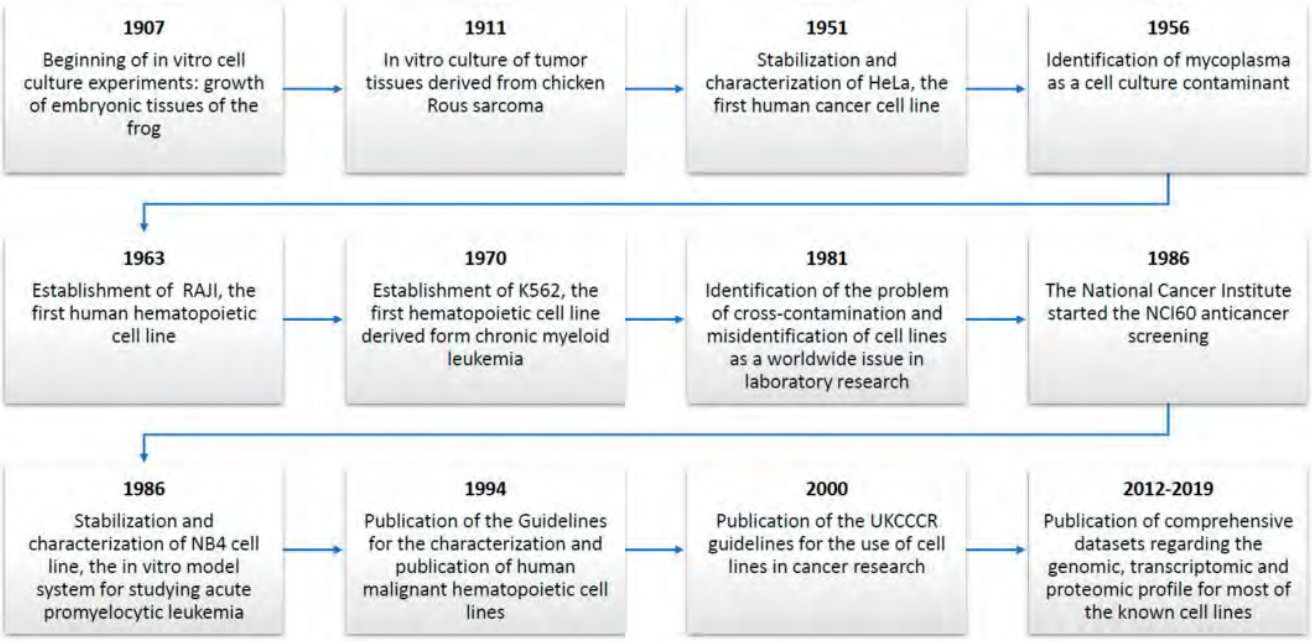

Figure 50 : Summary of historical major events in cancer cell lines progress
From Mirabelli et al, Cancers, 2019. [301]

B-NHL cell lines were used for better understanding of B cell biology and physiology. For example, FL cell lines represent an excellent model to mimic B cell differentiated in GC. Indeed, primary GC cells are difficult to maintain in culture. Eray et al established three FL cell lines in order to study antigenic selection and cytokines-mediated growth regulation of human GC B cells [302]. They fully characterized the B-cell lymphoma cell lines used (HF-1A3, HF-4.9, HF-28) by identifying specific markers of GC B-cell subset (IgM+, Iγδ+, CD23+, CD38+, CD44+), centroblasts markers (CD38+, CD39-CD77+) or centrocytes (CD38+, CD39-, CD77-) [302]. They also found differences in co-stimulatory molecule CD80 expression, which was higher in HF-1A3 and HF-28 cell lines. In addition, they studied the effect of cytokine incubation one these cell lines and found for instance that IL-6, IL-15 and IFNγ protected HF-1A3 cells from apoptosis. The characterization in terms of differentiation markers, co-stimulatory molecule expression and cytokine impact allowed to classify HF-4.9 as a model of

centroblasts, HF-1A3 as representative of centrocytes during selection stage and HF-28 as representative of centrocytes at late stage during transition to plasma cell stage [302]. B-NHL cell lines are also used to understand and discover new therapeutic targets. For example, in FL, *in vitro* studies helped in deciphering rituximab mechanism of action. For instance, my team and others have demonstrated that rituximab, an anti-CD20 monoclonal antibody, acts on B cells by indirect mechanisms of action, such as CDC and ADCC and direct mechanisms of action involving cell signaling pathways inducing cytotoxicity or inhibition of FL cell survival, as observed *in vivo* [222,242,303].

Although cell lines are important to decipher biological mechanisms, these models lack tumor heterogeneity and can dedifferentiate after several passages thus losing characteristics of tissue of origin. Sandberg and Ernberg showed in their study that 34 to 60 NCI60 cell lines displayed the same tissue-specific genes upregulation [304]. Another limitation is related to cross-contamination and mycoplasma infection that lead to false and non-reproducible data.

Advances in patient sample processing, opened a possibility to *in vitro* culture of tumor cells from blood or biopsies from various tumors. Moreover, high performance technologies such as single -cell RNA sequencing, promote a depp molecular characterization of tumor heterogeneity and permit to correlate it with drug response. In B-lymphoma, an elegant study analyzed malignant and non-malignant lymphocytes from twelve donors (nine with lymphoma: FL and DLBCL and three reactive LN) [305]. It resulted in detecting up to four transcriptionally distinct subpopulations of lymphoma cells, responding differently to *in vitro* treatments. Thus, these types of studies help to highlight new signatures of resistant subclones necessary to develop new therapies.

Nevertheless, 2D culture implies cell exposure to an uniform environment with sufficient nutriment and oxygen, whereas tumor cells growing in mass are exposed to a gradient of oxygen, chemical compounds and cell to cell signaling [306]. Thus, 3D models better recapitulate these important tumor features.

4.1.2. *In vivo* studies: bringing life to tumors

To overcome these limitations, *in vivo* models are essential in biology in order to mimic more closely cell-cell interactions and integrate the microenvironment surrounding tumor cells. Due to similar genomic and physiological characteristics between mice and human tumor biology, mice models are the main *in vivo* models used in cancer research.

Commonly used, xenograft models with tumor cell line transplanted subcutaneously or orthotopically into immunocompetent or immunodeficient mice, have been used for their availability and lower cost than other mice models such as transgenic mice. These models contributed

considerably and are still viable in discovery, characterization and validation of many drugs. For example, Mossner et al showed that anti-CD20 antibody (GA101) exhibits an enhanced direct and immune effector cell-mediated B-cell cytotoxicity by xenografting DLBCL cell line (SU-DHL4) into SCID Beige mice [235]. They demonstrated a higher tumor volume decrease with GA101 compared to rituximab. My team also used SCID Beige mice to characterize the mechanism of action of anti-CD20 mAb [71,233]. For this, SCID Beige mice were engrafted subcutaneously with RL cells, injected intraperitoneally with immune cells (NK or $\gamma\delta$ T cells) and treated with anti-CD20 mAbs (GA101 and Rituximab). Tumor size was strongly reduced in mice injected with immune cells in presence of rituximab. These results validate *in vitro* observations and allow to better understand the indirect mechanisms of action of these therapeutic Abs. However, this model exhibits a main limitation with the lack of relevance to pathology due to several factors: (i) a cell line was used thus not representing patients' heterogeneity; (ii) subcutaneous injection which is not the localization of FL cells (normally lymph node); (iii) administration of therapeutic antibody intraperitoneally is different from infusion in patients and (iv) poor projection of FL TME, which normally plays a critical role in the development of the pathology and is implicated in response to treatment [293].

As oncogenes and tumor suppressors genes are the main actors in oncogenesis, the need to modify gene expression in an *in vivo* model is essential. For this purpose, several genetically engineered mouse models (GEMMs) were established. For instance, transgenic mice were established to constitutively or conditionally express oncogene or silence tumor-suppressor genes in order to investigate oncogenic contribution of several genetic alterations in both solid and hematological cancers [307–309] . The conventional methods of GEMMs generation are retroviral infection, microinjection of DNA constructs and gene-targeted transgene. When the aim of the model is to inactivate a specific gene they are called knock-out. On the opposite, when the objective is to modify mice genetic sequence to add foreign genetic material, in a specific locus, they are called knock-in. Adoptive transfer of manipulated HPC is a rapid and highly controlled gain and loss of function model. Indeed, after isolation of HPC from BM or from fetal liver, cells can be for example cultured in vitro and following the gene modification using reroviruses, they can be reinjected into irradiated mice to recapitulate pathology specific gene modifications [310].

Thanks to use of transgenenic murine models, it was possible to explain numerous gene mutations involved in B-cell lymphomagenesis. Berg et al demonstrated the cooperation between *MYC* and *EZH2* in the lymphomagenesis by crossing mice bearing *EZH2* mutation and mice bearing *MYC* mutation [311]. Beside, many prevalent genetic alterations have been successfully modeled in mice models to mimick B-NHL pathologies including *BCL2* translocation [312], alterations in histone

modification genes [106,107], *TNFRSF14* loss, missense *RRAGC* mutations [313] or *MEF2B*-activating mutations [314] (Table 9).

Gene	Disease	Mutation type	Mouse model	Approach	Target cell	Phenotype	Reference(s)
Myc/PI3K	BL	Deregulated expression + gain-of-function mutation	*R26Stop*^{FL}*Myc;R26Stop*^{FL}*P100**; Cγ1- Cre	Conditional KI	GC B cells	BL	Sander et al. 2012
Bcl2	FL, GCB-DLBCL	Deregulated expression	VavP-*Bcl2*	Transgene insertion	HPC	FL	Egle et al. 2004
			Bcl2-Ig	Transgene insertion	B cells	FL	McDonnell et al. 1989
			BCL2^{trac}	TI/adoptive transfer	B cells	FL	Sungalee et al. 2014
Kmt2d^{c}	FL, DLBCL	Genetic deletion	*Kmt2d*$^{fl/fl}$;VavP-*Bcl2*;Cγ1-Cre	Conditional KO	GC B cells	FL, DLBCL	Zhang et al. 2015
			Kmt2d$^{fl/fl}$;VavP-*Bcl2*;Cd19-Cre	Conditional KO	B cells	FL, DLBCL	Zhang et al. 2015
Crebbp^{c}	FL, DLBCL	Genetic deletion	*Crebbp*$^{fl/+}$;VavP-*Bcl2*;Cγ1-Cre	Conditional KO	GC B cells	FL	Zhang et al. 2017
			Crebbp$^{fl/fl}$;VavP-*Bcl2*;Cd19-Cre	Conditional KO	B cells	FL	Zhang et al. 2017
			Crebbp$^{fl/fl}$;Eμ-*Bcl2*; Mb1-Cre	Conditional KO	Early B cells	FL, DLBCL	García Ramírez et al. 2017
Ezh2^{c}	FL, GCB-DLBCL	Gain-of-function mutation	*Ezh2*$^{Y641F/+}$;*IμHABCL6*;Cγ1-Cre	cKI/adoptive transfer	GC B cells	DLBCL	Béguelin et al. 2016
			Ezh2$^{Y641F/N}$;VavP-Bcl2	Adoptive transfer	GC B cells	FL, DLBCL	Béguelin et al. 2013; Ennishi et al. 2019b
Mef2b	FL, DLBCL	Gain-of-function mutation	*Mef2b*$^{D83V/+}$;CD21-Cre	Conditional KI	GC B cells[a]	FL, DLBCL	Brescia et al. 2018
			Mef2b$^{D83V/+}$;*BCL2*-Ig;CD21-Cre	Conditional KI	GC B cells[a]	FL, DLBCL	Brescia et al. 2018
Rragc	FL	Gain-of-function mutation	*Rragc*$^{S74C/+}$ or *Rragc*$^{T89N/+}$; VavP-*Bcl2*	TI/adoptive transfer	All cells	FL	Ortega-Molina et al. 2019
Gna13	GCB-DLBCL, BL	Genetic deletion	*Gna13*$^{fl/fl}$;Mb1-Cre	cKO/adoptive transfer	GC B cells[b]	GC BCL	Muppidi et al. 2014
			Gna13$^{fl/fl}$;*R26Stop*^{FL}Myc;AID-Cre	Conditional KO	GC B cells	GC BCL	Healy et al. 2016
Bcl6	DLBCL	Deregulated expression	IμHABCL6	KI	GC B cells	DLBCL	Cattoretti et al. 2009
Prdm1	ABC-DLBCL	Genetic deletion	*Blimp1*$^{fl/fl}$;Cγ1-Cre	Conditional KO	GC B cells	DLBCL	Mandelbaum et al. 2010
			Blimp1$^{fl/fl}$;*R26Stop*^{FL}*Ikk2ca*; Cγ1-Cre	Conditional KO	GC B cells	DLBCL	Calado et al. 2010
Myd88	ABC-DLBCL	Gain-of-function mutation	*Myd88*$^{p.L252P/+}$;Cd19-Cre	Conditional KI	B cells	LPD, DLBCL	Knittel et al. 2016
Tet2	FL, GCB-DLBCL	Genetic deletion	*Tet2*$^{fl/fl}$;Vav-Cre	Conditional KO	HPC	BCL	Dominguez et al. 2018
			Tet2$^{fl/fl}$;IμHABCL6;Cγ1-Cre	cKO/adoptive transfer	GC B cells	BCL	Dominguez et al. 2018
miR-15a/16-1	CLL	Genetic deletion	*mir-15a/16-1*$^{fl/fl}$;Cd19-Cre	Conditional KO	B cells	CLL (DLBCL)	Klein et al. 2010
			mir-15a/16-1$^{-/-}$	KO	All cells	CLL (DLBCL)	Klein et al. 2010

Table 9 : Summary of existing genetically engineered mouse models (GEMMs) to mimic mature B-cell

From Pasqualucii and Klein, Cold Spring Harb Perspect Med, 2020 [315].

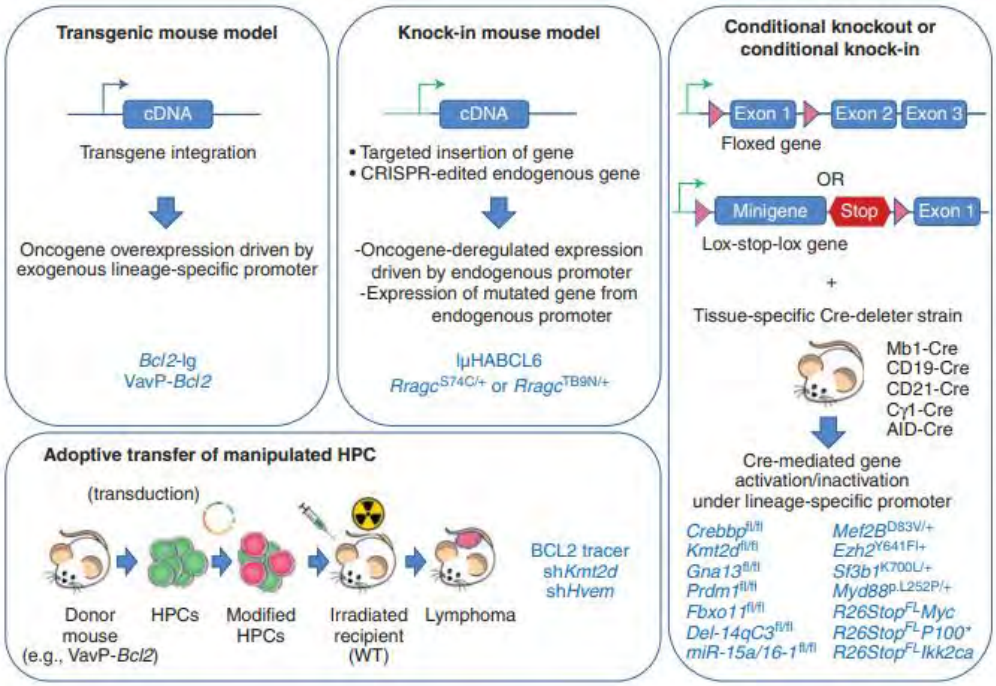

Figure 51 : Illustration of different GEMMs methods to generate B-cell malignancies mice models

Targeted alleles and experimental design are summarized. From Pasqualucii and Klein, Cold Spring Harb Perspect Med, 2020 [315].

Figure 51 summarizes strategies used to generate genetic alterations associated with human B-cell lymphomas (GEMMs): transgenic, knock-in mouse model, conditional knock-out or conditional knock-in adoptive transfer of manipulated HPC.

Although GEMMs provide more accurate modelling of tumor development as they are not transplanted but appear spontaneously, few limitations such as expression of target genes under strong and non-physiological promoters exist.

Among *in vivo* models, the patient-derived tumor xenograft (PDTX) model represents an attractive strategy to overcome previous described limitations. To establish PDTX, patient cells are directly implanted into immunodeficient mice to recreate an environment enabling tumor growth and drug effect monitoring. These models represent well the patient cells heterogeneity and genetic instability, relevant to identify mechanisms which drive tumorigenesis and to evaluate the efficacy of potential therapeutic candidates [316–318]. They exhibit remarkable similarities with donor samples by sharing genomic features and treatment efficacy. For example, in CRC, the success rate of PDTXs establishment is around 75% and they recapitulate the genetic alterations and histology of the fresh tumours [319,320]. Guenot et al did a comparative genome hybridization showing alterations stability between the xenograft and the initial CRC tumor [319]. In another study, Fichtner et al established a panel of 15 PDTX exhibiting maintenance of the histology and expression of tumor-associated markers such as EpCAM even after numerous passages [320]. Moreover, in this study, they demonstrated that response to chemotherapy was similar in PDTXs and CRC patients.

Lymphoma PDTXs represent a powerful model to investigate pathologies' biology and discover new targets. Nevertheless, the success of engraftment depends on many technical variables and on each neoplasm. Indeed, it has been shown that high grade lymphoma is easier engrafted than low grade lymphomas, such as FL, that rarely implant well [321]. However, few teams succeeded to create PDTXs from FL cell isolated from patients LN or BM [321–323]. Burack et al successfully engrafted low grade FL patient thawed cells isolated from LN, into mice to create so called OTX (omental tumor xenograft) and to study neoplastic cell proliferation, their dependency on TME and patient's variability [321]. Surprisingly, they found in some cases a supportive effect of CD4+ T cell not on expected neoplastic B cells, but on non-neoplastic B cells. Thus, with this study, they emphasize the importance of TME in maintaining survival and control of differentiation of neoplastic cells in comparison to normal cells. Gerstein et al succeeded to engraft two patient samples isolated from FL and DLBCL LN and one from BL BM in NSG mice [322]. The purpose of this study was to generate mouse "avatars" of patients to provide platform designed for drug response evaluation. Finally, Zhang et al, established sixteen PDTXs models originated from peripheral blood, apheresis, LN or spleen of different B-NHL such as DLBCL,

MCL, FL, MZL and BL[323]. Interestingly, in this study they investigated ibrutinib resistance after relapse and found that idelalisib (PI3Ki) was efficient in inhibiting tumor growth. Thus, these models represent powerful tools to study treatment resistance and discover new therapeutic strategies.

In consequence, to centralize all data obtained, international repositories of PTDXs such has PRoXe (Public Repository of Xenografts) for leukemia and lymphoma were created. This encourages the scientific community to use these relevant models for preclinical studies [324]. However, some disadvantages have to be considered including clonal drifting and evolution or loss of heterogeneity in immunocompromised animals lacking the host immune system. In order to produce a more human-relevant model, humanized mouse strains have been created where human hemopoietic precursors are engrafted. Nevertheless, they present the same economical, technical and ethical challenges than other models. In addition, they still do not reproduce the full human immune system and some mismatches between the host and human cells are still present. All benefits and limitations from mice models in preclinical research are listed in table 10.

Approach	Benefits	Limitations	Refs
GEMM **Spontaneous or directed genetic modification on different levels of the murine organism (proteins, tissues, whole mouse)**	Various established molecular tools and transgene delivery methods. Inducible and conditional models with temporal and spatial control. Functional immune system. No interspecies incompatibilities.	Time consuming (generation time and screening). Costly. Genetic heterogeneity and lack of reproducible gene expression and phenotypes (random transgenesis). Off-target effects and lethality of mutations. Single human proteins in a fully murine system (e.g. RANKL).	Wu et al 2015 Kostenuik et al 2009 Suri et al 2016 Xue et al 2014
CDX and PDX **Subcutaneous implantation of human cells or tissue into immunodeficient mice**	Well-established cell lines for various diseases. PDXs commercially available (champions Oncology, CrownBio). Hight-thoughput applications. Easy and quick generation of models. Applicable in personalized medicine.	Immunodeficient host. Mainly ectopic/subcutaneous implantation. Interspecies incompatibilities. Limited genetic heterogeneity (CDX). Genetic and phenotypic alteration of transplant in host (PDX).	Krepler et al 2016 Gao et al 2015 Kemper et al 2015 Girotti et al 2016
Humanized **Humanization of the immune system and selected mouse organs using orthotopic implantations/injections and TE & RM methods**	Humanized immune system and humanized microenvironment in organs of interest. Reduced interspecies incompatibilities. Modular generation of models. High-throughput applications Applicable in personalized medicine.	Degree of humanization limited. Expertise in various fields needed. Complex surgical procedures for some applications.	Baldwin et al 2017 Wagner et al 2016 Holzapfel et al 2015 Hesami et al 2014

Table 10 : Preclinical mouse models in research: benefits and limitations
Adapted from Landgraf et al, Trends in Biotechnology, 2018 [325]

4.1.3. 3D models: a bridge between *in vitro* and *in vivo* models

4.1.3.1. History

As previously described, *in vitro* and *in vivo* models present many benefits but also some serious limitations. Thus, 3D models appear to feel the gap as they present advantages of both models such as reproducibility, screening perspectives and above all, they mimic the pathology.

The first 3D models developed in preclinical studies were established in 1970. Radiobiologists used spheroids to better mimic tumoral architecture and study treatment's effect [326,327]. A few years later, in the field of oncology, Mina Bissell was a pioneer in thinking that context and cell architecture were one of the main drivers of cancer development [328–331]. To explore this concept, her team investigated the function of acinus, the basic unit of a mammary gland. They separated epithelial cells that produce milk in mammary glands and cultured them in a petri dish. They observed that without their surrounding microenvironment and scaffold, they were not functional. In contrast, by adding scaffold such as matrigel, they observed milk production, showing that the adjacent microenvironment was able to send signals to epithelial cells in order to drive functionality. "We got milk!" is the favorite sentence of M. Bissel when she gives conferences. Moreover, she was one of the first to highlight the importance of the ECM in cell function. Indeed, many studies determined ECM involvement in different processes in breast cancer such as differentiation, organ function, progression and metastasis [332]. Moreover, studies from Bissel's team showed that once tumor cells are cultured in a "healthy" scaffolding, they are able to revert their malignant phenotype to a normal one, bringing evidence that microenvironment is a crucial driver in cancer development [333]. Thanks to the work of this team and many others, 3D models started to gain credibility and begin to be more often used in cancer research (Figure 52).

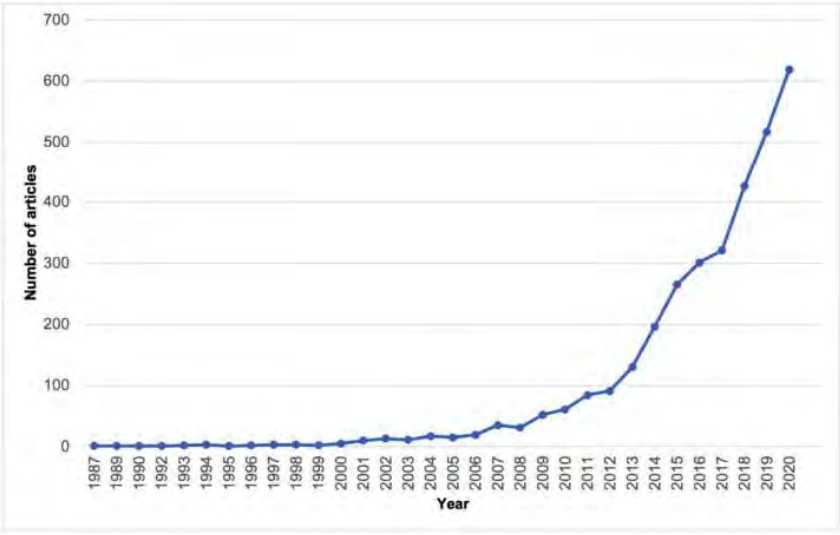

Figure 52 : Increasing number of published articles containing the terms "3D *in vitro* tumor models" from 1987 to 2020

From Martinez-Pacheco and O'Driscoll, Cancers, 2021. [334]

4.1.3.2. Methodology and nomenclature description: welcome to the jungle

Since that discovery and paradigm change, many technics were applied to culture cells in 3D and they can be categorized as followed: microfluidic device (tumor-on-chip), scaffold-based method and scaffold-free method[335]. From these procedures, different nomenclatures emerged such as spheroid, multicellular tumor spheroid (MCTS), multicellular layer models, organoids, tumoroid, organ-on-chip... To clarify all of these terms, here are some definitions:

- spheroids are a type of three-dimensional cell modeling that better simulate a live cell's environmental conditions compared to a two-dimensional cell model [336].
- organoids are "mini-organs" produced *in vitro* in 3D that derived from one or a few cells from a tissue, embryonic stem cells or induced pluripotent stem cells [337].
- finally, tumor organoids or tumoroids are 3D primary tumor cell cultures with histological and mutational features of the original tumor [338].

It is important to note that even if these methods and nomenclatures can be distinguished, some of them can be at the frontier of each other (Figure 53).

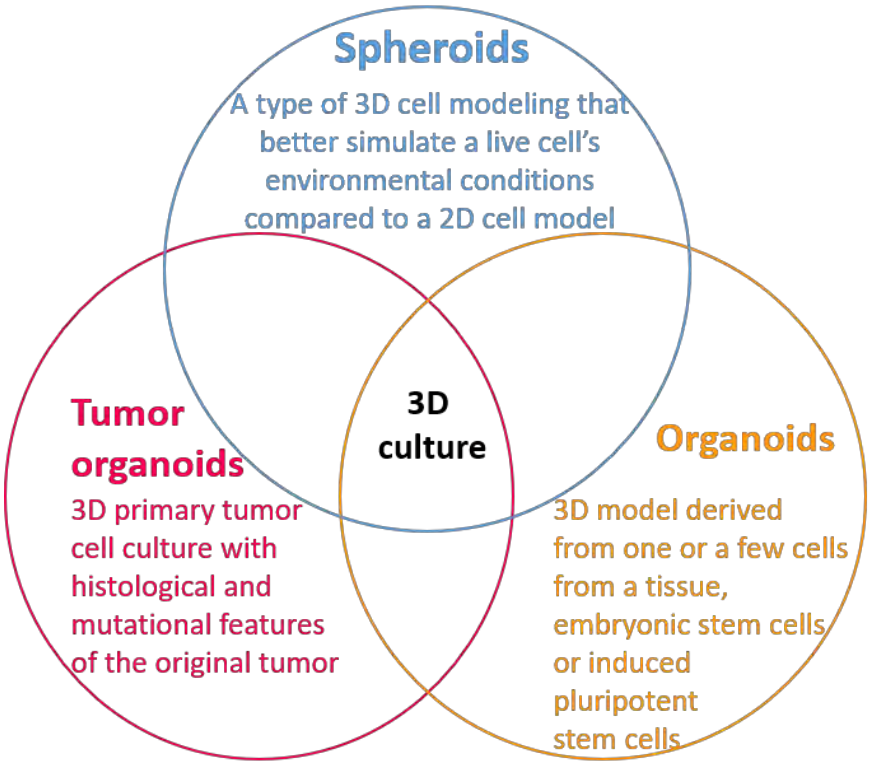

Figure 53 : 3D models definition entanglement

Once the nomenclature is defined, it is important to describe the technics used to generate them.

Microfluidic devices or organ/tumor on chip are micro-engineered biomimetic models that allow co-culture of tumor cells (cell line or primary cells) with other relevant cell types placed strategically in order to recreate a tumor microenvironment (TME). The advantage of this method is that all physical parameters can be strictly controlled and monitored thanks to micro-channels mimicking vasculature. These micro-channels are embedded in inert materials like glass, silicon and polydimethylsiloxane (PDMS). Usually, tumor cells are in layers containing matrix and endothelial cells while immune cells (macrophages, T cells) travel through the dedicated microchannels [339,340]. In figure 54 is representing an illustration of a study that investigated breast tumor cells circulation and involvement in metastasis. Song et al established a chip composed by two layers of porous PDMS containing an endothelium channel to mimic vasculature. The porous composition of PDMS allows chemokine to diffuse and to study their interaction with cancer cells [341].

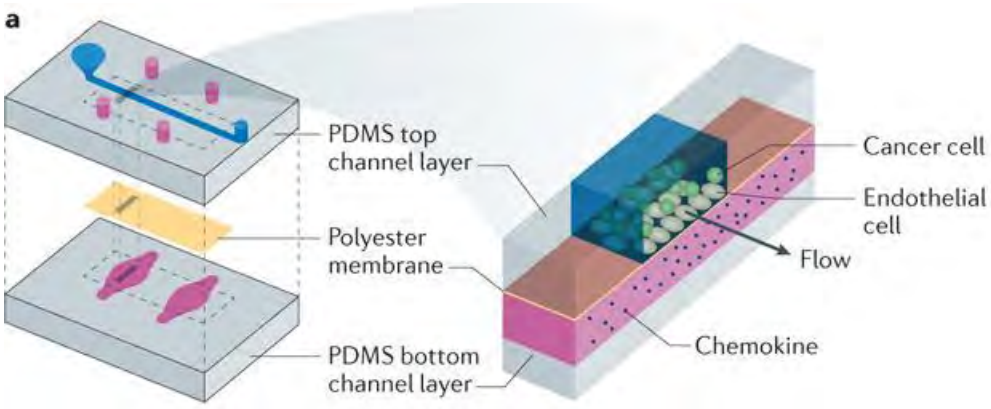

Figure 54 : Illustration of tumor-on-a-chip presenting an endothelium channel allowing perfusion of chemokine through a porous membrane
From Esch et al, Nat Rev Drug Discov, 2015 [339].

These models represent potent devices to study physiological processes and also to perform preclinical drug screening in a complexified and relevant microenvironment. For example, with a glioblastoma on-a-chip, Cui et al integrated the immune TME to study PD-1 IT [342]. Over the last decade, many models helped in studying tumorigenesis processes such as intravasation [343], extravasation [344], angiogenesis [345], invasiveness [346], migration [347] and adhesion [341]. Moreover, this method allows a real time imaging of these processes. For example, Zhang et al created a multi-organoid platform composed of liver cancer and cardiac organoids [348]. With multiple sensors (optic, biochemical, physical), the dynamic monitoring of organoid morphology, temperature, oxygen and pH was possible. After treatment with doxorubicin, they were able to monitor and mimic drug efficacy and cardiac toxicity.

Even if this method presents increasing potential, some limitations need to be emphasized. Indeed, PDMS structure have physicochemical properties that are far from ECM. For instance, PDMS exhibit the disadvantage to absorb small hydrophobic molecules and this may affect drug concentration and its effect [349]. To overcome this issue, other materials are under development such as poly(methyl methacrylate), polystyrene, polycarbonate and cyclic olefin copolymer [350]. Another important problem in the field is the standardization and automatization of chip manufacturing, as for the most, they are not suitable for industrial large-scale manufacturing. Finally, low culture volumes and cell number used in these models can cause some detection sensitivity problem [335]. Measurement technics need to fit clinical methods to be able to enroll them in clinical settings [351]. This field evolves with body-on-chip that aim to integrate and connect different organ on-a-chip together, in order to assess interaction between them. However, the challenge to develop a common culture media that can support various types of cells and mediate their biochemical communication still remains unsolved.

Scaffold-based methods provide structural and physical support to mimic cell interactions and aggregation. They are usually composed of natural hydrogels and ECM components and are covalently modified with synthetic hydrogels often based on polyethylene glycol (PEG). Hydrogels are used for their water-insoluble and synthetic or natural polymers properties that mimic tissue elasticity [352]. One of the most common hydrogels commercially available is matrigel, an ECM-based natural hydrogel derived from secreted basement membrane extracts of Engelbreth-Holm-Swarm mouse sarcoma cells. It is composed of laminin, collagen, heparin sulfate proteoglycans, entactin and other soluble factors such as chemokines and growth factors. Scaffold-based methods can be categorized as matrix embedded or not [353], matrix encapsulation [354], bioreactors (including spinner flasks) [355] or micropatterned plate [335,356,357]. Addition of ECM helps in deciphering importance of cell-ECM interactions in cell organization and function and to evaluate its consequence in drug response. For example, Ingeson-Carlsson et al used a 3D collagen embedded model to study RAF and MEK inhibitors on tumor cell migration with two cell lines mutated for BRAF (BCPAP and SW1736). They found that depending on cell culture conditions (2D or 3D), the response to anti-tumor drug was different [353]. Great advances have been made in bioprinting which allows an unlimited access to a large variety of scaffolds. Some of them directly integrate cells with bioinks, mainly composed with hydrogels and other are used to only support surrounding cells [358]. Although these technologies present high potential in terms of ECM mimicking and drug testing, the main limitation of scaffold are their: batch-to-batch variability (matrigel), difficulty to automate, gel's opacity which prevents imaging and alteration of drug and compound penetration. In summary, the main issue in these models is to choose the appropriate 3D scaffold materials on the basis of the desired application.

Scaffold-free approaches are produced with different technics such as: soft agar colony formation [359], spontaneous aggregation, hanging drop (HD) [360], spinner flask rotary cell cultures, ultra-low attachment plates (ULA), and magnetic levitation methods [335]. In these methods, no artificial material is added to support cell growth and shaping, allowing an easier process, image and reproducibility. Thus, they are commonly used for drug screening studies. However, besides these great advantages, the main limitation is the lack of TME mimicking matrices. Altogether, most of these technics aim to generate spheroids which are the most well characterized and widely applied models (Figure 55). They all present advantages and disadvantages summarized in table 11.

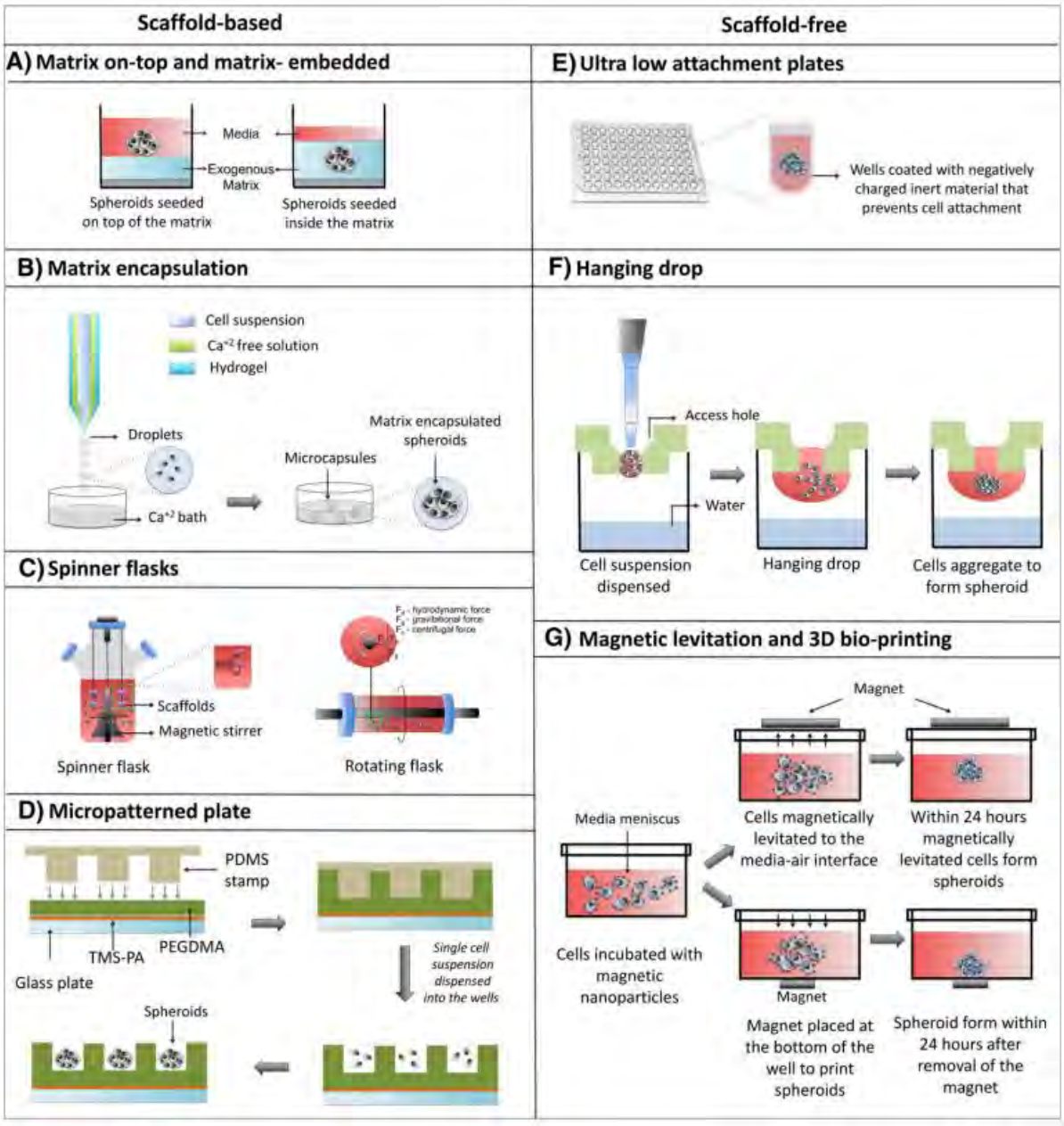

Figure 55 : Scaffold-based and Scaffold-free methods description

A) Matrix on-top and matrix-embedded, the spheroid is placed above or is included in a matrix; B) Ultra low Attachment plates, thanks to its composition cells stay in suspension and aggregate; C) Spinner flasks, cells are

in movement thanks to a rotation allowing their aggregation, D) micropatterned plate, cells are stuck in small pattern to force their aggregation; E) Hanging drop, thanks to gravity forces cells in droplets aggregates; G) Magnetic levitation and 3D bio-printing, cells are mixed with bead and in contact with magnet to force their aggregation. From Nath and Devi, Pharmacology & Therapeutics, 2016 [335].

Techniques	Advantages	Disadvantages	Applications
Matrix-on-top and matrix-embedded	• Cells can be recovered post culture if self-aggregating protein based hydrogel is used.	• Hydrogel requires special handling.	• Ideal for evaluation of cell–cell and cell–matrix interactions, drug screening, and cancer cell metabolism.
		• Yields heterogenous spheroids requiring sorting before assay.	• Allows hypoxia related studies
		• Challenging to stain and image matrix-embedded spheroids.	• Allows evaluation of cancer stem cell niche.
Matrix encapsulation (microfluidic device)	• Yields homogenous spheroids circumventing the need for sorting before assay.	• Slower growth rate due to confinement.	
		• Increased occurrence of necrosis due to confinement.	
		• Capsule may burst if the matrix shell is thin.	
Micropatterned plates	• Spheroids can be imaged with relative ease.	• Well surface needs to be coated to create low adhesion surface.	
	• Post culture recovery is possible	• Generates spheroids of variable sizes.	
	• ECM component is present.	• Multiple spheroids in a well can overwhelm assay chemistry.	
Hanging drop	• Large number of spheroids obtained in a limited space.	• Labor-intensive.	• Ideal for studying invasive potential of cancer cells.
	• Reduced reagent consumption.	• For long-term culturing, spheroids are transferred from the hanging drop to a second plate that can hold larger volume of media.	• Allows evaluation of cancer stem cell niche.
	• Post culture recovery is possible.	• Spheroids are transferred to a secondary plate for endpoint analysis.	• Ideal for drug screening.
Ultra-low attachment plates	• Inexpensive and easy to handle.	• Generates spheroids of variable sizes.	
	• Large number of spheroids can be obtained in a limited space (96 well or 384 well).	• May have a mixture of attached cells and spheroids.	
	• Endpoint analysis can be done on the same plate.		
	• Post culture recovery is easy.		
	• Can be multiplexed with imaging and other biochemical assays.		
Magnetic levitation and magnetic bioprinting	• Endpoint analysis can be done on the same plate.	• Limited number of spheroids	
	• Can be multiplexed with imaging and other biochemical assays.	• Cells need to be pre-treated with magnetic beads.	
		• Beads are expensive.	
		• Beads at high concentration might be toxic for cells.	

Table 11 : Spheroid generation methods advantages and disadvantages
From Nath and Devi, Pharmacology & Therapeutics, 2016 [335]

4.1.3.3. Focus on spheroid and organoids/tumoroids in cancer research

4.1.3.3.1 Bringing the missing dimension to preclinical studies

Spheroids are established with one or multicellular mixture from cell lines or primary cells and are referred as “micro-tumors”. Their aggregation can be promoted with several methods such as forced-floating method with specific plates allowing spheroid formation completed with a centrifugation or not in order to help cell aggregation (ULA plates for commercially available plates), or with gravity methods such as HD where cells contained in a small volume are disposed on a lid allowing aggregation and then transferred to wells containing a higher volume of medium allowing cell proliferation and 3D growth (Figure 55). It is important to underline that the cell type co-cultured, the 3D method used and the addition of ECM, may influence the cellular morphology and physiology. Thus,

these parameters need to be taken into account in cell growth influence and cell-cell interaction. Moreover, depending on cell type, different behavior of spontaneous aggregation, proliferation and shape can be observed.

Spheroids rapidly became one of the most commonly models used in cancer research due to their properties to recapitulate cancer features such as proliferation, differentiation, motility and metabolism [361]. Spheroids allow to study mechanisms such as hypoxia, cell migration, invasion, ECM and, TME implication and treatment sensitivity in a more relevant models than in conventional 2D culture and easier workflows than in case of *in vivo* models [306]. To obtain a spheroid from 2D cultures, cells need to go through a spheroidization process composed by different steps with a high cell proliferation rate followed by a stabilization that allows the shaping of the spheroid (Figure 56 A) [362]. Because of their 3D structuration, spheroids can, contain different phenotypes, functions and metabolic behaviors depending on the cell layer. In general, spheroids display spherical shape composed by an external layer of proliferative cells, an intermediate zone with quiescent and senescent cells and an inner apoptotic and necrotic core (Figure 56 B). Riffle et al characterized in a A673 spheroid (Human Ewing Sarcoma cell line) distribution of Ki67 proliferative cells and caspase 3 dead cells respectively located in the periphery and the inner part of the model, reflecting the different cell behavior depending on cell layer [363]. Changes in nutrients, oxygens and drug diffusion dependent on the cell layer explains these different features of proliferation and death [364]. This has been demonstrated in many models since the importante studies from Carlsson et al in 1988 that explained the relation between pH, oxygen pressure and growth of spheroids [353]. They established the $\Delta pO_2/\Delta pH$ coefficient to present metabolic differences between the spheroids derived from different cell types. In a more recent and sophisticated study using phase fluorimetry on oxygen-sensor microbeads, the oxygen measurements were performed in various spheroid culture environment [365]. Interestingly, spatial oxygen mapping enabled to create a computational model of oxygen diffusion. Hypoxia, or oxygen deficiency, is a well-known hallmark of tumors that modify cell metabolism from oxidative phosphorylation to anaerobic glycolysis leading to lactate release responsible for the inner cell acidification [366]. 3D structures are interesting models to understand hypoxia impact on tumor progression and drug resistance. Indeed, acidification has been shown to be involved in immunomodulation and chemotherapy resistance [367]. Efficacy treatment is observed to be decreased in poor oxygenated and proliferative layers for cytostatic drugs such as rapamycin or chemotherapy that preferentially target proliferative cells. Oloumi et al showed that V79 (Chinese Hamster cells) spheroid were 10 times more resistant than monolayers culture to etoposide (topoisomerase II inhibitor) [368]. Imamura et al compared the efficacy of paclitaxel and doxorubicin on 2D and 3D cultured cells [369]. They showed that 3D models are more accurate in displaying tumor features such as : hypoxia,

dormancy, anti-apoptotic features and displayed drug resistance compared to 2D cultures. Nevertheless, in some cases, drugs are more efficient in 3D than in 2D as demonstrated in a study performed by Doh et al where 60 drugs were tested [370]. They observed for 28.3% of drugs, a higher efficacy in 3D than 2D. Among the drugs used, the ones targeting mTOR were more efficient in 3D [370]. In addition to oxygen gradient, gradient of lactate, glucose, ATP and DNA strand breaks are also been described to affect drug response [361].

Another spheroid feature that can affect cell behavior in terms of proliferation, survival and response to therapy is cell-cell interaction [361]. The cell cohesiveness is dependent among others on on desmosomes, dermal junctions [371] and ECM secreted proteins. This latter called matrisome is composed by glycoproteins, glycosaminoglycans, proteoglycans, ECM-sequestered growth factors, vascular endothelial growth factor, platelet derived growth factor or hepatocyte growth factor [372] (Figure 56). Thus, even without adding any ECM scaffold, some ECM component can be secreted by tumor cells themselves (including : collagens, fibronectin, laminine, elastin) and support some tumor features [373,374]. The importance of cell-cell interactions and cell-matrix adhesions in gene expression, activation of downstream signaling pathway and influence drug sensitivity has been reported in many studies. For example, two teams using pancreatic tumor spheroids showed an increase of chemotherapeutic resistance when the cell-adhesion molecules, SNED1, DARP32 and miR-146a, were overexpressed [375,376]. Moreover, it has been reported in breast and lung cancer spheroids, that interaction between β1-integrin with collagen I, collagen IV, laminin and fibronectin induces a protective effect against chemotherapeutic drugs [377]. On the opposite side, inhibition of β1-integrin allows an increase in trastuzumab and pertuzumab (anti-HER2) sensitivity of tumor cells in a model of breast cancer spheroids [378]. Moreover, many studies have depicted differential gene expression profile concerning cellular processes, such as: proliferation, hypoxia, ECM secretion or cell cycle between 3D models and 2D culture. The similar profiles observed in 3D culture and patients strongly support the relevance of these models compared to conventional 2D cultures [379–381]. Altogether, spheroids, by recapitulating many tumor features, including spatial distribution and ECM, appear as relevant models for preclinicals studies in cancer researchs.

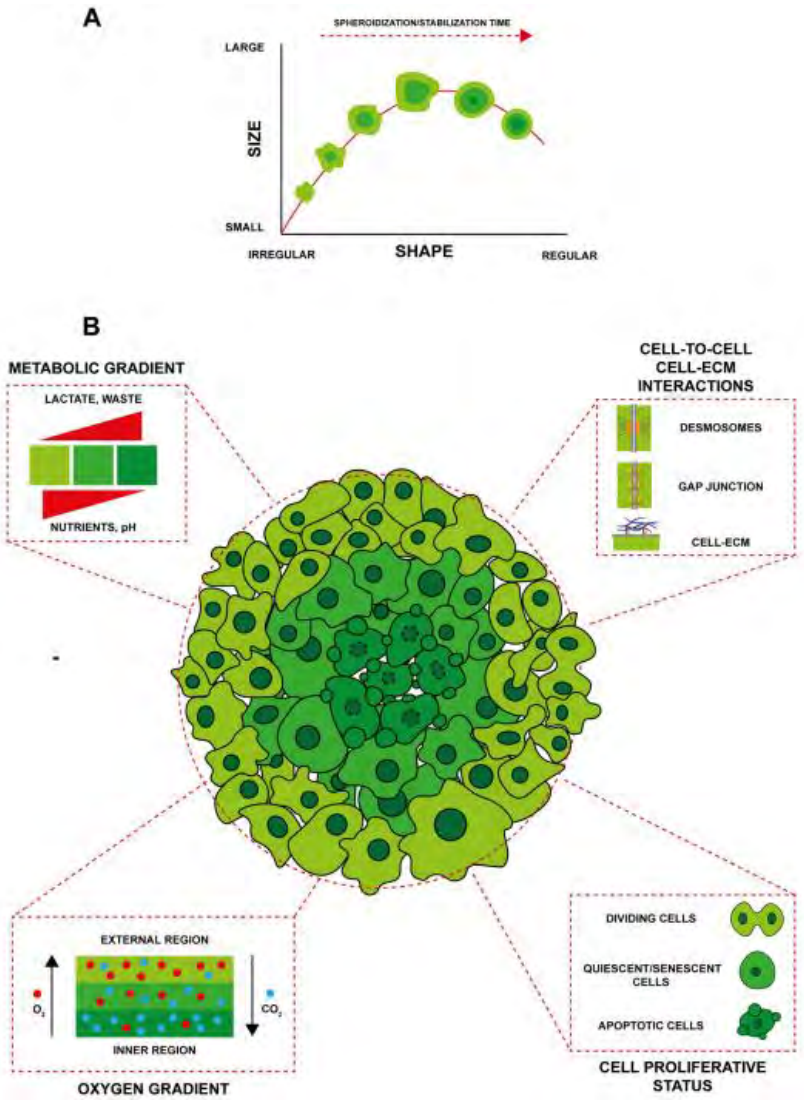

Figure 56 : Illustration of spheroid spatial organization composed by layers with differential phenotypic, metabolic and functional features

A. The spheroidization process composed by three steps: high proliferation, stabilization, model shaping, proliferation decrease. B. Several metabolic, oxygen, cell proliferation status depending on the layer and different cell-to-cell and cell-ECM interactions. From Zanoni et al, J Hematol Oncol, 2020 [306]

With all the features recapitulated by 3D models, preclinical studies gain another dimension. Indeed, these models allow to monitor local drug penetration, tissue distribution and binding in a medium-high throughput manner. Huge development in imaging technics (confocal microscopy and light sheet microscopy) permit to monitor drug penetration [382]. Even if spheroids can be composed by only one type of cells, it is possible to complexify the 3D structure by adding other cell types such as fibroblasts, immune cells or endothelial cells to partially recreate the TME. For example, to study in depth drug resistance due to ECM it is interesting to perform co-culture of spheroids with cancer associated fibroblasts (CAF), which produce large amounts of ECM. Cavaco et al used a pancreatic spheroid model co-cultured with CAFs deficient or not for integrin-α3 and demonstrated a decrease of invasion in comparison to the WT CAFs [383]. Jeong et al, showed that CAF confer resistance to

paclitaxel when co-cultured with a CRC spheroid [384]. Immune cells are also important actors in tumor progression. To explore their role, many studies integrate them in co-cultures with different cancer cell types. For example, in a study using spheroids of CRC, Courau et al targeted NKG2D axis and showed an increase in NK cell infiltration followed by a higher cytotoxicity [385]. They were also able to highlight an interesting synergic effect towards primary colorectal cancer-derived spheroids by combining anti-MICA/B and anti-NKG2A antibodies. In parallel to the IT revolution, co-culture of spheroids with immune cells gained great interest in the area of preclinical studies [386]. The study of such mechanisms *in vivo* involves the use of complex mice models. On the other hand, classical 2D cultures are also used but without the consideration of cell architecture and spatial organization of cells within a tumor which can also play a key role. For example, in the clinic, it has been observed that the lack of $CD8^+$ T cell infiltration in the tumor is a mechanism of resistance to IT [387]. Peranzoni et al showed that CD8+T exclusion is correlated in human lung squamous-cell carcinomas with poor clinical outcome and low lymphocyte motility [388]. Another interesting application appears with the huge development of CAR-T cell-based therapies, where 3D models appear also as relevant models to study their efficacy. This therapeutic approach had great success in hematological malignancies leading to CD19 CAR-T cell approval by the FDA. Nevertheless, in solid cancer, the results are less encouraging and led researcher to identify several blocking elements such as heterogenous antigen expression, limited T cell survival before reaching tumor sites or immunosuppressive TME. These immunological and physical barriers can be investigated in 3D models as they exhibit spatial organization allowing a better study of CAR-T cell infiltration and survival. For instance, changing targeted antigen can increase CAR-T cell potential. Wallstabe et al established a microphysiologic three-dimensional composed of lung and breast cancer cell lines (A549 and MDA-MB-231) models to evaluate ROR1 (receptor tyrosine kinase–like orphan receptor 1–) CAR-T cells. With this model, they were able to assess anti-tumor activity by measuring apoptosis and IFN-γ secretion and they observed deep infiltration of CAR-T cells [389]. Zhang et al proposed to target membrane proximal epitope of mesothelin to increase anti-tumor function in solid tumors and showed its potential with 3D spheroid cancer cell lines of gastric (HGC-27) and ovarian (SKOV-3) cancer cell lines. In these experiments, CAR-T cells were able to secrete high amount of IFNγ and lead to apoptosis of cancer cells.

4.1.3.3.1 Organoids and tumoroids: heterogeneity and functionality matters

Although spheroids help in deciphering many aspects of cancer biology, they recapitulate only some activities of the modeled organs. To overcome this limitation, numerous teams have established organoids to better understand tumor development in functional artificial mini-organs. Organoids are developed from single adult stem cell (aSC), embryonic stem cell (ESC) or pluripotent stem cells (iPSCs)

to recapitulate *in vivo* micro-architecture of the organ [390]. Many protocols exist depending on the cell type and supplement of specific growth factors such as cytokines required to obtain the appropriate model [391]. Hans Clevers's group was the pioneer to establish such models, firstly on colorectal cancer and discovered gut stem cells and their location in intestinal crypts [392]. A few years later, they cultured these stem cells in a long term fashion and created the first "mini-gut" organoids that structure spontaneously similarly to real gut [393]. Clevers's group has also been pioneer in the establishment of models developed from patient-derived tumor specimens, called "tumoroid" or "tumor organoids" that are 3D primary tumor cell culture with histological and mutational features of the original tumor [390,394,395]. These models present many advantages such as patient specificity, 3D spatial organization, possibility to create biobank/library used for preclinical studies [396]. They are also largely used for immunotherapeutic studies with mainly two approaches: the first one called holistic approach, consists of using endogenous immune cells from the patient [397] and the second one called reductionist approach, is the co-culture of cancer cells with immune cells isolated and expanded separately from the same patient (Figure 57) [395]. Both approaches help to better characterize cell-cell interaction and enable to create platform for immunotherapeutic drug testing. Since this discovery, a wide variety of healthy tissues organoid have been created such as colon [398,399], breast [400], liver [401], lung [402], pancreas [403], ovary [404], bladder [405] and many others (Figure 58).

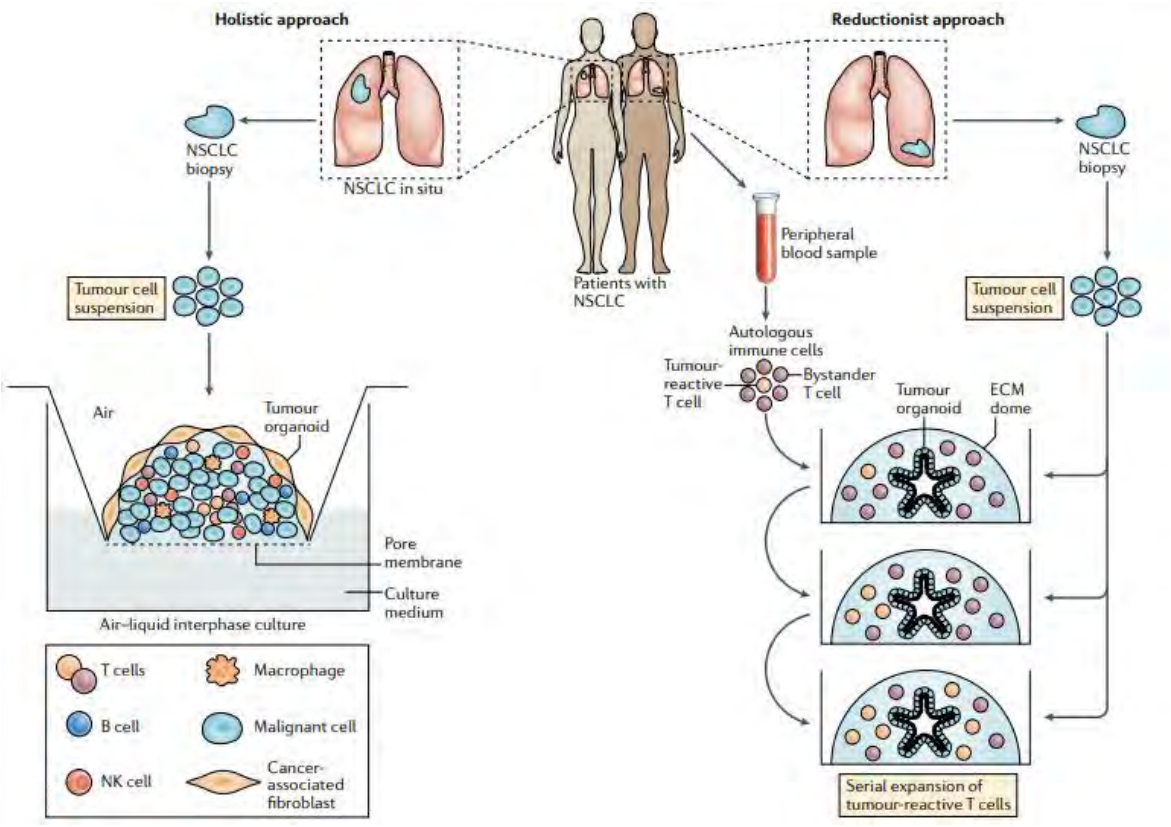

Figure 57 : Illustration of holistic and reductionist approach used in immune-oncology organoid model generation with NSCLC example

From Bar-Ephraim, Kretzshmar and Clevers, Nat Rev Immunol, 2020 [406]

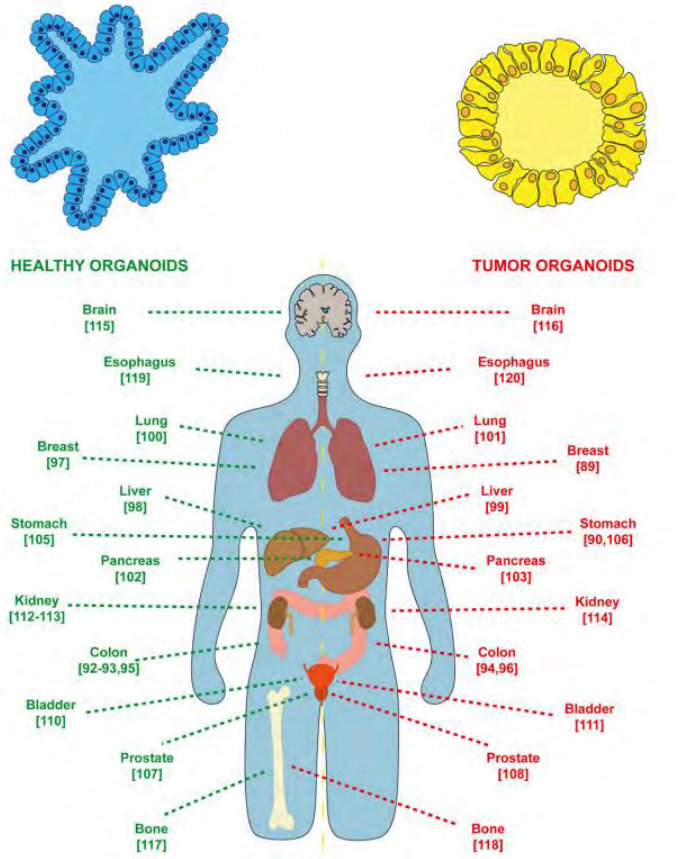

Figure 58 : Existing models of organoids and tumor organoids
From Zanoni et al, J Hematol Oncol, 2020 [306]

Over the past decade, 3D models such as organoids became essential in immuno-oncology studies because of their more accurate TME reconstruction [386]. These models are used to assess immune cell infiltration, test immunotherapies such as therapeutic antibodies and discover new targets. The main challenge of recreating a TME in a tumoroid is to mimic the tumor of origin considering not only the type of cells present but also their proportion and their localization. Despite, IT advent, failure of correlation between level of target expression and patient response encouraged researchers to investigate IT mechanism of action in relevant model. Even if targeting PD-1/PD-L1 axis is known to be efficient in some cancers, it is more difficult to predict its efficiency in some patients. Thus, to solve this issue, some teams have established patient derived organoid (PDO) of NSCLC, CCRC and melanoma and determined nivolumab efficacy. For instance, Neal et al observed that patients responding to treatment presented T cells expressing higher level of IFNG, PRF1 and GZMB transcripts [407].

This study highlights the complexity of the IE mechanisms and how important prediction of patient response to a specific IT is. Currently, two clinical trials involving cancer organoids to evaluate response to IT (NCT03778814, NCT02718235) are ongoing, confirming their great potential as preclinical models predicting patient response.

For some cancers, it is possible to have an access to healthy and tumor tissues from the same patient and grow them in 3D culture to assess drug effect and drug toxicity at the same time. This approach leads to select less toxic drugs and propose an efficient treatment associated with less side effects. For example, cardiac and kidney organoids are already used for toxicological studies [408,409].

One of the main stakes of cancer research relies on understanding and investigating metastasis mechanism and evolution. Approaches combining organoids and organ-on-chip called multi-organ-on-a-chip will allow to study this process. Recently, one team has engineered an impressive lung-brain-liver-bone-on-a-chip model to study in the context of lung cancer, metastasis spreading [410]. With this model, they were able to show different distribution of cancer cells in each organ over time.

In addition to help scientists to study tumors complex biology, organoids are also interesting models to select the most appropriate treatment for patients, opening perspectives to personalized medicine. This part will be developed in 4.4.

4.2. Towards regenerative medicine: the example of artificial lymph node model

In order to better understand the pathology, it is also important to know more about physiological mechanism in healthy organs. Thanks to scientists, engineers and physicians efforts in tissue engineering, the field of regenerative medicine is flourishing [411]. Regenerative medicine has the ambition to replace, regenerate or restore a fully functional tissue, or organ.

In the case of LN, many studies have tried to recreate artificial LN in the context of regenerative medicine, but also in order to increase the knowledge about this organ in more relevant models presenting the same architecture complexity as in the body. Indeed, SLO such as LN are microarchitectures essential for the immune response initiation. More than one hundred of LN are placed strategically all around the body, based on tissues sites they drain such as skin and mucosa, in order to readily face any threat [412]. Distinct B and T compartments associated with stromal FDC and FRC show a remarkably rich and organized microenvironment. This specific cellular compartment organization is maintained by gradient of chemokine secretion by stromal cells, FDC (for B cells) and FRC (for T cells) [413]. Another important feature of this structure is the presence of specialized blood vessels called high endothelial venules (HEV), that facilitate extravasation of circulating lymphocytes into the LN. This impressive organization of LN is necessary for efficient antigen screening and recognition. The ECM (collagen, glycosaminoglycans, …) plays also an important role in proliferation, differentiation and migration of the cells, by mediating cell adhesion and communication such as antigens transit for further presentation by specialized cells [414]. With the first studies performed with conventional 2D culture and *in vivo* models, our understanding of organogenesis, the cellular and

molecular elements essential for the recruitment and organization of lymphocytes into LN are better known. Given this spatial complexity, the main challenge of engineering artificial LN is to replicate as closely as possible the LN microenvironment into a 3D structured model. Current models mimic only a few aspects of this microenvironment complexity. One of the first models of LN was established with collagen sponge scaffolds carrying a thymus-derived lymphotoxin-β receptor and a stromal cell line expressing vascular cell adhesion molecule-1 (VCAM-1) [415]. This model was implanted in mice and showed all the features of an organized secondary lymphoid-like structure composed of B and T cell zones, GC and networks of FDCs. Another study did a first attempt to create a GC-like model with collagen-infused PEG gels. This model was able to foster intra-scaffold migration of encapsulated T cells and DCs but no GC formation was observed [416]. This was enabled after implantation in mice.

A sophisticated model called human artificial LN (HuALN) was engineered with a miniaturized membrane-based perfusion bioreactor, containing a hydrogel matrix preloaded with DCs, T and B lymphocytes derived from PBMCs [417]. The model was further complexified by adding mesenchymal cells. In this study, the model was used to simulate the immunological outcomes in response to vaccines, pathogens and even pharmaceutical drugs [418,419]. Interestingly, Seifert et al, found an increase in MSC proliferation when co-cultured with immune cells showing the importance of cell-cell interaction in cell behavior [417]. Also using HuALN, Giese et al analyzed immune responses to viral antigens. In order to do that, researchers used antigen restimulation and measured the response based on cytokines released (IL-2, IL-10, IL-6 and TNFα) to spent medium [418]. They observed early proinflammatory response (TNFα) that diminished during the first days of culture but after restimulation with antigen, they observed a second release of TNFα and of Th2 promoting cytokines such as IL-6 and IL-10. In addition, they observed donor variability in cytokines response and a moderate IL-2 release. In the study of Radke et al, this system was used to test two vaccines presenting minor structural differences [419]. By the analysis of cytokines in the supernatant, they were able to observe the immune responses induced by both vaccines.

Singh's lab is one of the most active in the field of LN modelisation. They designed a model capable of mimicking the LN GC *in vitro*, thus providing an interesting tool to understand B cell maturation and to design innovative antibody-based therapeutics [420]. In this model, murine naive B cells and CD40L and BAFF-expressing stromal cells are encapsulated into an arginylglycylaspartic acid functionalized gelatin hydrogel where silicate nanoparticules are added to modulate scaffold stiffness and porosity. They showed a potentiation of CD40L/BAFF signaling in presence of the 3D structure and an increase of GC B cells proliferation and rapid differentiation to the GC phenotype after addition of IL-4, a phenomenon difficult to observe in conventional 2D culture [420,421]. Further evolution of this model made by replacing gelatin with a synthetic polymer containing integrin ligands, allowed to

investigate the role of α4β1- and αvβ3 integrins in GC B cells differentiation [422]. In this context, Singh's group was able to observe that $\alpha 4\beta 1$ integrin receptor induces more robust CD19+GL7+ phenotype in a ligand concentration dependent manner compared to the previous model. Finally, they developed a scaffold made of maleimide (MAL)-functionalized PEG, that modulates B cell differentiation and enriches antigen-specific GC B cells in the presence of T-cell like signals [423]. Thus, this model represents an *ex vivo* antigen-specific platform offering many biotechnology applications, from antigen testing, to vaccine development and to generation of antibodies [423].

Another model was developed in order to mimick the paracortical region of LN [424]. This microfluidic system allows to study more specifically the T cell compartment of LN. Moura Rosa et al showed that the interaction between DCs and T-cells is dependent on the shear stress applied on the subtype of T-cells. Indeed, CD4+ T cells exhibit long and stable contacts with APCs, whereas CD8+ T cells present only transient interactions with DCs [425]. This interesting microphysiological model allows the study of pMHC-TCR binding in a controlled mechanical forces device. With the same concept of studying T cells and DC interaction, Mitra et al created a model to investigate DC chemotaxis and T cell activation which is composed by two PDMS layers, one representing the chemotaxis compartment and the other the T cell compartment [426]. By applying a chemokine gradient (CCL19), they were able to monitor T cell activation by measuring intracellular calcium levels. Thus, they showed that mature DC respond better to chemokine gradient and migrate to the T cell compartment where they can activate them. On the opposite, immature DC were not able to respond to chemokine gradient and to activate T cells [426]. To study both B and T cell zones, Ross et al, created an *ex vivo* microfluidic device from isolated mouse LN slices [424]. By using a model composed of a three-layers PDMS with a perfusion chamber and microfluidic channels, they were able to show a higher drug retention in the B-cell zone than the T-cell zone.

In the field of regenerative medicine, recreating a functional LN is a great interest. Lenti et al succeeded to generate a functional synthetic lympho-organoid (LOs) by using LN stromal progenitors and decellularized ECM matrix-based scaffolds [427]. After resection of LN, LOs models were transplanted allowing the restoration of lymphatic drainage and perfusion. Moreover, after immunization, LOs were able to support activation of antigen-specific immune responses as observed in physiology [427].

In conclusion, designing an artificial LN is one of the challenges that scientists have tried to solved for many years now. Many models have emerged and all have contributed to a better knowledge about LN spatial and function complexity. Promising studies in the field of regenerative medicine have been established to give more and more hope in the ambitious task of recreating a full

functional LN. Moreover, some of the studies can help in designing new models in hematological disease emerging from LN in order to better characterize and treat them.

4.3. Existing 3D models in B-NHL

B-NHL are characterized by tumoral cells growing in dense aggregates with their surrounding microenvironment mostly in LN. This feature is not recapitulated in classical cell suspension. Subsequently, the need to establish 3D models to better recapitulate the pathology became essential. In order to create a relevant 3D model for B-NHL, many criteria need to be taken into account. Among them, the model needs to be reproducible and relevant to the pathology by recreating the TME suitable for preclinical studies. Each B-NHL subtypes presenting its own genetic and microenvironment features, we decided to present in the following part the existing results obtained on two indolent B-NHL (FL and MCL) and one aggressive B-NHL (DLBCL) (Table 12).

4.3.1 Follicular lymphoma 3D modelling

Our group was pioneer in the establishment of a 3D model from FL cell line [71,145,234,381,428]. This model called HD-MALC for multicellular aggregates of lymphoma cells, was obtained by the HD method [145,381]. HD-MALC formed compact ovoid aggregates reaching a diameter of ~1 mm by three weeks of culture and exhibiting relevant hallmarks of FL cells. Indeed, gene expression analysis showed 612 genes differentially expressed. Among them, 451 genes involved in induction of anti-apoptotic function, NF-κB pathway and response to hypoxia, were significantly upregulated in cells grown as HD-MALC compared to cell cultured in suspension (2D) and reflected patient gene expression profile [381]. Following studies explored the mechanisms of action of anti-CD20 mAbs in these 3D organized models [71,234,428]. Thus, it was observed huge differences between the efficacy of drugs in 2D compared to 3D models, with higher direct activity towards FL cells in HD-MALC compared to cells in suspension [234]. Moreover, cell cultured in suspension exhibit the same sensitivity towards two anti-CD20 mAbs, whereas once cultured in aggregates, GA101 was more potent compared to rituximab by inducing not only apoptosis but also senescence and lysosomal cell death [234]. Another antibody-based therapy was tested with the daratumumab (anti-CD38 mAb) showing a penetration within the HD-MALC and an efficacy towards FL cells [429]. Indirect mechanisms of action of anti-CD20 mAbs such as ADCC was also detedted with HD-MALC co-cultured with NK or γδ T cells [71,233]. These co-cultures mimic the infiltration of immune cells within the FL LN, their activation through the expression of CD69, GrB and perforin and the consecutive killing of target FL cells. Characterization of the IE signature expressed in FL allowed the identification of PD-1 as an ICP expressed by γδ T cells infiltrating FL LN [28,71,175]. In this context, HD-MALC co-cultured with PD-1+ γδ T cells allowed to validate *in vivo* experiments showing

that PD-1 targeting enhances ADCC induced by anti-CD20 mAbs [71]. Although the HD method was very useful to better understand FL biology and drug responses in more relevant models than cell suspension, it was not suitable for drug screening due to the need of manual processing. Moreover, one could speculate that methylcellulose added for HD-MALC formation, may induce matrix-driven alterations in growth, expression profiles, cell behavior or in drug responses. To circumvent this issue, FL cell lines 3D models were established with ULA plates and called ULA-MALC. This study led to my first co-author scientific publication and will be developed in the result section of the manuscript.

Despite the contribution of 3D models established with cell lines in the knowledge of FL pathology and the understanding of mAbs mechanisms of action, they lack TME representation. In FL, TME is highly heterogeneous by the presence of immune cells, stromal cells, ECM components and blood vessels, representing a real niche where all these elements crosstalk and influence drug response [205,293]. Indeed, Dave et al demonstrated that FL patients' survival correlates with molecular features of non-malignant immune cells present in the tumor at diagnosis [149]. Thus, relevant models integrating FL TME represent necessary preclinical models to predict response to therapy and better model the interaction between each component of this heterogeneous milieu.

For the moment, only two different methods were developed to establish 3D model with cells from FL patients. The first one, recently published, was based on FL purified B cells encapsulated with matrigel and co-cultured with normal tonsil stromal cells (TSC) to provide pro-survival signals [430]. FL B cells were found mixed with stromal cells within 3D spheroids and exhibited a good cell viability until day 14, higher than the condition where FL cells were cultured in 2D with TSC. Although this study is promising and opens new strategies to culture in 3D FL B cells, it was performed with purified FL B cells and TME was represented by normal TSC which reflects only partially TME (Figure 59).

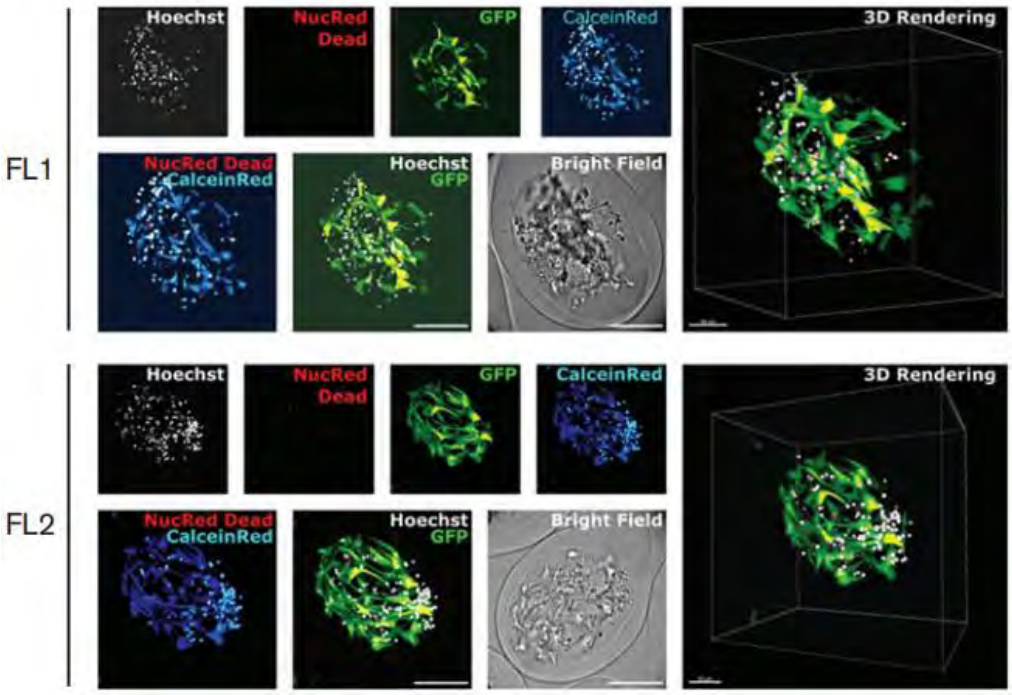

Figure 59 : Primary FL cell survival in cellular capsules

Imaging after 3 days of encapsulation of purified FL B cells and TSC cells (a) of encapsulation. Multicolor live/dead (CalceinRed/NucRed Dead) imaging of patient B cells with GFP-TSC and nuclei counterstaining with Hoechst were depicted. Spheroids were imaged on a spinning disk microscope. Individual channels are depicted on the top, overlays of NucRed Dead and Calcein Red and of Hoechst and GFP on the lower panels. From Lamaison et al, blood advances 2021.[430]

Another type of method integrating immune TME was recently developed by our group where bulk thawed FL cells from FL LN were cultured in 3D during several days in an enriched culture medium allowing to maintain cell survivaly (Faria et al, in preparation). These 3D models called PDLS, which stands for Patient-Derived Lymphoma Spheroids are mainly composed by B and T cells, allowing a full workflow enabling the characterization in depth of patients samples by 2D and 3D imaging, immunohistochemistry and multiparametric flow cytometry analyses. This work led to a scientific publication in preparation and will be developed in the results section of the manuscript.

4.3.2 Mantle cell lymphoma 3D modelling

MCL represents an indolent B-NHL which can transform to aggressive B-NHL that ultimately leads to unfavorable clinical outcome [431]. MCL cells can migrate from blood to multiple tissues. The proliferative rate, the molecular signatures and the sensitivity to drugs have been described to be different when cells are in the blood compared to cells localized in the BM or LN. Thus, preclinical models are needed to better characterize these discrepancies and to propose specific targeting strategies [432].

Only two studies established cell line-based models of MCL. First, a four layers 3D polystyrene scaffold model was developed with primary stromal cells that was generated from human neonatal skin to be more representative of the lymphoma microenvironment [433]. This model exhibits an increase in cell proliferation of tumor cells cultured around this stromal cell scaffold, compared to 2D co-culture with stromal cells. Interestingly, 3D models established with a cell line derived from LN (HBL2) or cell line derived from BM (Z-138), showed different aggregation patterns (clusters developed for HBL2 cells), a dependence from stromal cells-mediated pro-survival signals for Z-138 cells and proliferation rates higher for HBL2. Interestingly, when HBL2 clusters were placed in suspension without the stroma, cells stay in the same state and the suspension phenotype was not reverse. Moreover, it has been observed that interaction with the stroma cells triggered cellular and signaling modification in the tumor cells. Thus, this 3D polystyrene scaffold model represents a relevant model for MCL and should be interesting for the development of patient-derived cells 3D models which have not yet been published.

The second model proposed a multicellular spheroid representative of early-stage MCL closer to the pathology [434]. This model was established with the JeKo-1 cell line in order to study unknown polyclonal nature of this disease. After a prolonged culture (10 to 20 passages), cells formed irregular-shaped multicellular spheroids (Figure 60) [434]. After 20 passages, the so called Jeko-1-spheroids become regular with a high viability. Interestingly, storage in liquid nitrogen and thawing to perform future studies was possible with this method and cell line. Jeko-1-spheroids exhibited expression of CD34, CD38, IgM and CD10 with a mixed of pre-B, immature B and mature B cells showing that MCL pathogenesis might not be restricted to mature B cells. Moreover, these 3D models present higher levels of oncogenes and stem cell markers compared to cell suspension culture suggesting that spheroids are more representative of the disease. This was confirmed by JeKo-1-spheroid xenograft which fully recapitulate the heterogeneity of polyclone tumors as attested by the total number of organs involved, immune phenotypes and the oncogenic capability. Indeed, a higher spreading followed by extensive complications was observed attesting the disease progression. In this study, Tang et al revealed four subpopulations with CD19+/IgM+, CD19-/IgM-, CD19+/IgM-, CD19-/IgM- in healthy donor samples and they observed that the subpopulation CD19+/IgM- was absent in the four patients tested and JeKo-1-spheroid cells [434]. All four subpopulations from healthy donors were cultured and no colonies formation were observed. On the other hand, three subpopulations found in patients and spheroid model were able to form colonies with a variability depending on the subclone. Furthermore, when the subclones were separately injected into *in vivo* models, a strongest tumorigenic ability with more severe effects was observed, even if the subclone CD19-/IgM+ exhibited the highest tumorigenic ability. In perspectives, the authors proposed to use this model to study the chemoresistance related to the subclones which could become an interesting approach to predict treatment response depending on the presence of these subclones in each patient. Altogether, this model seems to be useful to study the polyclonal nature of MCL disease thus improving diagnosis and prognosis. Moreover, further studies to identify new pathways could conduct to develop more efficient treatment for MCL.

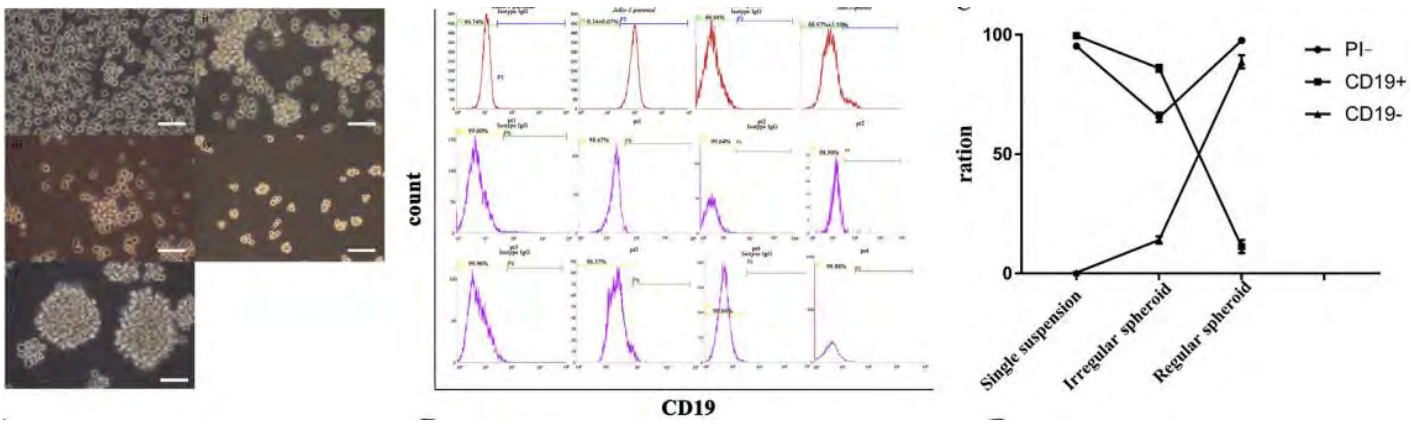

The growth characteristics of JeKo-1-parental and JeKo-1-spheroid cell lines; there were approximately 1% multicellular spheroid in JeKo-1- parental culture (i); irregular multicellular spheroid in JeKo-1-parental prolonged culture (ii); death of single cells in JeKo-1- parental prolonged culture (iii); restoration of proliferation (iv); establishment of JeKo-1-spheroid culture (v); bar Z 60um. Tang et al, 2019. [434]

4.3.2 DLBCL 3D modelling

In DLBCL, several 3D models partially integrating the TME were developed. One of the first model was composed by adhesive peptides comprising integrin specific to B and T cell lymphoma cells [435]. Briefly, PEG-MAL macromers were conjugated with thiolated cell adhesive peptides RGD or REDV (peptide: PEG-MAL 1:4). Integrins are known to have an indirect effect on recruiting focal adhesion proteins which controls levels of cyclins and genes essential for cell proliferation such as c-Jun and E2F [436]. Tian et al measured the cell-cycle progression in HBL-1 B lymphoma cells and observed a phase S reduction when cells were cultured in RGD functionalized 3D models with FDCs, compared to models with REDV ligand [435]. Thus, this result suggests an enhanced proliferation when cells are exposed to a REDV ligands. In this study, authors highlighted how 2D studies can obscure important drug effect related to microenvironment such as integrins. On the opposite, they also depicted how 2D culture could overestimate the efficacy of certain compounds due to unhindered drug diffusion in suspension. When they compared doxorubicin efficacy on 2D and 3D, they observed a resistance in 3D models but not in 2D culture. These studies not only allow the characterization of a new model and demonstrate the importance of microenvironment in drug response, they also alert the community on the use of matrigels or collagens. Indeed, even if it can provide cell support, the lack of batch reproducibility and information on exact composition represents a bias in the experiments. Thus, to overcome this problem, a synthetic hydrogel was developed containing bio-adhesive ligands and protease degradable cross-linkers specific to lymphoma. In more details, maleimide functionalized 4-arm PEG (PEG-MAL) that reacts with thiolated peptides to form a bio-adhesive hydrogel was used. Hydrogels were functionalized with 25% thiolated peptides presenting αvβ3 binding RGD ligands or α4β1 binding REDV ligands and cross-linked using matrix metalloproteinase (MMP) 9 degradable, di-thiolated peptide (NH2-GCRDVPMSMRGDRCGCOOH). Integrins are modeling the lymphoma microenvironment by mediating adhesion to ECM components (fibronectin and laminin) and in signaling processes. Moreover, the supportive FDC were also integrated to the system to better recapitulate the pathology. In this context, drug resistance to chemotherapeutics agents such as doxorubicin and histone deacetylase inhibitor (HDACi), such as panobinostat, was assessed [437]. Although this elegant model is promising to study specific biological features of DLBCL, its main limitation is the lack of cells from the TME such as T cells and macrophages which play a key role in this pathology [437].

This missing part was added by Mannino et al who developed a DLBCL-on-chip [438]. This model consists of the embedment of DLBCL cells from a cell line, T cells and macrophages, in hyalyronic acid-based hydrogel into a PDMS macrostructure [438]. Moreover, an "endothelialized channel" was integrated, represented by a round transversal punch where endothelial cells were added to create a microvessel. Interestingly, this artificial microvasculature allowed to monitor targeted tumor response and spatial reagent concentration. In this context, the effect of an anti CSF-1R, an antibody targeting macrophages, was evaluated after perfusion in the system and resulted in a significant macrophages cell death as expected. Interestingly, this model allows cell collection for further flow cytometry investigations. Beside the important knowledge brought by this model, it is important to underline that the technology developed is easy to reproduce in any lab without any advanced microfabrication facilities. Even though this model presents impressive versability, the authors did not study the interactions between all the cell types composing the system and no drug used for patient treatment was tested to assess the efficacy againsts B cells. Moreover, although this complex system seems interesting to study drug by drug effect, it appears complicated to use in a screening perspective (Figure 61).

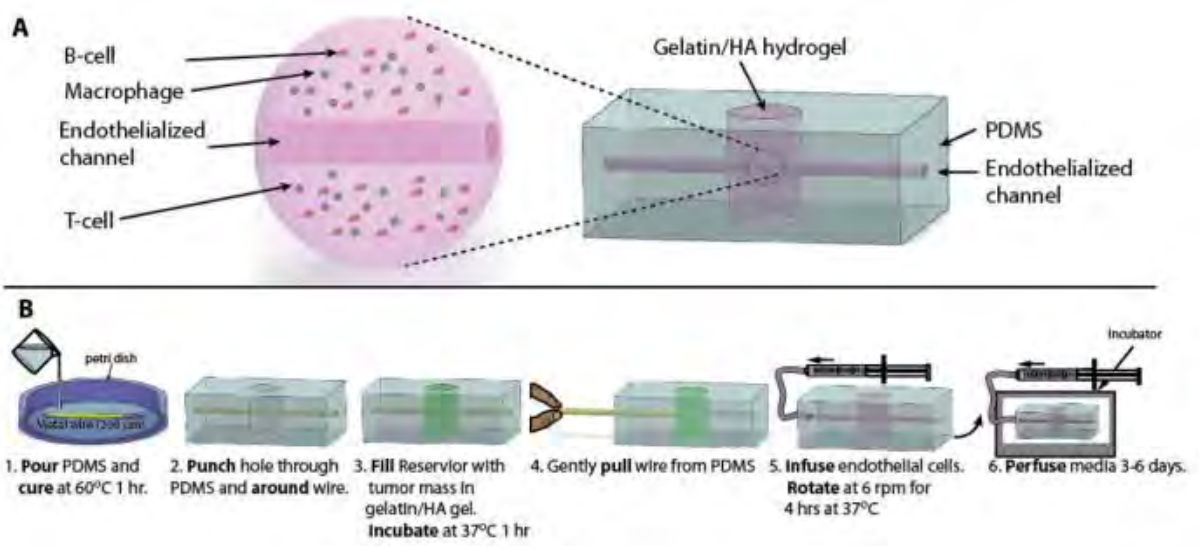

Figure 61 : The DLBCL-on-a-chip microvasculature model is fabricated using common laboratory items

A) An overall schematic highlighting the embedded DLBCL hydrogel (Left) within the PDMS macrostructure (Right) B) Schematic of the fabrication process. PDMS was molded around a stainless steel wireand a hole was punched out. This hole was filled in with the DLBCL hydrogel and allowed to polymerize. The hydrogel was then sealed with a plasma bonded glass coverslip. The stainless-steel wire was removed and the resulting microchannel was cultured with endothelial cells. From Mannino et al, Lab Chip, 2017.[438]

In a more screening reliable method, a droplet microfluidics-based platform was developed to generate DLBCL spheroids [439]. This model was composed by three cell types with a DLBCL cell line (SUDHL-10), a fibroblast cell line (HS-5) and lymphocytes from healthy donors (PBMC), with a ratio of 1:1:3 respectively [439]. The objective was to provide a model to test immunomodulatory drug activity, such as lenalidomide, in a high throughput manner thanks to the integrated action of spheroids in a

docking array (250 spheroids). In the first part of the study, rheology was performed on the engineered hydrogel composed of alginate (1%) and puramatrix (0.15%) to favor cell adhesion and aggregation while allowing cell proliferation. Long-term culture (14 days) was possible with a system of continuous perfusion of media which also able to infuse drugs and collect secreted cytokines at giving time points. Moreover, cell proliferation and death were compared between 2D culture monolayer and complex 3D co-culture. 2D monolayers appear more sensitive to cytotoxicity induced by lenalidomide and less proliferative than 3D culture. Moreover, it was observed an effect only on B cells after lenalidomide treatment and not on T cells and fibroblasts. A reduced secretion of several pro-inflammatory cytokines and markers such as CCL2, CCL3, CCL4, IL-6, IL-8, CD137 and ANG-1 was also observed in the collected media of treated cells. On the opposite, granzyme B secretion was increased in the condition with activated PBMC. Altogether, this study allowed to observe that lenalidomide induced B-cell death in the presence of activated immune cells and decrease of pro-inflammatory cytokines, confirming its anti-tumor effect. This model offers great opportunity to assess immunomodulatory drug effect in a high throughput manner by providing a high number of spheroids. Nevertheless, to be able to assess the effect of several drugs, the system needs to be replicable or needs to be improved.

Another group developed a 3D model with FL (DOHH2) and DLBCL (ABC type HLY1 and GBC type SUDHL4) cell lines encapsulated in alginate capsules [430]. They showed that DLBCL cell lines were able to proliferate and aggregate to form spheroids but not the FL cell line DOHH2, even after 17 days of culture. The lack of proliferation and aggregation prompted them to add a supportive microenvironment element in the condition of low number of cells seeded in each individual capsule (around eighteen cells/ capsule). In this condition, a high viability in the first weeks of culture (70-80%) was observed, which significantly decreased after two weeks of culture (around 50%). These models were characterized at two stages: a confluence stage and a post-confluence stage when cells disrupt alginate wall. Even after capsule dissolution, they observed that the integrity of cell aggregates was still present. They showed that cells were able to degrade the alginate wall, strongly supporting the action of secreted ECM. To address this question, comparative expression of laminin and collagen I in 3D and suspension culture was determined by immunofluorescence and RT-qPCR. Interestingly, ECM components were increased in 3D compared to 2D culture confirming that the degradation of alginate wall observed in this condition was probably due to ECM secretion.

To finish on DLBCL models, only one team established an *ex vivo* 3D model from DLBCL patient samples [440]. The HD method was used to form spheres which were embedded with collagen after 4-5 days of culture and co cultured with lymphoid-like fibroblasts from adipocyte derived stem cells and monocyte-derived macrophages. Such models allowed the study of the influence of cell interactions on B cells behavior. Indeed, it was observed an improved viability compared to *ex vivo* 2D cultures.

Moreover, this 3D co-culture system favors the stable expression of lymphoid fibroblast markers, in contrast to 2D co-culture in which a drop of expression was observed. Thus, this system allows the establishment of a very promising model which permits the study of the pathology in a relevant context without addition of exogenous cytokines or agents. Moreover, drug efficacy was determined and results obtained showed that rituximab induced a decrease of B-cell number in three out of four patients tested. Rituximab is known to act through three main mechanisms: direct cell death, ADCC or ADCP and finally CDC. Here, only a moderate phagocytosis was observed after rituximab treatment suggesting that the effect observed on B cell was due to a direct mechanism in the absence of immune cells. Another mechanism important in cancer development and involved in drug resistance is the secretion of ECM. Thus, by decreasing the content in collagen, Foxall et al, observed an increase of drug penetration and efficacy [440]. However, in this complex system, only B cell originate from DLBCL patients sample. Thus, it would be interesting to implement other populations isolated from the patient such as T cells to establish 3D models from bulk biopsies samples.

In summary, the progress in B-NHL modelling allowed many teams to engineer complex models integrating at least partially, the complexity of TME coming from FDC to ECM component and immune cell compartment (NK cells, γδ T cells, T cells, macrophages). All these studies applications, their advantages and disadvantages are summarized in table 12. In many of these studies, impact of spatial organization on gene expression, treatment response and immune cell activity was demonstrated. All of these showed that 3D models allow to more closely recreate the complexity of B-NHL, compared to classical suspension cultures, supporting the importance of conducting studies in 3D models. Unfortunately, even if many interesting models are available to study B-NHL biology and drug effect, a few of them are suitable for drug screening in a high throughput manner. Indeed, it is complicated to combine cell complexity, microenvironment and drug screening in one single model. For this reason, each model exhibits its own characteristics and allows to answer specific questions and altogether these different models will help in a better understanding of these pathologies. Another interesting perspective developed by a few teams is to use cells from patient to perform personalized medicine. Testing the specific drugs on patient-derived models taking into consideration the mutational landscape will allow to predict treatment response and guide clinician in the best therapeutic choice for each patient.

B-NHL subtype	Type of 3D model	Method /ECM mimicry (Yes/No)	Application or description	Advantages	Disadvantages	Ref
FL cell line (RL)	Spheroid (MALC : Multicellular Aggregates of Lymphoma Cells)	Hanging drop in 24well plates coated with agarose Yes: Methyl cellulosis	- importance of 3D modelling over 2D modelling [145,381] - Reflect anti-CD20 activity in 3D (GA101 > RTX) [234] - Co-culture with NK cells to model ADCC [428] - Co-culture with γδ T cells to increase anti-CD20 responses[71]	- Reproducible - Co-culture with effector cells introduce a part of FL microenvironment	- Difficult to handle - No drug screening possible - Do not recapitulate the full microenvironment - Do not recapitulate FL patient cell heterogeneity	133, 204, 334, 379, 392
FL and DLBCL cell lines (RL, SC1, DOHH2, WSU-NHL)	Spheroid ULA-MALC	ULA + centrifugation No	- 3D imaging tools and informatic solutions to highlight drug efficacy	- Easy to handle - Reproducible - Drug screening	- No co-culture, no microenvironment added - Do not recapitulate FL patient cell heterogeneity	441
FL and DLBCL (DOHH2, SUDHL-4, HLY1) + FL biopsies	3D alginate spheroid model	Microfluidic device printed in glass capillary + syringes mounted to pumps. 3 cones: one with alginate solution, second sorbitol solution, last cells in sorbitol or Matrigel/sorbitol solution Yes: alginate and matrigel/sorbitol	- Co-culture with tonsil stromal cells (TSC) isolated from routine tonsillectomy	- Mimick lymphoma cell niche thanks to the lymphoma B cells and stromal cells in co-culture - Suitable for testing new therapeutic agents thanks to high spheroid number generation	- Depending on the cell line, the growth is different - No drug screening	430
MCL cell line (HBL2 and Z138)	3D polystyrene (PS) scaffold	Four layers in a 90-degree angle to its immediate adjacent layer Yes: polystryrene	- MCL cells in co-culture with neonatal stromal cells in a scaffold mimicking ECM	- Mimic ECM with the artificial scaffold - Microenvironment added with stromal cells	- Artificial scaffold not representative of molecular composition of ECM - No drug screening possible	433
MCL cell line (JeKo-1) and MCL patient cells (blood and bone marrow)	Spheroid/ aggregates	Long term culture of JeKo-cells (>20 passages) forms spontaneous aggregates No	- Method for the enrichment of early-stage cells and experimental basis for the polyclonal nature of MCL pathogenesis	- No forced system, cells aggregates spontaneously - Possibility to create a reproducible spheroid bank - Drug screening possible	- Composed of only on cell type - No TME consideration	434
DLBCL cell line (HBL-1, Ocily-10, SC-1, DOHH2, WSU-DLCL-2, SUDHL-4)	Integric specific ligand functionalized 3D model	maleimide functionalized 4-arm polyethylene glycol (PEG-MAL) reacts with thiolated peptides to form a bio-adhesive hydrogel Yes: Hydrogel	- Co-culture with FDC (HK cell line) to mimic supportive cells of DLBCL microenvironement - Study of drug resistance to chemotherapeutics (doxorubicin) and histone deacetylase inhibitor (HDACi), Panobinostat	- Introduction of integrin microenvironment to a 3D model - Reproducible - Drug effect study	- Lack of other important microenvironment populations: T cells, macrophages. - Difficult to use drug screening	435
DLBCL A20 mouse B-cell lymphoma cell line	DLBCL-on-chip model	lymphoma-on-chip model Yes: hydrogel	- embedment of DLBCL cells from a cell line, T cells and macrophages, in hyalyronic acid-based hydrogel into a PDMS macrostructure	- Chip easy to reproduce with basic lab equipment - Introduction of an artificial vasculature	- Not suitable for drug screening - Use of mouse DLBCL cell line	438
SUDH-L1 DLBCL B cell line (+ T cells purified from healthy PBMC donors + HS-5 fibroblast cell line)	Spheroids Microfluidic	droplet microfluidics-based platform Yes: hydrogel (combination of alginate and puramatrix)	- The spheroids consist of three cell types (cancer, fibroblast and lymphocytes) in a novel hydrogel combination of alginate and puramatrix, which promoted cell adhesion and aggregation.	- Cellular interactions between three cell types - Spatiotemporal monitoring and secretome profiling in a high-throughput manner	- Use of cell lines not representative of patient heterogeneity	439
DLBCL (Patient cells)	Spheroids	Hanging drop method	- novel 3D spheroid co-culture system with ADSC-derived stoma cells	- first DLBCL patient 3D model performed with patient B cells - Test of relevant drugs used in the clinic (anti-CD20 mAb)	- Other tumor microenvironement compounds do not come from patient sample	440

Table 12 : Summary of available studies on B-NHL 3D models

4.4. Personalized medicine era in cancer: 3D models another string to the bow

4.4.1 Definition: the end of "one size fits all"

New technologies such as transcriptomic (next generation sequencing, RNA sequencing, CiteSeq…), proteomics (mass spectrometry) and imaging (light sheet microscope, confocal microscope…) highlighted inter-individual variability and demonstrated the importance of this consideration in new treatment strategies. Since individuals are unique at the molecular, physiological, environmental exposure and behavior levels, it seems unappropriate to treat patients exhibiting a same pathology with a same molecule. To overcome this paradox, the concept of personalized medicine emerged. Personalized medicine includes other sub-concepts, such as: precision medicine (molecular features of the tumor), stratified medicine (biomarkers, diagnosis and drugs), P4 medicine (prevention), and individualized medicine (using patients own cells) (Figure 62). All of these concepts together form the personalized medicine defined by the U.S National Cancer Institute as "a form of medicine that uses information about a person's genes, proteins and environment to prevent, diagnose and treat disease.". Clinical applications of personalized medicine are various, from screening, diagnosis, prognosis, prediction of treatment efficacy to subgroup stratification of patients. The main aim of this concept is to replace the "one size fits all" model of medicine which is based on average responses of care, which does not reflect interpatient patient reality. To support this concept, combination of high throughput approaches can be used, including whole genome sequencing, single-nucleotide polymorphism analysis, microarray analysis or mass spectrometry. Moreover, it is important to evaluate the pros and cons of personalized medicine in terms of cost, test standardizations and ethical issues[442].

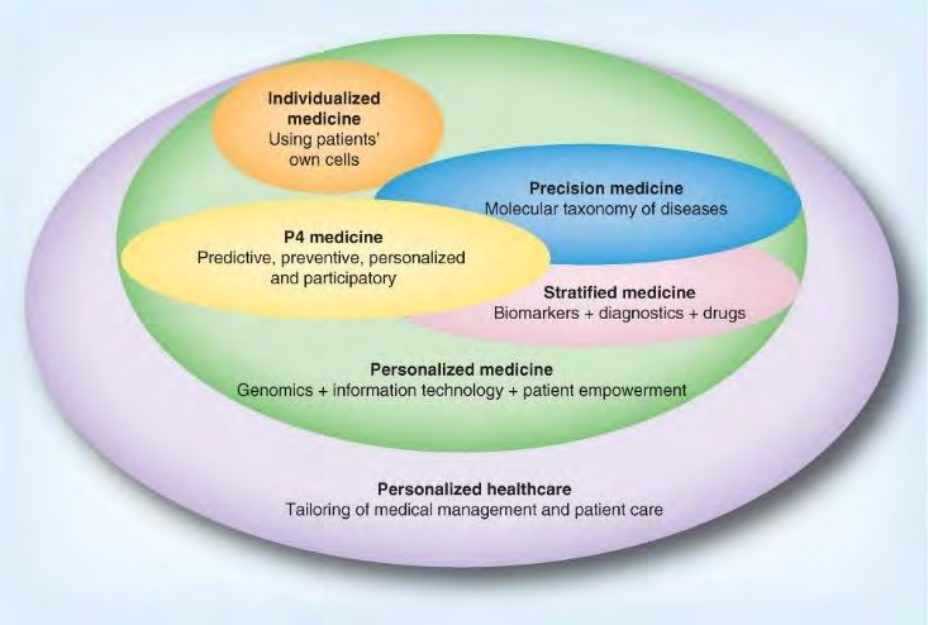

Figure 62 : Personalized medicine : one word many definitions

From Pkorska-Bocci et al, Per Med 2014 [443].

In this context, the interest in 3D models increased exponentially over the years and they became essential model for preclinical studies. Organoids or tumoroids remain the best model to perform personalized medicine thanks to their patient similarity in terms of genomic, architecture and treatment response.

4.4.2 Personalized medicine clinical applications

Personalized medicine, combined with other approaches such as histology, aims to better stratify patients in order to propose an adapted therapy. Indeed, by using molecular analysis at the protein, DNA and RNA levels it is possible to identify novel tumor subclasses and subclones presenting different prognostic outcome and predict response to treatment. For example, this molecular classification helped in discovering subclasses of cancers such as acute myeloid leukemia [444], breast cancer [445] or better differentiate BL and DLBCL [80].

As genetic alterations are one of the main hallmarks of cancer progression, identification of molecular characteristics of each patient allows to stratify them in subgroups of interest for a specific molecule or therapeutic strategy. Two main successful stories are exemplified by imatinib (Gleevec) [446] called “the magic bullet” in chronic myeloid leukemia and trastuzumab (Herceptin)[447] in breast cancer, both treatment revolutionized patient management in these cancers. Indeed, abnormal protein tyrosine kinase activity in chronic myeloid leukemia and overexpression of the HER-2 receptor in breast cancer are two predictive markers for treatment responses. Thus, only patients with these alterations are eligible for imatinib and trastuzumab treatments. Although biomarkers are at the heart of personalized medicine, it is important to distinguish predictive and prognostic biomarkers. A predictive biomarker helps to predict depending on treatment given whereas prognostic biomarker is not based on treatment. A well-known example is the IGHV status prognostic biomarker in patients with CLL. Indeed, patients with mutated IGHV present good outcomes with both fludarabine and ibrutinib based therapy. On the opposite, patients with unmutated IGHV present shorter PFS with fludarabine-based therapy than with ibrutinib [448]. In FL, no clearly defined biomarkers are used in the clinic but some studies showed that patients with EZH2 mutations may benefit more from CHOP/CVP than bendamustine. The opposite is true for patients without the mutation who are more sensitive to bendamustine [448]. In clinical routine, biomarkers are used with other approaches such as imaging features with for instance metabolic tumor volume measurement. This parameter has become commonly used to predict response and guide treatments. For example, the use of PET-directed therapy in Hodgkin’s lymphoma in dose de-escalation choice after treatment response proved its efficacy with minimizing the toxicity [449,450].

Personalized medicine uses different levels of tumor features from molecular, to genetics and to metabolic parameters. Identifying variation in genes encoding enzymes responsible for drug metabolism, drug transporters or drug target is also important to predict treatment dose and safety. For example, polymorphisms in cytochrome P450 (CYP450) enzymes can lead to different drugs metabolism causing overdose or no drug response [451]. Molecular characteristics can also enable to identify predisposition genes for certain pathology and a support in patient care. Indeed, higher susceptibility to develop breast cancer is observed when mutation are found in *BRCA1* and *BRCA2* tumor suppressors genes [452]. To overcome this risk, preventive surgical measures, regular screening or receiving adjuvant therapies are possible strategies that exemplify personalized medicine approach [453]. Another example is the genetic testing to identify inherited mutations in the DNA mismatch repair genes, *MLH1* and *MSH2*, who have a higher risk of developing colon cancer [454]. In this case early screening colonoscopy enable early cancer detection and treatment.

4.4.3 Organoids: another string to the bow of personalized medicine

Preclinical models are essential to discover new targets and to understand mechanism of action and drug resistance. They are also important to identify new biomarkers to guide treatment strategy in a personalized manner. Because genomics alone is not enough to identify therapeutic options for the majority of patients with advanced disease, drug screening using 3D cultures are potent strategies to evaluate new molecules (Figure 63).

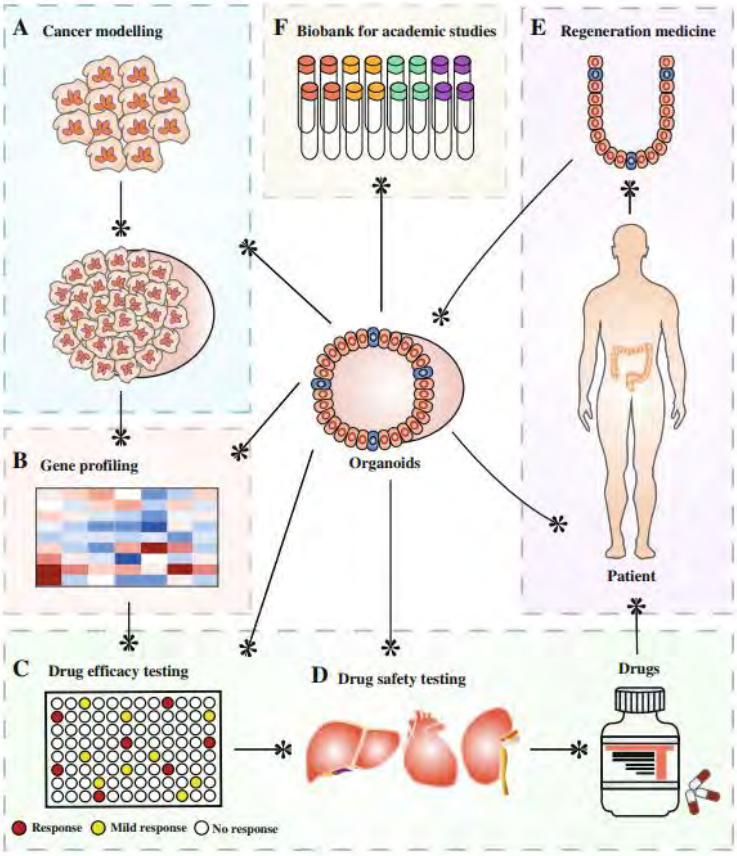

Figure 63 : Possible applications of organoids from cancer modelling, From Pauli et al, Cancer Discov, 2017 [455]

Many organoids have been established from epithelial tissues such as breast, colon, brain and lung as discussed in part 4.1.3.3.1. In order to demonstrate the relevance of these models in preclinical settings, patient responses have been compared to the matched PDO response showing their robustness and high predictivity. For example, Tiriac et al showed that pancreatic PDO presented therapeutic profiles similar to patient outcomes and enable longitudinal chemo-sensitivity and evaluation of metastasis [456]. They also extracted, based on organoid gene expression, a chemo-sensitivity signature able to predict responses to chemotherapy from many patients [456]. In another study, by combining genomic analysis profiling of DNA repair mutational status and functional testing on patient-derived high grade serous ovarian cancers organoids, Driehuis et al were able to identify targetable DNA damage repair defects with specific therapy [457]. For example, PDO with defect in homologous recombination correlated with PARP inhibitor sensitivity and a functional defect in replication fork protection corresponded to a good response to carboplatin and CHK1 and ATR inhibitor. Very interestingly, Driehuis et al, provided guidelines to establish PDO and prepare a drug screening platform that could be standardize to offer to the community a reliable general protocol [457]. They described a semi-automated system where organoids are seeded in 384-well plates and chemotherapeutic screens are performed to evaluate their sensitivity [457]. An interesting feature of organoids, is the possibility to create biobanks to preserve heterogeneity of patient's tumors and increase the possibility to perform various tests on these models. Sachs et al generated more than 100 breast cancer organoids capturing this cancer heterogeneity [400]. However, even if PDO present great opportunity for drug discovery, *in vivo* models are still essential to validate drugs before transferring to clinical trials because of their off-target effect assessment that is not possible with organoids. Thus, it is important to use PDO as the first preclinical model to identify best agents and test doses in order to confirm specificity and sensitivity before going to costly and time-consuming *in vivo* studies. In this context, Pauli et al, implemented an impressive number of organoids (145 specimens from 18 different tumor types) in clinical studies with PDX established in parallel to first chose in PDO [455]. This platform allows, for example, to identify in the endometrial adenocarcinoma patient sample, an efficient combination of buparlisib with olaparib.

So far one of the most impressive forms of personalized approaches developed in cancer immunotherapies are the CAR-T cells. Nevertheless, even if this approach resulted in notable successes, CAR-T cells failed to induce therapeutic response in some patients, which among others has been attributed to patient-specific level of neo-antigens or limited trafficking of CAR-T cells into the tumor. The use of 3D models is an opportunity to better understand the barriers impeding CAR-T cell efficacy [458,459]. For instance, Jacob et al used patient-derived glioblastoma organoids (GBOs) co-cultured with 2173-BBz anti-EGFRvIII CAR T cells that specifically bind to mutant EGFRvIII commonly

found in glioblastomas and recapitulated in GBO. In their protocol, they have optimized the ratio of CAR-T cells to tumor cells to model and observe CAR-T cell infiltration and proliferation, target antigen loss and tumor cell killing frequency on a clinically relevant timescale. Thus, they were able to monitor the efficacy and specificity of engineered CAR-T cells *in vitro* before initiating therapy in patients, in order to stratify patients for clinical trials and to better predict therapeutic responses [410].

For now, personalized medicine is more of a concept than a highly applicable approach in cancer treatment strategies. Indeed, more proofs of concept need to be brought in the existing studies to show that this strategy can outperform traditional medicine protocols. Moreover, it is important to emphasize that 3D models are potent tool for personalized medicine and are implemented in larger strategies where computational models, animal models, social and political elements need to be considered. Thus, interdisciplinary and collaborative works are the key to a successful personalized medicine.

Summary Goodbye flat *lymphoma* biology (4)

In this part, cancer models' evolution was described and 3D models were presented as important tools to better understand solid cancer and in a lower extend hematological malignancies such as B-NHL. The third dimension has proven over the years its capacity to recapitulate tumor spatial organization, cellular morphology and physiological characteristics better than conventional 2D cultures. As presented, 3D models are in constant evolution and are following technology advances to continue to overcome their limitations. These models are more and more used in preclinical testing and precision medicine. However, we are still far from fully recapitulating all of the patient-specific stromal, immune, structural, chemical and molecular aspects of TME that represent cancer evolution and complexity. New methods and technologies such as organ-on-a-chip and bioprinting in combination with already existing organoid models represent an exciting advance in the field. It is important to underline that animal models are still necessary and many efforts are focused on development of humanized murine models. Altogether, the use of these 3D models in personalized medicine will help clinicians to propose adapted drugs making them transferable from bench to bedside (Figure 64).

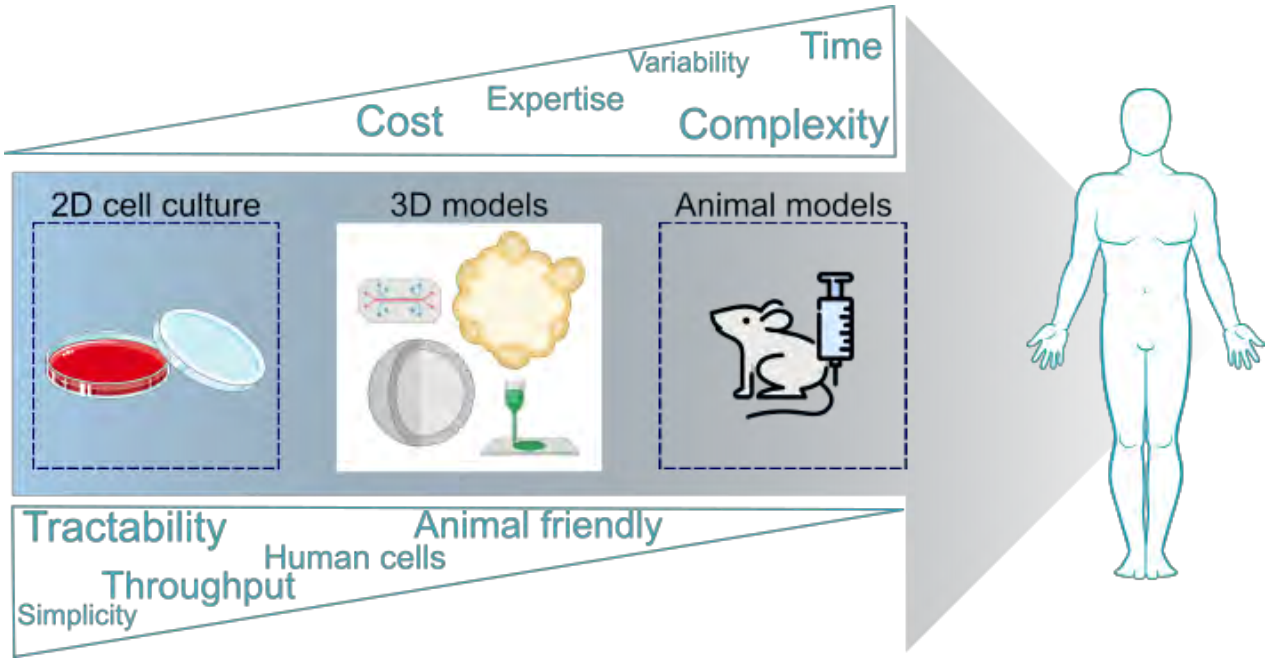

Figure 64 : 3D models at the service of personalized medicine: filling the gap between 2D cell culture and animal models

II. THESIS OBJECTIVES

FL genesis and progression is highly dependant on many parameters such as epigenetic, genetic and microenvironment features that shape tumor capacity to create an immunosuppressive environment. The introduction of rituximab in combination with polychemotherapy, has revolutionized patients' OS. Nevertheless, up to 20% are refractory to these treatments and unfortunately all FL patients will relapse. This observation led researchers and clinicians to increase FL therapeutic armamentarium. In order to control immunosuppressive environment, many chemo-free strategies have emerged using IT to eradicate tumor through immune cell cytotoxic activity. Discovery of novel therapeutic targets, test of new drugs, and relevant models are needed in this pathology that highly relies on its microenvironment and spatial organization. 3D models represent a key tool in tailoring new treatment strategies, as they reflect the pathology in term of: (i) spatial architecture, (ii) transcriptomic and protein profiles and (iii) treatment responses.

In this context, IMLINFO's project was initiated in 2018 to create a repository of NHL associated to a 3-dimension (3D) culture platform, that will allow the determination of efficacy of new IT treatments such as adenosine inhibitors. This consortium was composed by 7 partners: two research centers (CRCT, Toulouse and IDIBAPS, Barcelona), one start-up (IMACTIV3D, Toulouse), hospitals (Toulouse, Barcelona and Girona) and one pharmaceutical company developing adenosinergic pathway inhibitors (PaloBioFarma, Barcelona). Thanks to this europen consortium and grant, I started my PhD in March 2019.

My specific PhD objectives were as following: (i) establishment of 3D cultures from FL cell lines (MALC) and FL patient samples (PDLS), (ii) characterization of the transcriptomic and phenotypic profiles of PDLS (immune cell population composition, expression of adenosinergic pathway markers and ICP…), (iii) test efficacy of IT on PDLS and (iv) identification of new therapeutic targets such as CD39. These investigations aim to highlight new therapeutic pathways that were not considered so far and that could help in improving patient's therapeutic choice in a personalized way.

III. RESULTS

Although the great advances observed in FL patients' management after the introduction of rituximab-CHOP therapy, 20 to 30% of patients are refractory and relapses are unavoidable. This disease presents complex features that need to be taken into account for discovering new therapeutics that can target microenvironment, genetic and epigenetic mutations but also IE mechanisms. In this context, the need of a relevant *in vitro* culture model is crucial and 3D models appeared perfectly adapted. For this reason, we have focused our work on generating FL 3D models first from cell lines and then from patients' samples in order to better recapitulate FL features and find new therapeutic targets.

1. ULA-MALC: a scaffold-free model adapted for drug screening

1.1. Methodology and study context

10 years ago, my team developed a FL 3D model to evaluate the impact of spatial organization on FL biology and treatment response. MALC were produced by adaptation of the HD method where RL cell's suspension was prepared in complete medium containing 1% methylcellulose (a gelling agent that forces cell-cell interaction). 20µL of this suspension were dropped into coverslips of a 24-well culture plate and after 24 hours' incubation, all drops were transferred by returning the coverslip to a dish previously coated with 4% agarose. All of the MALC culture medium was then renewed every 5 days. (Figure 65).

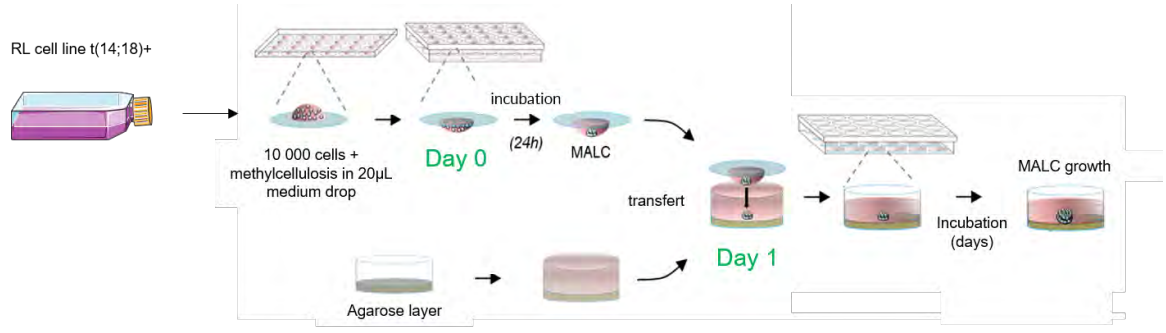

Figure 65 : Hanging-drop MALC (HD-MALC) method illustration

Although the HD method allowed a better understanding of FL biology and drug responses in a more relevant model than 2D cultures, it was not suitable for drug screening due to the manual transfer of neoaggregates into agarose-precoated wells. Moreover, one could speculate that

methylcellulose (MC), which is added for HD-MALC formation, may induce matrix-driven alterations in growth, expression profiles, cell behavior or in drug responses. This has never been explored.

Thus, the first part of my PhD was dedicated to develop a new method allowing the production of a higher number of spheroids, in a reproducible and easy procedure. In order to fit the scaffold-free strategy chosen by my team, the "ultra-low attachment method" was the most adapted. In this method, 100µL of cell suspension were placed into 96-wells plate ultra-low attachment plate and a centrifugation (1000rpm, 10 min) was than performed to promote cell aggregation. The plate was placed into an incubator at 37°C and 5% CO_2. 100µL of medium were renewed every 3 days in order to provide sufficient nutriments to the cell culture and spheroid growth. 3D culture of several B- NHL cell lines were tested and as shown in figure 66. RL MALC were the most compact and spherical models obtained. Thus, we in depth characterized this model by 2D and 3D imaging and corrobated the observations obtained with flow cytometry analysis. This study was published in Cancers in 2021 where I was signed as the first co-author.

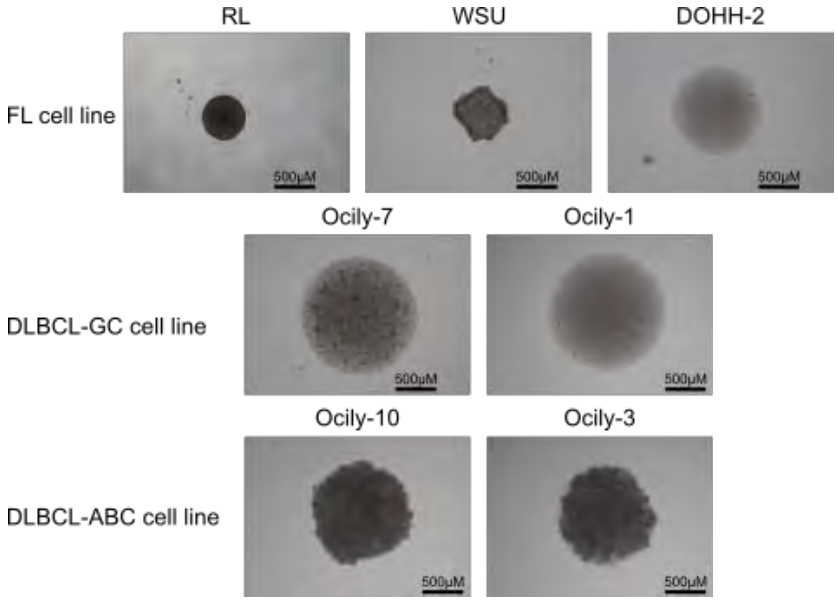

Figure 66 : Picture of representative ULA-MALC at day 3 of culture established with different B-NHL cell line
Pictures were obtained taken with an inversed microscope at 4X equipped with a camera (Nikon Eclipse TE200). Scale 500µm

1.2. Scientific publication: 3D Model Characterization by 2D and 3D Imaging in t(14;18)-Positive B-NHL: Perspectives for *In Vitro* Drug Screens in Follicular Lymphoma

This study, entitled 3D Model Characterization by 2D and 3D Imaging in t(14;18)-Positive B-NHL: Perspectives for *In Vitro* Drug Screens in FL, was published in Cancers in 2021 and comprises two parts (Figure 67). The first one aimed to characterize biologically the MALC established with a cell seeding density defined to be the most suitable to obtain a robust and reproducible model. The second one aimed to characterize in depth the effect of different drugs. Morphological features and cell growth behavior were evaluated by classical microscopy (2D imaging) and response to different treatments was evaluated by a high-content analysis system to determine the robustness of the model. We showed that the ULA method allowed the development of regular, spherical and viable ULA-MALC. However, discrepancies in the results obtained after 2D imaging analyses on drug-treated ULA-MALC prompted us to develop 3D imaging and specific analyses. We showed by using light-sheet microscopy and specifically developed 3D imaging algorithms that 3D imaging and dedicated analyses were necessary to characterize the real morphological properties of 3D models and drug effects. This study proposed a new method but also imaging tools and informatic solutions, developed for FL necessary for future preclinical studies.

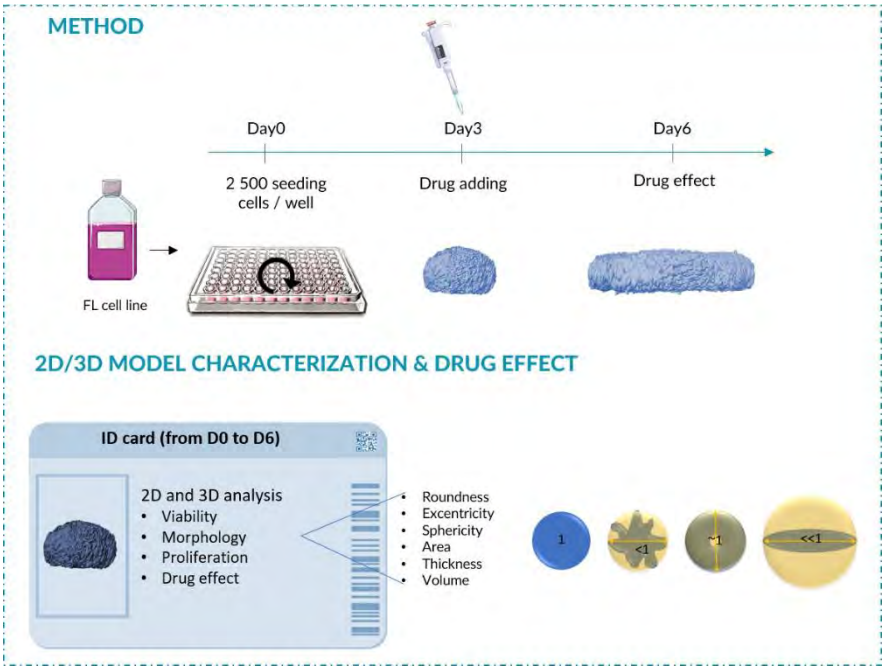

Figure 67 : Graphical abstract of scientific publication representing the workflow and model characterization

cancers

MDPI

Article

3D Model Characterization by 2D and 3D Imaging in t(14;18)-Positive B-NHL: Perspectives for In Vitro Drug Screens in Follicular Lymphoma

Fabien Gava [1,2,3,4,5,6,†], Carla Faria [1,2,3,4,5,6,†], Pauline Gravelle [1,2,3,4,5,6,7], Juan G. Valero [8,9], Cèlia Dobaño-López [8,9], Renaud Morin [10], Marine Norlund [10], Aurélie Gomes [10], Jean-Michel Lagarde [10], Cédric Rossi [11], Julie Bordenave [1,2,3,4,5,6], Laetitia Pieruccioni [12], Jacques Rouquette [12], Alba Matas-Céspedes [8,9], Jean-Jacques Fournié [1,2,3,4,5,6], Loïc Ysebaert [1,2,3,4,5,6,13], Camille Laurent [1,2,3,4,5,6,7], Patricia Pérez-Galán [8,9] and Christine Bezombes [1,2,3,4,5,6,*]

1 Centre de Recherches en Cancérologie de Toulouse, INSERM UMR1037, CEDEX 1, 31037 Toulouse, France; fabien.gava@inserm.fr (F.G.); carla.faria@inserm.fr (C.F.); pauline.gravelle@inserm.fr (P.G.); julie.bordenave@inserm.fr (J.B.); jean-jacques.fournie@inserm.fr (J.-J.F.); ysebaert.loic@iuct-oncopole.fr (L.Y.); Laurent.Camille@iuct-oncopole.fr (C.L.)
2 Université Toulouse III Paul-Sabatier, CEDEX 9, 31062 Toulouse, France
3 ERL 5294 CNRS, CEDEX 4, 31055 Toulouse, France
4 Institut Universitaire du Cancer-Oncopole de Toulouse, CEDEX 9, 31059 Toulouse, France
5 Laboratoire d'Excellence 'TOUCAN-2', CEDEX 1, 31037 Toulouse, France
6 Institut Carnot Lymphome CALYM, 69495 Pierre-Bénite, France
7 Department of Pathology, Institut Universitaire du Cancer de Toulouse, CEDEX 9, 31059 Toulouse, France
8 Department of Hemato-Oncology, IDIBAPS, 08036 Barcelona, Spain; garcia32@clinic.cat (J.G.V.); cdobanol@clinic.cat (C.D.-L.); alba.matas87@gmail.com (A.M.-C.); PPEREZ@clinic.cat (P.P.-G.)
9 Centro de Investigación Biomédica en Red-Oncología (CIBERONC), 28029 Madrid, Spain
10 IMACTIV-3D, 1 Place Pierre Potier, 31106 Toulouse, France; renaud.morin@imactiv-3d.com (R.M.); marine.norlund@imactiv-3d.com (M.N.); aurelie.gomes@imactiv-3d.com (A.G.); jean.michel.lagarde@imactiv-3d.com (J.-M.L.)
11 CHU Dijon, Hématologie clinique, Hôpital François Mitterand, 21000 Dijon, France; cedric.rossi@chu-dijon.fr
12 RESTORE Research Center, Université de Toulouse, INSERM, CNRS, EFS, ENVT, 31100 Toulouse, France; Laetitia.PIERUCCIONI@cnrs.fr (L.P.); Jacques.ROUQUETTE@cnrs.fr (J.R.)
13 Department of Hematology, Institut Universitaire du Cancer de Toulouse, CEDEX 9, 31059 Toulouse, France
* Correspondence: christine.bezombes@inserm.fr
† These authors contributed equally to this work.

Citation: Gava, F.; Faria, C.; Gravelle, P.; Valero, J.G.; Dobaño-López, C.; Morin, R.; Norlund, M.; Gomes, A.; Lagarde, J.-M.; Rossi, C.; et al. 3D Model Characterization by 2D and 3D Imaging in t(14;18)-Positive B-NHL: Perspectives for In Vitro Drug Screens in Follicular Lymphoma. *Cancers* **2021**, *13*, 1490. https://doi.org/10.3390/cancers13071490

Academic Editor: Ellen Leich

Received: 29 January 2021
Accepted: 6 March 2021
Published: 24 March 2021

Simple Summary: Follicular lymphoma is an indolent B cell lymphoproliferative disorder of transformed follicular center B cells, which accounts for 20–30 percent of all non-Hodgkin lymphoma (NHL) cases. Although huge efforts have been made in the last 10 years, this pathology is still considered as incurable, leaving open the discovery and testing of new therapeutic targets requiring relevant preclinical models. Here, we report a realistic 3D model of t (14;18)-positive B-NHL cell culture (ultra-low attachment (ULA)-multicellular aggregates of lymphoma cells (MALC)), which monitored by state-of-the-art 2D and 3D imaging, allows more robust drug testing.

Abstract: Follicular lymphoma (FL) is an indolent B cell lymphoproliferative disorder of transformed follicular center B cells, which accounts for 20–30 percent of all non-Hodgkin lymphoma (NHL) cases. Great advances have been made to identify the most relevant targets for precision therapy. However, no relevant models for in vitro studies have been developed or characterized in depth. To this purpose, we generated a 3D cell model from t(14;18)-positive B-NHL cell lines cultured in ultra-low attachment 96-well plates. Morphological features and cell growth behavior were evaluated by classical microscopy (2D imaging) and response to treatment with different drugs was evaluated by a high-content analysis system to determine the robustness of the model. We show that the ultra-low attachment (ULA) method allows the development of regular, spherical and viable ULA-multicellular aggregates of lymphoma cells (MALC). However, discrepancies in the results obtained after 2D imaging analyses on drug-treated ULA-MALC prompted us to develop 3D imaging and specific analyses. We show by using light sheet microscopy and specifically developed 3D imaging

algorithms that 3D imaging and dedicated analyses are necessary to characterize morphological properties of 3D models and drug effects. This study proposes a new method, but also imaging tools and informatic solutions, developed for FL necessary for future preclinical studies.

Keywords: follicular lymphoma; 3D model; spheroid; drug testing; 2D imaging; SPIM

1. Introduction

Follicular lymphoma (FL) is the second most common type of non-Hodgkin lymphoma (NHL). It is composed of malignant cells derived from germinal center B cells, both centrocytes and centroblasts, with a follicular growth pattern. In most cases, FL cells exhibit the t(14;18) translocation leading to the expression of the antiapoptotic Bcl-2 protein. It is located primarily in lymph nodes and characterized by a nodular pattern with variable-sized and usually closely packed follicles. FL usually has an indolent course and excellent overall survival. However, the disease remains incurable with conventional approaches and is characterized by repeated relapses [1,2]. Thus, FL research should focus on the development of new and more efficient molecules targeting key pathways leading to disease pathogenesis. To this end, relevant in vitro models should be amenable for testing new drugs in preclinical settings. Classically, these studies are performed with cancer cells cultured in suspension (2D), but 3D aggregate cultures, also named spheroids, are widely recognized as more physiologically relevant to normal and diseased human tissues [3]. Advantages for using spheroids in the study of solid cancers have been recognized for over 50 years [4] and their historical timeline was described recently [5–7]. These 3D models reproduce cell–cell and cell–matrix interactions, spatial organizations, mechanical constraints, nutrients and O_2 gradients, critical parameters able to influence the biology of the disease and the response to treatments. Spheroids are essential for in vitro studies, filling the gap between conventional 2D cultures, from which they are very different [8], and animal models. They also offer useful properties for drug screening [9–13]. Although these 3D cell cultures are routinely used for the study of solid cancers, in NHL and more particularly FL, very few models exist. We are pioneers in the development of MALC (multicellular aggregates of lymphoma cells) models with the hanging drop (HD) method in 24-well plates (HD-MALC) with t(14;18)-positive B-NHL cell lines. This 3D model exhibits transcriptomic profiles similar to FL patients with an overexpression of gene families involved in survival pathways, including the NF-κB pathway, cell cycle regulation or hypoxic responses [14–16]. These models can be easily cocultured with cytotoxic immune cells such as NK or T lymphocytes, allowing the study of anti-CD20 antibody responses, drug penetration, immune cell infiltration and immune-escape mechanisms targetable by immunotherapy [17,18]. Although the HD method allowed a better understanding of FL biology and drug responses in a more relevant model than 2D cultures, it is not suitable for drug screening due to the manual transfer of neoaggregates into agarose-precoated wells. Moreover, one could speculate that methylcellulose (MC), which is added for HD-MALC formation, may induce matrix-driven alterations in growth, expression profiles, cell behavior or in drug responses. This has never been explored.

In order to avoid these biases and to improve the throughput necessary for testing drug efficacy, we adapted a MC-free method of t(14;18)-positive B-NHL cell culture in ultra-low attachment (ULA) 96-well plates where cells were induced to self-aggregate into MALC (ULA-MALC). Morphological features and cell growth behavior were evaluated by classical microscopy (2D imaging) and response to treatment with different drugs was evaluated by a high-content analysis system to determine the robustness of the model. Furthermore, 3D imaging and 3D analyses were specifically developed to characterize in depth the ULA-MALC model and drug effects.

2. Materials and Methods

2.1. Cell Lines and Drugs

The human aggressive t(14;18)-positive B-NHL cell line RL (t14:18; CD19+; CD20+; CD21+; CD22+; Hle-1+; HLA DQ+; HLA DR+; CD25-) was purchased from the American Type Culture Collection (ATCC, Rockville, MD, USA) and the transformed FL cell lines DOHH2 (t14:18; $CD3^-$; $CD10^+$; $CD13^-$, $CD19^+$; $CD20^+$; $CD34^-$, $CD37^+$; $CD38^+$; $CD80^+$; $CD138^-$, $HLA\text{-}DR^+$), WSU-NHL (t14:18; $CD3^-$; $CD10^+$; $CD13^-$; $CD19^+$; $CD20^+$; $CD34^-$; $CD37^+$; $CD38^+$; $CD80^+$; $HLA\text{-}DR^+$) and SC-1 ($CD3^-$; $CD10^+$; $CD13^-$; CD19+; $CD34^-$; $CD37^+$; $CD38^+$; cyCD79a(+); $CD80^+$; $CD138^+$; $HLA\text{-}DR^+$) were obtained from the DSMZ Collection (Braunschweig, Germany). These cell lines carry additional alterations besides BCL-2 overexpression due to t(14;18): RL carries p53/mut [19], whereas DOHH2 and SC-1 show Myc amplification DSMZ refs ACC47 and ACC558 respectively).

The cells were cultured in suspension (referred to as 2D culture) in complete RPMI 1640 medium supplemented with glutamine (Dominique Dutscher, Brumath, France) with 10% of FBS (Life Technologies, Villebon sur Yvette, France) and 1% of penicillin/streptomycin (Sigma-Aldrich, St Quentin Fallavier, France) at 37 °C in a humidified atmosphere containing 5% CO_2. Mycoplasma contamination was routinely tested by using Mycoplasma Alert (Lonza, Basel, Switzerland).

Rituximab (RTX, Mabthera) and obinutuzumab (GA101) were provided by Roche (Boulogne-Billancourt, France) and Roche (Zurich, Switzerland) respectively. Venetoclax (ABT-199, Bcl2 inhibitor), rapamycin (mTOR inhibitor), ibrutinib (BTK inhibitor), lenalidomide (immunomodulator) and bendamustin (alkylating agent) were all purchased from Euromedex (Souffelweyersheim, France).

2.2. ULA-MALC Generation

Of the complete medium 100 µL containing 2500, 5000 or 10,000 FL cells were seeded in 96-well round bottom ULA plates (Corning, Samois sur Seine, France), centrifuged and cultured at 37 °C in a humidified 5% CO_2 atmosphere. Of fresh medium 100 µL was added every 3 days to avoid spheroid shrinking and to counterbalance liquid evaporation.

2.3. ULA-MALC Characterization by 2D Imaging

After 3, 6 or 9 days of culture, ULA-MALC was visualized by bright field (BF) and fluorescent microscopy on an automated spinning disk confocal HCS device equipped with a 5× objective (Operetta, Perkin Elmer, Villebon sur Yvette, France). To visualize cell death, propidium iodide (PI) at 1 µg/mL (Life technologies, Villebon sur Yvette, France) was added directly into the wells for 1 h prior to imaging. For each well, 1 field and 16 stacks per field (10 µm step) were acquired. Morphological parameters (BF area) and cell death (PI area and PI intensity and laser 532 nm) were determined on stacks of images combined with maximum projection and analyzed by the Columbus software. Cell death was measured in relation to the total BF area.

Two-dimensional imaging was also performed using an inverted microscope (Nikon Eclipse TE200) and several morphological parameters were extracted based on an adapted macro from [20–22]:

- Projected area was calculated as previously described [21,22] according to the formula:

$$R = \sqrt{S/\pi} \quad (1)$$

  R = radius and S = measured area of 2D projection).
- Volume was calculated as described [23] according to the formula:

$$V = \frac{4}{3}\pi R^3 \quad (2)$$

- Sphericity index (SI): the spherical geometry shape was calculated according to Equations (3) and (4):

$$\text{Cir} = \frac{4\pi \cdot \text{Area}}{\text{Perimeter}^2} \quad (3)$$

$$\text{SI} = \sqrt{\text{Cir}} \quad (4)$$

  ULA-MALC were considered spherical when SI = 1.
- Roundness index (RI) corresponded to the circularity of the ULA-MALC where a perfect circle = 1.
- Solidity is an indicator of the roughness of the spheroidal surface. This index was determined to assess its regularity.

For live imaging, ULA-MALC from centrifugation to day 1 of culture were observed with BF (4× magnification) with Incucyte S3 Live-Cell Analysis System (Sartorius, Göttingen, Germany) or Cytation TM 1 (Biotek, Winooski, VT, USA) at 37 °C and 5% CO_2.

2.4. ULA-MALC Characterization by 3D Imaging

ULA-MALC were fixed at different days of culture directly in the wells with 4% PFA (Alfa Aesar, Haverhill, MA, USA) overnight at 4 °C and rinsed with PBS. Nuclei were labeled with 1 µg/mL propidium iodide for 1 h at room temperature. ULA-MALC were then rinsed with PBS and included in 1% low-melting agarose (Life Technologies). 8 mm disks were punched and cleared with the methanol-benzyl alcohol/benzyl benzoate (BABB) technique as previously described [24,25]. Cleared samples were immersed in a quartz chamber filled with BABB during acquisition due to a 3D-printed disk holder. Acquisitions were performed with selective plane illumination microscope (SPIM) technology [26]. Two microscopes were used: SPIM [27] for MALC from day 1 to day 4 and MacroSPIM [28,29] only for MALC at day 5 and day 6. An ULA-MALC at day 2 of culture was used to check for potential differences between image acquisitions by SPIM and MacroSPIM. For both microscopes, 2 µm-step Z-stacks at 5× magnification with a pixel size of 1.3 µm for SPIM and 1.28 µm for MacroSPIM were generated. Driving module/software for those microscopes have been developed by INSCOPER (Rennes, France). Open-source image processing package ImageJ and IMARIS 7 software (BitPlane, South Windsor, CT, USA) were used.

An image processing pipeline was specifically developed and implemented to automatically segment the ULA-MALC samples in 3D from SPIM and MacroSPIM acquisitions. The images were first resampled to obtain a 3D isotropic resolution sufficient for morphological characterization. A 3D non-local denoising algorithm was then used to improve the signal-to-noise ratio, with the degree of smoothing automatically estimated with respect to the standard deviation of noise in the image. A segmentation based on hysteresis thresholding was finally implemented, performing a dual thresholding to reduce isolated pixels and improve the connectivity of the resulting segmentation. This method is particularly suited for the segmentation of ULA-MALC MacroSPIM images since the distribution of the gray levels in such images can be bivariate (background and homogeneous sample) or trivariate (background and heterogeneous sample with high and low intensity regions). The lower and upper thresholds used in hysteresis segmentation were initialized using values centered around the threshold estimated by the classical Otsu method [30], which minimizes the intraclass variance of the resulting segmentation. The algorithm's output is a 3D binary mask image from which various 3D morphological parameters were estimated:

- Volume.
- Eccentricity:

$$e1 = \sqrt{1 - \frac{c^2}{a^2}} \quad (5)$$

$$e2 = \sqrt{1 - \frac{c^2}{b^2}} \quad (6)$$

with a: longest ellipsoid axis, b: second longest ellipsoid axis, c: shortest ellipsoid axis. Eccentricity = 0 for a perfect sphere and increases following ellipsoid deformation with a maximum of 1.

- Sphericity:

$$S = 36\pi \frac{Volume^2}{Surface^3} \quad (7)$$

- A sphere is considered perfect when S = 1 and decreases with the rugosity or deformation of the shape.
- Roundness:

$$R = \frac{6}{\pi} \cdot \frac{Volume}{majoraxis^3} \quad (8)$$

- Roundness = 1 for a perfect sphere and decreases with deformation.

2.5. Visualization of Proliferative Cells in Whole ULA-MALC

To visualize proliferative cells in whole ULA-MALC, we adapted protocols from [20,31] as follows: after 3 or 6 days of culture, ULA-MALC (2500 cells seeding) were fixed as described in the previous section. ULA-MALC were then incubated in a blocking solution composed of PBS/FBS 1%/Triton X-100 0.3% for 8 h at room temperature (RT) under mild agitation on an orbital shaker. Incubation with the primary antibody (mouse anti-human Ki67 clone MIB-1, Agilent technologies, Les Ulis, France), diluted at 1/100e in blocking solution, was performed for 3 days at RT under mild agitation. After several washes with PBS during 24 h, the secondary antibody (goat anti-mouse Alexa Fluor 488 IgG, Life Technologies), diluted at 1/100e in blocking solution, was incubated for 3 days at RT under mild agitation. After 24 h of washes in PBS, Ki67+ cells reflecting proliferative cells were visualized by 2D (Operetta) or 3D imaging (SPIM) as described in the previous sections.

2.6. Determination of Cell Death by Flow Cytometry

After 3 or 6 days of treatment, 3 ULA-MALC were pooled, mechanically dissociated, washed in PBS and transferred into FACs analysis tubes. Of 7-aminoactinomycin D (7AAD, BD Biosciences, Le Pont de Claix, France) 5 µL was then added according to the manufacturer's instructions and dissociated cells were analyzed on a LSRII flow cytometer (BD Biosciences). Dead cells ($7AAD^+$) versus living cells (7AAD) were analyzed by Cytobank.

2.7. Determination of Cell Viability by Trypan Blue Assay

After 3 or 6 days of culture, five pooled ULA-MALC were mechanically dissociated and cells were counted by trypan blue assay on a Malassez cell. The cell viability was determined with the formula: % of viability = (number of live cells/(number of live cells + number of dead cells)) × 100 where dead cells incorporate trypan blue.

2.8. Statistics

For all the results obtained and presented in Figures 1–6 and Figures S1–S4, we applied various statistical analysis. Data shown Figures 1 and 2 and Figure S1 are means ± SD. For comparing three or more parameters, one-way ANOVA was used in Figures 3 and 4, Figures S3 and S4 whilst side-by-side Mann–Whitney tests were used in Figure 6. All tests were performed with GraphPad Prism software. p values: **** = $p < 0.0001$, *** = $p < 0.0005$, ** = $p < 0.01$ and * = $p < 0.05$.

3. Results

3.1. Determination of Optimal Cell Seeding Density for ULA-MALC Formation

Cell seeding density to perform 3D cultures can influence cell behavior and drug response [20,22], we therefore tested several conditions for optimizing ULA-MALC formation. ULA-MALC were first established with the RL t(14;18)-positive B-NHL cell line at 2500, 5000 or 10,000 cells/well and were morphologically observed during several days

of culture (Figure 1). For all cell seeding densities, rapid and constant growth of single ULA-MALC per well was observed with a compact and round-type morphology that was apparently stable from day 3 to day 8 (Figure 1A). Parameters classically used for spheroid characterization such as sphericity, roundness, solidity and area (assuming that ULA-MALC were perfect spheres, see Material and Methods) were analyzed after bright field imaging and determined according to [22] (Figure 1B). The area varied between 0.08 and 1.5 mm^2 from day 1 to day 8 of culture for 2500, 0.12 and 1.52 mm^2 for 5000 and 0.19 and 1.9 mm^2 for 10,000 cell densities. For all densities, ULA-MALC appeared spherical (SI > 0.9) and circular (RI > 0.9) with a regular surface (solidity index > 0.9) during cell culture. These culture conditions ensured the low variability required for in vitro assays as previously commented [10,32,33]. Cell death was determined on whole ULA-MALC by 2D imaging (Figure 1C) or on dissociated ULA-MALC using flow cytometry (Figure 1D). After 6 days of culture, ULA-MALC developed with 2500 or 5000 seeding concentrations exhibited a very low level of cell death as attested by the determination of PI area and intensity and $7AAD^+$ cells (less than 10%). However, with 10,000 cells, we observed an increase in basal cell death and result variability as attested by the higher standard deviation. After 9 days of culture, cell death increased in a concentration dependent manner with a higher variability.

Altogether, 2500–5000 cells would be the optimal cell seeding to modelize a well formed RL-ULA-MALC up to 6 days of culture. Similar results were obtained with three other t(14;18)-positive B-NHL cell lines (DOHH2, WSU-NHL and SC-1) (Figure S1). However, ULA-MALC performed with RL were more cohesive, thus prompting us to pursue our investigation with this cell line.

3.2. Biological Characterization of ULA-MALC

Live imaging performed in the first hours of culture showed that RL cells (2500 cell seeding density) aggregated spontaneously after the centrifugation step (day 0) (Figure 2A, insert) and then entered into a spheroidization process [13] consisting of aggregate compaction with an observable decrease of ULA-MALC size during the first days of culture followed by a constant growth (Figure 2A). For longer culture times, round-type morphology was still observed with a ULA-MALC diameter evolving between 320 µm at day 1, 500 µm at day 3, 1200 µm at day 6 and 1320 µm at day 8 (Figure 2A). Cell viability oscillated between 90 and 100% during the first 6 days of culture and then decreased after 8 days of culture (Figure 2B). The number of living cells per ULA-MALC increased from roughly 6000 cells at day 1 to approximately 32,000 cells at day 3, exponentially reaching 150,000 cells/ ULA-MALC after 8 days of culture (Figure 2C). At this cell density, the MALC area exponentially grew from 0.085 mm^2 at day 1 to 1.6 mm^2 at day 8 of culture (Figure 2D), concomitantly with its diameter (Figure 2E). Visualization of proliferative cells in whole ULA-MALC was determined by Ki67 detection after 3 or 6 days of 3D culture (Figure 2F). Ki67 labeling was homogeneously distributed thus showing that, in contrast to solid cancers [34–37], no regionalization of proliferation appeared in the t(14;18)-positive B-NHL cell 3D model in these conditions.

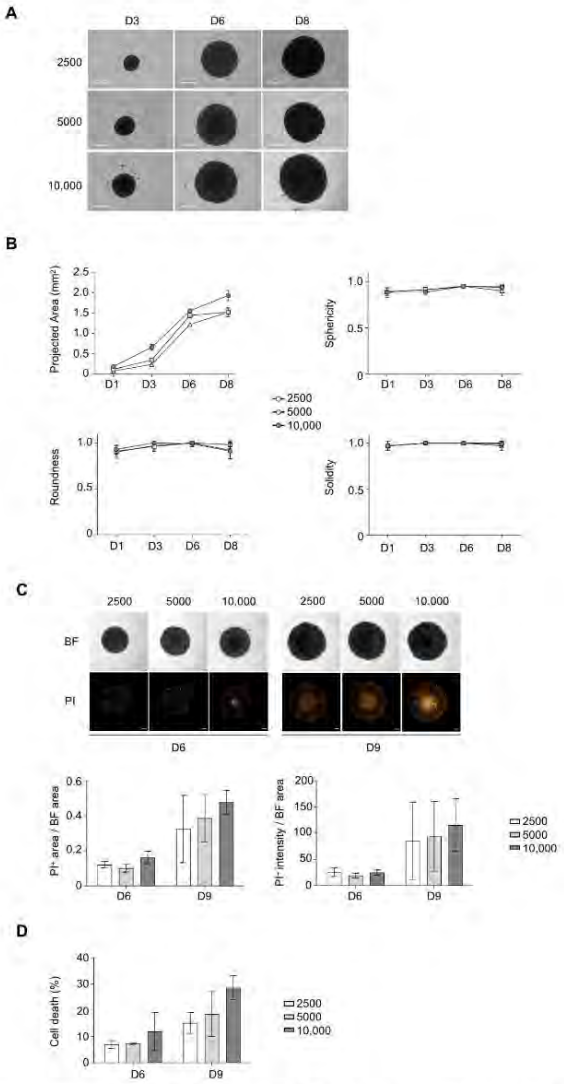

Figure 1. Influence of cell density on ultra-low attachment (ULA)-multicellular aggregates of lymphoma cells (MALC) biology. ULA-MALC established with RL cells was cultured at different cell seeding densities (2500; 5000 and 10,000 cells) and different biological characteristics were determined at different culture times. (**A**) Growth and morphology observed by bright field (BF) microscopy at 4× after 3, 6 and 8 days (D) of culture. Scale: 500 µm. These pictures are representative of 3 independent experiments each comprising 6 individual ULA-MALC. (**B**) Morphological properties (projected area, sphericity, roundness and solidity) determined after 1, 3, 6 and 8 days (D) of culture by 2D imaging analysis with the specific macro developed (see Material and Methods section). These graphs are the mean ± SD of $n = 3$ independent experiments each comprising at least $n = 10$ individual ULA-MALC. (**C**) Cell death visualization and quantification on whole ULA-MALC at day 6 and 9 following propidium iodide (PI) labeling and 2D imaging. Experiment performed on 3 independent experiments each comprising 7 individual ULA-MALC. Upper panel, representative pictures of bright field (BF) or propidium iodide (PI) at 5× magnification, scale: 200 µm. Lower panel, mean ± SD of the ratio of area or intensity of propidium iodide (PI) in relation to the bright field (BF) area. (**D**) Cell death quantification by flow cytometry after 7AAD labeling of dissociated MALC. This graph represents mean ± SD of the percentage of cell death (7AAD+) measured in 3 independent experiments of 3 pooled ULA-MALC.

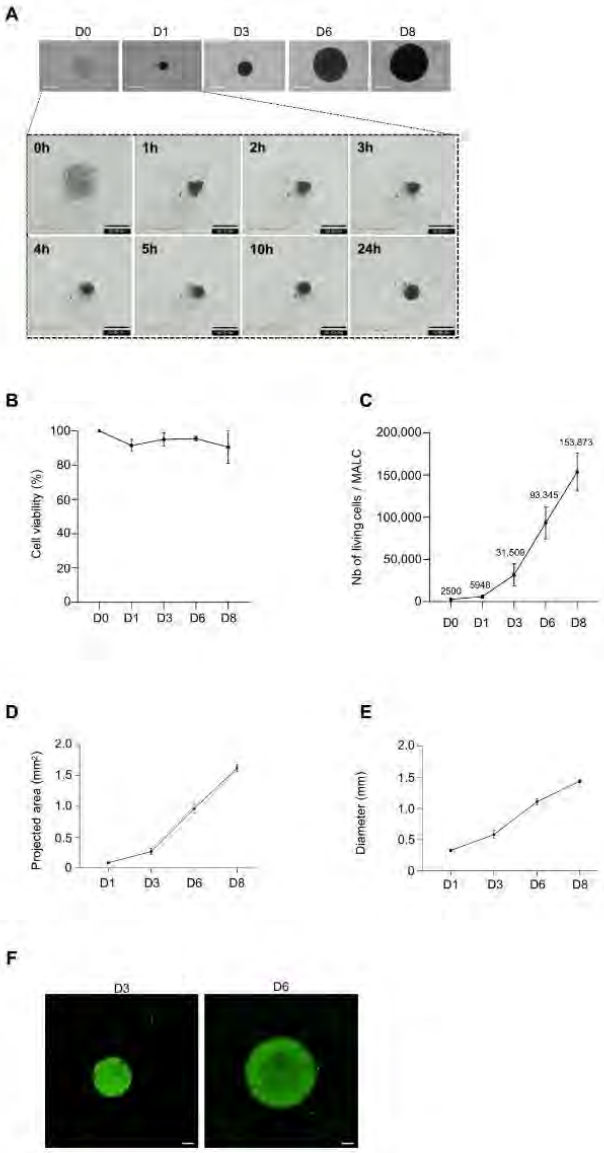

Figure 2. Two-dimensional characterization of ULA-MALC at 2500 cell seeding density. ULA-MALC established with RL cells were cultured at 2500 cell seeding density and observed at different times (D = day) by 2D imaging. (**A**) Upper panel, bright field (BF) pictures of ULA-MALC observed from day 0 to day 8 with an inverted microscope. Magnification 4×, scale 500 µm. Lower panel, ULA-MALC aggregation observed during the first 24 h at the indicated times (h = hour). Magnification: 4×, scale: 500 µm. Pictures are representative of 3 independent experiments each comprising 30 individual ULA-MALC. (**B**) ULA-MALC viability determined by Trypan blue exclusion assay. Results are expressed in percentage of viable cells in relation to day 0 (D0) and represent the mean ± SD of 3 independent experiments each comprising at least 11 individual ULA-MALC. (**C**) Living cells in ULA-MALC determined by Trypan blue exclusion assay. Results are expressed in number (Nb) of living cells per ULA-MALC and represent the mean ± SD of 3 independent experiments each comprising at least 11 individual ULA-MALC. Exact number of live cells is presented in the figure at each culture time. (**D**,**E**) Projected area (D) and diameter (E) of ULA-MALC measured at day 1, 3, 6 and 8 of culture by 2D imaging at 4× magnification. These graphs represent the mean ± SD of 3 independent experiments each comprising at least 30 individual ULA-MALC. (**F**) Ki67 labeling visualized 2D imaging (magnification 5×, scale: 200 µm) on whole ULA-MALC at day 3 and 6 of culture. Pictures are representative of 2 independent experiments each comprising 3 individual ULA-MALC.

All spheroid morphological parameters including area, roundness, circularity, sphericity and solidity extracted from 2D imaging were over 0.8 and stable over time (Figure S2).

Altogether, our ULA method maintains the viability of RL cells in 3D and spheroid morphological features over time.

3.3. Determination of Optimal Cell Density for Drug Testing

Spheroids are relevant and powerful models for testing drug sensitivity compared to cell suspension cultures [6,13,38–40]. In order to evaluate the most favorable cell seeding density for the drug assay, we first tested ABT-199 (a Bcl2 inhibitor) a classical apoptosis inducer in FL. Global morphology was observed by bright field imaging and cell death determined by propidium iodide labeling on entire ULA-MALC with an automated confocal microscope. After 3 days of treatment, ABT induced a concentration-dependent reduction of ULA-MALC size at the three different cell seeding densities tested, compared to the untreated condition (Figure 3A). These effects were more pronounced after 6 days of treatment (Figure S3). The basal level of cell death observed in the untreated condition was also increased confirming results obtained by flow cytometry (Figures 1C and 3A). Several morphological parameters were extracted such as area, and cell death induction estimated by the area and intensity of incorporated propidium iodide. After 3 days of treatment at a 2500 cell seeding density, ABT-199 at 100 nM induced a significant reduction of ULA-MALC area compared to the untreated condition (Figure 3B). This was concomitant with an increase of cell death as attested by the increase of propidium iodide area and intensity (Figure 3C). Flow cytometry performed on dissociated ULA-MALC confirmed that ABT-199 induced cell death ($7AAD^+$ cells) in a dose-dependent manner (Figure 3D). Experiments performed with 5000 or 10,000 cells exhibited similar results suggesting that cell density did not influence ABT-199 responses (Figure 3).

Altogether, these experiments showed that 2500 cells represent the most suitable cell seeding density for developing regular, spherical ULA-MALC exhibiting a very low basal level of cell death.

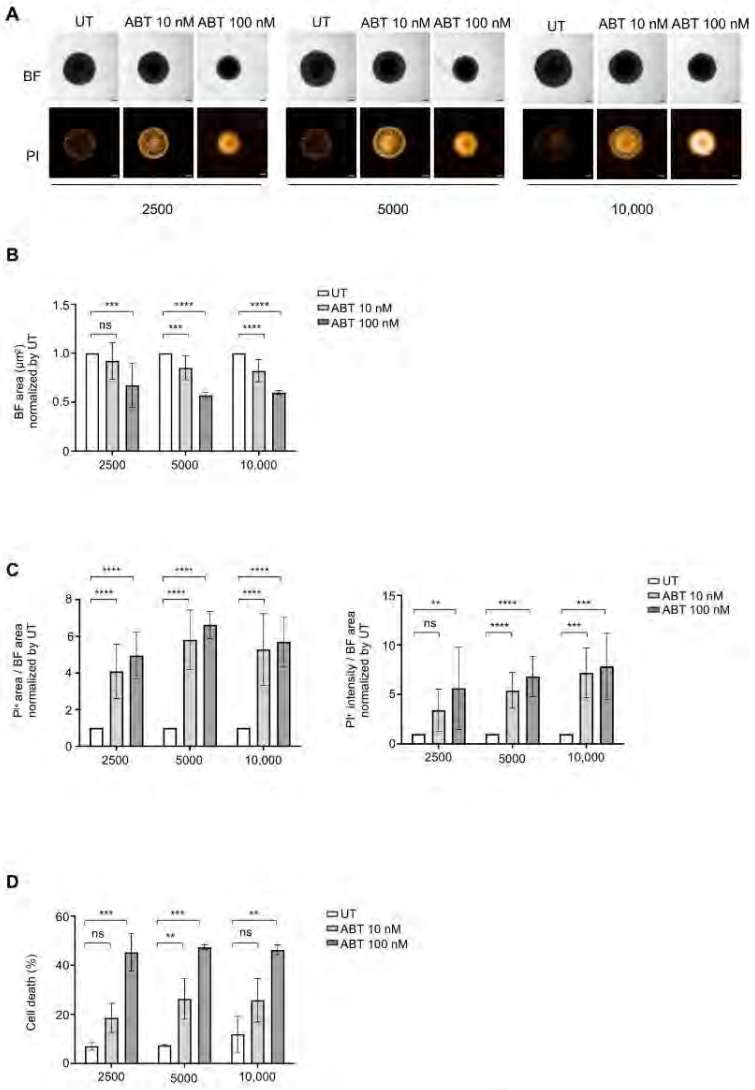

Figure 3. Influence of cell density on drug response after 3 days of treatment. ULA-MALC were seeded at different cell densities (2500; 5000 and 10,000 cells) and treated or not (UT) at day 3 of culture with ABT-199 (ABT) at 10 nM and 100 nM. Cell death was visualized and measured 3 days post-treatment (i.e., D6 of culture). Results are representative (pictures) or the mean ± SD (graphs) of 3 independent experiments each comprising 5 individual ULA-MALC. *p* values: **** = $p < 0.0001$, *** = $p < 0.0005$ and ** = $p < 0.01$ (**A**) Global morphology (BF) and propidium iodide (PI) labeling were visualized by 2D imaging, 5× magnification and scale: 200 µm. (**B**) Bright field (BF) area measured after 3 days of treatment. Results represent the mean ± SD of the global BF area normalized to the untreated condition (UT). (**C**) Quantification of cell death after propidium iodide (PI) labeling on whole ULA-MALC cultured at 2500, 5000 and 10,000 cell seeding densities and treated or not (UT) with ABT-199. PI area in relation to BF area (left panel) and PI intensity in relation to BF area (right panel), all normalized to the untreated condition (UT). (**D**) Cell death measured by flow cytometry in dissociated ULA-MALC cultured at 2500, 5000 and 10,000 cell seeding densities and treated or not (UT) with ABT-199. Results represent the mean ± SD of the percentage of cell death ($7AAD^+$).

3.4. Drug Sensitivity Testing

We then determined whether the ULA-MALC model was adapted for a larger scale drug testing assay. Thus, we tested five different drugs known to directly target different pathways in FL [2,41] and determined their efficacy based on: i) their impact on morphology (area and roundness) measurable on entire ULA-MALC and ii) cell death induction quantified in a dissociated or whole 3D model. Each molecule was also tested in the presence of RTX or GA101 as used in the clinic [2,42]. Here we detailed the results obtained after 3 days of treatment (Figure 4). Observation of ULA-MALC by bright field microscopy (Figure 4A) and analysis of area (Figure 4B left panel) using an automated confocal microscope revealed that all drugs, except ibrutinib, strongly reduced ULA-MALC area compared to the untreated condition. RTX and GA101 alone had a potent effect on the area by reducing BF area by 62% and 73% respectively. However, a combination with drugs did not enhance their effect. Roundness was only affected when drugs were combined with GA101 (except for ibrutinib) (Figure 4B, right panel). Moreover, we were able to visualize (Figure 4A) and quantify (Figure 4C) propidium iodide incorporation in whole ULA-MALC treated or not with anti-CD20 mAbs combined with drugs. At the basal level, we observed propidium iodide labeling mainly in the periphery of the ULA-MALC. This pattern was similar in lenalidomide, ibrutinib and bendamustine treated conditions. However, in ULA-MALC treated with the rapamycin/anti-CD20 mAbs combination, doxorubicin and, as expected, in the positive control (ABT-199), propidium iodide distribution was more potent and diffuse. Anti-CD20 mAbs induced a diffuse propidium iodide distribution in ULA-MALC with a more potent labeling in the periphery in the presence or absence of drugs (Figure 4A). Propidium iodide intensity and propidium iodide area were determined in whole ULA-MALC. Except for GA101, none of the drugs tested induced an increase in cell death (Figure 4C). However, when cell death was measured by flow cytometry in dissociated ULA-MALC, we were able to detect an increase in $7AAD^+$ cells in doxorubicin and bendamustine treated ULA-MALC. Combination of RTX or GA101 with drugs did not modify the effects induced individually (Figure 4D). Although day 9 of culture exhibited a higher acceptable basal level of cell death (10% at 2500 cell seeding density) and result variability (Figure 1C,D), we also evaluated the effect of drugs after 6 days of treatment (Figure S4). A similar pattern was observed for bright field area with an effect observed for all drugs except ibrutinib. However, after 6 days of treatment, doxorubicin and bendamustin alone induced a significant decrease in ULA-MALC roundness that was not accompanied by propidium iodide intensity or area variation. Indeed, no variation in propidium iodide area was observed in all the conditions tested. In contrast, for some conditions such as RTX alone or in combination with rapamycin, and GA101 combined with rapamycin, ibrutinib or bendamustin, propidium iodide intensity significantly increased compared to the untreated condition (Figure S4). These discrepancies prompted us to develop 3D imaging and specific analysis to better characterize the 3D t(14;18)-positive B-NHL model and drug effects.

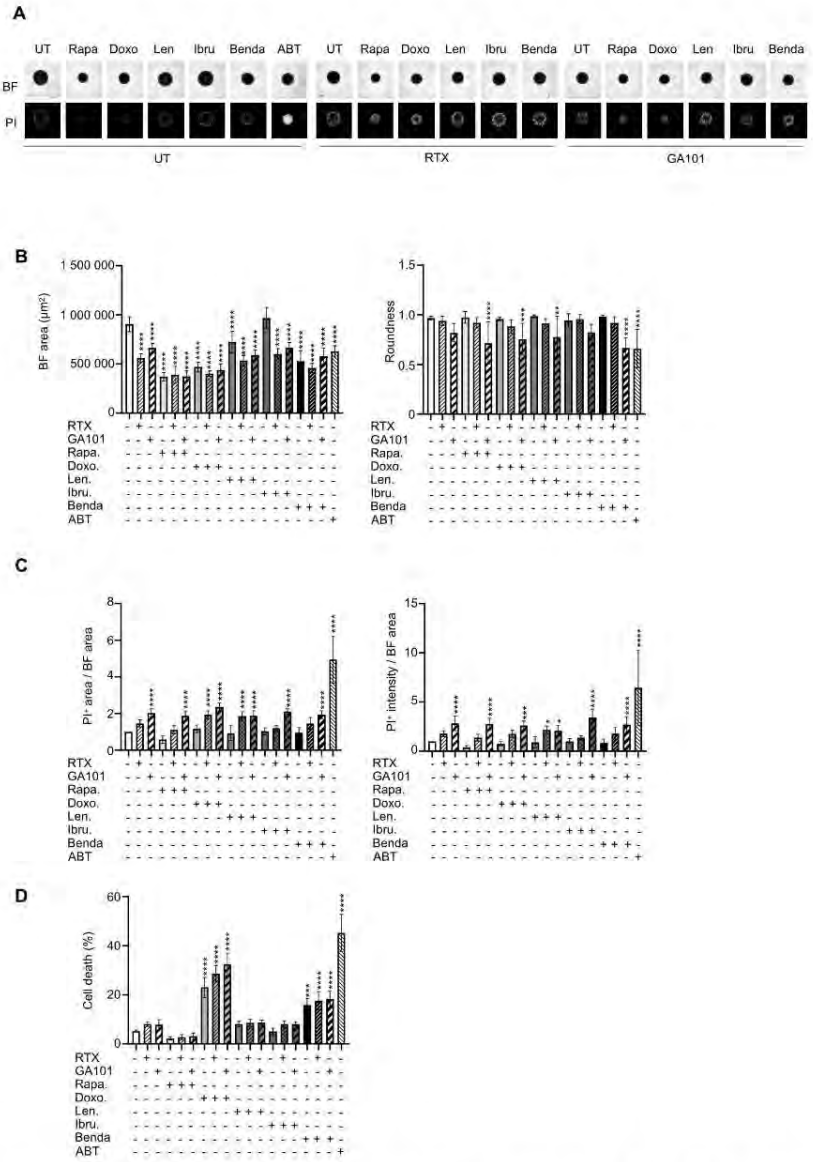

Figure 4. Drug response of ULA-MALC after 3 days of treatment. ULA-MALC were seeded at 2500 cells and treated or not (UT) after 3 days of culture with rapamycin (Rapa, 10 nM), doxorubicin (Doxo, 0.1 µM), lenalidomide (Len, 5 µM), ibrutinib (Ibru, 500 nM), bendamustine (Benda, 10µg/mL) in combination or not with rituximab (RTX) or GA101 (10 µg/mL). ABT-199 (ABT) at 100 nM was used as the positive control. Figures represent results obtained after 3 days of treatment and are representative (pictures) or the mean ± SD (graphs) of 3 independent experiments each comprising 5 individual ULA-MALC. *p* values: **** = $p < 0.0001$, *** = $p < 0.0005$, ** = $p < 0.01$ and * = $p < 0.05$. (**A**) Visualization of global morphology (BF) and propidium iodide (PI) labeling by 2D imaging, 5× magnification and scale: 200 µm. (**B**) Bright field (BF) area and roundness determined by 2D imaging analysis with the specific macro developed (see the Methods section). Results represent the mean ± SD. (**C**) Cell death quantification after PI labeling by 2D imaging on whole ULA-MALC. Results represent the mean ± SD of PI area in relation to BF area (left) and PI intensity in relation to BF area (right), all normalized to the untreated condition. (**D**) Cell death quantification by flow cytometry in dissociated ULA-MALC. Results represent the mean ± SD of the percentage of cell death ($7AAD^+$).

3.5. Three-Dimensional Imaging to Characterize the 3D Model

High-resolution images of intact spheroids, especially the inner layers, are very difficult to obtain by classical fluorescent microscopy, or confocal microscopy, due to the thickness of the model [43]. Classical optical microscopes allow a penetration depth of approximately 50–100 µm whilst the ULA-MALC diameter thickness varied between 325 and 1435 µm from day 1 to day 8 at 2500 cell seeding density suggesting an important thickness (Figure 2E). Thus, in depth 3D imaging using a light sheet fluorescent microscope (LSFM or SPIM for selective plane illumination microscope), which allows the highest penetration depth (>1 cm) compared to other optical sectioning microscopes [44], was necessary to achieve an in depth characterization of such a 3D model. Central image of SPIM z-stack showed a homogeneous cell distribution within ULA-MALC from day 1 to day 4, but at day 5 and day 6 we observed a difference of cell density between the peripheral layers of the ULA-MALC compared to the inner layers (Figure 5A, top panel). IMARIS tridimensional reconstruction of SPIM z-stack acquisitions from day 1 to day 6 allowed the visualization of the 3D structure of ULA-MALC and its evolution over time (Figure 5A, bottom panel). From day 1, the RL 3D model exhibited a flat side, a morphological feature impossible to observe by 2D imaging, suggesting that ULA-MALC were not perfectly spherical, in contrast to what we expected based on 2D imaging analysis (Figure 1C, SI > 0.9). This shape allowed us to define a maximum thickness/height starting from the flat bottom to the round top on a side view and a maximum diameter from a top view (Figure 5B). On day 1, thickness and diameter were close: 265 µm and 360 µm respectively (Figure 5B). Over time, ULA-MALC grew keeping this flat bottom, resembling a half sphere, and from day 4, the top of MALC began to flatten, with an exacerbation of the process at day 5 and day 6 (Figure 5A). These observations were confirmed by thickness and diameter quantifications (Figure 5B), with a thickness of MALC increasing up to day 3 (390 µm) and then decreasing over time (310 µm at day 6) whilst the diameter increased consistently, from 550 µm at day 3 to 1300 µm at day 6. These data suggested that this model reached a structural limitation in terms of thickness at 3 days of culture at this cell density, and increased only in terms of diameter after day 3. Although 2D imaging allowed the morphological characterization of ULA-MALC, 3D imaging and specific analyses appeared more adapted and necessary to study this model in more detail. Ki67 visualization at different layers from the top to the bottom (one image every 70 µm) confirmed the results obtained in Figure 2F where we observed a homogeneous distribution of proliferative cells in the whole ULA-MALC at day 3 of culture (Figure 5C and video S1).

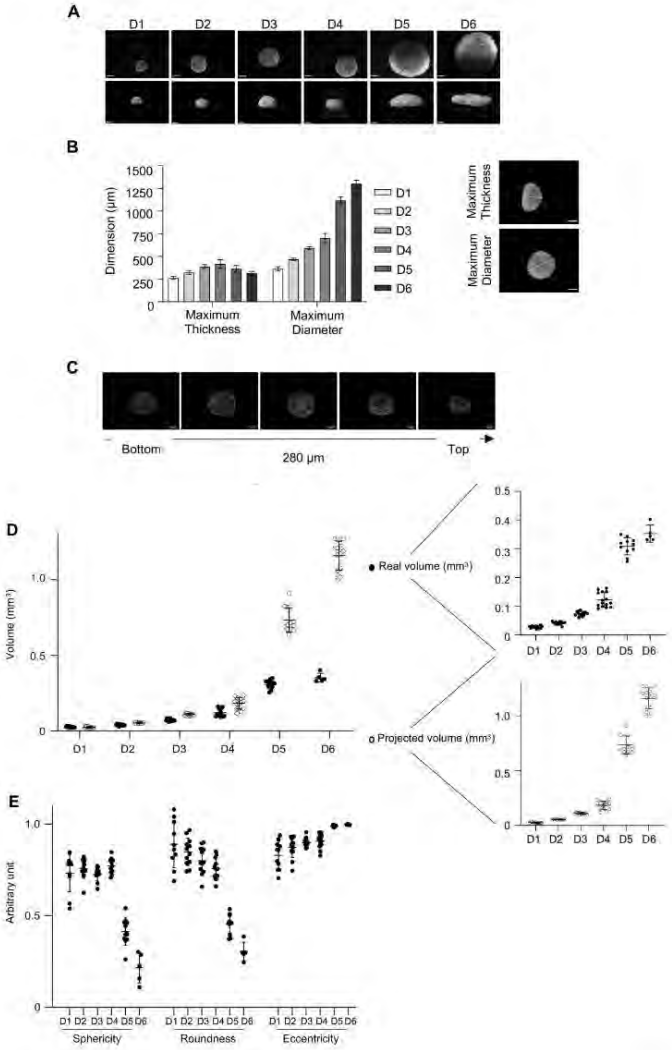

Figure 5. Three-dimensional characterization of ULA-MALC. ULA-MALC were cultured at a 2500 cell seeding density and observed at different times (D = day) by selective plane illumination microscope (SPIM) microscopy. (**A**) Pictures of center (upper panel) and 3D representation (lower panel) of ULA-MALC cultured during the indicated times (5× magnification, scale: 200 µm). These pictures are representative of 12–15 individual ULA-MALC (depending on the condition). (**B**) Quantification of maximum thickness and maximum diameter of ULA-MALC cultured during the indicated times. Histograms represent the mean ± SD of 12–15 individual ULA-MALC (depending on the condition). Insert, representative images of ULA-MALC at day 3 of culture (5× magnification, scale 200 µm). The white line represents the maximum thickness (upper) and maximum diameter (lower) used for quantification. (**C**) Ki67 labeling visualization by 3D imaging in ULA-MALC at day 3 of culture. Images were extracted from SPIM z-stack, from the bottom (left) to the top (right) of the MALC with a difference of 70 µm between them. Magnification 5×, scale: 200 µm. These pictures are representative of 2 independent experiments comprising 3 individual ULA-MALC. (**D**) Projected and real volumes of ULA-MALC after different days (D) of culture. Results are presented on global (left) or individual graphs (right) and are expressed by the mean ±SD of 5–15 individual ULA-MALC (depending on the condition). (**E**) Sphericity, roundness and eccentricity measured on ULA-MALC cultured during the indicated times (D = day). The graph represents the mean of each parameter ± SD of 5–15 individual ULA-MALC (depending on the condition).

The particular shape of MALC required dedicated quantification from 3D images to assess specific morphological properties. Thus, by developing dedicated algorithms, we were able to quantify the "real volume" and morphological properties of ULA-MALC over time. ULA-MALC real volume increased progressively from day 1 (0.028 mm^3) to day 3 (0.069 mm^3) and more rapidly at day 4 (0.14 mm^3) and day 5 (0.30 mm^3), doubling every 24 h (consistently with exponential cell proliferation, see Figure 2C), and slowing down at day 6 (0.35 mm^3) (Figure 5D). Projected volume obtained with 2D imaging was dramatically different with an overestimation, especially from day 4 to day 6. Indeed, at day 6 of culture for example, real volume was 0.35 mm^3, whilst the projected volume was estimated at 1.15 mm^3 (Figure 5D).

The quantification of morphological properties confirmed that ULA-MALC were not perfect spheres as early as day 1, exhibiting a sphericity comprised between 0.72 and 0.78 and roundness between 0.75 and 0.88 from day 1 to day 4. After 5 days of culture, sphericity and roundness strongly decreased, with values dropping down to 0.25 and 0.23 respectively at day 6 (Figure 5E). With 2D images these values were close to 1 for both parameters (Figure 1B). We were also able to measure the eccentricity and showed an important ellipsoid deformation (very close to 1 at day 5 and day 6), in line with the drop in sphericity and roundness (Figure 5E). These results showed that both volume and sphericity dramatically changed between day 4 and day 5 with a huge increase in the real volume measured concomitantly to a potent loss in sphericity.

Altogether, the different results obtained from inverted and light sheet microscopes underlined the critical necessity to develop specific 3D imaging and dedicated analyses to realistically characterize the morphological properties of a 3D model.

3.6. Three-Dimensional Imaging to Evaluate Drug Sensitivity

Finally, we evaluated by SPIM the real direct effect of drugs after 3 days of treatment on whole ULA-MALC (Figure 6). Observation of the central image of SPIM z-stack (Figure 6A, top panel) showed that GA101 and ABT-199 treatment reduced the MALC diameter, although the peripheral cell layers were still more dense than the inner layers compared to the untreated condition. In contrast, we observed a potent decrease in volume after rapamycin treatment with a homogeneous effect on the ULA-MALC. This result, associated with the poor cell death induced by rapamycin (Figure 4), strongly suggests that this drug had a cytostatic effect on ULA-MALC, slowing the growth whereas the other drugs seemed to be cytotoxic. IMARIS tridimensional reconstructions of SPIM z-stack acquisitions confirmed that drug treatment altered the shape and volume of ULA-MALC (Figure 6A, bottom panel). Interestingly, GA101 seemed to compact the 3D structure as attested by the 3D reconstruction and central image from SPIM z-stack compared to the untreated condition, whilst the appearance of the rapamycin treated MALC was very close to the day 3/day 4 untreated ULA-MALC (Figure 5A). 3D image analysis showed that all the drugs did not significantly affect ULA-MALC thickness except for GA101 and ABT-199 100 nM for which we observed a slight increase (Figure 6B). In contrast, the diameter was significantly reduced after all treatments compared to untreated ULA-MALC with the highest effect observed in the presence of GA101 (Figure 6B). This was consistent with the impact on ULA-MALC growth observed by 2D imaging (Figure 4). Real volume quantification exhibited a significant and drastic drop induced by all treatments compared to untreated ULA-MALC (<0.15 mm^3 vs. 0.35 mm^3) (Figure 6C). Once again, the projected volume calculation led to a global overestimation in untreated and treated conditions, although the tendency was the same as for the real volume (drug treatments decrease MALC volume). However, more importantly, compared to real volume, it highlighted greater differences between untreated/treated conditions and between the different treated conditions (Figure 6C). Thus, volume quantification based only on diameter could potentially lead to important misinterpretations of drug effects in such 3D models.

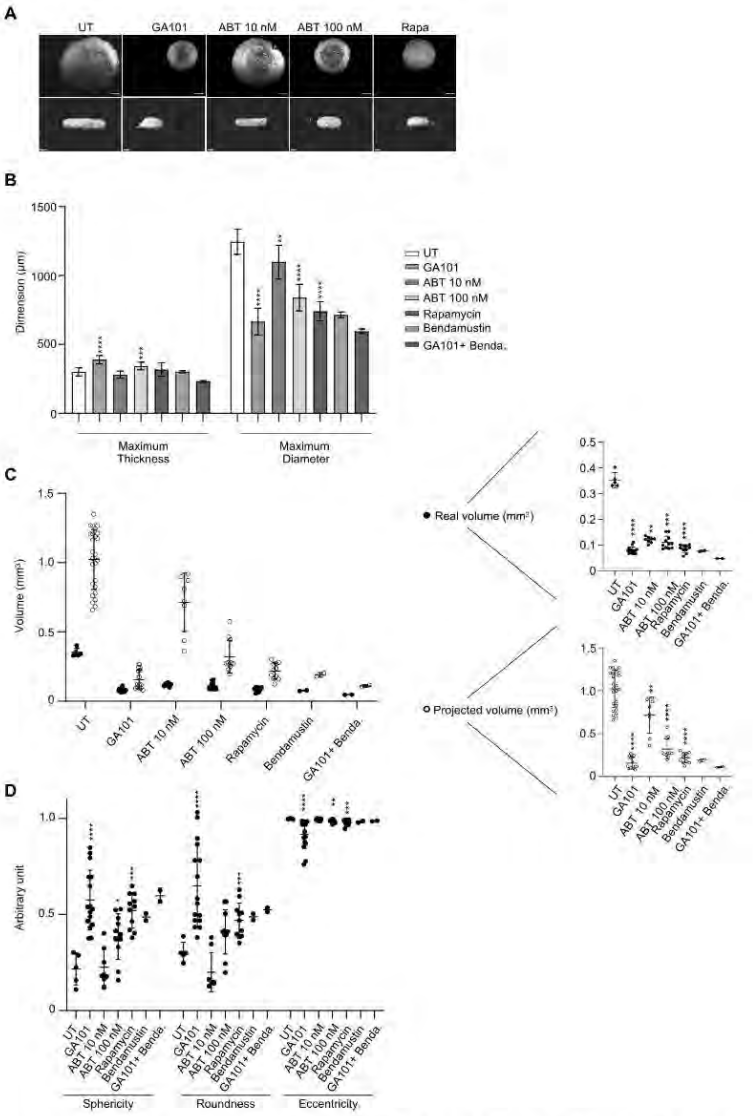

Figure 6. Three-dimensional characterization of drug effect. ULA-MALC (2500 cell seeding density) at day 3 of culture were treated or not (UT) with GA101 (10 µg/mL), ABT-199 (ABT, 10 or 100 nM), rapamycin (Rapa 50 nM), bendamustine (Benda 10 nM) and observed after 3 days by SPIM microscopy. *p* values: **** = $p < 0.0001$, *** = $p < 0.0005$, ** = $p < 0.01$ and * = $p < 0.05$. Bendamustin and GA101 + Bendamustin conditions were excluded from statistical tests due to a low number of replicates ($n = 2$). (**A**) Pictures of center (upper) and 3D representation (lower) of ULA-MALC treated or not (UT) with the indicated drugs (5× magnification, scale: 200 µm). These pictures are representative of 5–6 independent experiments comprising 8–25 individual ULA-MALC (depending on the condition). (**B**) Quantification of maximum thickness and maximum diameter of treated or not (UT) ULA-MALC. Histograms are the mean ± SD of 1–6 independent experiments comprising 2–25 individual ULA-MALC (depending on the condition). (**C**) Projected and real volumes of ULA-MALC treated or not (UT) with different drugs. Results are presented on global (left) or individual graphs (right) and are the mean ± SD of 1–6 independent experiments comprising 2–25 individual ULA-MALC (depending on the condition). (**D**) Sphericity, roundness and eccentricity of ULA-MALC treated or not (UT) with different drugs. The graph represents the mean of each parameter ± SD of 1–6 independent experiments comprising 2–11 individual ULA-MALC (depending on the condition).

In contrast, in 2D imaging, we showed that GA101, ABT-199 100 nM and rapamycin significantly increased sphericity (GA101, ABT-199 100 nM, rapamycin) and roundness (GA101 and rapamycin) (Figure 6D). The magnitude of this increase was consistent with the effect on ULA-MALC volume with the highest effect observed in GA101-treated MALC (Figure 6C). The effect of these drugs on these parameters was inversely correlated with their effect on eccentricity in agreement with our observation on thickness (Figure 6B). With regard to GA101, the effect was probably due to its potent cell aggregation property [45].

In conclusion, 3D characterization of treated ULA-MALC revealed important information as to drug effects on structuration, shape, volume and morphology. Although 2D imaging only allowed the observation of cytostatic or cytotoxic effects, 3D imaging highlighted other drug specific characteristics.

4. Discussion

Three-dimensional cultures are essential for cancer research as they allow cellular responses that more closely mimic those occurring in patients compared to cell suspension cultures. As their characteristics are closer to the native tumor microenvironment [3,46], these models represent powerful tools for studying pathology and drug efficacy. Techniques developed for 3D structure formation are numerous and depend on the type of experiment performed, but can be divided in two main types: scaffold-based and scaffold-free techniques. Both methods exhibit advantages and disadvantages explained in a very recent review [8]. These techniques are generally well documented in solid cancer cells with many articles dedicated to this field of research. However, this is not the case for lymphoma research, which benefits from a reduced number of publications (less than 150 referenced in PubMed). We are pioneers in the development of 3D models using t(14;18)-positive B-NHL cell lines and the HD technique to develop MALC (HD-MALC). Although this gave us a better understanding of the influence of spatial organization on gene and protein expression, drug distribution and efficacy in the presence or absence of immune cells [14–18], we cannot exclude that the addition of MC to favor cell aggregation does not influence cell signaling or behavior. Indeed, this may directly lead to alterations in growth and drug responses. To our knowledge, no study to date, has investigated the direct influence of MC, but, based on renal cell carcinoma cell line studies, it is known that both cell–cell interactions and O_2 diffusion may be affected [47]. Another important point to consider is the use of 24-well plates in the HD method, which is not adapted for drug testing assays. Indeed, the transfer from the drop into agarose-coated wells was very difficult to perform. Considering both arguments, we adapted a scaffold free technique to our model using the ULA method and a centrifugation step allowing 100% of MALC formation. With this technique, cells do not display differences in gene and mutation expression profiles compared to the HD technique and 2D culture. Spheroids are not stressed by transfer, avoiding the risk of damaging the 3D structure. Moreover, ULA-MALC is centrally located in a non-agarose precoated well, which facilitates imaging. Altogether, this method seems to be reliable, robust, simple, it can be standardized and easily used for medium/high throughput screening for lymphoma therapies as described in solid cancers by others [6,10]. However, this is important to note that this model established with t(14;18)-positive B-NHL does not account for the contribution of the microenvironment and may be more representative of aggressive/transformed NHL, which can proliferate independent of surrounding cells. Nevertheless, it can be complexified by adding immune cell such as gamma delta T lymphocytes [17], NK cells [18] or cells from the tumor microenvironment such as macrophages or dendritic cells.

We determined the most appropriate seeding cell density for ULA-MALC formation based on morphological parameters visualized by phase contrast microscopy and extracted with a macro adapted from Ivanov and colleagues [13]. ULA-MALC grew fast, and appeared round, spherical and regular when their indexes were higher than 0.9 according to Zanoni [13] and Santo [48], for all densities tested. We observed a slight drop in spheroid roundness after 6 days of culture when 10,000 cells were used to elaborate the ULA-MALC.

As described by Gong and colleagues [49], this may be due to an increase in cell death as observed on entire ULA-MALC after PI staining or dissociated ULA-MALC after 7AAD labeling. Cell death is a physiological phenomenon in spheroids due to the absence of vasculature, the presence of a hypoxic core and cells at different stages of maturation in different locations (viable, proliferative and quiescent) [12,35]. The drop of roundness was also correlated with an increase in the total spheroid area and an increase of SD attesting a higher variability between the experiments when this cell density was used. Thus, the 2500 cell seeding density and day 3 of culture appear to be the most adaptable for drug treatment as viable cells are homogeneously distributed and this avoids the loss of sphericity and compactness.

ULA-MALC enters rapidly in a spheroidization process exhibiting a round-type morphology probably due to strong cell–cell interactions [13]. Moreover, ECM, which is increased in 3D compared to 2D t(14;18)-positive B-NHL cell culture [15], may ensure total compactness. This was not the focus of our study, but it would be interesting to investigate the kinetics of ECM production in ULA-MALC and to determine its role in the spheroidization process. Three-dimensional culture may influence the response to treatment. In solid cancers, it is well established that 3D cultures are more resistant than cell suspensions because of the lower drug accessibility, the activation of genes involved in survival and drug resistance in response to hypoxia and the low rate of proliferating cells (for drugs that are active against proliferating cells) [8]. In t(14;18)-positive B-NHL, we observed that the response to anti-CD20 mAbs was different between 3D cultures (HD-MALC) and 2D cultures [15]. In this study, we investigated whether the density could impact direct drug responses using a classical inhibitor of FL cells. ABT-199 was efficient in decreasing area and cell death in ULA-MALC whatever the seeding cell density used. This confirms that cell density and/or spheroid diameter does not influence the drug response. The mechanisms that could explain the discrepancies between solid and hematological cancers are not known. For small pharmacological inhibitors, the drug can homogeneously penetrate spheroids whatever its volume and induce a similar effect. However, unpublished data from our group suggests that MALC volume strongly influences anti-CD20 mAbs efficacy reflecting pre- and clinical observations [50–52].

Another critical point highlighted in our study is the level of cell death measured by flow cytometry, which did not correlate with the level observed and measured by 2D imaging. This may be due to the fact that for flow cytometry, ULA-MALC are dissociated and that the percentage of cell death is measured as the mean fluorescent intensity (i.e., 7AAD) per 50,000 cells. In contrast, for 2D imaging, the operetta system allows light to penetrate at a depth ranging from 50 to 100 µm. The fluorescent intensity (propidium iodide) measured therefore represents the accumulation of signal that the microscope can get from the first layers of the ULA-MALC. Moreover, although we can acquire several images at different levels on the z-axis (z-stack) and achieve a maximum projection with the associated software (Columbus), we can only obtain partial information corresponding to the top of the sample, leading to misinterpretation. The Operetta system is considered to be a high-content imaging system, providing high-resolution, high sensitivity and high speed required for 3D cell-culture model imaging. With our study, we identified two major limitations for ULA-MALC imaging using this equipment. Firstly, our system is not equipped with a water immersion objective and secondly, ULA-MALC are not cleared, which strongly limits the penetration. Clearing methods are numerous, aqueous or solvent-based, and necessary for in depth imaging of large samples such as spheroids [53,54]. They have been classically developed for light sheet microscopy but also for confocal and multiphoton microscopy [31,55,56]. We tried aqueous methods to attempt to clear MALC in the ULA 96 well plates but unfortunately, we did not yet obtain satisfactory results. We are still working to develop a new process allowing a global workflow in 96 well plates comprising clearing steps that avoid manipulation or transfer into new devices.

In parallel, SPIM, which exposes a sample to up to 5000 times less energy than confocal fluorescence microscopy, minimizes photo-bleaching and photo-induced cell

damage. Light sheet illumination is becoming an important tool for spheroid, organoid, tissue and small animal imaging. It holds great promises for the analysis of large numbers of samples with simple preparation, fast recording speed, high resolution and multi-channel fluorescence imaging [57]. High throughput screening/imaging with SPIM is under development [58,59]. This technical improvement has triggered great interest on behalf of the "spheroid community" and accessible and commercial devices are up and coming. This will bridge the gap between high content screening 2D imaging and precise in-depth 3D imaging.

With the SPIM and specifically developed algorithms, we were able to determine the real morphology of ULA-MALC, which is, in contrast to the information obtained from the automated confocal microscope, non-spherical. According to Zanoni [13], untreated ULA-MALC are not "spherical" but are more "ellipsoidal" between day 1 and day 4 and become "irregular" after 5 days of culture. This is confirmed by the 3D reconstruction observed after SPIM imaging and the increase in the eccentricity index, which mirrors the decrease in sphericity. The drop in roundness observed by SPIM during culture time corresponds to an increase in cell death and a possible lesser compaction leading to an increase in total area. We also show here that SPIM imaging is crucial to morphologically characterize the effect of drugs. Now, it should be interesting to investigate the localization of drug-induced cell death in a working window where ULA-MALC are more spherical and compact (day 2-day 4) and where images can be acquired by classical SPIM.

Here we developed a new technique to generate t(14;18)-positive B-NHL 3D cell culture that is easy to handle, inexpensive, robust and reliable. This method allows, by a simple workflow, an increase in the throughput for drug testing offering new perspectives for preclinical studies. Moreover, our study reveals potent discrepancies between the results obtained from 2D and 3D imaging and warns the scientific community as to possible misinterpretations following 2D imaging. Numerous investigations using spheroids are based on 2D imaging performed on uncleared samples without any complementary in depth characterization of the model used, nor the drug effect induced. We show here that without 3D imaging and development of specific informatics solutions, we can draw wrong conclusions.

5. Conclusions

Altogether, this study proposed a new method, imaging tools and informatic solutions developed for t(14;18)-positive B-NHL, but also warned the general spheroid community. By improving such investigations on 3D models, we contributed to the development of alternative assays to reduce animal testing and costs, which is necessary for future preclinical studies. This study opened encouraging perspectives in terms of model development for the use of coculture with immune cells to explore the activity of immunotherapy including external effectors. Moreover, this work established the methodological basis and workflow for the development of patient derived spheroids (PDLS) integrating tumor microenvironment. This may allow in the future a better B-NHL biological characterization and preclinical studies in a more relevant and complexified system better recapitulating disease heterogeneity and microenvironment contribution.

Supplementary Materials: The following are available online at https://www.mdpi.com/2072-6694/13/7/1490/s1, Figure S1: Influence of cell density on ULA-MALC biology for SC1, DOHH2 and WSU-NHL cell lines, Figure S2: Morphological 2D characterization of ULA-MALC at 2500 cell seeding density, Figure S3: Influence of cell density on drug response after 6 days of treatment, Figure S4: Drug response of ULA-MALC after 6 days of treatment, Table S1: Statistics for Figures 3, 4 and 6, Video S1: Visualization of Ki67 labeling by SPIM.

Author Contributions: F.G. and C.F. contributed equally to this work. F.G., C.F. and C.B. designed the experimental strategy, organized the experiments and collected and analyzed the data. C.B. and P.P.-G. supervised and discussed the experiments. C.F., F.G., P.G., C.R., J.B., J.G.V., C.D.-L. and A.M.-C. performed in vitro experiments. C.F. performed experiments on the operetta system, analyzed data with the Columbus software and developed a macro adapted from Ivanov. F.G. developed specific

technologies and performed experiments for SPIM acquisition, F.G. and L.P. acquired 3D images, and F.G., J.R., R.M., M.N., A.G. and J.-M.L. analyzed and discussed about the 3D SPIM data. R.M. generated the specific algorithms for 3D image processing. P.G. and J.B. performed experiments for NGS analysis and P.G. and C.L. supervised NGS analysis. J.-J.F. and L.Y. discussed about the manuscript. C.F., F.G. and C.B. wrote the manuscript. All authors discussed and approved the manuscript. All authors have read and agreed to the published version of the manuscript.

Funding: This work is part of an Interreg POCTEFA program (IMLINFO EFA281/16/). This study is also funded by Institut Claudius Regaud CLCC (CIEL, R20027BB), Région (iMALC, n°16003518) and FEDER (iMALC, n°16006947/MP0008755), institutional grants from INSERM, Université Paul Sabatier and CNRS. C. Rossi receives a grant from ITMO Cancer (Plan Cancer 2014–2019). P. Gravelle is supported by the CALYM Carnot Institute.

Institutional Review Board Statement: Not applicable.

Informed Consent Statement: Not applicable.

Data Availability Statement: The supplementary data are available here.

Acknowledgments: We are grateful to our healthcare professionals for their boundless investment during the COVID-19 crisis. Authors thank L Ligat, M Farcé and M Tosoloni from the Pôle technologique du CRCT for their advice on flow cytometry, 2D imaging, 2D imaging analysis, J Colombelli for MacroSPIM development (Advanced Digital Microscopy Core Facility, IRB, Barcelona, Spain), J Bursztyka and L Davignon from Perkin Elmer for their advices on Operetta System, all members of JJ Fournié's team (CRCT, Toulouse, France) for their stimulating comments, Anne-Marie Benot for administrative support and Cathy Greenland for English proofreading.

Conflicts of Interest: R.M., M.N., A.G. and J.-M.L are employees of Imactiv3D.

References

1. Carbone, A.; Roulland, S.; Gloghini, A.; Younes, A.; von Keudell, G.; López-Guillermo, A.; Fitzgibbon, J. Follicular Lymphoma. *Nat. Rev. Dis. Primers* **2019**, *5*, 83. [CrossRef] [PubMed]
2. Dada, R. Diagnosis and Management of Follicular Lymphoma: A Comprehensive Review. *Eur. J. Haematol.* **2019**, *103*, 152–163. [CrossRef] [PubMed]
3. Pampaloni, F.; Reynaud, E.G.; Stelzer, E.H.K. The Third Dimension Bridges the Gap between Cell Culture and Live Tissue. *Nat. Rev. Mol. Cell Biol.* **2007**, *8*, 839–845. [CrossRef] [PubMed]
4. Sutherland, R.M.; McCredie, J.A.; Inch, W.R. Growth of Multicell Spheroids in Tissue Culture as a Model of Nodular Carcinomas. *J. Natl. Cancer Inst.* **1971**, *46*, 113–120. [PubMed]
5. Simian, M.; Bissell, M.J. Organoids: A Historical Perspective of Thinking in Three Dimensions. *J. Cell Biol.* **2017**, *216*, 31–40. [CrossRef]
6. Horvath, P.; Aulner, N.; Bickle, M.; Davies, A.M.; Nery, E.D.; Ebner, D.; Montoya, M.C.; Östling, P.; Pietiäinen, V.; Price, L.S.; et al. Screening out Irrelevant Cell-Based Models of Disease. *Nat. Rev. Drug Discov.* **2016**, *15*, 751–769. [CrossRef]
7. Bissell, M.J. Goodbye Flat Biology—Time for the 3rd and the 4th Dimensions. *J. Cell Sci.* **2017**, *130*, 3–5. [CrossRef]
8. Jensen, C.; Teng, Y. Is It Time to Start Transitioning From 2D to 3D Cell Culture? *Front. Mol. Biosci.* **2020**, *7*, 33. [CrossRef]
9. Kunz-Schughart, L.A.; Freyer, J.P.; Hofstaedter, F.; Ebner, R. The Use of 3-D Cultures for High-Throughput Screening: The Multicellular Spheroid Model. *J. Biomol. Screen* **2004**, *9*, 273–285. [CrossRef]
10. Friedrich, J.; Seidel, C.; Ebner, R.; Kunz-Schughart, L.A. Spheroid-Based Drug Screen: Considerations and Practical Approach. *Nat. Protoc.* **2009**, *4*, 309–324. [CrossRef]
11. Pampaloni, F.; Stelzer, E. Three-Dimensional Cell Cultures in Toxicology. *Biotechnol. Genet. Eng. Rev.* **2010**, *26*, 117–138. [CrossRef] [PubMed]
12. Sirenko, O.; Mitlo, T.; Hesley, J.; Luke, S.; Owens, W.; Cromwell, E.F. High-Content Assays for Characterizing the Viability and Morphology of 3D Cancer Spheroid Cultures. *Assay Drug Dev. Technol.* **2015**, *13*, 402–414. [CrossRef] [PubMed]
13. Zanoni, M.; Piccinini, F.; Arienti, C.; Zamagni, A.; Santi, S.; Polico, R.; Bevilacqua, A.; Tesei, A. 3D Tumor Spheroid Models for in Vitro Therapeutic Screening: A Systematic Approach to Enhance the Biological Relevance of Data Obtained. *Sci. Rep.* **2016**, *6*, 19103. [CrossRef]
14. Gravelle, P.; Jean, C.; Familiades, J.; Decaup, E.; Blanc, A.; Bezombes-Cagnac, C.; Laurent, C.; Savina, A.; Fournié, J.-J.; Laurent, G. Cell Growth in Aggregates Determines Gene Expression, Proliferation, Survival, Chemoresistance, and Sensitivity to Immune Effectors in Follicular Lymphoma. *Am. J. Pathol.* **2014**, *184*, 282–295. [CrossRef] [PubMed]
15. Decaup, E.; Jean, C.; Laurent, C.; Gravelle, P.; Fruchon, S.; Capilla, F.; Marrot, A.; Al Saati, T.; Frenois, F.-X.; Laurent, G.; et al. Anti-Tumor Activity of Obinutuzumab and Rituximab in a Follicular Lymphoma 3D Model. *Blood Cancer J.* **2013**, *3*, e131. [CrossRef] [PubMed]

16. Gravelle, P.; Jean, C.; Valleron, W.; Laurent, G.; Fournié, J.-J. Innate Predisposition to Immune Escape in Follicular Lymphoma Cells. *Oncoimmunology* **2012**, *1*, 555–556. [CrossRef] [PubMed]
17. Rossi, C.; Gravelle, P.; Decaup, E.; Bordenave, J.; Poupot, M.; Tosolini, M.; Franchini, D.-M.; Laurent, C.; Morin, R.; Lagarde, J.-M.; et al. Boosting Γδ T Cell-Mediated Antibody-Dependent Cellular Cytotoxicity by PD-1 Blockade in Follicular Lymphoma. *Oncoimmunology* **2019**, *8*, 1554175. [CrossRef]
18. Decaup, E.; Rossi, C.; Gravelle, P.; Laurent, C.; Bordenave, J.; Tosolini, M.; Tourette, A.; Perrial, E.; Dumontet, C.; Poupot, M.; et al. A Tridimensional Model for NK Cell-Mediated ADCC of Follicular Lymphoma. *Front. Immunol.* **2019**, *10*, 1943. [CrossRef]
19. Poulain, S.; Roumier, C.; Bertrand, E.; Renneville, A.; Caillault-Venet, A.; Doye, E.; Geffroy, S.; Sebda, S.; Nibourel, O.; Nudel, M.; et al. *TP53* Mutation and Its Prognostic Significance in Waldenstrom's Macroglobulinemia. *Clin. Cancer Res.* **2017**, *23*, 6325–6335. [CrossRef]
20. Ivanov, D.P.; Grabowska, A.M. Spheroid Arrays for High-Throughput Single-Cell Analysis of Spatial Patterns and Biomarker Expression in 3D. *Sci. Rep.* **2017**, *7*, 41160. [CrossRef]
21. Yen, J.C.; Chang, F.J.; Chang, S. A New Criterion for Automatic Multilevel Thresholding. *IEEE Trans. Image Process.* **1995**, *4*, 370–378. [CrossRef]
22. Amaral, R.L.F.; Miranda, M.; Marcato, P.D.; Swiech, K. Comparative Analysis of 3D Bladder Tumor Spheroids Obtained by Forced Floating and Hanging Drop Methods for Drug Screening. *Front. Physiol* **2017**, *8*, 605. [CrossRef]
23. Spears, C.P. Volume Doubling Measurement of Spherical and Ellipsoidal Tumors. *Med. Pediatr. Oncol.* **1984**, *12*, 212–217. [CrossRef]
24. Dent, J.A.; Polson, A.G.; Klymkowsky, M.W. A Whole-Mount Immunocytochemical Analysis of the Expression of the Intermediate Filament Protein Vimentin in Xenopus. *Development* **1989**, *105*, 61–74. [PubMed]
25. Dodt, H.-U.; Leischner, U.; Schierloh, A.; Jährling, N.; Mauch, C.P.; Deininger, K.; Deussing, J.M.; Eder, M.; Zieglgänsberger, W.; Becker, K. Ultramicroscopy: Three-Dimensional Visualization of Neuronal Networks in the Whole Mouse Brain. *Nat. Methods* **2007**, *4*, 331–336. [CrossRef]
26. Huisken, J.; Stainier, D.Y.R. Selective Plane Illumination Microscopy Techniques in Developmental Biology. *Development* **2009**, *136*, 1963–1975. [CrossRef]
27. Lorenzo, C.; Frongia, C.; Jorand, R.; Fehrenbach, J.; Weiss, P.; Maandhui, A.; Gay, G.; Ducommun, B.; Lobjois, V. Live Cell Division Dynamics Monitoring in 3D Large Spheroid Tumor Models Using Light Sheet Microscopy. *Cell Div.* **2011**, *6*, 22. [CrossRef]
28. Colombelli, J.; Lorenzo, C. Light Sheet Fluorescence Microscopy Applications for Multicellular Systems. In *Fluorescence Microscopy*; Elsevier: Amsterdam, The Netherlands, 2014; pp. 109–120. ISBN 978-0-12-409513-7.
29. Abadie, S.; Jardet, C.; Colombelli, J.; Chaput, B.; David, A.; Grolleau, J.-L.; Bedos, P.; Lobjois, V.; Descargues, P.; Rouquette, J. 3D Imaging of Cleared Human Skin Biopsies Using Light-Sheet Microscopy: A New Way to Visualize in-Depth Skin Structure. *Skin Res. Technol.* **2018**, *24*, 294–303. [CrossRef]
30. Otsu, N. A Threshold Selection Method from Gray-Level Histograms. *IEEE Trans. Syst. Man Cybern.* **1979**, *9*, 62–66. [CrossRef]
31. Dekkers, J.F.; Alieva, M.; Wellens, L.M.; Ariese, H.C.R.; Jamieson, P.R.; Vonk, A.M.; Amatngalim, G.D.; Hu, H.; Oost, K.C.; Snippert, H.J.G.; et al. High-Resolution 3D Imaging of Fixed and Cleared Organoids. *Nat. Protoc.* **2019**, *14*, 1756–1771. [CrossRef]
32. Thoma, C.R.; Zimmermann, M.; Agarkova, I.; Kelm, J.M.; Krek, W. 3D Cell Culture Systems Modeling Tumor Growth Determinants in Cancer Target Discovery. *Adv. Drug Deliv. Rev.* **2014**, *69–70*, 29–41. [CrossRef] [PubMed]
33. Weiswald, L.-B.; Bellet, D.; Dangles-Marie, V. Spherical Cancer Models in Tumor Biology. *Neoplasia* **2015**, *17*, 1–15. [CrossRef] [PubMed]
34. Sutherland, R.M. Cell and Environment Interactions in Tumor Microregions: The Multicell Spheroid Model. *Science* **1988**, *240*, 177–184. [CrossRef] [PubMed]
35. Hirschhaeuser, F.; Menne, H.; Dittfeld, C.; West, J.; Mueller-Klieser, W.; Kunz-Schughart, L.A. Multicellular Tumor Spheroids: An Underestimated Tool Is Catching up Again. *J. Biotechnol.* **2010**, *148*, 3–15. [CrossRef]
36. Laurent, J.; Frongia, C.; Cazales, M.; Mondesert, O.; Ducommun, B.; Lobjois, V. Multicellular Tumor Spheroid Models to Explore Cell Cycle Checkpoints in 3D. *BMC Cancer* **2013**, *13*, 73. [CrossRef]
37. Riffle, S.; Pandey, R.N.; Albert, M.; Hegde, R.S. Linking Hypoxia, DNA Damage and Proliferation in Multicellular Tumor Spheroids. *BMC Cancer* **2017**, *17*, 338. [CrossRef]
38. Weeber, F.; Ooft, S.N.; Dijkstra, K.K.; Voest, E.E. Tumor Organoids as a Pre-Clinical Cancer Model for Drug Discovery. *Cell Chem. Biol.* **2017**, *24*, 1092–1100. [CrossRef]
39. Eglen, R.M.; Randle, D.H. Drug Discovery Goes Three-Dimensional: Goodbye to Flat High-Throughput Screening? *Assay Drug Dev. Technol.* **2015**, *13*, 262–265. [CrossRef]
40. Edmondson, R.; Broglie, J.J.; Adcock, A.F.; Yang, L. Three-Dimensional Cell Culture Systems and Their Applications in Drug Discovery and Cell-Based Biosensors. *Assay Drug Dev. Technol.* **2014**, *12*, 207–218. [CrossRef]
41. Cheson, B.D. New Agents in Follicular Lymphoma. *Best Pract. Res. Clin. Haematol.* **2011**, *24*, 305–312. [CrossRef]
42. Kahl, B.S.; Yang, D.T. Follicular Lymphoma: Evolving Therapeutic Strategies. *Blood* **2016**, *127*, 2055–2063. [CrossRef]
43. Achilli, T.-M.; Meyer, J.; Morgan, J.R. Advances in the Formation, Use and Understanding of Multi-Cellular Spheroids. *Expert Opin. Biol. Ther.* **2012**, *12*, 1347–1360. [CrossRef]
44. Costa, E.C.; Silva, D.N.; Moreira, A.F.; Correia, I.J. Optical Clearing Methods: An Overview of the Techniques Used for the Imaging of 3D Spheroids. *Biotechnol. Bioeng.* **2019**, *116*, 2742–2763. [CrossRef]

45. Alduaij, W.; Ivanov, A.; Honeychurch, J.; Cheadle, E.J.; Potluri, S.; Lim, S.H.; Shimada, K.; Chan, C.H.T.; Tutt, A.; Beers, S.A.; et al. Novel Type II Anti-CD20 Monoclonal Antibody (GA101) Evokes Homotypic Adhesion and Actin-Dependent, Lysosome-Mediated Cell Death in B-Cell Malignancies. *Blood* **2011**, *117*, 4519–4529. [CrossRef]
46. Hutmacher, D.W. Biomaterials Offer Cancer Research the Third Dimension. *Nat. Mater.* **2010**, *9*, 90–93. [CrossRef]
47. Matak, D.; Brodaczewska, K.K.; Lipiec, M.; Szymanski, Ł.; Szczylik, C.; Czarnecka, A.M. Colony, Hanging Drop, and Methylcellulose Three Dimensional Hypoxic Growth Optimization of Renal Cell Carcinoma Cell Lines. *Cytotechnology* **2017**, *69*, 565–578. [CrossRef] [PubMed]
48. Santo, V.E.; Estrada, M.F.; Rebelo, S.P.; Abreu, S.; Silva, I.; Pinto, C.; Veloso, S.C.; Serra, A.T.; Boghaert, E.; Alves, P.M.; et al. Adaptable Stirred-Tank Culture Strategies for Large Scale Production of Multicellular Spheroid-Based Tumor Cell Models. *J. Biotechnol.* **2016**, *221*, 118–129. [CrossRef] [PubMed]
49. Gong, X.; Lin, C.; Cheng, J.; Su, J.; Zhao, H.; Liu, T.; Wen, X.; Zhao, P. Generation of Multicellular Tumor Spheroids with Microwell-Based Agarose Scaffolds for Drug Testing. *PLoS ONE* **2015**, *10*, e0130348. [CrossRef] [PubMed]
50. Daydé, D.; Ternant, D.; Ohresser, M.; Lerondel, S.; Pesnel, S.; Watier, H.; Le Pape, A.; Bardos, P.; Paintaud, G.; Cartron, G. Tumor Burden Influences Exposure and Response to Rituximab: Pharmacokinetic-Pharmacodynamic Modeling Using a Syngeneic Bioluminescent Murine Model Expressing Human CD20. *Blood* **2009**, *113*, 3765–3772. [CrossRef]
51. Cottereau, A.S.; Versari, A.; Luminari, S.; Dupuis, J.; Chartier, L.; Casasnovas, R.-O.; Berriolo-Riedinger, A.; Menga, M.; Haioun, C.; Tilly, H.; et al. Prognostic Model for High-Tumor-Burden Follicular Lymphoma Integrating Baseline and End-Induction PET: A LYSA/FIL Study. *Blood* **2018**, *131*, 2449–2453. [CrossRef]
52. Meignan, M.; Cottereau, A.S.; Versari, A.; Chartier, L.; Dupuis, J.; Boussetta, S.; Grassi, I.; Casasnovas, R.-O.; Haioun, C.; Tilly, H.; et al. Baseline Metabolic Tumor Volume Predicts Outcome in High-Tumor-Burden Follicular Lymphoma: A Pooled Analysis of Three Multicenter Studies. *J. Clin. Oncol.* **2016**, *34*, 3618–3626. [CrossRef]
53. Richardson, D.S.; Lichtman, J.W. Clarifying Tissue Clearing. *Cell* **2015**, *162*, 246–257. [CrossRef]
54. Muntifering, M.; Castranova, D.; Gibson, G.A.; Meyer, E.; Kofron, M.; Watson, A.M. Clearing for Deep Tissue Imaging. *Curr. Protoc. Cytom.* **2018**, *86*, e38. [CrossRef]
55. Li, W.; Germain, R.N.; Gerner, M.Y. Multiplex, Quantitative Cellular Analysis in Large Tissue Volumes with Clearing-Enhanced 3D Microscopy (Ce3D). *Proc. Natl. Acad. Sci. USA* **2017**, *114*, E7321–E7330. [CrossRef] [PubMed]
56. Rios, A.C.; Capaldo, B.D.; Vaillant, F.; Pal, B.; van Ineveld, R.; Dawson, C.A.; Chen, Y.; Nolan, E.; Fu, N.Y.; 3DTCLSM Group; et al. Intraclonal Plasticity in Mammary Tumors Revealed through Large-Scale Single-Cell Resolution 3D Imaging. *Cancer Cell* **2019**, *35*, 618–632.e6. [CrossRef] [PubMed]
57. Pampaloni, F.; Stelzer, E.H.K.; Masotti, A. Three-Dimensional Tissue Models for Drug Discovery and Toxicology. *Recent Pat. Biotechnol.* **2009**, *3*, 103–117. [CrossRef] [PubMed]
58. Gualda, E.J.; Pereira, H.; Vale, T.; Estrada, M.F.; Brito, C.; Moreno, N. SPIM-Fluid: Open Source Light-Sheet Based Platform for High-Throughput Imaging. *Biomed. Opt. Express* **2015**, *6*, 4447–4456. [CrossRef]
59. Eismann, B.; Krieger, T.G.; Beneke, J.; Bulkescher, R.; Adam, L.; Erfle, H.; Herrmann, C.; Eils, R.; Conrad, C. Automated 3D Light-Sheet Screening with High Spatiotemporal Resolution Reveals Mitotic Phenotypes. *J. Cell Sci.* **2020**, *133*. [CrossRef]

1.3. Conclusion, complementary results and study perspectives

This study proposed an easy to handle, inexpensive, robust and reliable method to develop and analyze in depth 3D model established with FL cell lines. With this simple workflow, the throughput drug tested was increased, thus offering new perspectives for drug screening in FL.

First, we compared three different cell seeding densities and analyze by 2D and 3D imaging the ULA-MALC formed. All cell seeding densities allowed a well-shaped 3D model but cell viability was higher with the lower density at late days of culture. We then assessed drug efficacy by 2D imaging and observed that the level of cell death measured after with PI staining did not correlate with the level of cell death measured by flow cytometry. The reason evoked to explain these differences was that for flow cytometry analysis, ULA MALC were dissociated and that the percentage of cell death corresponded to the mean fluorescence intensity (i.e., 7AAD) per 50 000 cells. In contrast, for 2D imaging, columbus analyses determined the level of PI intensity of dead cells localized only on the first 50 to 100 µm of ULA-MALC. Moreover, although we were able to acquire several images at different levels on the z-axis (z-stack) and achieved a maximum projection with the associated software (Columbus), we only obtained partial information corresponding to the surface of the sample, leading to misinterpretation. The Operetta system is considered to be a high-content imaging system, providing high-resolution, high sensitivity and high speed required for 3D cell-culture model imaging. However, with our study, we identified two major limitations for ULA-MALC imaging using this equipment. First, our system is not equipped with a water immersion objective and second, ULA-MALC were not cleared, which strongly limited the full imaging of the sample.

These discrepancies prompted us to develop 3D imaging and specific analyses' algorithms to better characterize the 3D t (14;18)-positive B-NHL model and drug effects. The quantification of morphological properties confirmed that ULA-MALC were not perfect spheres as they exhibited a sphericity comprised between 0.72 and 0.78 and roundness between 0.75 and 0.88 from day 1 to day 4. After 5 days of culture, sphericity and roundness strongly decreased, with mentioned parameter's values dropping down to 0.25 and 0.23 respectively at day 6. With 2D images these values were close to 1 for both parameters. We were also able to measure the eccentricity and showed an important ellipsoid deformation (very close to 1 at day 5 and day 6), in line with the drop in sphericity and roundness. These results showed that both volume and sphericity dramatically changed between day 4 and day 5 with a huge increase in the real volume measured concomitantly to a potent loss in sphericity. Moreover, upon treatment, we showed that in contrast to 2D imaging, GA101 (10µg/mL), ABT-199 at 100 nM and rapamycin (10nM) significantly increased sphericity and roundness. In

conclusion, 3D characterization of treated ULA-MALC revealed important information about the real drug effects on structuration, shape, volume and morphology. Although 2D imaging only allowed the observation of cytostatic or cytotoxic effects, 3D imaging highlighted other drug specific characteristics.

Altogether, our study revealed potent discrepancies between the results obtained from 2D and 3D imaging and warned the scientific community to possible misinterpretations following 2D imaging. Numerous investigations using spheroids are based on 2D imaging performed on uncleared samples without any complementary in depth characterization of the model used, nor the drug effect induced. We showed here that without 3D imaging and development of specific informatics solutions, we could draw wrong conclusions. The perspectives are numerous and particularly one of our interests, is to develop cell clearing in plates in order to image the whole MALC in a higher throughput. In this context, with Dr Fabien Gava from my team, we obtained preliminary results of different clearing methods applied to RL ULA-MALC. As presented in the figure 68, TDE and Scale S4, two aqueous clearing agents, are able to clear almost completely the model. With the z-stack galery and the orthogonal view, we can appreciate how much deeper we are able to image the model after clearing process in comparison with uncleared sample.

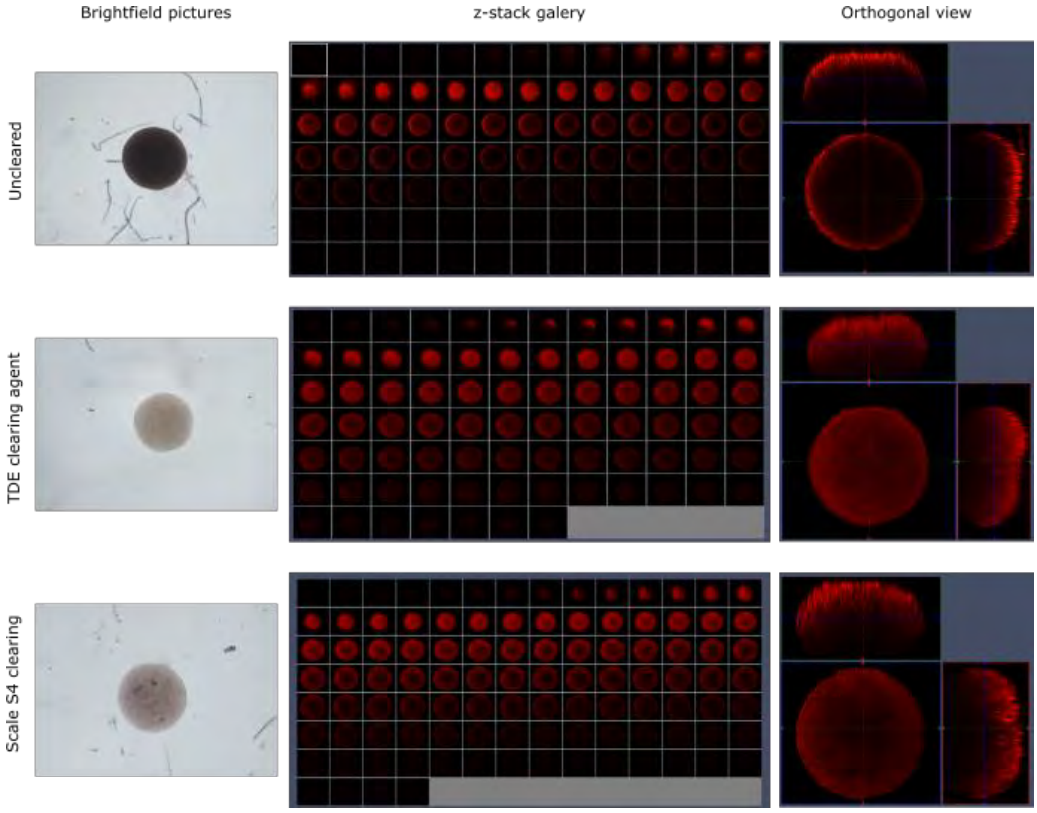

Figure 68 : Illustration of aqueous clearing agent efficacy on ULA-MALC model.
From left to right, brightfield pictures obtained with the inversed microscope Nikon Eclipse TE200, z-stack galery and orthogonal view after PI staining analyzed with Imaris after acquisition with confocal microscope Zeiss 880.

Clearing was performed after overnight fixation of MALC in 4% PFA, washings, and different bath of TDE or scale S4 added directly to the well.

Another perspective opened with the ULA-MALC model and 3D imaging is the localization's study of biological processes such as cell death induced by drug treatment. In this context, we determined the localization of caspase 3 positive dead cells on MALC treated by rapamycine, GA101 or bendamustine. As shown in figure 69, we were able to visualize the cell death induced by drugs thus allowing a new application of the 3D models we developed.

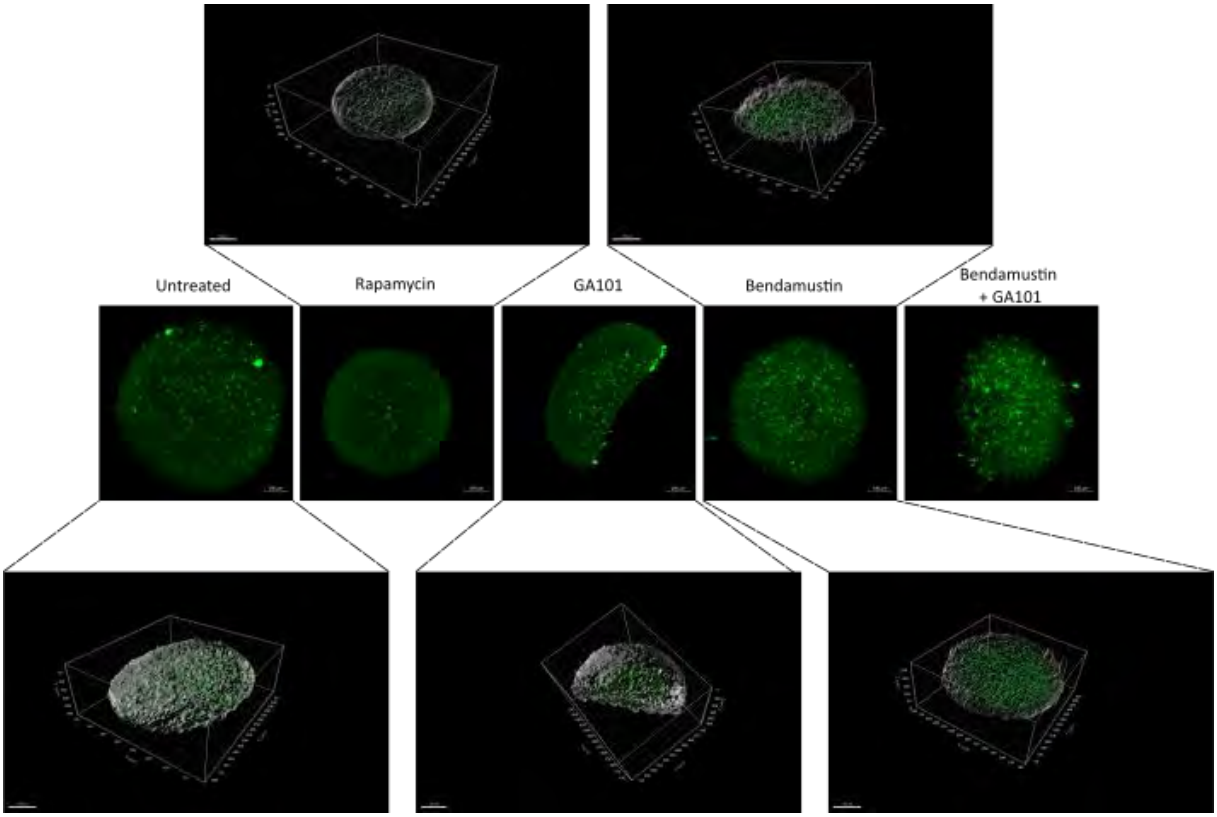

Figure 69 : Caspase 3 visualization in ULA-MALC upon treatment with rapamycin, GA101, bendamustine or combination of bendamustine and GA101
Confocal imaging was performed with the Zeiss 880 and 3D reconstruction with imaris software.

Finally, in a context of IT development and drug testing, our model and the methods of characterization associated, appear crucial. Indeed, co-cultures with immune cells such as γδ T cells allow the investigation of mechanisms such as ADCC (Figure 70 left). Moreover, by complexifying the model with the addition of other cellular cell types such as FDC (Figure 70 right), it is also possible to render more relevant to the pathology. Altogether, such models will open new perspectives of *in vitro* investigations such as immune cell infiltration, FL-FDC interaction or testing drugs targeting both tumoral cells and TME.

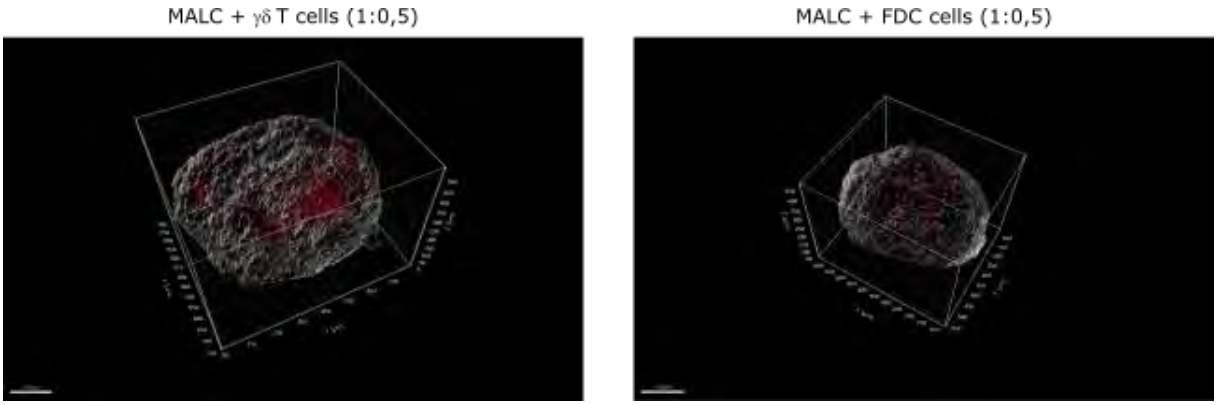

Figure 70 : MALC co-cultured with γδ T cells or FDC cells (ratio 0,5:1)
Confocal imaging was performed with the Zeiss 880 and 3D reconstruction with imaris software. γδ T cells or FDC were stained with cell far red dye.

In conclusion, ULA-MALC model is a promising preclinical tool to decipher drug mechanisms and discover new therapeutic targets. With this study, we contributed to the development of alternative assays to reduce animal testing and costs which is necessary for future preclinical studies. Moreover, this study opens encouraging perspectives in terms of model development for the use of co-culture with immune cells to explore the activity of IT. Despite these huge improvements and encouraging perspectives, ULA-MALC model exhibits a main limitation as it does not recapitulate FL heterogeneity observed between patients nor the full interactions with the TME. This was the aim of the second study presented in the next part.

2. Patient-Derived Lymphoma Spheroids: a tool towards personalized medicine

2.1. Model establishment, methodology and study context

In order to recreate *in vitro* FL immune TME, we developed a 3D model called PDLS for Patient-Derived Lymphoma Spheroids established with FL biopsies. First of all, we needed to answer to four main questions (Figure 71).

- Sample type: can we work with fresh or thawed cells from LN biopsies? How the dissociation method is affecting cell population composition?
- Methodology: is ULA-centrifugation suitable for patient cells aggregation?
- Cell seeding density: do we use the same as for ULA-MALC?
- Medium: what type of enriched medium and cytokines suitable for maintaining FL cells alive?

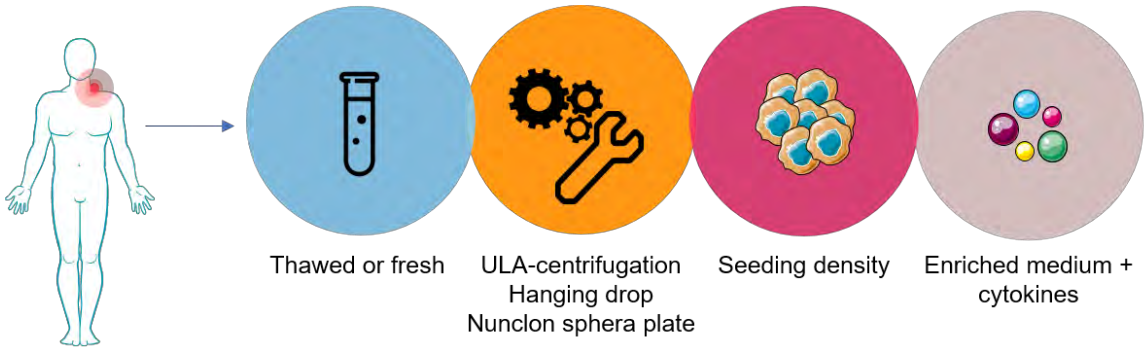

Figure 71 : Technical questions concerning development of PDLS models

About the first issue, we have tested both fresh and thawed samples obtained from IUCT-Oncopole. Although viability of fresh samples was better, the fact that we did not have the diagnosis at the time of 3D culture led us to work with thawed samples. The samples were biobanked after mechanical dissociation following surgery and preserved in albumin medium in nitrogen until use.

Regarding the methodology, we performed assays on reactive LN in order to preserve rare patients' samples that revealed that ULA method was more suitable to obtain a well-structured 3D model compared to the HD method, as illustrated in figure 72.

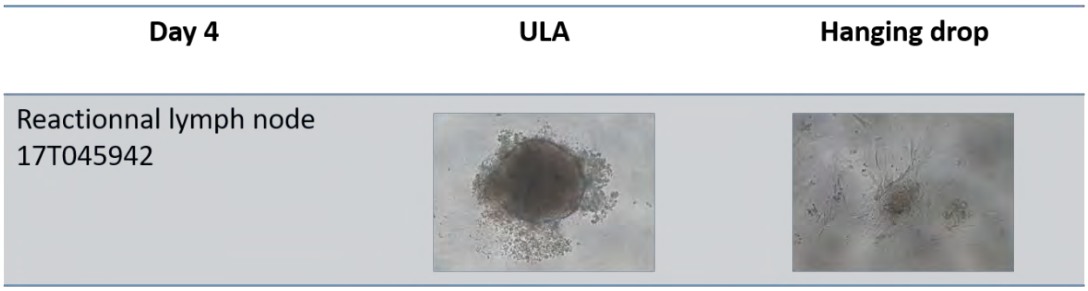

Figure 72 : Morphological comparison of 3D model from reactionnal LN performed with ULA or HD method
100 000 cells were seeded / model and after 4 days of culture, pictures were obtained with inverted microscope equipped with a camera (Nikon Eclipse TE200), magnification 4X.

Then, in collaboration with my PhD codirector's team (IDIBAPS, Barcelona), we determined the most suitable cell seeding density (from 2500 to 100 000 cells/models) and enriched medium to obtain viable and aggregated cells. Five different media containing enriched medium, ODN, IL-15, IL-2, IL-4 and/or CD40L were tested (Table 13).

Composition	#1	#2	#3	#4	#5
IMDM + HiClonel serum	+	+	+	+	+
IMDM + Hiclonel + Mongini enrichment	-	+	+	+	+
ODN + IL-15	-	-	+	+	+
IL-2+IL-4	-	-	-	+	+
CD40-L	-	-	-	-	+

Table 13 : Different media tested for PDLS generation

The different media and cytokines were selected according to the following considerations:

- Mongini et al established a medium which favors survival of primary B cells [460]. This medium contains apotransferrin (40µg/mL), HEPES (20mM), NE-AA (1X), sodium pyruvate (1mM), 2-β-mercaptoéthanol (5.10^{-5}M), Gentamicine (50µg/mL) allowing a better survival of primary cultured B cells [460].
- IMDM and Hiclone I serum are used for γδ T cells culture. Thus, in order to preserve their survival, we decided to replace RPMI and FBS serum with mentioned combination [232].
- IL-15 has been showed to promote *in vitro* clonal expansion of B-CLL cells[461] and is implicated in monocytes-T cell interaction which favor FL B cell growth [156].
- TLR9 promotes *in vitro* clonal expansion of B-CLL cells and it can be activated by ODN, a CpG oligonucleotide, a short synthetic single stranded DNA molecule containing CpG motifs [461].
- IL-2 is a well-known cytokine that induces T cell proliferation and activation [462].
- IL-4 is important for TFh cells survival, which play a key role to support FL B cells survival [152].

In figure 73, represents an example of PDLS established with thawed LN cells from FL patients with 3 different seeding densities (2 500, 5 000, 10 000, 25 000 cells and 50 000 cells) with 5 different media referred as # 1 to 5 (Table 13).

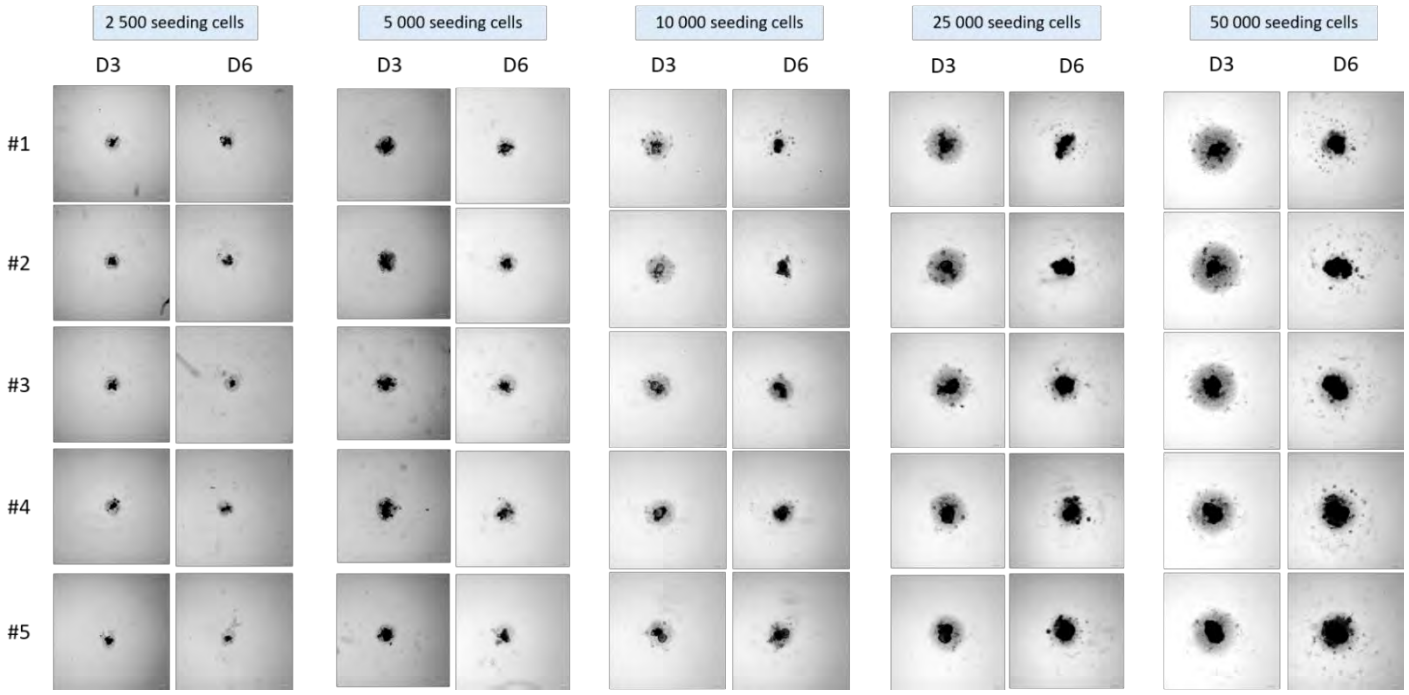

Figure 73 : PDLS tested with several media and cell seeding densities (patient #19T003217)

After day 3 and 6, pictures were obtained with the Operetta system. Scale = 200µm.

First of all, we observed that PDLS presented a structure composed by two-parts: a dense 3D aggregate localized in the center and a thin monolayer around. Both of these parts increase with growing cell density. To our opinion, 25 000 and 50 000 cell seeding exhibited the best 3D structuration and presented the cell number suitable for flow cytometry analyses. Regarding the media tested, #5 was the one leading to the best 3D structuration.

To better characterize the influence of cell densities and cytokines, we assessed cell viability by trypan blue counting and determined B/T ratio by flow cytometry analysis. As shown in figure 74, after 3 days of culture, a better viability was obtained with media #3 and #5 for lower densities (2500 and 5000). For higher densities, no differences were observed between the media tested. After 6 days of culture, 25000 cell seeding combined with the medium #5, was the most suitable condition in term of viability and cell number necessary for further flow cytometry analysis.

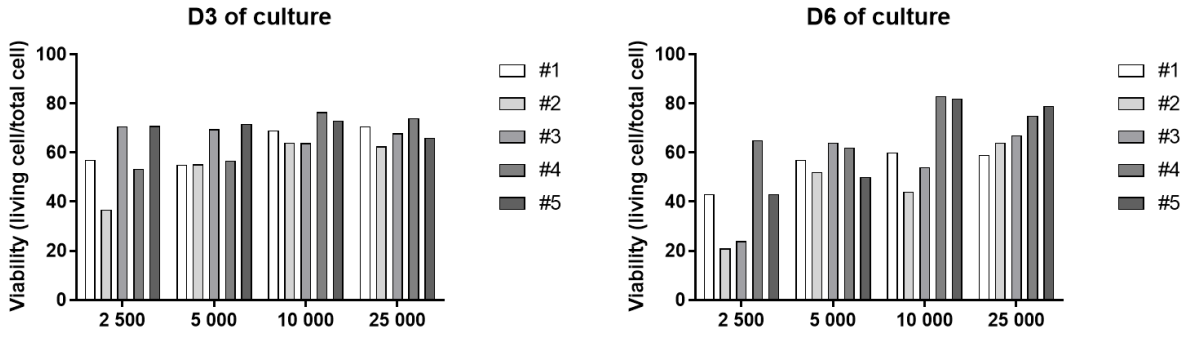

Figure 74 : Evaluation of cell viability at day 3 and day 6 of 3D culture with different cell seeding densities and media

10 PDLS per conditions were pooled and viable cells were counted by a trypan blue assay at day 3 and 6 of 3D culture.

We then evaluated the influence of cell seeding density and medium on the proportion of B and T cells (Figure 75). At day 3 of culture no important differences in B and T percentages were observed between media, with a percent of B cells around 50 to 60% and a percent of T cells around 15 to 20%. Nevertheless, the 50 000 cells seeding density presented a lower percent of CD19 (around -20%) with all media compared to 10 000 and 25 000 cell seeding densities. At day 6 of culture, important differences were observed between media #1, #2, #3 and #3, #4, #5. Indeed, around 20% less B and T cells were observed with media #1, #2, #3. In contrast, media #4 and #5 were the most suitable media to keep the highest proportion of alive B and T cells.

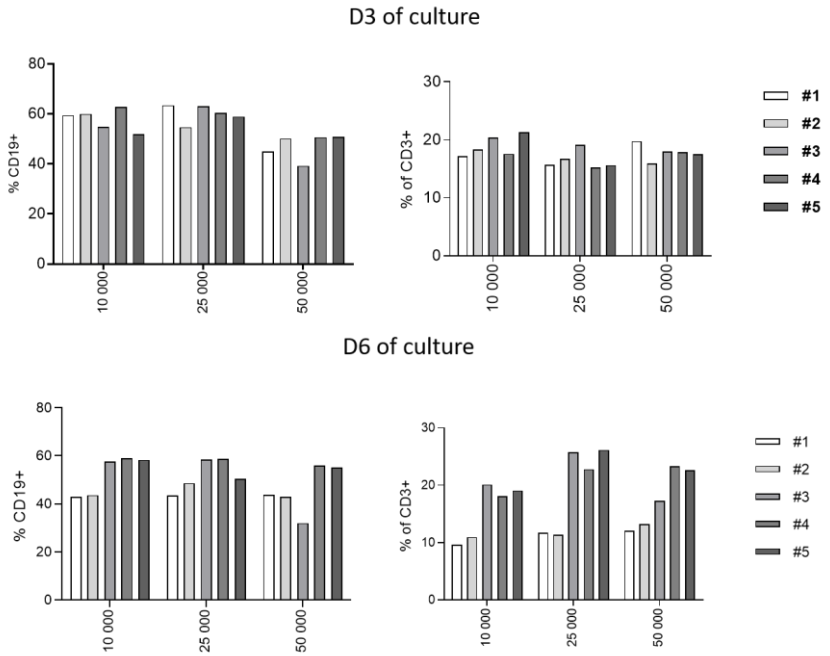

Figure 75 : Determination of B and T cell percent in PDLS cultured at different cell seeding densities and with different media at day 3 and 6 of 3D culture

10 PDLS were pooled, dissociated, stained for CD19 and CD3 and then analyzed by flow cytometry.

Altogether, the results obtained with 25 000 cells seeding in medium #5 combined all the criteria required for PDLS establishment: 3D structuration, high cell viability during culture, high B/T cells proportion and high cell number to perfom flow cytometry analyses.

Based on these results, we performed a study which fully characterized PDLS from FL biopsies by 2D and 3D imaging. Moreover, we aimed to present solid evidences that PDLS could be recognized as preclinical models integrating immune microenvironment and useful to identify new therapeutic targets.

2.2. Scientific publication (in preparation): Patient-Derived Lymphoma Spheroids integrating immune tumor microenvironment as preclinical follicular lymphoma models for personalized medicine

Patient-Derived Lymphoma Spheroids integrating immune tumour microenvironment as preclinical follicular lymphoma models for personalised medicine

Carla Faria,[1-4,] Fabien Gava,[1-4] Pauline Gravelle,[1-5] Celia Dobaño-López,[6,7] Juan Garcia-Valero,[6,7] Nathalie Van Acker,[5,8] Cathy Quelen,[1-5,8] Gael Jalowicki,[2] Renaud Morin,[9] Cédric Rossi,[10] Jean-Michel Lagarde,[9] Jean-Jacques Fournié,[1-4] Loïc Ysebaert,[1-4,11] Camille Laurent,[1-5,8] Patricia Pérez-Galàn,[6,7,§] and Christine Bezombes,[1-4,§]

[1] Université de Toulouse, Inserm, CNRS, Université Toulouse III-Paul Sabatier, Centre de Recherches en Cancérologie de Toulouse, Toulouse, France

[2] Institut Universitaire du Cancer-Oncopole de Toulouse, Toulouse, France

[3] Laboratoire d'Excellence 'TOUCAN-2', Toulouse, France

[4] Institut Carnot Lymphome CALYM

[5] Department of Pathology, Institut Universitaire du Cancer de Toulouse, CHU Toulouse, Toulouse, France

[6] Department of Hemato-Oncology, IDIBAPS, Barcelona, Spain

[7] Centro de Investigación Biomédica en Red-Oncología (CIBERONC), Madrid, Spain

[8] Imag'IN Platform, Institut Universitaire du Cancer de Toulouse, CHU Toulouse, Toulouse, France

[9] IMACTIV-3D, 1 Place Pierre Potier 31106 Toulouse, France

[10] Department of Hematology, Hôpital François Mitterrand, Dijon, France and U1231 INSERM

[11] Department of Hematology, Institut Universitaire du Cancer de Toulouse, CHU Toulouse, Toulouse, France

[§]co-corresponding authors: christine.bezombes@inserm.fr, PPEREZ@clinic.cat

Abstract:

Keywords: Follicular lymphoma, 3D preclinical model, immune tumour microenvironment, immunotherapy, immune check point, personalized medicine

Introduction

Cancer is a highly heterogeneous disease and the tumour microenvironment (TME) is complex, dynamic and represents a vital component. The importance of the TME in lymphoid malignancies varies significantly depending on the lymphoma subtype [1]. For follicular lymphoma (FL), one of the two most frequent non-Hodgkin lymphomas (NHL), TME plays a fundamental role in which immune and stromal cells support survival, proliferation and migration of tumoural B cells [2]. Its composition can be divided into two compartments. A cellular component including CD4+ T cells comprising CD4+ T follicular helper (TFh) cells, CD4+ T follicular regulatory (TFr) cells, CD4+ T regulatory cells (Treg) and also CD8+ cytotoxic T cells (CTL), follicular dendritic cells (FDC), fibroblastic reticular cells (FRC), mesenchymal stromal cells (MSC) and tumour-associated macrophages (TAM). A non-cellular compartment composed of cytokines, pro-angiogenic factors and ECM components also plays a key role [3],[4],[5]. This rich, well-interconnected and supportive network may account for the incurability of this indolent lymphoma. Thus, a better understanding of this pathology with relevant *in vitro* models is essential to identify therapeutic targets and to perform preclinical studies. In the era of personalized medicine, our aim was to develop models that can be reliable and representative of both intra- and inter-tumour heterogeneity.

The culture of lymphoma B cells in suspension (2D) is not at all representative of the 3D spatial organization and architecture of a lymph node, rendering results obtained, especially for drug efficacy, difficult to interpret. Indeed, these models do not mimetize the neoplastic heterogeneity and drug response of the parental tumour.

Three-dimensional (3D) cell cultures are largely used and studied for solid cancers and their advantages have been recognized for over 50 years [7],[8]. In contrast to 2D cultures, cell–cell and cell–matrix interactions, spatial organisation, mechanical constraints, nutrients and O_2 gradients, are well-known parameters that influence disease biology and response to treatments that are recapitulated in 3D models. They also offer useful properties for drug screening [9],[10],[11],[12]. In contrast to solid cancers, relevant 3D models for B-NHL are poorly described [13]. Amongst them, spheroids/organoids from DLBCL cell lines or fresh samples from patients are the most developed [14],[15],[16],[17],[18]. We were pioneers in the development of 3D cultures established with FL cell lines [19],[20],[21],[22],[23]. The first 3D model called MALC (multicellular aggregates of lymphoma cells) was developed based on the hanging drop (HD) method in 24-well plates (HD-MALC) with t (14;18)-positive B-NHL cell lines. This 3D model exhibits transcriptomic profiles similar to that of FL patients with an overexpression of gene families involved in survival pathways including the NF-□B pathway, cell cycle regulation or hypoxic responses. When co-cultured with immune cells such as NK or gamma

delta T cells, this model allowed the study of therapeutic monoclonal antibody responses such as anti-CD20 and immune escape mechanisms targetable by immunotherapy. It also enabled the visualisation of drug penetration and immune cell infiltration within the MALC thus deciphering the mechanisms existing in FL biopsies [22],[23],[24]. Another model, which did not exhibit differences in gene expression or mutational profiles compared to the HD-MALC, was recently developed to allow drug screening [25]. Based on a scaffold-free technique, cells were seeded in ULA plates, avoiding the risk of damaging the 3D structure due to transfer when established with the HD method. Moreover, ULA-MALC was centrally located in a non-agarose precoated well, which facilitated imaging. Thus, we characterized this 3D model in depth with 2D and 3D imaging and specific algorithms showing that this simple, reliable and robust method could be standardised and easily used for medium/high throughput screening for lymphoma therapies as described in solid cancers by others[8],[26]. However, these models were not representative of FL heterogeneity observed between patients nor the interactions with the TME. One group recently established a 3D model including ECM, tonsil stromal cells and isolated primary FL B cells to study the dynamic relationship between lymphoma B cells and their microenvironment [18]. Although these models, including mechanical constraints, brought new interesting perspectives, they were artificially reconstituted and did not include immune TME, a key component in the era of immunotherapeutic strategies and personalised medicine, particularly in FL.

Thus, we developed a new 3D model called patient-derived lymphoma spheroids (PDLS) established from a FL biopsy that recreates *in vitro* FL immune TME and provides a suitable preclinical platform for drug testing and discovery of new therapeutic targets. To this purpose, we decided to establish 3D cultures without any scaffold, nor matrix (matrigel, collagen…) in order to attribute the results obtained to the PDLS *per se* and not to the component used to maintain the primary cells in 3D. Maintaining primary FL cells *in vitro* is known to be challenging. Here, we established a simple, robust and reproducible workflow allowing the maintenance of viable cells isolated from FL biopsies. We characterised in depth PDLS by 2D and 3D imaging but also by multiparametric flow cytometry analyses and evaluated their sensitivity towards two monoclonal antibodies (anti-CD20 and anti-PD-1). Altogether, our results present a proof of concept for using PDLS as representative preclinical FL models integrating patient immune microenvironment heterogeneity and bring strong evidence that these models are essential for future investigations in personalised medicine.

Materials and Methods

Drugs and mAbs. Obinutuzumab (GA101) an anti-CD20 mAb was provided by Roche (Basel, Switzerland) and used at 10 µg/mL. Anti-PD-1 mAb of class IgG4 (Nivolumab) was obtained from the department of Pharmacy at the IUCT (Toulouse) and used at 10 µg/mL.

Patient samples. Lymph nodes were obtained from 10 patients (see table 1 for patients characteristics annotated from #1 to #10) at the department of Hematology (IUC, Toulouse-Oncopole, France), who were diagnosed between 2018 and 2021 with FL (Grade II according to the WHO classification [27]). Tissue samples were collected and processed following the standard ethical procedures of the Helsinki protocol, after obtaining written, informed consent from each donor and local ethical committee approval for the study (Comité de Protection des Personnes Sud-Ouest et Outremer II).

Patient number	Age	Sexe	Ann Arbor Stage	FLIPI	GELF	B symptoms	BM involvement	Treatment response	Primary treatment	Date of diagnostic	Last follow-up	Relapse/ transformation
#1	73	M	IV	4	>1	no	yes	PR	EPI-R-CHOP	23/12/2020	2022-02-09	no
#2	43	M	IV	1	1	no	no	CR	GA101-CHOP+ GA maintenance	13/03/2020	2022-01-19	no
#3	59	F	I-II	0	0	no	no	*NA*	Surveillance	21/05/2019	2020-05	yes (tFL)
#4	78	M	III	2	0	no	no	CR	GA101-CVP + GA maintenance	24/09/2019	2022-01-20	no
#5	83	F	III	3	>1	no	no	ongoing	GA101-CVP	05/09/2019	2022-03-04	no
#6	57	F	IV	3	1	no	*NA*	CR	R-chemotherapy + RTX maintenance	04/01/2019	2022-02-09	no
#7	70	F	IV	3	0	no	no	*NA*	surveillance	20/03/2021	2022-02-25	no
#8	72	F	IV		1	yes	yes	CR	EPI-R-CHOP	27/03/2021	2022-02-08	no
#9	65	F	IV	3	3	yes	yes	CR	EPI-R-CHOP	11/05/2021	2022-01-21	no
#10	67	F	IV	4	2	no	no	CR	4 GA101-CHOP + 2 R-CHOP + RTX maintenance	30/01/2019	2021-11-17	no

Table 1 : **FL patient characteristics**. *PR :* partial response, *CR :* complete response, *NA :* not applicable. *R* : rituximab, *GA* : GA101/Obinutuzumab, *C* : cyclophosphamide, *H* : hydroxyadriamycin,*O* : oncovin, *P* : prednisone, V : vincristine, *EPI-R-CHOP protocol* : R-CHOP + TAZEMETOSTAT + 2 RTX + RTX maintenance. *tFL* : transformed follicular lymphoma

Primary FL cell culture and PDLS generation. Fresh tissues from lymph nodes were dissociated using the gentleMACS™ Octo Dissociator (Miltenyi, Paris, France). Cell suspensions were frozen in 4% human albumin (VIALEBEX 40 mg/ml, LFB Biomedicaments)/10% DMSO until FL diagnosis. After diagnosis, cells were thawed in complete medium and their phenotypes were analysed by Fortessa X20 (BD Biosciences Le Pont de Claix, France) after staining by fluorochrome-labelled antibodies (see flow cytometry section). PDLS were established according to the following protocol: 25 000 cells in 100 µL of enriched medium supplemented with cytokines (IMDM medium + 10% HiClone serum, 5.10^{-5}M 2-ME, 50 µg/ml gentamicin, 40 µg/ml apotransferrin, 1 mM sodium pyruvate, 1X nonessential amino acids and 20 mM HEPES, 0.2 µM ODN, 15ng/mL IL-15, 10ng/mL IL-2, 50ng/mL IL-4, 50ng/mL CD40L) were seeded in 96-well round bottom ULA plates (Corning, Samois sur Seine, France), centrifuged 10 minutes at 1 000 rpm and cultured at 37 °C in a humidified 5% CO_2 atmosphere. At day 3 of culture, 100 µL of fresh enriched medium containing or not treatments were added and PDLS were cultured at 37 °C in a humidified 5% CO_2 atmosphere until the different time points.

PDLS immunohistochemistry. PDLS were fixed at day 6 of culture directly in the wells with 4% PFA (Alfa Aesar, Haverhill, MA, USA) overnight at 4 °C. PDLS were then rinsed with PBS and included in 1% low-melting agarose (Life Technologies, Villebon sur Yvette, France), quickly labelled with China ink before being included in paraffin. Automated classical immunohistochemistry (IHC) was performed using the Benchmark ULTRA (Roche, Ventana Medical Systems, Innovation Park Drive Tucson, Arizona, USA) on FFPE tissue sections (3µm). After dewaxing, tissue slides were heat pre-treated using a CC1 (pH8) buffer (Roche) at 98°C. The slides were blocked for endogenous peroxidase activity and incubated with primary antibodies (see table 2). The target was then visualised using the OptiView DAB detection kit (Roche). The tissue slides were counterstained using hematoxylin (Roche) for 8 minutes followed by post-coloration using Bluing reagent for 4 minutes at room temperature (Roche). The slides were then dehydrated (ethanol and xylene) and mounted using xylene-based mounting. The antibodies used for IHC labelling are listed in table 2.

Antibody	Species	Clone	Supplier
BCL2	Rabbit	SP66	ROCHE
CD10	Rabbit	SP67	ROCHE
CD20	Mouse	L26	ROCHE
CD21	Rabbit	EP3093	ROCHE
CD3	Rabbit	2GV6	ROCHE
CD79a	Rabbit	SP18	ROCHE
Ki67	Rabbit	30-9	ROCHE

Table 2: Primary antibodies used for IHC labelling

PDLS characterisation by 2D imaging. After 72 hrs of treatment, PDLS were visualized by brightfield illumination (BF) on a high throughput microplate imager for high-content analyses device equipped with a 5X objective (Operetta, Perkin Elmer, Villebon sur Yvette, France). Morphological parameters (BF area, roundness) were analysed by the Columbus software associated.

Visualisation of cell aggregation by live-cell imaging. After centrifugation in ULA plate, PDLS were imaged from D0 to D6 (D = day) with Incucyte S3 Live-Cell Analysis System (Sartorius, Göttingen, Germany), placed in a standard tissue culture incubator to acquire automatically phase images at 4X magnification.

PDLS characterisation by 3D imaging. PDLS were fixed at different days of culture directly in the wells with 4% PFA overnight at 4 °C and rinsed with PBS. Nuclei were labelled with 10 µg/mL Propidium Iodide (PI) (Life technologies) for 4 hrs at room temperature under agitation. PDLS were then rinsed

with PBS and included in 1% low-melting agarose (Life Technologies). 8 mm disks were punched and cleared with the methanol-benzyl alcohol/benzyl benzoate (BABB) technique as previously described [28],[29]. Acquisitions were performed with an 880 confocal microscope (Zeiss, Oberkochen, Germany) at 10X magnification. IMARIS 7 software (BitPlane, South Windsor, CT, USA) was used for PDLS 3D representations.

Image analyses (volume, sphericity, eccentricity and roundness quantification) were performed using the processing pipeline described in [25]. As compared to the ULA-MALC samples analysed therein, the PDLS samples were more irregular in terms of shape and were frequently associated with surrounding artefactual cellular residues. A pre-processing stage based on watershed segmentation and morphological parameter selection was implemented for this purpose in order to get rid of all the unwanted residues.

Flow cytometry analyses. After 3 days of treatment, PDLS (n=10 of each FL sample) were mechanically dissociated, pooled, washed and stained with combinations of fluorochrome-labelled antibodies (see the table 3). Immune cell composition of PDLS was determined as follows: for T cell populations (CD3+CD4+ cells for CD4+ T cells, CD3+CD8+ for CD8+ T cells, CD56+CD3- for NK cells, gamma9+CD3+ for gamma delta T cells, CD3+CD4+CXCR5+ICOS+ for TFh/TFr, CD3+CD4+CXCR5-ICOS- for non-TFh), for B cell populations (CD10+CD19+ for B tumoural cells, CD10-CD19+ for healthy B cells) and immune checkpoint on T cells (CD39, CD73, PD-1, BTLA, LAG-3, TIGIT, TIM-3) and immune checkpoint on B cells (CD39, CD73, PDL1, PDL2, PD-1). B cell depletion was determined by flow cytometry and normalised by untreated condition percentage. 5 µl of 7-aminoactinomycin D (7AAD, BD Biosciences, Le Pont de Claix, France) were then added according to the manufacturer's instructions and dissociated cells were analysed on a Fortessa X20 flow cytometer (BD Biosciences). Dead cells ($7AAD^+$) were excluded from the analyses with Cytobank. Cytokine release was determined by measuring TNF, IFN, Granzyme B, IL-6, IL-8, IL-10 concentrations in the supernatant of PDLS at day 6 of 3D culture using a BD cytometric bead array (CBA) human soluble protein master kit following provider's instructions (BD Biosciences).

Provider	Antibody	Chanel	Clone	Isotypes
BD	CD19	APC	HIB19	Mouse IgG1, κ
BD	CD10	BV605	HI10a	Mouse BALB/c IgG1, κ
Biolegend	CD3	APC-Fire	UCHT1	Mouse IgG1, κ
BD	CD4	BUV395	RPA-T4	Mouse IgG1, κ
BD	CD8	BV510	RPA-T8	Mouse IgG1, κ
BD	CD56	PerCP-Cy5.5	B159	Mouse IgG1, κ
BD	Vd2g9	FITC	B3	Mouse IgG1, κ
BD	CXCR5	BV650	Clone RF8B2	Rat LOU
BD	CD25	BV421	M-A251	Mouse BALB/c IgG1, κ
BD	ICOS	BV605	DX29	Mouse IgG1, κ
BD	CD39	PE	TU66	Mouse IgG2b, κ
BD	CD73	BUV737	AD2	Mouse IgG1, κ
BD	PD-1	PE-Cy7	EH12.1	Mouse IgG1, κ
BD	PDL2	BV650	MIH18	Mouse IgG1, κ
BD	7-AAD	PE-Cy5		
BD	CD107a	PE	H4A3	Mouse BALB/c IgG1, κ
BD	CD69	APC	FN50	Mouse IgG1, κ
BD	IFNγ	BV711	B27	Mouse IgG1, κ
BD	TNFα	PE-Cy7	MAb11	Mouse IgG1, κ

Table 3: Primary antibodies, dye for viability and kit for cytokines used for flow cytometry analyses

Determination of cell number by trypan blue assay. After 3, 4 and 6 days of culture, PDLS (n=10 of each FL sample) were mechanically dissociated and cells were counted by trypan blue assay on a Malassez cell. Cell viability was determined according the formula: % of viability = [number of live cells/ (number of live cells + number of dead cells)] × 100.

3'mRNA sequencing. After thawing, cells from FL biopsies were cultured in suspension overnight in RPMI medium supplemented with FBS and the next day RNA was extracted (Direct-zol RNA Minipep kits – Zymo Research). In parallel, cells from the same sample were cultured in 3D in an enriched medium supplemented with cytokines and after 3 days, PDLS were mechanically dissociated and RNA extraction was performed. Libraries were prepared with 500 ng of RNA using the QuantSeq 3'mRNA-Seq Library Prep Kit-FWD (Lexogen, Vienna, Austria) and UMI Second Strand Synthesis Module (Lexogen) following the manufacturers' instructions. 13 cycles of library amplification were performed. The libraries were quantified using the Qubit™ dsDNA HS Assay Kit (Invitrogen, Life Technologies) and equimolar pooling was performed at 8nM. The pooled libraries were sequenced on single read 75 pb run, on an Illumina NextSeq550DX instrument (Illumina). Expected read depth was 15 millions of

uniquely mapped reads per sample. The data analyses were performed by the pipeline on the BlueBee® Genomics Platform.

Correlogram & correlation curves. Correlogram was obtained with Open source Rstudio (RStudio Team (2020), PBC, Boston, MA URL http://www.rstudio.com/) and corrplot package. For each variable, the values of the 7 PDLS were used to calculate side-by-side correlation coefficients and correlation matrix (non-parametric Spearman's correlation). Associated Correlation curves were generated based on the same data set with GraphPad Prism 9.

Statistics. For all the results obtained and presented in figures 1 and 9, we applied various statistical analyses. For comparing three or more parameters, one-way ANOVA was used in figure 1B (see table 4), whilst t-tests were used to compare each day 3 to day 6 culture for each patient in figure 1B and each treatment with untreated condition in figure 9A and B. All tests were performed with GraphPad Prism software. p values: **** = $p < 0.0001$, *** = $p < 0.0005$, ** = $p < 0.01$ and * = $p < 0.05$.

AREA CENTER

	Day 3									Day 6								
	#1	#2	#3	#4	#5	#6	#7	#8	#9	#1	#2	#3	#4	#5	#6	#7	#8	#9
#1		ns	****	****	**	****	ns	ns	****		ns	ns	**	ns	ns	ns	ns	**
#2			****	****	ns	***	ns	****	****			ns	ns	ns	ns	ns	ns	ns
#3				****	****	****	****	*	****				ns	ns	ns	ns	ns	ns
#4					****	ns	****	****	ns					ns	ns	****	**	ns
#5						ns	****	****	****						ns	**	ns	ns
#6							****	****	ns							**	ns	ns
#7								ns	****								ns	****
#8									****									**
#9																		

AREA PERIPHERY

	Day 3									Day 6								
	#1	#2	#3	#4	#5	#6	#7	#8	#9	#1	#2	#3	#4	#5	#6	#7	#8	#9
#1		ns	ns	ns	ns	ns	ns	ns	ns		ns	ns	ns	ns	*	****		ns
#2			ns	**	ns	ns	ns	ns	ns			ns	ns	ns	*	****		ns
#3				ns	***	ns	ns	ns	*				ns	ns	ns	****		ns
#4					****	ns	ns	ns	****					ns	ns	****		ns
#5						****	****	*	ns						***	****		ns
#6							ns	ns	**							****		ns
#7								ns	**									****
#8									ns									
#9																		

ROUNDNESS

	Day 3									Day 6								
	#1	#2	#3	#4	#5	#6	#7	#8	#9	#1	#2	#3	#4	#5	#6	#7	#8	#9
#1		*	**	****	ns	****	****	ns	****		**	ns	*	ns	***	ns	*	ns
#2			ns	****	**	****	****	ns	****			*	ns	*	ns	*	ns	ns
#3				****	***	****	****	ns	****				ns	ns	***	ns	ns	ns
#4					****	ns	ns	****	****					ns	ns	ns	ns	ns
#5						****	****	*	****						***	ns	ns	ns
#6							ns	****	ns							**	ns	ns
#7								****	ns								ns	ns
#8									****									ns
#9																		

Table 4: Statistics for figure 1B

Results

PDLS morphologically mimetize FL lymph nodes

In order to establish viable PDLS with FL lymph nodes, the first step aimed to determine the most suitable cell seeding densities and culture medium conditions. 10 000, 25 000 and 50 000 cells seeding densities were tested in different media (see supplemental Fig. 1) containing or not various cytokines supporting the survival/proliferation of B cells and T cells such as IL-15 [30],[31], ODN [31], CD40L [30], IL-4 [32], IL-2 [33],[34]). Based on a viability of up to 70%, 25 000 cells per well was the optimal cell seeding concentration to obtain spheroids and the enriched medium contained all cytokines (IL-15, ODN, CD40L, IL-4, IL-2).

Global morphology was examined by 2D imaging with a high throughput imaging confocal system (Fig. 1). We observed 3 different patterns (morphotypes) across the PDLS established from 9 different FL biopsies (Fig. 1A and supplemental figure 2). Most of them (patients #2, #4, #6, #7, #8 and #9) presented a thin monocellular layer and a round and dense cell aggregate in the clearly delineated center. For patient #5 we observed a second pattern with a thin layer that was more or less enlarged and the central aggregate was less structured and looked less dense. Finally, a third pattern exhibited a reduced and destructured thin layer and a large and disorganized central structure with no clear delimitation between monocellular layer and aggregated parts (#1 and #3).

In all cases, cell aggregation was very fast and dynamic as attested by live-cell imaging (video 1). After 6 days of culture, we observed a significant global increase of the PDLS size for most patients (6 out of 9). No strong variation of morphotype was observed compared to day 3 of culture, except for the patient #1 for which the aggregated part was enlarged. For patient #8, the inform aggregated central part became rounder and denser, and more predominant over the monolayer. Different parameters of spheroid morphology were determined (Fig.1B). With regard to the PDLS area, two criteria were measured: the center/core, composed of viable cells and the periphery/thin layer, composed mainly of dead cells (data not shown). Most PDLS presented an increase in the central area between day 3 and day 6 ranging from 13 to 152% corresponding to patient #5 and #7 respectively (Fig. 1B). For the periphery areas, 3 different profiles were observed (Fig. 1B). For PDLS established from patients #3 and #7, we observed a significant increase of the area between day 3 and day 6 of culture, whereas for patients #5 and #9 a decrease was measured. In contrast, for PDLS established from patients #1 and #2, no variation was observed. Similar to the area increase, roundness of core/center for most PDLS increased between day 3 and day 6 of cultures ranging from 22% to 115% for patients #3 and #2 respectively. We only observed a decrease in PDLS for patients #7 and #9. There

was an important variation in roundness observed from 0.2 (#5 at D3) to 0.8 (#6 at D6) according to the different types of morphology (Fig. 1A).

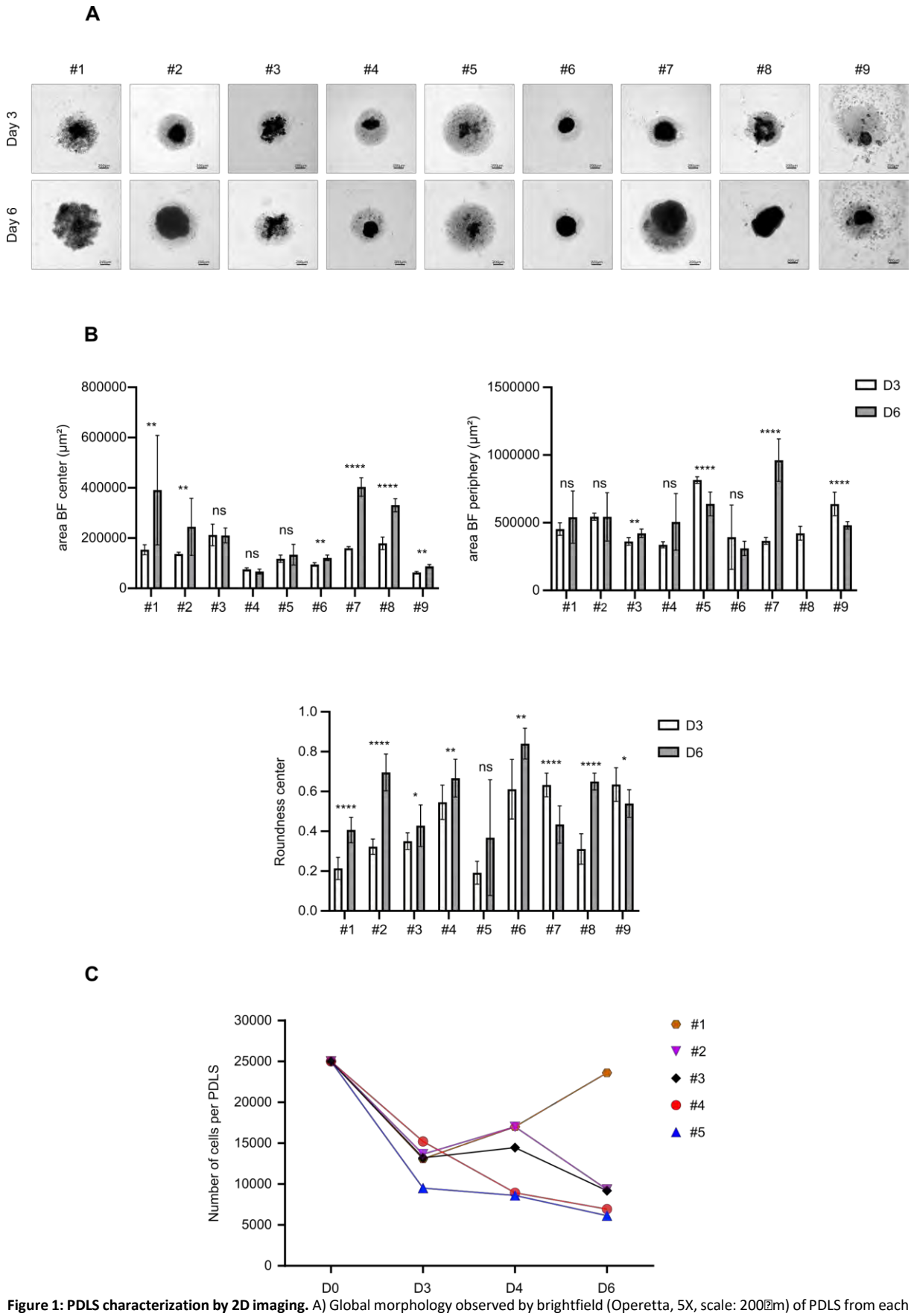

Figure 1: PDLS characterization by 2D imaging. A) Global morphology observed by brightfield (Operetta, 5X, scale: 200µm) of PDLS from each patient in untreated condition at D3 and D6. B) 2D imaging parameters. Graphs representing center/core and periphery areas (µm²) and roundness quantification (Columbus software) at D3 and D6 based on 2D brightfield images, with means +/- SD of up to 10 PDLS replicates for each patient. C) Cell number counting determined by Trypan blue assay during 3D culture.

Viable cell number was determined during the 3D culture from the thawing (day 0) up to day 6 of culture (Fig.2A). At day 3 of culture, a drop in the total cell number was observed compared to day 0, with an inter-patient variability ranging from 39.2% for #4 to 62% for #5. Except for one patient (#1) for which the total cell number increased between day 3 and day 6 of culture, in all PDLS tested (n=9), we noticed a decrease with a maximum of 62% for patient #4. However, viability was highly maintained for all PDLS (>60%) during this time course, but no longer at 9 days, where viability reached approximately 40% (data not shown).

IHC and FISH were then performed to determine the distribution of different immune cell types composing these PDLS and the bcl2 translocation (Fig.2A and Fig. 2B). Setting up of these experiments on PDLS samples was challenging due to their frailty. Thus, a protocol was set up to allow the inclusion of these samples in paraffin, which consisted in a first pre-inclusion step in agarose. This allowed a protection of the model, but it also facilitated the localisation of PDLS in paraffin thanks to a China ink coloration of agarose before the cutting of sections. The obtention of robust IHC and FISH results validated this pre-analytic process. On IHC (Fig.2A), a majority of B cells (CD20, CD79) was observed. On this FL case, CD10 staining was diffuse. T cells were present and mainly localised around PDLS, like a surrounding crown. No FDC were observed, potentially due to the non-enzymatic dissociation and freezing cycle. Proliferation was assessed by Ki-67 staining, which corresponded mainly to proliferative T cells. A FISH experiment was performed with a “break apart” probe to assess *BCL2* rearrangements in PDLS. As shown in Figure 2B, both normal B cells (green arrow) and lymphomatous B cells (yellow arrows), characterised by a *BCL2* split, were present. Altogether, these results confirmed that PDLS are structured models containing both tumour B cells and microenvironment cells.

Finally, RNA extractions and 3’mRNA sequencing were performed on 3 patient samples after thawing and after 3 days of 3D culture. Differential expression analyses between patient cells and 3D PDLS showed an enrichment of pathways and genes involved in cell cycle in the 3D models (Fig. 2C and Fig. 2D) which can be, in part, explained by favourable culture conditions. Comparison of these transcriptomes in view of several gene signatures involved in immune escape and outcome to validate the relevance of our model is currently under investigation in the laboratory.

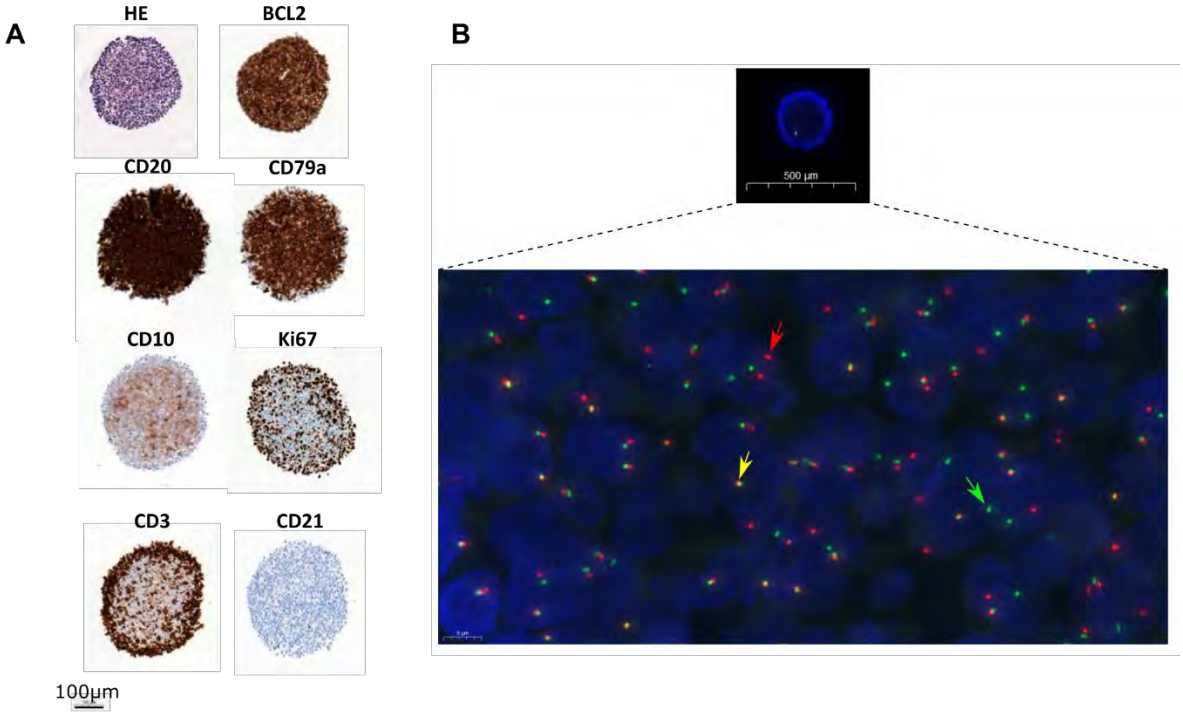
A
HE
BCL2
CD20
CD79a
CD10
Ki67
CD3
CD21
100µm
B
500 µm
C
Genes encoding cell cycle related targets of E2F transcription factor
HALLMARK E2F TARGETS
HALLMARK G2M CHECKPOINT
HALLMARK TNFA SIGNALING VIA NFKB
HALLMARK MITOTIC SPINDLE
HALLMARK APOPTOSIS
HALLMARK MTORC1 SIGNALING
HALLMARK INFLAMMATORY RESPONSE
HALLMARK ESTROGEN RESPONSE LATE
HALLMARK IL2 STAT5 SIGNALING
HALLMARK MYC TARGETS V1
Genes regulated by NF-kB in response to TNF
Genes involved in the G2/M checkpoint, as in progression through the cell division cycle
Genes important for mitotic spindle assembly
4
8
12
16
Fold Enrichment
N. of Genes
20
30
40
50
60
70
-log10(FDR)
20
40
60
D
- log10 (FDR)
0.0
0.5
1.0
1.5
-4
-2
0
2
4
6
log2 fold change
Upregulated
Downregulated

Figure 2: Global PDLS characterization by different approaches. A) IHC on sliced PDLS #4. B) FISH on sliced PDLS#4. C) RNA seq on thawed lymph node FL biopsies cultured in suspension and in 3D analysed at day 3. D) Volcano plot of genes significantly regulated in 3D model compared to initial FL biospies (log2 fold change threshold = 1, -log10 (FDR) threshold = 1).

Although 2D imaging provided us with important information with regard to aggregation, morphological patterns and parameters during the time of culture, this method is not suitable for in depth characterisation [25]. Thus, PDLS from 6 patients were imaged by 3D imaging (Fig. 3A) and morphological parameters such as real volume, sphericity and roundness were extracted (Fig. 3B). 3D imaging confirmed the above-depicted morphological patterns (See supplemental Fig. 2 for PDLS structure classification): Pattern #P1 that corresponded to a monocellular layer (in 2D) surrounding a compact, ovoid and well 3D-structured PDLS for patients #2, #4 and #6. Pattern #P2 that corresponded to a monocellular layer (2D) surrounding an irregular and poorly 3D-structured PDLS for patient #5. Finally, Pattern #P3 that corresponded to scrambled aggregates with no clear delimitation between 2D and 3D parts for patients #1 and #3.

For all the PDLS imaged in 3D, real volume increased between day 3 and day 6 of culture with the highest difference observed for patient #3 (Fig.3B). In contrast, sphericity and roundness did not mirror volume variation, but both exhibited same profiles and range of values, with an increase observed in 3 out of 6 patients (#1, #2, #4) (Fig.3B). For the others, patient #3 exhibited no sphericity and roundness variation, patient #5 exhibited no sphericity variation but displayed a decrease in roundness and finally patient #6 exhibited a decrease in both parameters. Moreover, we noticed a large scale of volume variation (0.0045 mm^3 to 0.05mm^3), sphericity (0.004 to 0.83) and roundness (0.03 to 0.88). Thus, PDLS displayed 3 patterns (#P1, #P2 and #P3) of distinct sphericity, roundness and volume.

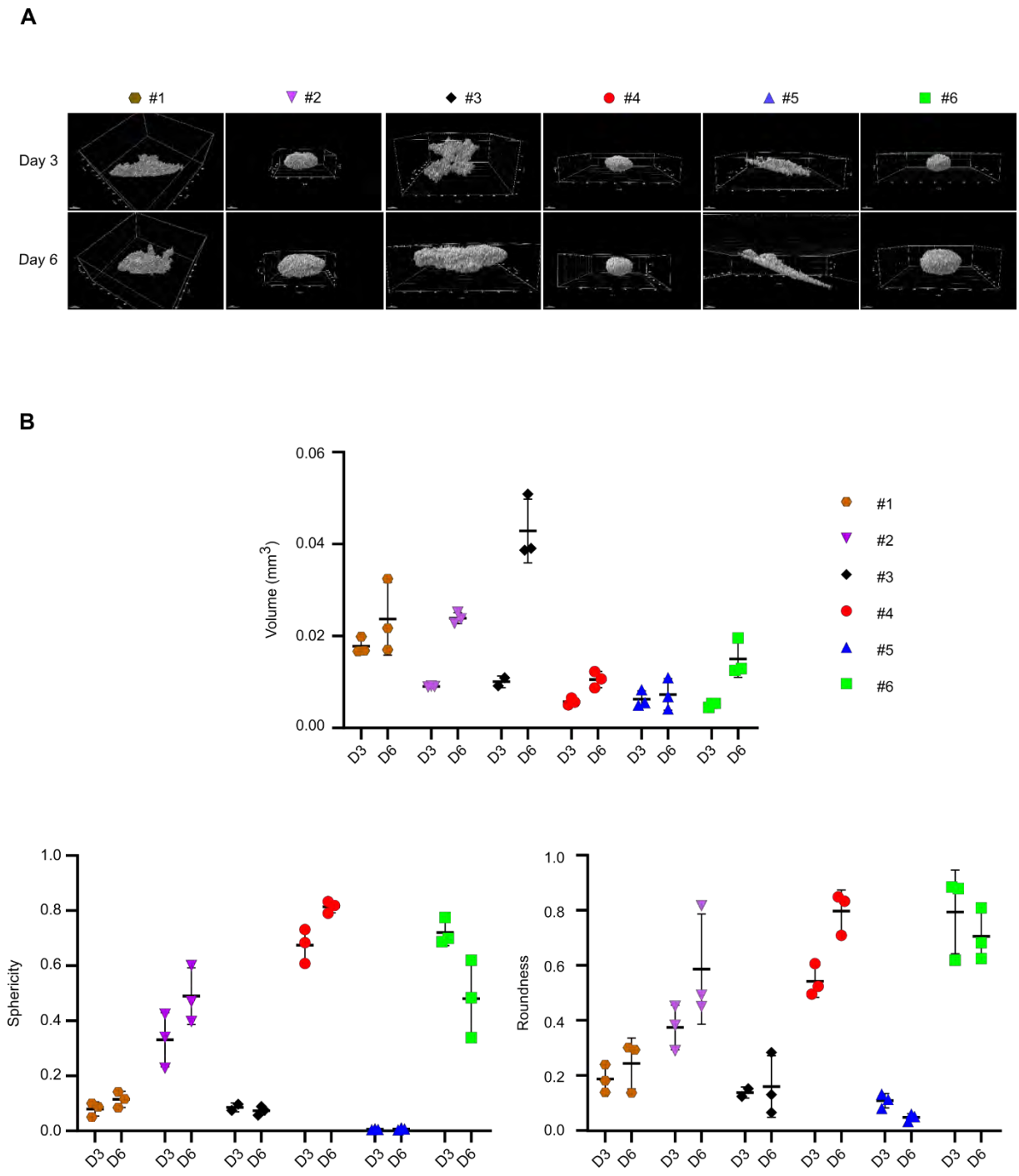

Figure 3: PDLS 3D imaging. A) 3D reconstruction by IMARIS from 880 confocal acquisitions at 10X magnification of PDLS labelled with PI and cleared by BABB for patients #1 to #6 at D3. B) Volume and morphology 3D quantification. Based on 3D acquisitions (A), Volume (mm^3), roundness and sphericity were calculated for each patient and represented as graphs. Mean +/- SD of up to 3 replicates per condition.

In total, FL biopsies can be cultured in 3D with an enriched medium which maintains a high viability. Moreover, 2D and 3D imaging analyses highlighted the inter-patient variability in terms of aggregation dynamics, morphology and behaviour during the time of culture. Very importantly, PDLS exhibited FL features as revealed by IHC and RNA sequencing, demonstrating that these 3D models closely represent their source biopsies.

PDLS Immune tumour microenvironment composition

FL TME is mainly composed of CD21+/CD35+ FDC, CD21+/CD35- FRC, CD68-CAF, CD4+ T, CD8+ T, gamma delta T and NK cells[2],[22],[35],[36]. We therefore performed multiparametric flow cytometry analyses to determine the composition of PDLS established from 9 different FL biopsies after 3 and 6 days of 3D culture and compared them to the initial biopsies (day 0). Unexpectedly, stromal cells were not detected in the biopsies after thawing and after 3D cell culture. On average, B lymphocytes (60% of total cells) were the prominent population composing the thawed samples, followed by CD4 (13%), CD8 (3%), NK (0.2%) and gamma delta T (0.07%) cells (Fig. 4A). Importantly, 3D cultures did not affect the percentage of each cell subtype at day 3 and only a slight decrease was observed for B cells with 44% of CD19+ cells at day 6. More precisely, biopsies and PDLS exhibited an inter-patient variability with regard to their content. B cells at day 0 ranged from 25% for the minimum (#5) to 84% for the maximum (#8) with a relatively stable percentage during the time of culture except for the patient exhibiting the lower level. In that case, percentage of B cells increased at day 3 (54%) and decreased at day 6 (12%). This variability was also observed for patient #6 for which the CD19+ cell rate decreased by 40%. Concerning the conventional T lymphocytes, the mean percentage of CD4+ and CD8+ cells for all patients was around 13% and 3% respectively at day 0 and day 3. At day 6, we observed an increase in the percentage of CD4+ for patients #5, #6 and #8 and of CD8+ cells for patients #5 and #6 (Fig. 4A).

Phenotyping of CD3+CD4+CXCR5+ICOS+ and CD3+CD4+CXCR5-ICOS- cells revealed that 40% of CD4+ T cells were TFh and 20% were non-TFh (Fig. 4B left). Individually, 3 profiles of patients were distinguished with a high percentage of TFh (more than 50% of CD4+ cells for patients #2 and #8), medium expression (around 30 % for patients #1, #3, #5, #7 and #9) and low percentage of TFh (less than 10% for patient #4). Regarding non-TFh cells, 3 different profiles also appeared with a high percentage (around 36% for patients #3 and #7), medium expression (around 20% for patients #1, #2, #4, #9) and low percentage (<10% for patients #5 and #8) (for more details, see supplementary results).

For innate immune cells, the percentage was very low ranging for NK cells between 0% for patient #5 and 1% for patient #7 and for gamma delta T cells, the percentage was quite similar between each PDLS of approximately 0.1% (Fig. 4B right).

The exact number of each immune cell sub-type was determined and presented at day 3 for each patient separately (Fig. 4C). Except for patient #2 who exhibited an equivalent number of CD4+T and CD19+ cells, for all other PDLS, B lymphocytes were the major cell population (range: n=3 000-7 000 cells over 10 000 total cells). PDLS were also composed of CD4+T (n=275-2300), to a lesser extent CD8+ T (n=61-250) cells but very few NK (n=39) and gamma delta T (n=11) cells.

Finally, we determined the basal level of T cell activation in 3 patients by measuring the amount of cytokines and granzyme B in the culture medium (Fig. 4D). Here again, 3 different profiles were observed: high (patient #7) intermediate (patient #9) or very low level of secreted cytokines (patient #8) (for more details, see supplementary results).

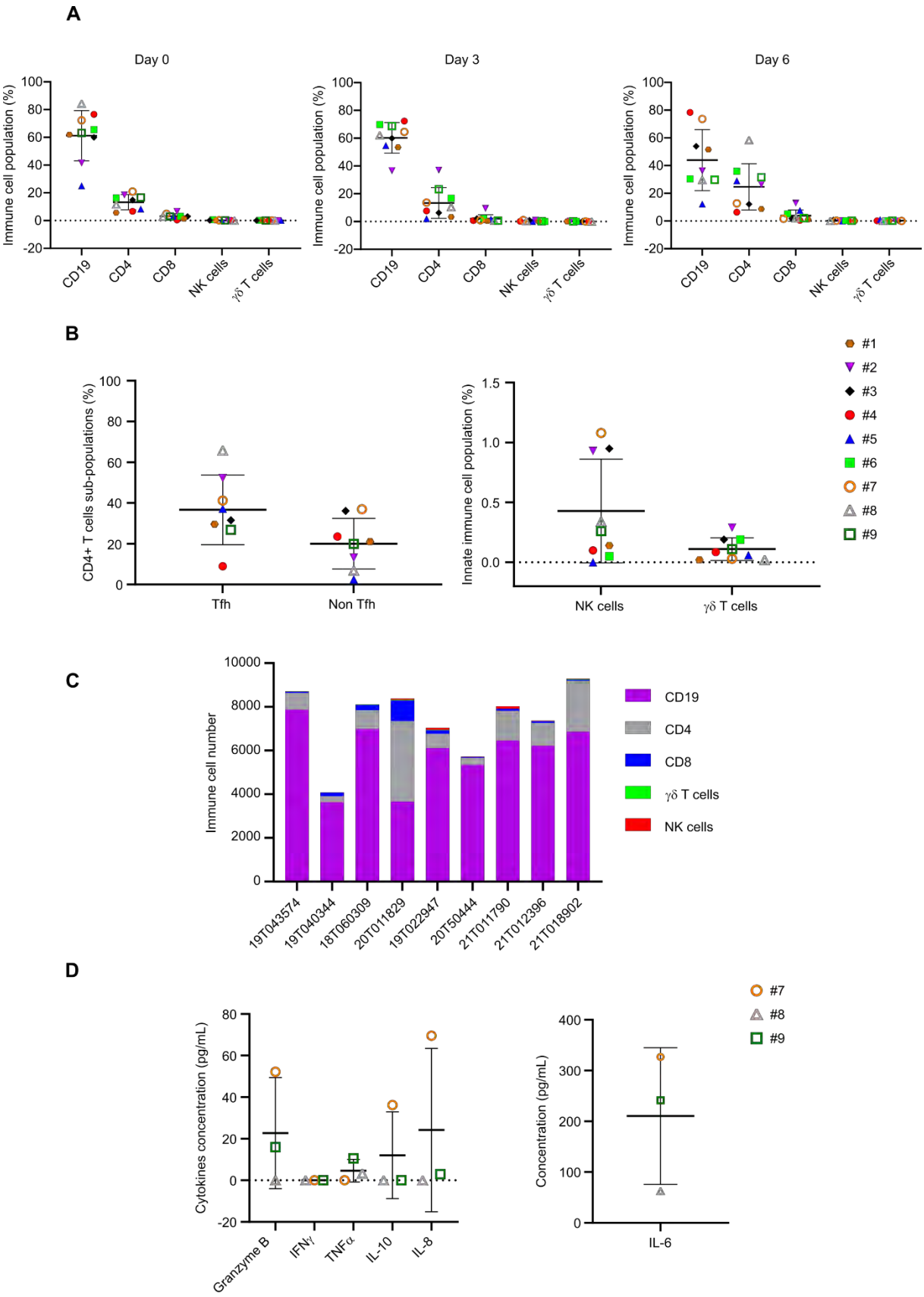

Figure 4: Immune cell distribution and cytokine release A) Percentage of immune cell evaluated by flow cytometry at day 0, day 3 and day6 of 3D culture. B) Percentage of TFh (CD3+CD4+CXCR5+ICOS+), non-TFh (CD3+CD4+CXCR5-ICOS-), NK (CD3-CD56+) and gamma delta T cells (CD3+TCRgamma9+) in PDLS at day 3 evaluated by flow cytometry. C) Cell count evaluated by flow cytometry at day 3 of PDLS immune cell composition. D) Cytokine release (Granzyme B, IFNg, TNFa, IL-10, IL-8, IL-6) were evaluated by flow cytometry at day 6 of culture.

***Altogether, these results highlighted PDLS as a relevant model exhibiting similar features to FL patients such as proportion of B/T cells and variability of immune cell composition. Moreover, these results also showed that PDLS culture conditions maintained the viability of cells composing the immune TME during the cell culture*.**

Immune escape characterisation

To further characterise PDLS, we investigated in detail the profile of immune checkpoint expression on different cell subtypes. BTLA-4, TIGIT, LAG-3, PD-1, TIM-3, CD39 and CD73 expression was determined at the cell surface of CD4 T and CD8 T cells after thawing (day 0, supplemental Fig. 3) and at day 3 and 6 of 3D culture (Fig. 5). Globally, no variation was observed during the culture (data not shown) and as presented in figure 5A, three different patterns of expression were observed. A high proportion (50-55%) of CD4+ cells expressed BTLA-4, TIGIT and PD-1, a medium (around 20%) percentage expressed CD39 and less than 10% expressed LAG-3, TIM-3 and CD73. On CD8+ lymphocytes, TIGIT and PD-1 were expressed by approximately 50% of cells, then TIM-3, CD39 and BTLA-4 by roughly 20-30% and less than 20% expressed LAG-3 and CD73. We also determined ICP expression on tumoural B cells (CD19+CD10+) and observed that PD-1 expression was less than 10% and CD39 around 20%. No CD73, PDL1 and PDL2 expression was measured. In healthy B cells (CD19+CD10-), the percentage of CD39 and CD73 was higher with approximately 50% and 30% respectively (Fig. 5B).

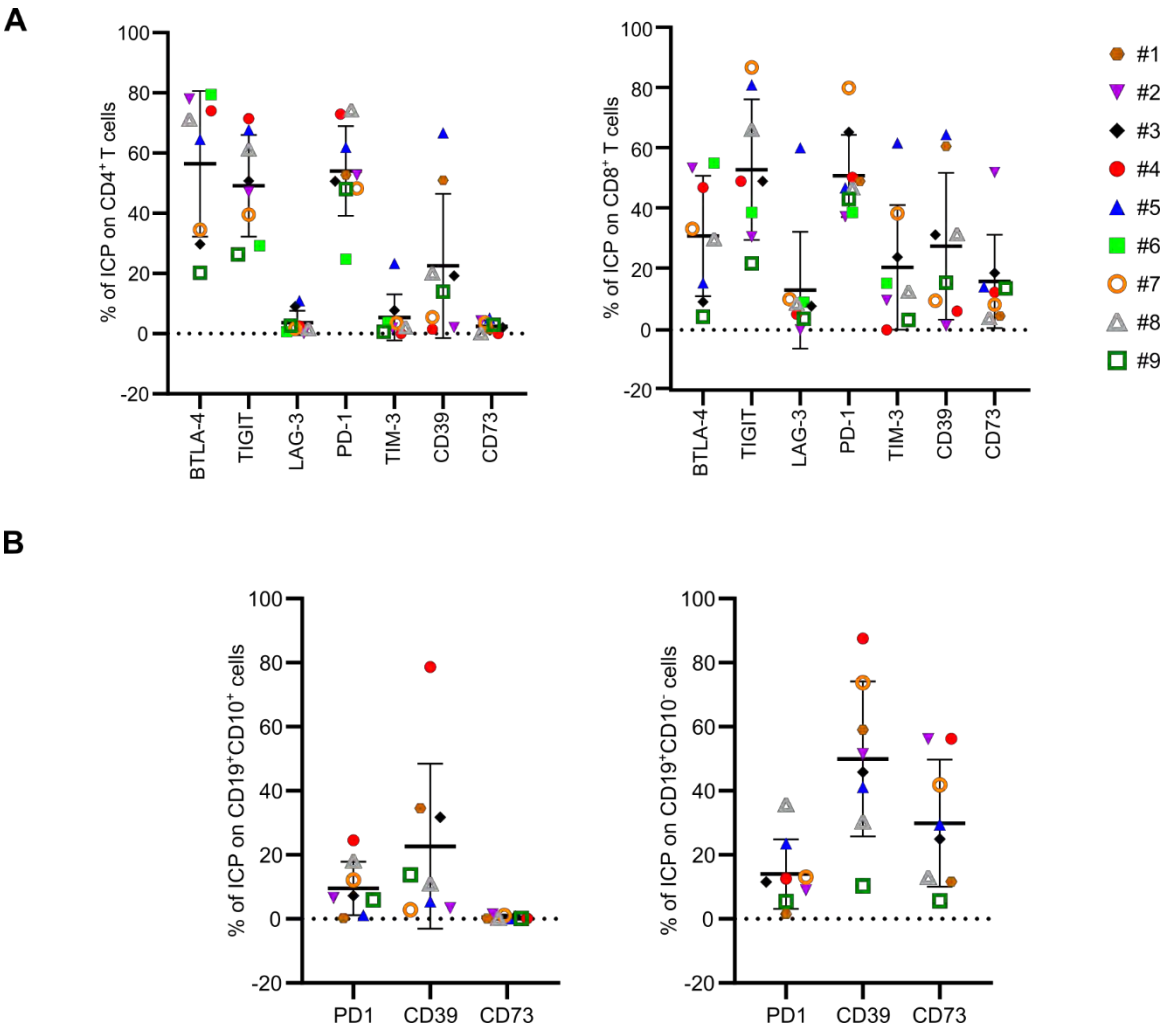

Figure 5: PDLS immune checkpoint characterization 10 PDLS from 8 different FL patients at day 3 of culture were pooled and the percentage of ICP was analysed by flow cytometry. A) percent of BTLA-4, TIGIT, LAG-3, PD-1, TIM-3, CD39, CD73 on CD4+ and CD8+ T cells. B) Percent of PD-1, CD39, CD73 on tumoural cells (CD10+CD19+) and healthy B cells (CD10-CD19+).

FL is characterised by the co-expression of ICP such as PD-1/TIM-3 [37], PD-1/TIGIT [38], PD-1/LAG-3 [39], PD-1/BLTA4 [40] which predicts patient outcome. Thus, we determined the level of double ICP expression on both CD4+ and CD8+ cells by applying different gating strategies (Fig.6A-E) and observed that globally, CD4+ were mainly PD-1+TIM-3- (48%) (Fig. 6A), PD-1+TIGIT+ (46%) (Fig. 6B), PD-1+BTLA-4+ (44%) (Fig. 6C) and PD-1+LAG-3- (48%). CD8+ were mostly PD-1-TIM-3- (42%) (Fig.6A) and PD-1+TIGIT+ (42%) (Fig.6B). Regarding BTLA-4 and PD-1, the percentage of PD-1-BTLA-4-, PD-1+BTLA-4- or PD-1+BTLA-4+ CD8+ cells were quite similar (30, 28 and 23% respectively) (Fig. 6C). For LAG-3 and PD-1, we observed 37% of PD-1-LAG-3- and 39% of PD-1+LAG-3- CD8+ cells. Finally, we determined the level of PD-1/CD39 as CD39 appeared to be an important marker in NHL [41],[42] and its co-expression with PD-1 was recently described in exhausted TIL in epithelial malignancies [43]. PDLS analyses revealed that CD39+ CD4+ or CD8+ cells were mainly PD-1+ with 16 and 21% respectively compared to 3.8 and 5.6% for PD-1- CD4+ and CD8+ cells (Fig. 6E).

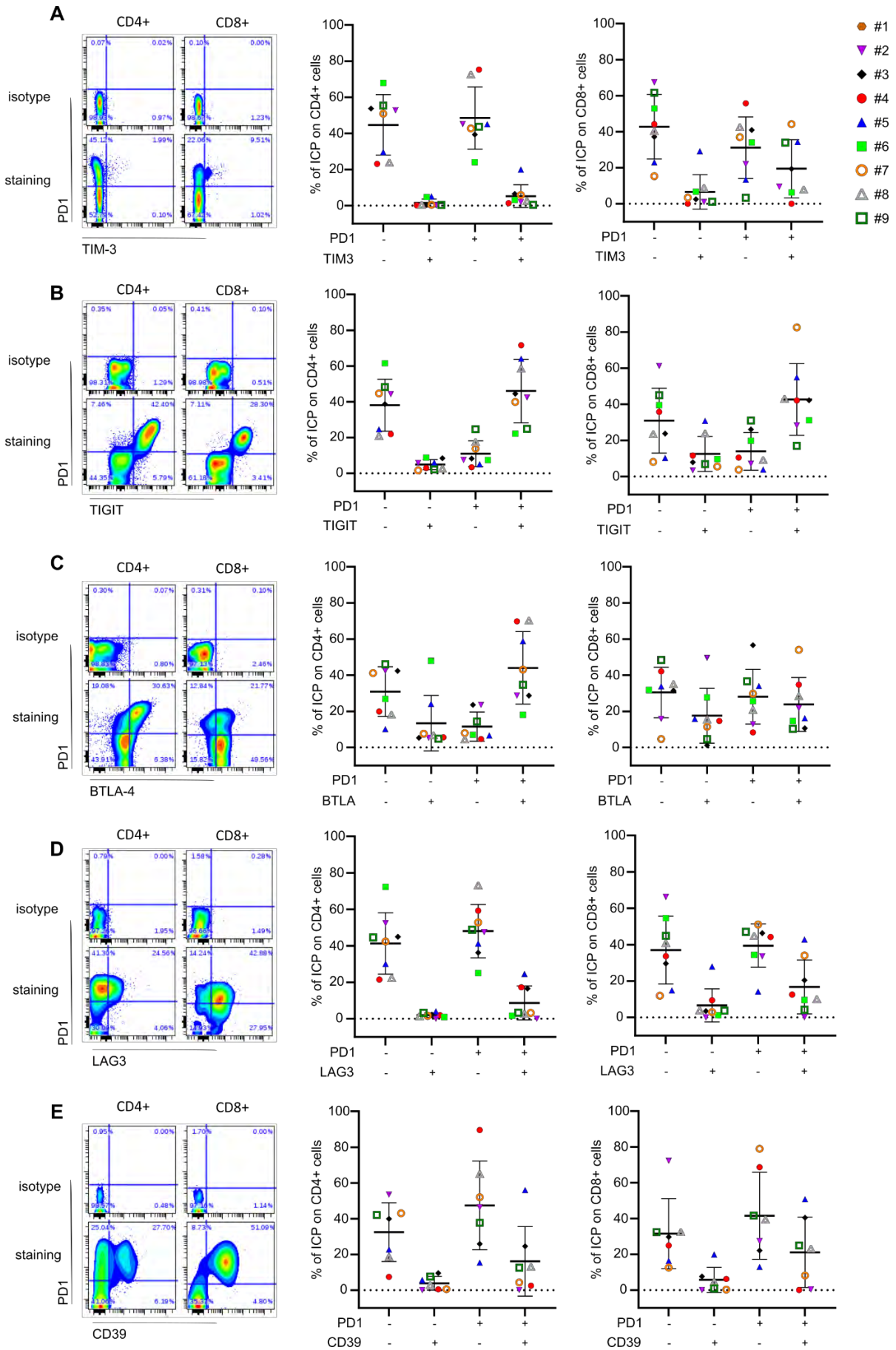

Figure 6: PDLS immune checkpoint characterization. 10 PDLS from 8 different FL patients at day 3 of culture were pooled and the percentage of ICP was analysed by flow cytometry. Left panel present gating strategies. Right panels represent percentage of CD4+ and CD8+ T cells expressing double ICP. PD-1/ TIM-3 (A), PD-1/TIGIT (B), PD-1/BTLA-4 (C), PD-1/LAG-3 (D) an PD-1/CD39 (E).

Co-expression of TIGIT and PD-1 on intratumoural T cells from FL has been described and this accounts for hyporesponsive T cells [38]. Thus, we further characterized the ICP expressing cells by analysing the percentage of CD4+ and CD8+ cells expressing one, two, three or four ICP (ie: PD-1, TIGIT, BTLA-4, TIM-3) (Fig. 7) according to [44]. LAG-3 was not included in this analysis as it was expressed by less than 3% of cells. Thus, the most frequent subpopulation in PDLS at day 3 of culture was PD-1+TIGIT+BTLA-4+TIM-3- cells with a mean of 31% for CD3+ and 34% for CD4 TILs. PD-1-TIGIT-BTLA-4+TIM-3- cells as well as the quadruple negative population were also largely represented with 12% and 20% respectively. The other populations were less than 3%. In more detail, the most frequent CD8+ TILs were PD-1-TIGIT-BTLA-4+TIM-3- with 11% and the quadruple negative with 14%. 13% were PD-1+TIGIT+BTLA-4+TIM-3- and 10% PD-1+TIGIT+BTLA-4-TIM-3+. For CD4+ cells, PD-1+TIGIT+BTLA-4+TIM-3- was the most frequent subpopulation with 34%, then PD-1-TIGIT-BTLA-4+TIM-3- with 18% and the quadruple negative population with 20%. The rest was less than 5%.

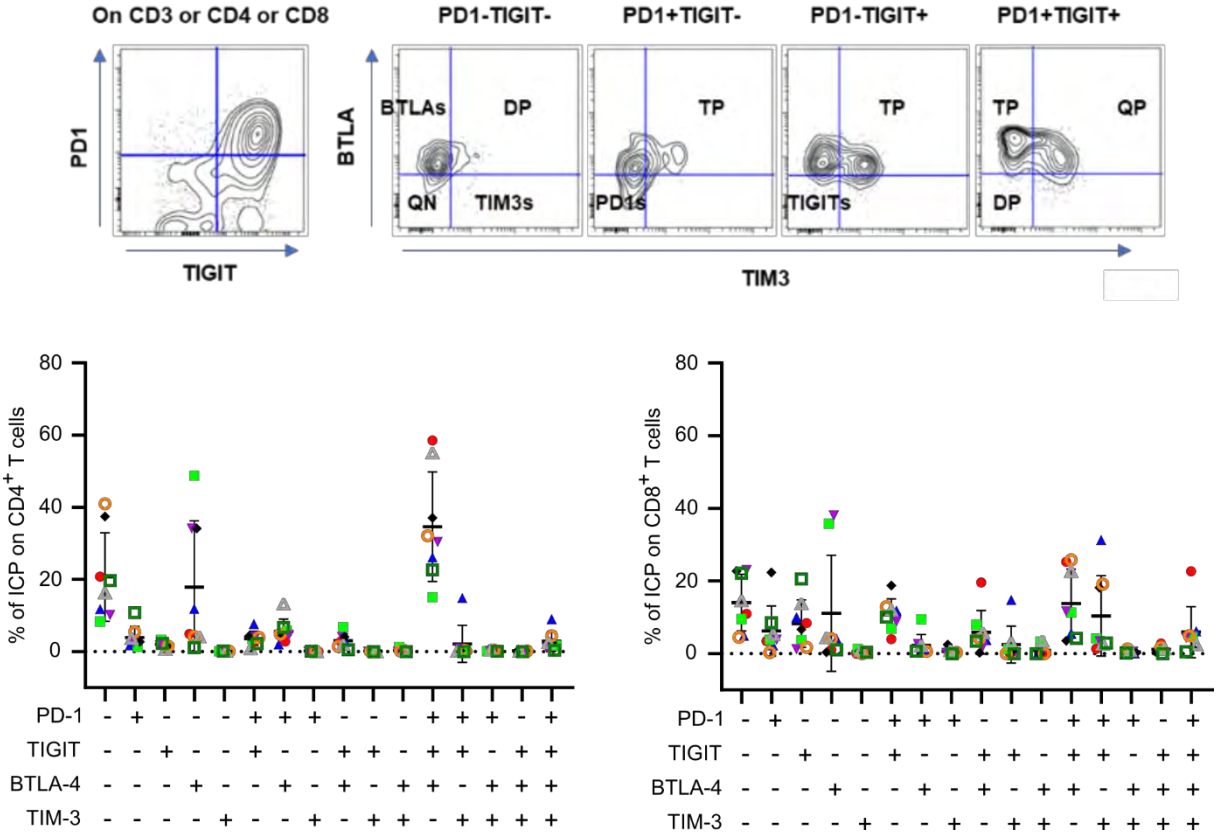

Figure 7: simple, double, triple and quadruple immunecheckpoint characterization. Gating strategy used for determining simple, double, triple and quadruple ICP populations (upper panel) and simple, double, triple and quadruple positive percent of cells expressing ICP (BTLA-4, TIGIT, PD-1, TIM-3) on CD3+, CD4+ and CD8+ T cells of 9 different FL patients at day 3 of culture (lower panel).

Altogether, these flow cytometry analyses highlighted the inter-patient variability in terms of ICP co-expression and unveiled PD-1+TIGIT+BTLA-4+TIM-3- as the main T cell phenotype in FL tumours. Moreover, CD39+PD-1+ TILs also appeared as an interesting population infiltrating FL tumours. Thus, these results strongly support the use of PDLS for testing immunotherapy in a context of personalised medicine.

PDLS as preclinical FL models

Finally, we aimed to determine whether PDLS could represent preclinical models for drug screening. For this purpose, we tested an anti-CD20 mAb used for FL therapy, obinutuzumab (GA101) combined or not with the anti-PD-1 mAb, nivolumab. We established a workflow adapted for medium throughput screening in 96-well plates and developed specific tools to study the effect of therapies on PDLS morphology and behaviour as well as B cell depletion. 2D imaging allowed a global characterisation of PDLS by BF microscopy and the observation of different patterns after drug treatment (Fig. 8A and 8B). Anti-CD20 mAb induced a decrease of the PDLS center area, which represents the zone where viable cells aggregate, in 3 out of 8 patients (#1, #5, #9) and an increase in 2 patients (#4 and #3). Anti-PD-1 mAb induced different morphological behaviours with an increase in 3 PDLS (#1, #2, #3) and a decrease for patients #4, #9 and especially #5. However, combination treatment did not enhance the effect induced by anti-CD20 mAb as a single drug (Fig. 8B left graph). BF periphery area (grey zone) representing dead cells (not shown) was measured (Fig 8B, right graph). No potent variation was observed after anti-CD20 treatment except for two patients (#4 and #7) where a decrease was observed. In contrast, anti-PD-1 mAb treatment induced a slight increase in the BF periphery area in 4 out of 8 patients and a really potent increase for patient #4, while the 2 other patients displayed a small decrease. Anti-CD20 and anti-PD-1 mAbs combination did not modify the effects induced by single drugs except for patients ##6 and #9 where combination induced a larger periphery area.

We next investigated in depth by 3D confocal imaging the effect of these therapeutic antibodies (Fig. 8C). First, we observed the already described 3D shape differences between patients in untreated condition (UT). Anti-CD20 alone or in combination with anti-PD-1 seemed to strongly modify #3 and #2 PDLS morphology.

As for Fig. 3B, volume, sphericity and roundness extracted from 3D imaging were determined by specific algorithms developed for ULA-MALC [25] and PDLS (Fig. 8D). We observed a decrease of PDLS volume in the 3 patients tested after anti-CD20 treatment and two of them were also sensitive to anti-PD-1 treatment (#4 and #2). Combination seemed to enhance the volume decrease in the

patients' sensitive to single drugs. Sphericity and roundness were also determined but exhibited potent inter-patient variation. For patient #4, both sphericity and roundness decreased after anti-CD20 or anti-PD-1 mAbs treatment and combination did not enhance these effects. For patient #2, anti-PD-1 mAb alone affected sphericity, whereas roundness was decreased by both single drugs, but surprisingly not with the combination where an increase was observed. Finally, for patient #3, which was the most non spherical model (sphericity= 0.07 in untreated condition), anti-CD20 mAb increased the sphericity and roundness, whereas anti-PD-1 mAb decreased sphericity and increased roundness. The combination did not modify the effect of single drugs on sphericity or roundness (Fig. 8D).

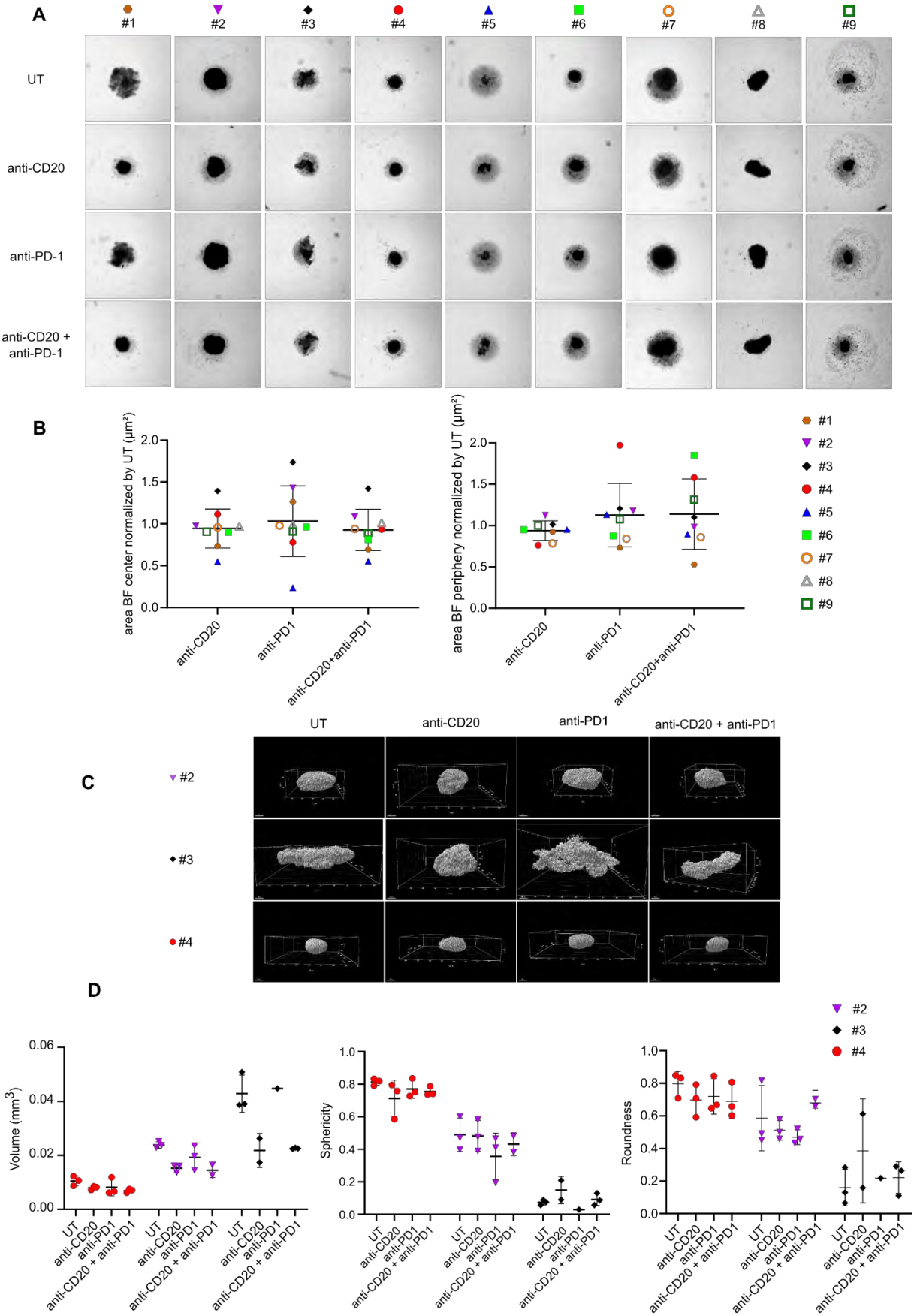

Figure 8: Drug effect on PDLS 3D morphology and volume. A) Global morphology with BF images (Operetta, 5X, scale: 200□m) of PDLS from each patient in untreated (UT) condition and treated conditions (anti-CD20, anti-PD-1, anti-CD20+anti-PD-1) at D6 of culture after 72h of treatment. B) 2D imaging parameters. Graphs representing center/core and periphery areas (□m²) quantification (Columbus software) based on 2D BF images in (A), with mean +/- SD of the 8 patients pooled (for each condition, the value for each patient correspond to the mean of up to 10 PDLS replicates). C) 3D reconstruction by IMARIS from 880 confocal acquisitions at 10X magnification of PDLS labeled with PI and cleared by BABB for patients #2, #3 and #4 at D6 in untreated and treated conditions. D) Volume and morphology 3D quantification. Based on 3D acquisitions (C), Volume (mm³), roundness and sphericity were calculated for each patient and each condition and represented as graphs. Mean +/- SD of up to 3 replicates per condition.

Altogether, these results showed the ability to assess the effect of immunotherapies on the volume and the morphology of PDLS and the inter-patient variability. It also underlined the importance of studying therapeutic efficacy beyond 2D imaging.

Flow cytometry analyses were then performed on dissociated PDLS to evaluate the effect of treatment on target cells based on B cell depletion. Thus, we observed that in 8 out of 9 PDLS tested, anti-CD20 mAb induced a potent CD19+ B cell depletion (up to 80%) in a similar fashion at 24 hrs and 72 hrs of treatment (Fig. 9A), which correlated with a decrease in the B cell number (Fig. 9B). Regarding anti-PD-1, only 3 out of 9 PDLS responded to treatment. Interestingly, 2 out of 9 patients exhibited an increase of B cell depletion once anti-CD20 was combined to anti-PD-1 mAb as early as 4 hrs of treatment (Fig.9C). For PDLS from patients #2, #3 and #4 the B cell depletion observed was correlated with 3D volume variation in response to treatments (Fig. 8D).

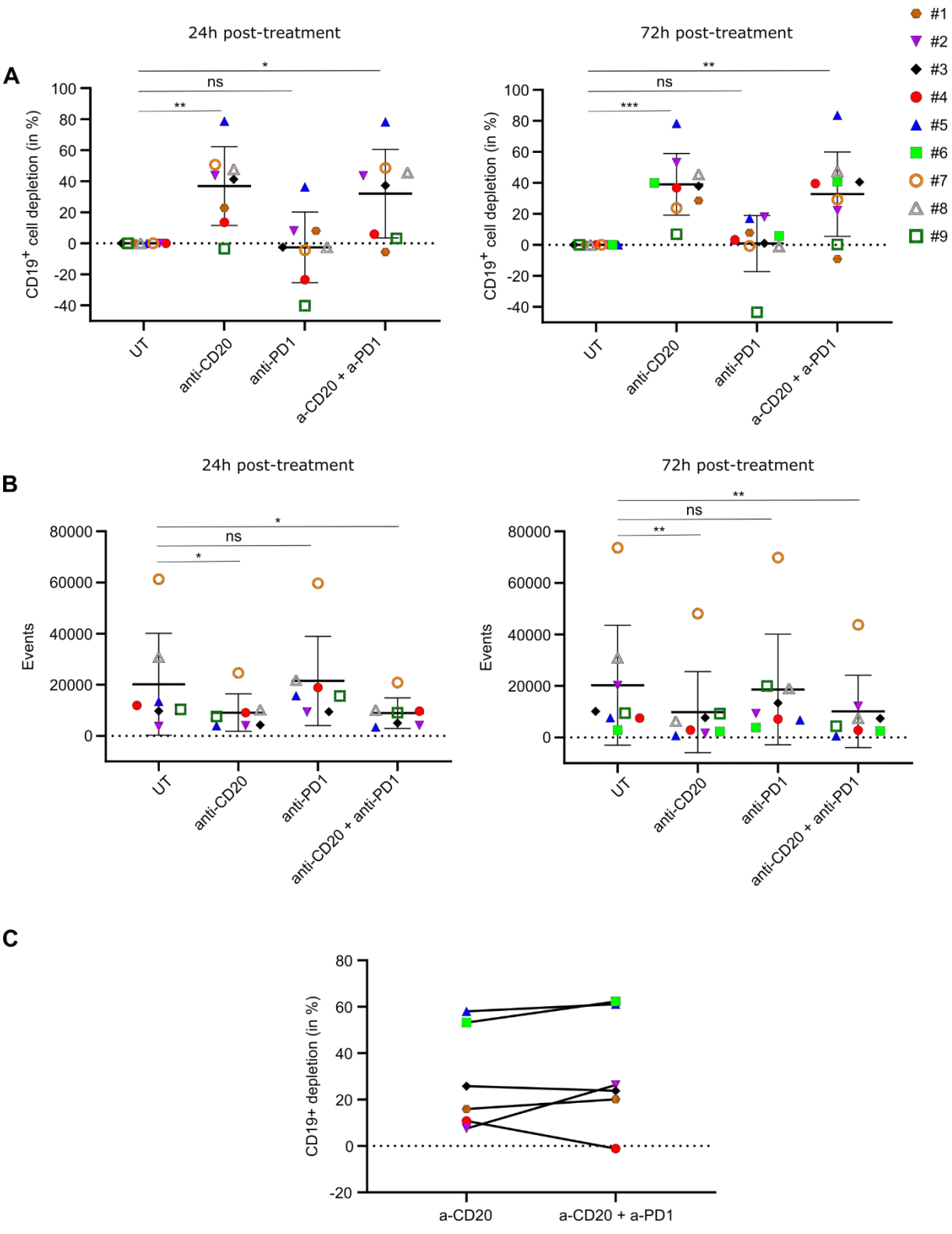

Figure 9: B cell depletion evaluation upon anti-CD20 and anti-PD-1 mAb treatments Flow cytometry analyses were performed after pooling 10 PDLS from 6 to 9 different FL patients 24 hrs and 72 hrs after treatment with anti-CD20 (GA101 10µg/mL) and/or anti-PD-1 (10µg/mL). A) Depletion in percentage of CD19+ B cells at 24 hrs and 72 hrs post-treatments. B) Event counting by flow cytometry upon treatments 24 hrs and 72 hrs post-treatment. C) CD19+ B cell depletion measured after 4 hrs of treatment with anti-CD20 combined or not with anti-PD-1 mAb.

Based on results obtained by flow cytometry (Fig.5, 6, 7 and 9), a correlogram was established to assess potential correlations between B depletion and ICP expression on CD4+ and CD8+ populations. To do so, double positive (PD-1+/TIM-3+, PD-1+/TIGIT+, PD-1+/BTLA+, PD-1+/LAG-3+) and triple positive (PD-1+/TIM-3+/LAG-3+) population percentage and B cell depletion percentage obtained after 72 hrs of treatment with anti-CD20 and anti-PD-1 alone or in combination were used to generate a matrix of correlation represented as a correlogram (Fig. 10A). With this side-by-side comparison, we observed notably that the percentage of PD-1+/TIM-3+ double positive CD8+ population only was negatively correlated with the B depletion after 72 hrs of treatment with anti-PD-1, anti-CD20 and combination of both (detailed in Fig. 10B). PD-1+/BTLA+ percentage in CD4+ population was negatively correlated with B depletion but only in response to anti-PD-1 treatment. PD-1+/LAG-3+ percentage in both CD4+ and CD8+ populations were negatively correlated with B cell depletion in response to the two single treatment (anti-CD20 and anti-PD-1) but not to the combo, with a higher score for CD4+ populations after treatment with anti-CD20 mAb (-0.68). Interestingly, it seemed to be the same tendency for triple positive PD-1+/TIM-3+/LAG-3+ percentage but to a lesser extent.

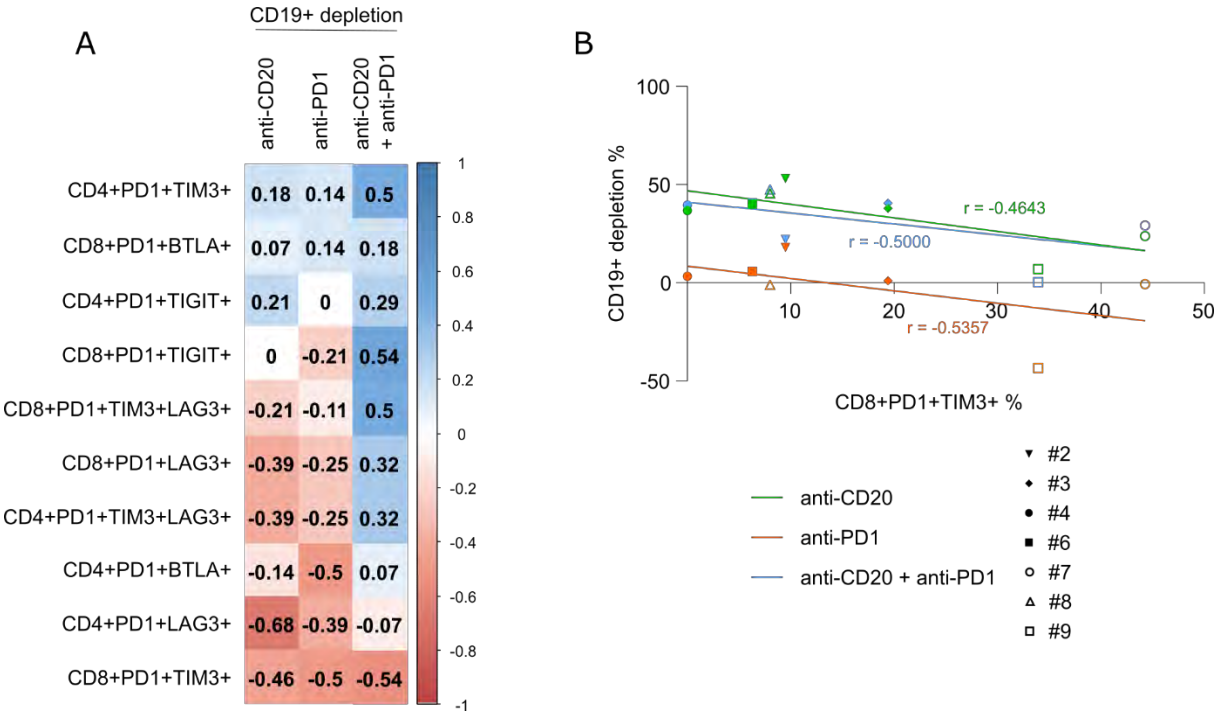

Figure 10: Correlations between ICP expression and B cell depletion A) Values from PDLS (7 different FL patients) gathered for all the parameters listed: percentage of PD-1+/TIM3+/LAG3- and PD-1+/TIM3+/LAG3+ CD4+ and CD8+ cells and percentage of B cell depletion (normalized by untreated condition) after 72 hrs of treatment by anti-CD20, anti-PD-1 and combination. Matrix of correlation based on correlation coefficients (non-parametric Spearman's correlation) of side-by-side represented as a graph. Correlation coefficients represented by squares where values and colour were determined according to correlation coefficients values. B) Correlation curves of percentage of

PD1+TIM3+ expressing CD8+cells (X axis) and percentage of B cell depletion after 72 hrs of treatment (Y axis) with correlation coefficients (r) extracted from correlogram in A.

Altogether, these correlations suggested a potential link between the expression of ICP and the response to anti-PD-1 and anti-CD20 mAbs and suggested PD-1+TIM-3+ expression on CD8+ cells as a marker of lower response to both single or combo treatment.

Discussion

PDLS are of particular relevance to understand FL biology and immune cell distribution. Indeed, IHC analyses revealed that the 3D FL model reproduces the same pattern of expression as observed in biopsies with CD79a, BCL2, CD10 and CD20 labelling and peripheral distribution of T cells. Moreover, with 3D imaging and specific algorithms developed recently for ULA-MALC [25], we were able to observe an inter-patient variability of shape with 3 different patterns of aggregation and different profiles of response to treatment. Indeed, PDLS from patient #3, which was not well structured and exhibited the least roundness and sphericity, was the one that responded better to mAbs. This could be explained by the fact that it is easier for the mAb to penetrate the 3D structure when it is less compact. Although the number of samples could not allow us to draw clear conclusions, these results highlight another application based on the use of PDLS as in vitro models to characterise the mechanisms of action of anti-lymphomatous drugs and model volume, aggregation, ECM production or mechanical constraints, parameters which can influence sensitivity to drugs. Obviously, we have to move on from PDLS towards tumouroids for a more optimal mimicry of the pathology. Thus, co-culture of FL samples with FRC, FDC, monocytes and/or endothelial cells from the same donor are needed to recreate in vitro, to some degree, a complete FL TME. Moreover, integration of microchannels could be of particular interest to study immune cell migration or drug perfusion.

We developed PDLS models from FL biopsies without any sorting in order to keep B cells and the TME. Unfortunately, we were faced with a major limitation due to the absence of FRC, FDC, MSC and TMA which are key actors in the supportive FL niche [3][5]. This was certainly due to the biopsy's mechanical dissociation and/or the freezing/thawing cycle needed to obtain the diagnosis in order to culture FL samples in an appropriate enriched medium. Our observation that primary FL cell viability increases when medium was supplemented (59% in medium #1, 64% in medium #2, 67% % in medium #3, 75% % in medium #4 and 79% in medium #5) indicates that these cells require a culture medium that mimics pro-survival signals provided by supportive missing cells from the TME. Thus, we defined an enriched medium supplemented with different cytokines (IL-15 [30],[31], ODN [31], CD40L [30], IL-4 [32], IL-2

[33],[34]) providing B cell survival or T cell proliferation. We are aware that these cytokines can induce a bias in the interpretation and to deal with this issue, we are currently performing experiments to improve the obtention of full FL TME with enzymatic FL biopsy dissociation that could avoid the use of cytokines in the medium. Unfortunately, until now, no convincing results have been obtained. Working on fresh samples would be the most appropriate but the feasibility of the global workflow could not be performed and the 3D culture would most likely not be optimal in a non-specific medium for FL.

The clinical development of effective cancer immunotherapies has allowed the identification of tumour environmental features that could predict for sensitivity to ICP blockade. While impressive efficacy was observed in Hodgkin and primary mediastinal-B cell lymphomas, disappointing results were obtained in FL or DLBCL [45]. NHL are categorised as inflamed or non-inflamed tumours [45]. Large-scale microarray profiling revealed four stages of IE in B-NHL: stage I represented by non-immunogenic tumours, stage II represented by immunogenic tumours without IE, stage III represented by immunogenic tumours with IE and stage IV represented by fully immune-edited tumours [36]. 73% of FL exhibit a stage III or IV showing a strong level of IE mechanism in these tumours. Tosolini et al also correlated each stage with OS and observed that stages I and IV presenting the least T cell activation presented the poorest OS. On the opposite, stages II and III presenting T cell activation exhibited a higher OS. This immune landscape of lymphoma is a critical point to predict the response to immunotherapy and to design new therapeutic approaches [45],[46]. FL is an indolent lymphoma with abundant levels of PD-1-positive infiltrating T-cells [47] that can co-express other exhausted markers such as TIM-3 [37], TIGIT [38], LAG-3 [39] or BTLA-4 [40] that predict patient outcome. Thus, it is becoming clear that FL specific features must be taken into account in pre-clinical studies to predict patient response. As characterised by multiparametric flow cytometry analyses, PDLS have similar and relevant inter-patient variability as that observed in the biopsy from which they originate. Indeed, the immune cell population characterisation revealed not only that PDLS were mainly composed, as expected, of B cells and T cells (CD8+ T cells, CD4+ T cells, TFh, non-TFh, NK and gamma delta T cells) in variable proportions amongst patients, but they also exhibited similar ICP expression profiles after 3 days of culture compared to day 0 (supplemental Fig.4). Moreover, by determining the percentage of ICP expressed on both CD4+ and CD8+ cells and measuring the B cell depletion

after anti-CD20 or anti-PD-1 mAb treatment or combination, we observed that the double expression of PD-1 and TIM-3 on CD8+ cells negatively correlated with the sensitivity to treatments. This is in accordance with clinical results obtained on FL patients where PD-1low TIM-3+ CD8+ cells were associated with a poor outcome in FL patients [37].

Conclusion

Altogether, we present evidence that PDLS are relevant pre-clinical FL models that can be used to help characterise FL pathology and predict patient response. They are also useful for drug testing, new target discovery, characterisation of mechanisms of action and/or resistance to anti-lymphomatous drugs. As TME can be classified into six specialised microenvironments, namely, hypoxic niche, immune microenvironment, metabolism microenvironment, acidic niche, innervated niche, and mechanical microenvironment [48], we firmly believe that PDLS, by modelling all these parameters, are powerful theragnostic biomaterials that combine therapy with diagnosis necessary for individualised therapies for patients. This is all the more true in the current context of the development of CAR-T cells for refractory/relapsed FL. By combining tumour modelling of each patient with medical imaging and bioinformatic tools to analyse genomic data, it should be possible to provide a full ID card of each patient and to propose personalised therapies in a disease that remains incurable.

Acknowledgements: We are grateful to our healthcare professionals for their boundless investment during the COVID-19 crisis. Authors thank Julie Bordenave from Inserm CRCT, Toulouse, France for technical help on initial experiments on FL biopsies. L Ligat, M Farcé and M Tosoloni from the Pôle technologique du CRCT for their advice on flow cytometry, 2D imaging, 2D imaging analyses, all members of JJ Fournié/ C Laurent's team (CRCT, Toulouse, France) for their stimulating comments, Pascale Bernes-Lasserre, Aurélie Gomez, Marine Norlund and Valérie Lobjois from IMACTIV-3D (Toulouse) and Laetitia Pieruccioni and Jacques Rouquette from RESTORE Research Center, Toulouse) for their fruitful discussions and advice on 3D imaging. Stéphanie Grenard, Annie Alloy and François-Xavier Frenois from plateforme Imag'IN Platform, Toulouse for IHC experiments on PDLS. Authors also thank Anne-Marie Benot, Stephanie Nevouet and Muriel Bouas for administrative support and Cathy Greenland for English proofreading.

Author Contributions: FG, CF and CB designed the experimental strategy, organised the experiments and collected and analysed the data. CF, FG, PG, CDL, JGV, CR performed *in vitro* experiments. CF performed experiments of flow cytometry and on the operetta system, analysed data with the Columbus software and developed a macro adapted from Ivanov. NVA performed IHC and FISH experiments. CQ and GJ performed 3'RNA sequencing. FG performed experiments for SPIM and confocal imaging. FG performed experiments, RM generated specific algorithms for 3D image processing. FG, RM and JML analysed 3D imaging analyses. PG, NVA and CL developed IHC specifically for PDLS and analysed labelling. LY and CL selected FL samples and provided patients clinical datas. CB and PPG co-supervised and discussed the experiments. CF, FG and CB wrote the manuscript. All authors discussed and approved the manuscript.

Funding: This work was part of an Interreg POCTEFA program (IMLINFO EFA281/16/). This study was also funded by the Institut Claudius Regaud CLCC (CIEL, R20027BB), TOUCAN (G20000BB), imCORE network on behalf of F. Hoffmann-La Roche (TALYIES, R21080BB), institutional grants from INSERM, Université Paul Sabatier and CNRS. P. Gravelle was supported by the CALYM Carnot Institute and F. Gava by TOUCAN (G20000BB).

Conflicts of Interest: RM, PBL and JML are employees of Imactiv3D.

References:

1. Scott, D.W.; Gascoyne, R.D. The Tumour Microenvironment in B Cell Lymphomas. *Nat Rev Cancer* **2014**, *14*, 517–534, doi:10.1038/nrc3774.
2. Carbone, A.; Roulland, S.; Gloghini, A.; Younes, A.; von Keudell, G.; López-Guillermo, A.; Fitzgibbon, J. Follicular Lymphoma. *Nat Rev Dis Primers* **2019**, *5*, 83, doi:10.1038/s41572-019-0132-x.
3. Amé-Thomas, P.; Tarte, K. The Yin and the Yang of Follicular Lymphoma Cell Niches: Role of Microenvironment Heterogeneity and Plasticity. *Seminars in Cancer Biology* **2014**, *24*, 23–32, doi:10.1016/j.semcancer.2013.08.001.
4. Chraa, D.; Naim, A.; Olive, D.; Badou, A. T Lymphocyte Subsets in Cancer Immunity: Friends or Foes. *J Leukoc Biol* **2019**, *105*, 243–255, doi:10.1002/JLB.MR0318-097R.
5. Dobaño-López, C.; Araujo-Ayala, F.; Serrat, N.; Valero, J.G.; Pérez-Galán, P. Follicular Lymphoma Microenvironment: An Intricate Network Ready for Therapeutic Intervention. *Cancers (Basel)* **2021**, *13*, 641, doi:10.3390/cancers13040641.
6. Dobaño-López, C.; Araujo-Ayala, F.; Serrat, N.; Valero, J.G.; Pérez-Galán, P. Follicular Lymphoma Microenvironment: An Intricate Network Ready for Therapeutic Intervention. *Cancers (Basel)* **2021**, *13*, 641, doi:10.3390/cancers13040641.
7. Sutherland, R.M.; McCredie, J.A.; Inch, W.R. Growth of Multicell Spheroids in Tissue Culture as a Model of Nodular Carcinomas. *J Natl Cancer Inst* **1971**, *46*, 113–120.
8. Bissell, M.J. Goodbye Flat Biology - Time for the 3rd and the 4th Dimensions. *J Cell Sci* **2017**, *130*, 3–5, doi:10.1242/jcs.200550.
9. Kunz-Schughart, L.A.; Freyer, J.P.; Hofstaedter, F.; Ebner, R. The Use of 3-D Cultures for High-Throughput Screening: The Multicellular Spheroid Model. *J Biomol Screen* **2004**, *9*, 273–285, doi:10.1177/1087057104265040.
10. Friedrich, J.; Seidel, C.; Ebner, R.; Kunz-Schughart, L.A. Spheroid-Based Drug Screen: Considerations and Practical Approach. *Nat Protoc* **2009**, *4*, 309–324, doi:10.1038/nprot.2008.226.
11. Pampaloni, F.; Stelzer, E. Three-Dimensional Cell Cultures in Toxicology. *Biotechnol Genet Eng Rev* **2010**, *26*, 117–138, doi:10.5661/bger-26-117.
12. Sirenko, O.; Mitlo, T.; Hesley, J.; Luke, S.; Owens, W.; Cromwell, E.F. High-Content Assays for Characterizing the Viability and Morphology of 3D Cancer Spheroid Cultures. *Assay Drug Dev Technol* **2015**, *13*, 402–414, doi:10.1089/adt.2015.655.
13. Maura, R.; Francesco, A.; Simona, R.; Elena, S.; Claudio, A. Three-Dimensional Models: A Novel Approach for Lymphoma Research. *J Cancer Res Clin Oncol* **2022**, *148*, 753–765, doi:10.1007/s00432-021-03897-9.
14. Tian, Y.F.; Ahn, H.; Schneider, R.S.; Yang, S.N.; Roman-Gonzalez, L.; Melnick, A.M.; Cerchietti, L.; Singh, A. Integrin-Specific Hydrogels as Adaptable tumour Organoids for Malignant B and T Cells. *Biomaterials* **2015**, *73*, 110–119, doi:10.1016/j.biomaterials.2015.09.007.
15. Mannino, R.G.; Santiago-Miranda, A.N.; Pradhan, P.; Qiu, Y.; Mejias, J.C.; Neelapu, S.S.; Roy, K.; Lam, W.A. 3D Microvascular Model Recapitulates the Diffuse Large B-Cell Lymphoma tumour Microenvironment in Vitro. *Lab Chip* **2017**, *17*, 407–414, doi:10.1039/c6lc01204c.
16. Sabhachandani, P.; Sarkar, S.; Mckenney, S.; Ravi, D.; Evens, A.M.; Konry, T. Microfluidic Assembly of Hydrogel-Based Immunogenic tumour Spheroids for Evaluation of Anticancer Therapies and Biomarker Release. *J Control Release* **2019**, *295*, 21–30, doi:10.1016/j.jconrel.2018.12.010.
17. Foxall, R.; Narang, P.; Glaysher, B.; Hub, E.; Teal, E.; Coles, M.C.; Ashton-Key, M.; Beers, S.A.; Cragg, M.S. Developing a 3D B Cell Lymphoma Culture System to Model Antibody Therapy. *Front Immunol* **2020**, *11*, 605231, doi:10.3389/fimmu.2020.605231.
18. Lamaison, C.; Latour, S.; Hélaine, N.; Le Morvan, V.; Saint-Vanne, J.; Mahouche, I.; Monvoisin, C.; Dussert, C.; Andrique, L.; Deleurme, L.; et al. A Novel 3D Culture Model Recapitulates Primary FL B-Cell Features and Promotes Their Survival. *Blood Adv* **2021**, *5*, 5372–5386, doi:10.1182/bloodadvances.2020003949.

19. Gravelle, P.; Jean, C.; Valleron, W.; Laurent, G.; Fournié, J.-J. Innate Predisposition to Immune Escape in Follicular Lymphoma Cells. *Oncoimmunology* **2012**, *1*, 555–556, doi:10.4161/onci.19365.
20. Decaup, E.; Jean, C.; Laurent, C.; Gravelle, P.; Fruchon, S.; Capilla, F.; Marrot, A.; Al Saati, T.; Frenois, F.-X.; Laurent, G.; et al. Anti-tumour Activity of Obinutuzumab and Rituximab in a Follicular Lymphoma 3D Model. *Blood Cancer J* **2013**, *3*, e131, doi:10.1038/bcj.2013.32.
21. Gravelle, P.; Jean, C.; Familiades, J.; Decaup, E.; Blanc, A.; Bezombes-Cagnac, C.; Laurent, C.; Savina, A.; Fournié, J.-J.; Laurent, G. Cell Growth in Aggregates Determines Gene Expression, Proliferation, Survival, Chemoresistance, and Sensitivity to Immune Effectors in Follicular Lymphoma. *Am J Pathol* **2014**, *184*, 282–295, doi:10.1016/j.ajpath.2013.09.018.
22. Rossi, C.; Gravelle, P.; Decaup, E.; Bordenave, J.; Poupot, M.; Tosolini, M.; Franchini, D.-M.; Laurent, C.; Morin, R.; Lagarde, J.-M.; et al. Boosting Γδ T Cell-Mediated Antibody-Dependent Cellular Cytotoxicity by PD-1 Blockade in Follicular Lymphoma. *Oncoimmunology* **2019**, *8*, 1554175, doi:10.1080/2162402X.2018.1554175.
23. Decaup, E.; Rossi, C.; Gravelle, P.; Laurent, C.; Bordenave, J.; Tosolini, M.; Tourette, A.; Perrial, E.; Dumontet, C.; Poupot, M.; et al. A Tridimensional Model for NK Cell-Mediated ADCC of Follicular Lymphoma. *Front Immunol* **2019**, *10*, 1943, doi:10.3389/fimmu.2019.01943.
24. Vidal-Crespo, A.; Matas-Céspedes, A.; Rodriguez, V.; Rossi, C.; Valero, J.G.; Serrat, N.; Sanjuan-Pla, A.; Menéndez, P.; Roué, G.; López-Guillermo, A.; et al. Daratumumab Displays in Vitro and in Vivo Anti-tumour Activity in Models of B-Cell Non-Hodgkin Lymphoma and Improves Responses to Standard Chemo-Immunotherapy Regimens. *Haematologica* **2020**, *105*, 1032–1041, doi:10.3324/haematol.2018.211904.
25. Gava, F.; Faria, C.; Gravelle, P.; Valero, J.G.; Dobaño-López, C.; Morin, R.; Norlund, M.; Gomes, A.; Lagarde, J.-M.; Rossi, C.; et al. 3D Model Characterization by 2D and 3D Imaging in t(14;18)-Positive B-NHL: Perspectives for In Vitro Drug Screens in Follicular Lymphoma. *Cancers* **2021**, *13*, 1490, doi:10.3390/cancers13071490.
26. Horvath, P.; Aulner, N.; Bickle, M.; Davies, A.M.; Nery, E.D.; Ebner, D.; Montoya, M.C.; Östling, P.; Pietiäinen, V.; Price, L.S.; et al. Screening out Irrelevant Cell-Based Models of Disease. *Nat Rev Drug Discov* **2016**, *15*, 751–769, doi:10.1038/nrd.2016.175.
27. Jaffe, E.S. The 2008 WHO Classification of Lymphomas: Implications for Clinical Practice and Translational Research. *Hematology Am Soc Hematol Educ Program* **2009**, 523–531, doi:10.1182/asheducation-2009.1.523.
28. Dent, J.A.; Polson, A.G.; Klymkowsky, M.W. A Whole-Mount Immunocytochemical Analysis of the Expression of the Intermediate Filament Protein Vimentin in Xenopus. *Development* **1989**, *105*, 61–74.
29. Dodt, H.-U.; Leischner, U.; Schierloh, A.; Jährling, N.; Mauch, C.P.; Deininger, K.; Deussing, J.M.; Eder, M.; Zieglgänsberger, W.; Becker, K. Ultramicroscopy: Three-Dimensional Visualization of Neuronal Networks in the Whole Mouse Brain. *Nat Methods* **2007**, *4*, 331–336, doi:10.1038/nmeth1036.
30. Amé-Thomas, P.; Le Priol, J.; Yssel, H.; Caron, G.; Pangault, C.; Jean, R.; Martin, N.; Marafioti, T.; Gaulard, P.; Lamy, T.; et al. Characterization of Intratumoural Follicular Helper T Cells in Follicular Lymphoma: Role in the Survival of Malignant B Cells. *Leukemia* **2012**, *26*, 1053–1063, doi:10.1038/leu.2011.301.
31. Mongini, P.K.A.; Gupta, R.; Boyle, E.; Nieto, J.; Lee, H.; Stein, J.; Bandovic, J.; Stankovic, T.; Barrientos, J.; Kolitz, J.E.; et al. TLR-9 and IL-15 Synergy Promotes the In Vitro Clonal Expansion of Chronic Lymphocytic Leukemia B Cells. *J Immunol* **2015**, *195*, 901–923, doi:10.4049/jimmunol.1403189.
32. Pangault, C.; Amé-Thomas, P.; Ruminy, P.; Rossille, D.; Caron, G.; Baia, M.; De Vos, J.; Roussel, M.; Monvoisin, C.; Lamy, T.; et al. Follicular Lymphoma Cell Niche: Identification of a Preeminent IL-4-Dependent T(FH)-B Cell Axis. *Leukemia* **2010**, *24*, 2080–2089, doi:10.1038/leu.2010.223.

33. Coppola, C.; Hopkins, B.; Huhn, S.; Du, Z.; Huang, Z.; Kelly, W.J. Investigation of the Impact from IL-2, IL-7, and IL-15 on the Growth and Signaling of Activated CD4+ T Cells. *IJMS* **2020**, *21*, 7814, doi:10.3390/ijms21217814.
34. Maddaly, R.; Subramaniyan, A.; Balasubramanian, H. Cancer Cytokines and the Relevance of 3D Cultures for Studying Those Implicated in Human Cancers. *J Cell Biochem* **2017**, *118*, 2544–2558, doi:10.1002/jcb.25970.
35. Braza, M.S.; Caraux, A.; Rousset, T.; Lafaye de Micheaux, S.; Sicard, H.; Squiban, P.; Costes, V.; Klein, B.; Rossi, J.-F. Γδ T Lymphocytes Count Is Normal and Expandable in Peripheral Blood of Patients with Follicular Lymphoma, Whereas It Is Decreased in tumour Lymph Nodes Compared with Inflammatory Lymph Nodes. *J.I.* **2010**, *184*, 134–140, doi:10.4049/jimmunol.0901980.
36. Tosolini, M.; Algans, C.; Pont, F.; Ycart, B.; Fournié, J.-J. Large-Scale Microarray Profiling Reveals Four Stages of Immune Escape in Non-Hodgkin Lymphomas. *OncoImmunology* **2016**, *5*, e1188246, doi:10.1080/2162402X.2016.1188246.
37. Yang, Z.-Z.; Grote, D.M.; Ziesmer, S.C.; Xiu, B.; Novak, A.J.; Ansell, S.M. PD-1 Expression Defines Two Distinct T-Cell Sub-Populations in Follicular Lymphoma That Differentially Impact Patient Survival. *Blood Cancer J* **2015**, *5*, e281, doi:10.1038/bcj.2015.1.
38. Josefsson, S.E.; Beiske, K.; Blaker, Y.N.; Førsund, M.S.; Holte, H.; Østenstad, B.; Kimby, E.; Köksal, H.; Wälchli, S.; Bai, B.; et al. TIGIT and PD-1 Mark Intratumoural T Cells with Reduced Effector Function in B-Cell Non-Hodgkin Lymphoma. *Cancer Immunol Res* **2019**, *7*, 355–362, doi:10.1158/2326-6066.CIR-18-0351.
39. Yang, Z.-Z.; Kim, H.J.; Villasboas, J.C.; Chen, Y.-P.; Price-Troska, T.; Jalali, S.; Wilson, M.; Novak, A.J.; Ansell, S.M. Expression of LAG-3 Defines Exhaustion of Intratumoural PD-1+ T Cells and Correlates with Poor Outcome in Follicular Lymphoma. *Oncotarget* **2017**, *8*, 61425–61439, doi:10.18632/oncotarget.18251.
40. Carreras, J.; Lopez-Guillermo, A.; Kikuti, Y.Y.; Itoh, J.; Masashi, M.; Ikoma, H.; Tomita, S.; Hiraiwa, S.; Hamoudi, R.; Rosenwald, A.; et al. High TNFRSF14 and Low BTLA Are Associated with Poor Prognosis in Follicular Lymphoma and in Diffuse Large B-Cell Lymphoma Transformation. *J Clin Exp Hematop* **2019**, *59*, 1–16, doi:10.3960/jslrt.19003.
41. Hilchey, S.P.; Kobie, J.J.; Cochran, M.R.; Secor-Socha, S.; Wang, J.-C.E.; Hyrien, O.; Burack, W.R.; Mosmann, T.R.; Quataert, S.A.; Bernstein, S.H. Human Follicular Lymphoma CD39+-Infiltrating T Cells Contribute to Adenosine-Mediated T Cell Hyporesponsiveness. *J Immunol* **2009**, *183*, 6157–6166, doi:10.4049/jimmunol.0900475.
42. Cardoso, C.C.; Auat, M.; Santos-Pirath, I.M.; Rudolf-Oliveira, R.C.M.; da Silva, J.P.; Lange, B.G.; Siegel, D.; de Moraes, A.C.R.; Del Moral, J.A.G.; Santos-Silva, M.C. The Importance of CD39, CD43, CD81, and CD95 Expression for Differentiating B Cell Lymphoma by Flow Cytometry: CD39, CD43, CD81, AND CD95 FOR LYMPHOMA DIAGNOSIS. *Cytometry* **2018**, *94*, 451–458, doi:10.1002/cyto.b.21533.
43. Balança, C.-C.; Salvioni, A.; Scarlata, C.-M.; Michelas, M.; Martinez-Gomez, C.; Gomez-Roca, C.; Sarradin, V.; Tosolini, M.; Valle, C.; Pont, F.; et al. PD-1 Blockade Restores Helper Activity of tumour-Infiltrating, Exhausted PD-1hiCD39+ CD4 T Cells. *JCI Insight* **2021**, *6*, 142513, doi:10.1172/jci.insight.142513.
44. Balança, C.-C.; Scarlata, C.-M.; Michelas, M.; Devaud, C.; Sarradin, V.; Franchet, C.; Martinez Gomez, C.; Gomez-Roca, C.; Tosolini, M.; Heaugwane, D.; et al. Dual Relief of T-Lymphocyte Proliferation and Effector Function Underlies Response to PD-1 Blockade in Epithelial Malignancies. *Cancer Immunol Res* **2020**, *8*, 869–882, doi:10.1158/2326-6066.CIR-19-0855.
45. Kline, J.; Godfrey, J.; Ansell, S.M. The Immune Landscape and Response to Immune Checkpoint Blockade Therapy in Lymphoma. *Blood* **2020**, *135*, 523–533, doi:10.1182/blood.2019000847.
46. Laurent, C.; Charmpi, K.; Gravelle, P.; Tosolini, M.; Franchet, C.; Ysebaert, L.; Brousset, P.; Bidaut, A.; Ycart, B.; Fournié, J.-J. Several Immune Escape Patterns in Non-Hodgkin's Lymphomas. *Oncoimmunology* **2015**, *4*, e1026530, doi:10.1080/2162402X.2015.1026530.
47. Richendollar, B.G.; Pohlman, B.; Elson, P.; Hsi, E.D. Follicular Programmed Death 1-Positive Lymphocytes in the tumour Microenvironment Are an Independent Prognostic

Factor in Follicular Lymphoma. *Hum Pathol* **2011**, *42*, 552–557, doi:10.1016/j.humpath.2010.08.015.
48. Jin, M.-Z.; Jin, W.-L. The Updated Landscape of tumour Microenvironment and Drug Repurposing. *Signal Transduct Target Ther* **2020**, *5*, 166, doi:10.1038/s41392-020-00280-x.

Supplementary results:

Phenotyping (Fig. 4B)

Individually, 3 profiles of patients were distinguished with patients #2 and #8 which exhibited high percentage of TFh (52.21% and 65.87% respectively), patients #1, #3, #5, #7 and #9 exhibiting a medium expression and finally patient #4 presenting a low percentage of TFh (8.95%). Regarding non-TFh cells, 3 different profiles also appeared with patients #3 and #7 expressing the highest percentage (around 36%), patients #1, #2, #4, and #9 with a medium expression (around 20%) and patients #5 and #8 exhibiting the lowest percentage (<10%).

Cytokine release (Fig. 4C)

3 different profiles were observed with patient #7 exhibiting the highest levels of GrB, IL-10, IL-8 and IL-6 (52.17 pg/mL, 36.18 pg/mL, 69.54 pg/mL and 326.76pg/mL respectively), patient #9 with an intermediate level of GrB and IL-6 secretion (10.55 pg/mL and 241.47 pg/mL respectively) and finally patient #8 for which almost all cytokines were very low (0 to 3 pg/mL for GrB, TNFa, IFNg, IL-8, IL-10 and 62.87 pg/mL for IL-6).

Supplemental figures :

A

Composition	#A	#B	#C	#D	#E
IMDM + HiClonel serum	+	+	+	+	+
IMDM + Hiclonel + Mongini enrichment	-	+	+	+	+
ODN + IL-15	-	-	+	+	+
IL-2+IL-4	-	-	-	+	+
CD40-L	-	-	-	-	+

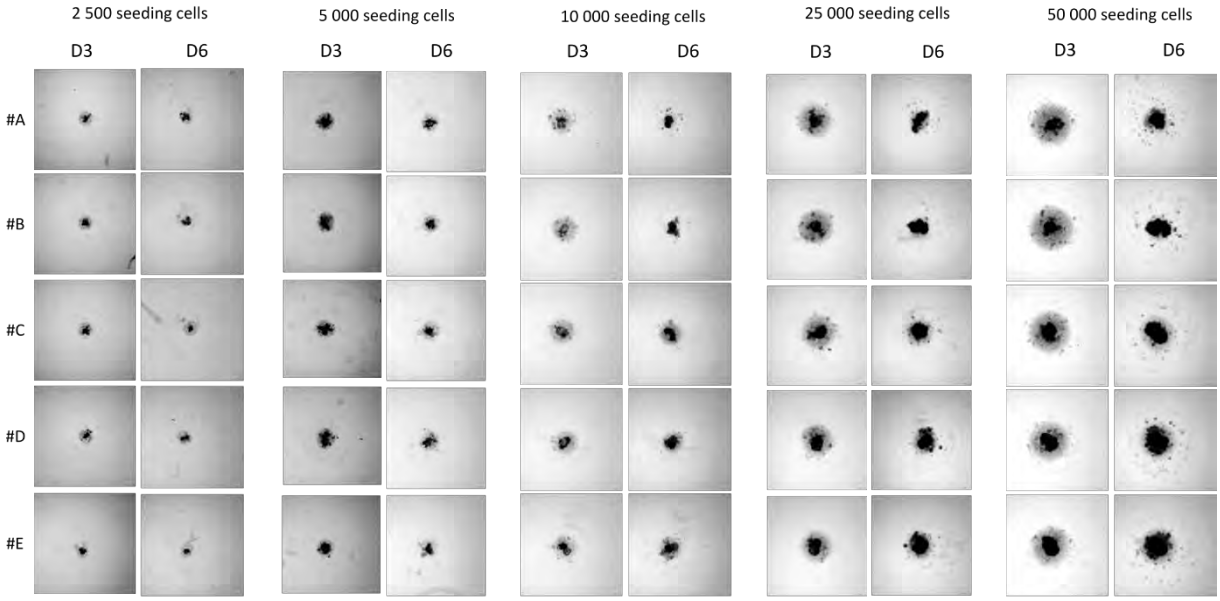

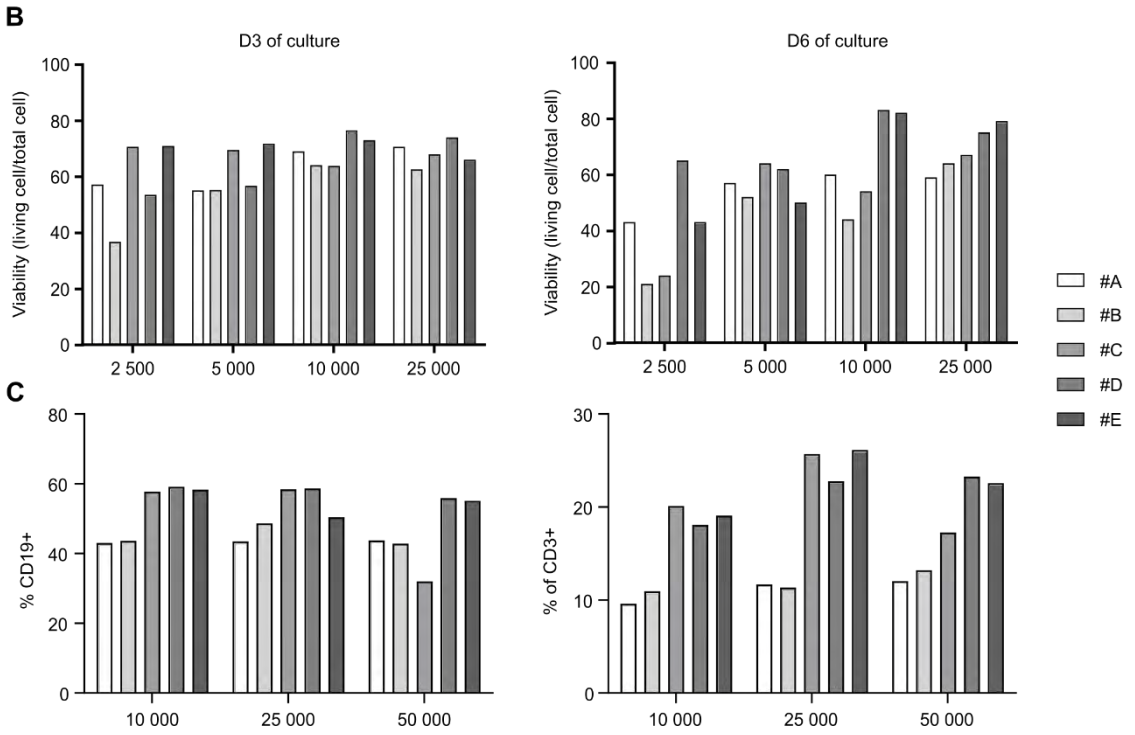

Supplementary Figure 1: Cell seeding densities and media testing on PDLS A) Table of different media tested. B. Illustration of PDLS from one patient cultured at different cell seeding densities and in different media. B) Trypan blue assay counting of living cells with different cell densities and media. C) Percentage of B and T cells in the different conditions of cell seeding and media.

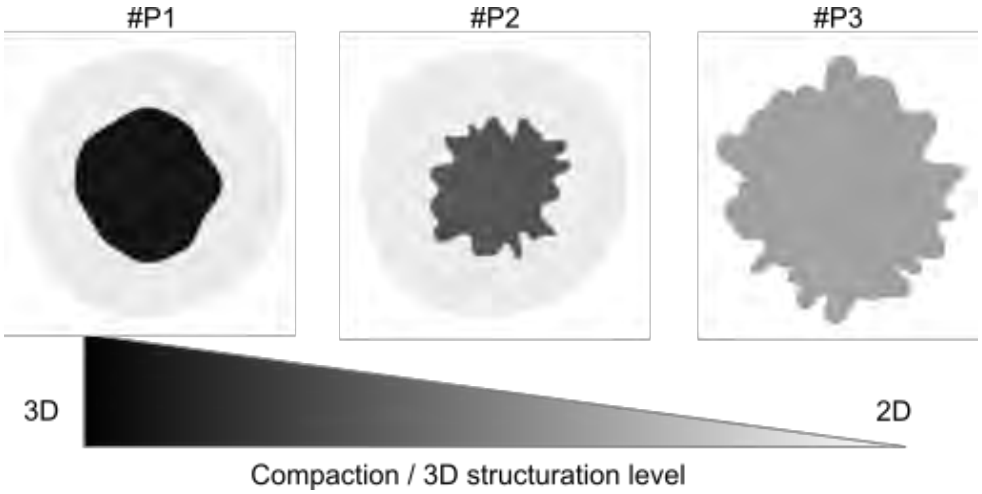

Supplementary Figure 2: Patterns of PDLS morphology Schematic morphological patterns according to the patients' PDLS. This classification is taking into account the number and shape of phases and the 3D structuration (white to black scale).

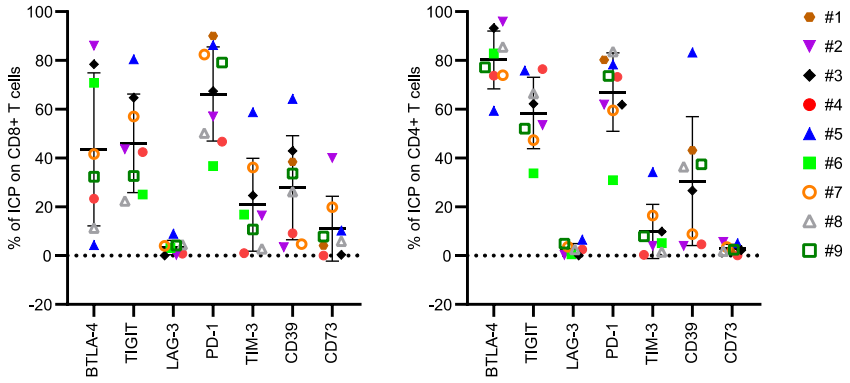

Supplementary Figure 3: PDLS immune checkpoint characterisation. 10 PDLS from 9 different FL patients were pooled and the percentage of ICP was analysed by flow cytometry. A. percentage of BTLA-4, TIGIT, LAG-3, PD-1, TIM-3, CD39, CD73 on CD4+ and CD8+ T cells at day 0, after sample thawing.

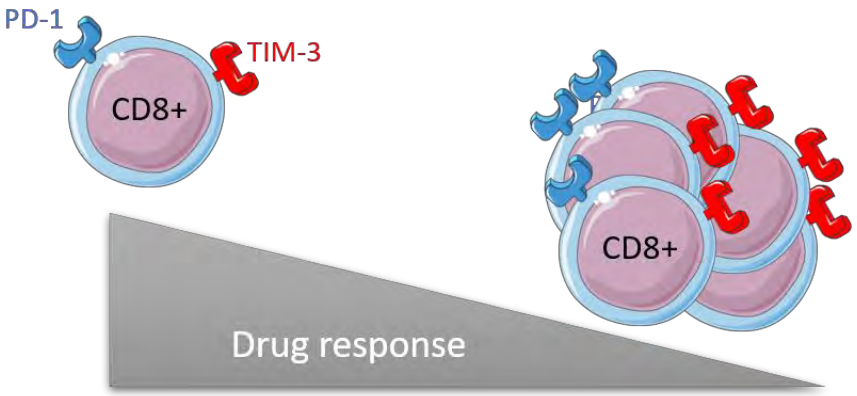

Supplementary Figure 4: Relationship between drug response and CD8+ T cells expressing PD-1 and TIM-3. The more CD8+ T cells express PD-1 and TIM-3 the less drug response will be efficient.

2.3. Conclusion, complementary results and study perspectives

Aware of MALC model limitations, the next challenge was to establish a 3D model with LN biopsies. Indeed, *in vitro* FL cell cultures are known to be difficult to maintain without TME [464]. So far, no 3D models using bulk cells coming from FL LN biopsies exist. A few teams, such as K. Tarte team, have started to work on patient cells but they all isolated B cells and did not take into account bulk cells from LN [430,440]. Thus, with the help of my co-director director's group, we performed several media testing before finding one allowing to develop an simple method to obtain high cell viability and a 3D shaping. Indeed, we continued to use the basic scaffold-free ULA method to help PDLS aggregation and based on studies from the literature, we supplemented the PDLS medium with cytokines (IL-2, IL-4, IL-15, ODN, CD40L) to ensure cell survival. Once the methodology was optimized, we characterized by multiparametric flow cytometry immune cell population distribution and ICP expression on B and T cells and we also performed 3D imaging to visualize PDLS shape. The immune cell population characterization revealed that PDLS were mainly composed, as expected, of B cellsand T cells (CD8+ T cells, CD4+ T cells, TFh, non-TFh, NK and γδ T cells) in variable proportion depending on the patients. Unfortunately, the mechanical dissociation method used for biopsy biobanking was not suitable to keep monocytes and stromal cell populations. Thus, to better integrate FL TME, it would be interesting in the future to test other biopsy processing such as enzymatic dissociation to assess if we are able to keep these populations that are extremely important in FL pathology.

In FL, our group and others have highlighted T-cell exhaustion in patients resulting in T-cell inhibition and loss of effective immune responses [167,169,175,465–468]. As this feature is a landmark of FL, we characterized by flow cytometry ICP expression in PDLS. Thus, PDLS reproduced ICP expression observed in patients, that correlated also with literature description. We observed that the T cells presenting a high triple expression TIGIT+, BTLA+, PD-1+ which was also described by Jossefson et al

[168,469]. Moreover, in their study, Yang et al found similar level of PD-1+ cells than we obtained in our study [470]. In contrast, we did not find the population PD-1+TIM3+LAG3+ as they depicted. Indeed, only few CD8+ cells expressed LAG3.

To better understand how immune cell population are distributed into PDLS we performed IHC on models slices and observed that the 3D FL model reproduces the same pattern of expression as observed in biopsies according to CD79a, Bcl-2, CD10 and CD20 labeling. Moreover, T cells exhibited a peripheral distribution, which correlated with observations in LN biopsy. With 3D imaging, we were able to observe an interpatient variability in shaping and pattern of aggregations. In order to improve the imaging of PDLS and characterize the interaction between cells composing FL LN, we are currently developing methods to observe by 3D-immunofluorescence the distribution of immune cells (Figure 76).

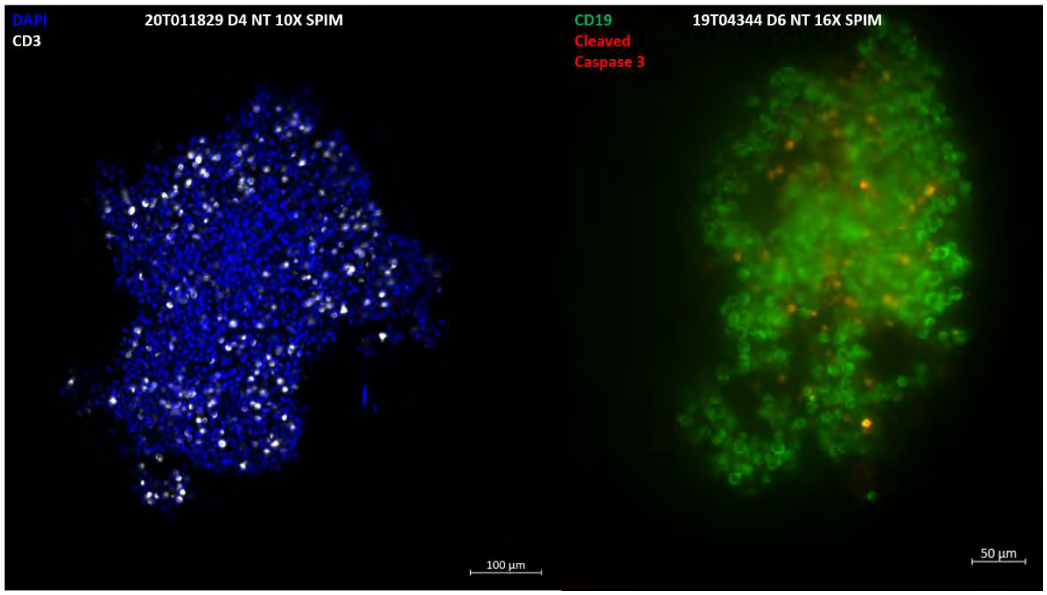

Figure 76 : 3D immunofluorescence performed on PDLS imaged with the SPIM

Left image represents staining of all cells with DAPI (blue) and in white CD3+ cells (alexafluor568) of untreated PDLS #20T011829 at day 4 of culture, 10X magnification. Right image represents staining of CD19 in green (alexafluor488) and cleaved caspase 3 in red (alexafluor532) of untreated PDLS #19T040344 at day 6 of culture at 16X magnification.

Unfortunately, with the low number of PDLS generated it was complicated to perform correlation of population distribution, ICP expression or even 3D morphology shaping. Nevertheless, this correlative approach is to be considered in the future with increasing number of patient samples in order to propose predictive therapy response. Indeed, many studies have already described how T cell distribution and number can impact therapy response. For example, Yang et al found that the number of PD-1low CD4+ and CD8+ T cells correlated with a poor prognosis in FL patients [470]. Nevertheless,

CD4+ PD-1high did not correlated with FL survival. Thus, this result indicates that PD-1 is not the only

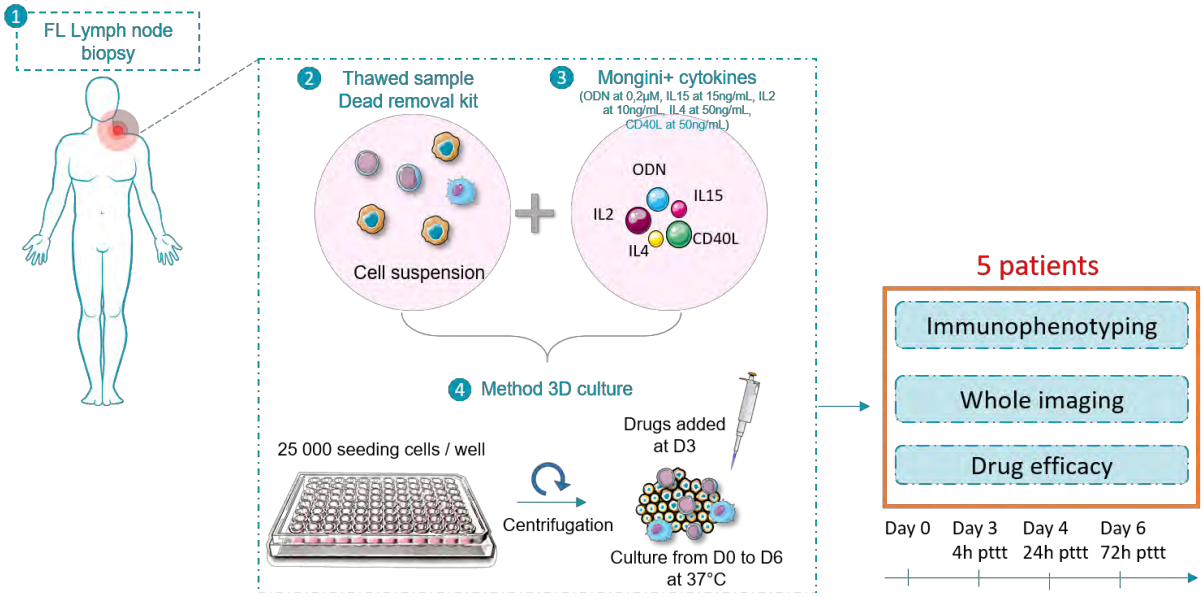

Figure 77 : PDLS workflow

After LN cells thawing, cells are cultured in an enriched medium and put into ULA plates to induce cell aggregation. After 3 days of 3D culture, drugs or added and immunophenotyping, whole imaging and drug efficacy is evaluated after 4h, 24h and 72h post-treatment.

actor in FL T-cell mediated tumor immunity. Other studies have depicted that the frequency of intratumoral TIM3+ CD4+ T cells predicts a poorer survival of FL patients [167]. Thus, PDLS models represent promising preclinical model to address biological question of FL progression but also to propose a platform for personalized medicine (Figure 77).

3. ULA-MALC and PDLS at the service of identifying new therapeutic targets in follicular lymphoma: the story of CD39 targeting

3.1 PDLS as preclinical models to identify new therapeutic targets

As described in the previous part, PDLS represent a relevant model to mimic FL pathology and to identify new potential targets. The full characterization of immune population and the expression of ICP led us to identify CD39 as a potential new target in FL. CD39 is an ectonucleotidase that catalyzes the degradation of ATP into ADP and then AMP, which in turns, is hydrolyzed by CD73 into adenosine[187]. Adenosine is a known immunosuppressive molecule presents in the TME and has become a target of recent promising therapeutic strategy [187].

Dr Juan Garcia from the team of my PhD co-director (IDIBAPS, Barcelona) analyzed the expression of CD39 in 75 non-purified tonsil cells (NP-TS) in comparison with 362 non-purified FL patient cells (NP-FL). These analyses were performed according to GEP public databases (GSE55267, GSE65135, GSE65136, GSE7307, GSE71810, GSE12195, GSE12366, GSE12453, GSE99316, GSE39503, GSE38712,

GSE31311, GSE15271, GSE10831, GSE3526, GSE21554, GSE53820, GSE12453, GSE93261) all generated with Affymetrix Human Genome U133 Plus 2.0, in order to compare, in bulk cells from normal and pathological samples expression of adenosine generating enzymes. As illustrated in figure 78 an increase of *ENTPD-1* expression, the gene coding for CD39, was observed in NP-FL compared to NP-TS.

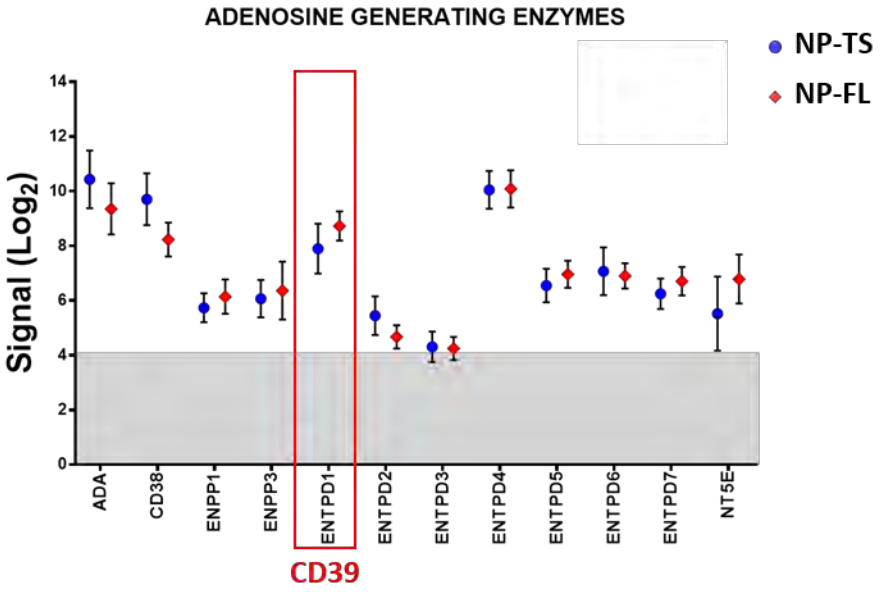

Figure 78 : Expression of several adenosine generating enzymes, comprising *ENTPD-1*, the gene encoding for CD39

GEP public databases generated with Affymetrix Human Genome U133 plus 2.0. All data were normalized using the expression console software v1.4.1.46 (Affymetrix) and by using the Limma package included in transcriptome analysis console (Applied Biosystems).

Analyses of *ENTPD-1* expression in centroblast, centrocyte, memory, naive, plasma cells and B cells from normal LN and from FL samples were also performed. This analysis revealed that *ENTPD-1* expression was lower in B cells from FL compared to normal LN and its level was similar to centrocytes (Figure 79).

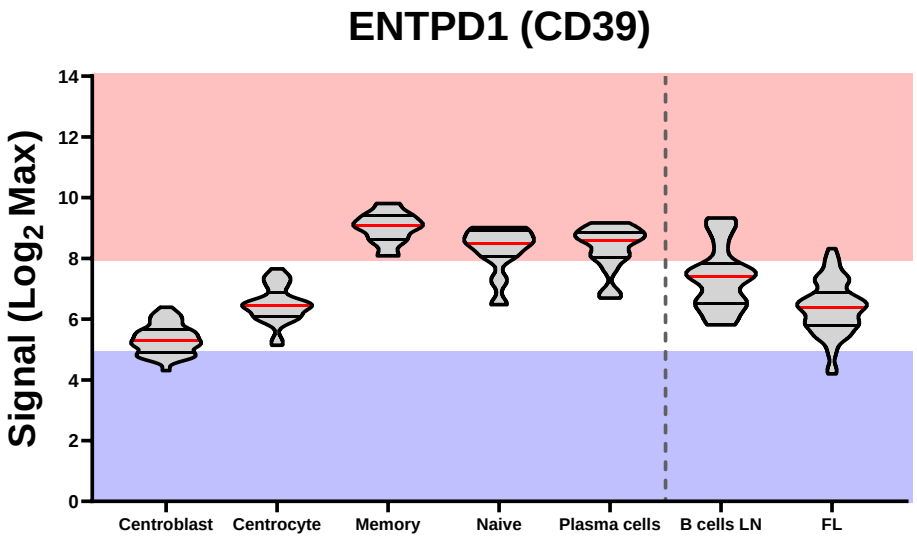

Figure 79 : Expression of *ENTPD-1* on several B cell subtypes
GEP public databases generated with Affymetrix Human Genome U133 plus 2.0. All data were normalized using the expression console software v1.4.1.46 (Affymetrix) and by using the Limma package included in transcriptome analysis console (Applied Biosystems).

Although these promising results conferred a strong rationale to point CD39 as an interesting target in FL, the technology used could not identify the population expressing CD39. Thus, we therefore investigated the profiles of CD39 expression both in B and T cells of PDLS established from FL patients. As illustrated in figure 80, an interpatient variability was observed with three different profiles: patients #19T040344, #20T04555 presenting high percent of CD39+ CD8+ and CD4+ T cells (around 60%). Patients #19T0022947, #21T012396 and #21T018902 presenting intermediate percent of CD39+ CD4+ and CD8+ T cells (around 20%); and finally, patients #19T043574, #21T011790 and #20T011829 presenting very low CD39+ CD4+ and CD8+ T cells (<10%). Regarding CD73, expression was only observed on CD8+ T cells in a small proportion (around 20%). Interestingly, we observed that almost all CD39+ cells were also PD-1+ whereas CD73+ cells did not express this ICP. Moreover, we explored more precisely the profile of CD39 expression on the different B cells subtypes according to their tumoral (CD10+) or non-tumoral (CD10-) phenotypes. We observed that tumoral cells exhibited a lower level of CD39 expression compared to healthy B cells with 20% *vs* 50% respectively (Figure 80). These results were in accordance with the literature showing high levels of CD39 on all these cell types [189]. Nevertheless, it had never been shown that FL tumoral cells exhibit lower CD39 expression than healthy B cells.

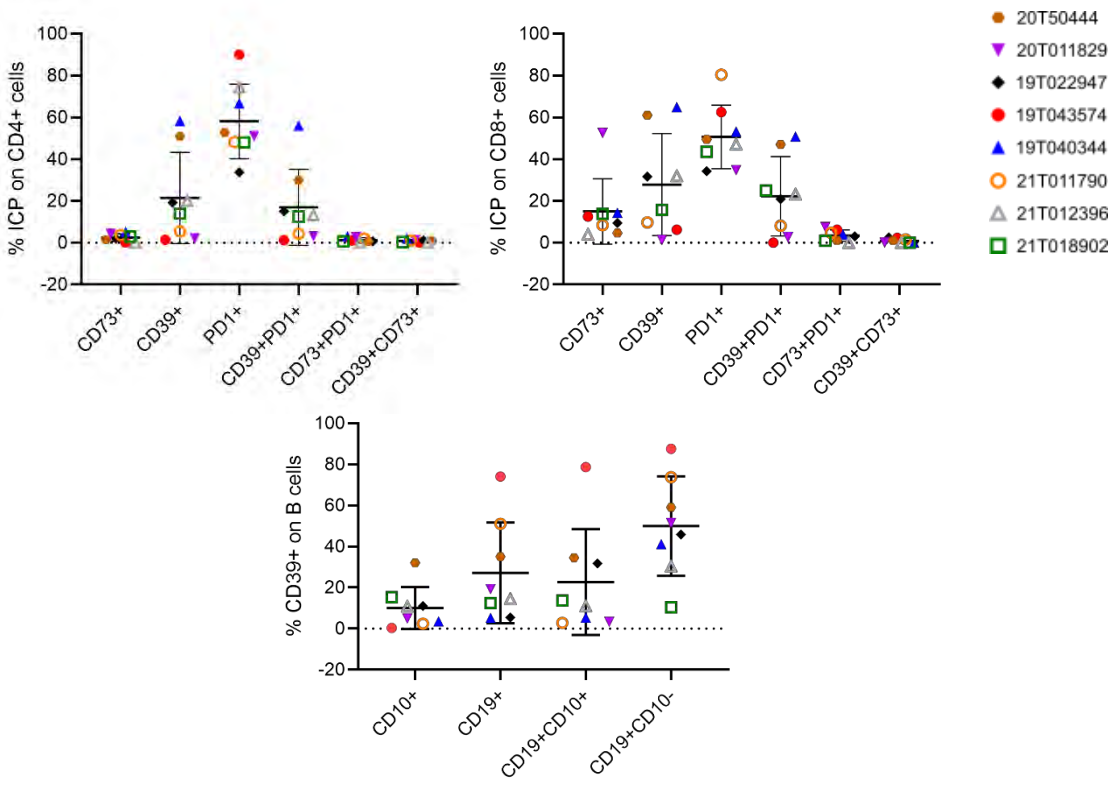

Figure 80 : Characterization of PD-1, CD39, CD73 expression on CD4+, CD8+ and B cells

For each patient tested, 10 PDLS were pooled, dissociated and stained with CD4, CD8, CD3, CD19, CD10 markers for the different cell populations and CD73, CD39and PD-1 for the ICP and analyzed by flow cytometry.

These results, with studies from the literature which underline the immunosuppressive action of CD39 prompted us to evaluate the effect of CD39 targeting. To do so and in the absence of anti-CD39 specific mAb at our disposal, we tested POM1 (sodium polyoxotungstate), a non-specific NTDPase inhibitor, classicaly used to inhibit CD39 for *in vitro* studies [471]. We designed experiments to evaluate the role of CD39 in the mechanisms of IE by combining POM1 with anti-CD20 (GA101) and anti-PD-1 (Nivolumab). First, we observed that POM1 at 10µM alone or in combination with either anti-CD20 and anti-PD-1 mAbs, or both, did not affect PDLS area (both center and periphery) whereas at 100µM, POM1 induced an increase in 2/6 patients and a decrease in 3/6 patients of the periphery area (Figure 81). The center area was also impacted with POM1 at 100µM, with 4/8 PDLS presenting a center area decreased and 3/8 patients when combined with anti-CD20 or anti-PD-1 or triple targeting (Figure 81).

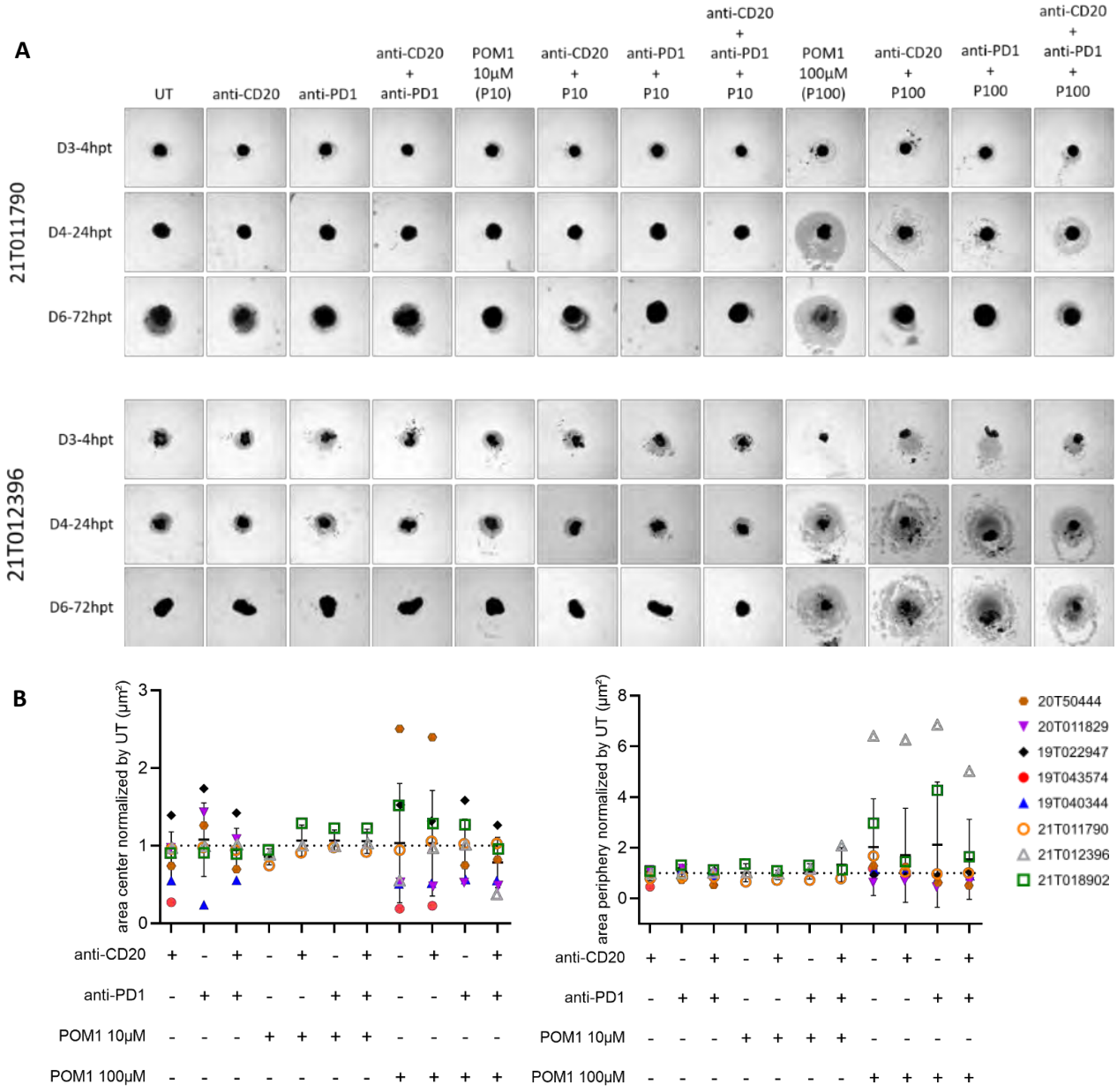

Figure 81 : PDLS morphology after CD39 targeting

PDLS were established from 8 different FL patients and after 3 days of culture were treated by GA101 at 10µg/mL and/or Nivolumab at 10µg/mL and/or POM1 at 10µM or 100µM A. Brightfield pictures obtained with Operetta at 10X magnification after 4h, 24h or 72h post-treatment. B. Quantification of center and periphery areas (µm²) was performed with the Columbus software.

Morphological feature is not sufficient to determine drug efficacy. Indeed, a drug can induce an increase of area when MALC/PDLS are destructurized or a decrease when it induces cell death or 3D structure shriking by increasing cell-cell interaction. Moreover, as we previously demonstrated [441], only on the morphology criteria, the cytotoxic effect can not be determined. In order to determine drug effect, we quantified CD19+ depletion by flow cytometry. First, we evaluated the effect of GA101 and observed a B cell depletion in all patients tested (10 to 80%) (Figure 82). In contrast, anti-PD-1 alone did not affect B cell count in a majority of samples. Interestingly, combination of both antibodies enhanced slightly the B cell depletion induced by GA101. 10µM, POM1 with or without combination, did not induced CD19+ cell depletion 72h post-treatment. Nevertheless, at 100µM, POM1 induced a significant CD19+ cell depletion in 5/7 PDLS (from 20 to 80%). In combination with an anti-CD20 mAb, depletion was increased in 3/5 responding PDLS and in combination with anti-PD-1 mAb, no additional effect was observed. For the triple combination anti-CD20 mAb, anti-PD-1 mAb and POM1, no increase in depletion was observed in comparison with double combinations.

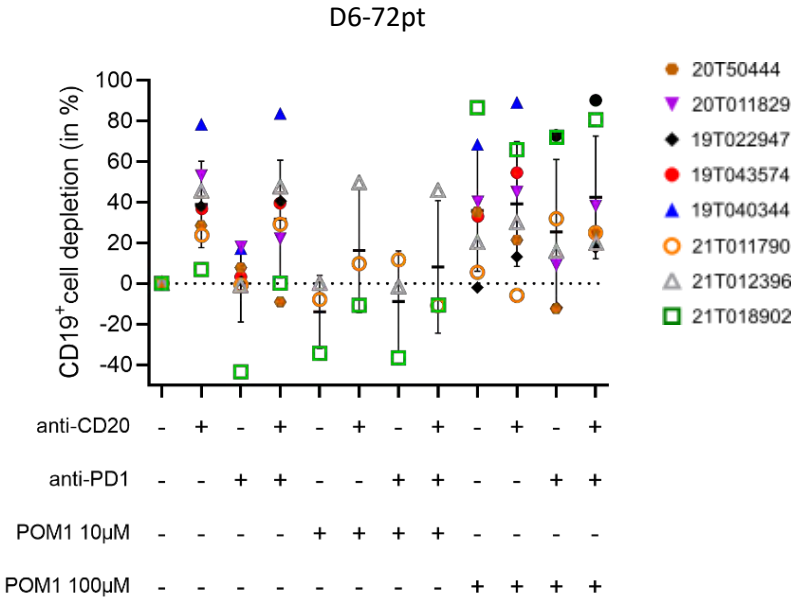

Figure 82 : CD19+ cell depletion 72h post-treatment

PDLS were established from 8 different FL patients and after 3 days of culture were treated by GA101 at 10µg/mL and/or Nivolumab at 10µg/mL and/or POM1 at 10µM or 100µM. 10 PDLS were pooled, dissociated, stained and analyzed by flow cytometry.

Altogether, these results showed an expression of CD39 in FL and that its targeting could enhance anti-CD20 or ant-PD-1 mAbs effect, supporting the role of this ectonucleotidase in the mechanisms of IE in FL.

3.2 Identification of CD39 role on immune cells

As presented with previous results we observed, that CD39 is expressed on both B and T cells in FL PDLS. Thus, in order to decipher its role when expressed by immune cells, we decided to conduct *in vitro* studies with MALC co-cultured with γδ T cells.

First of all, we benefited from the analyses of *ENTPD-1* expression on 37 B-NHL cell lines provided by my PhD codirectors' group (IDIBAPS, Barcelona). As illustrated in figure 83, different profiles of transcriptomic *ENTPD-1* expression were observed, with low (SUDHL7, SUDHL16), intermediate (RL, DOHH2, HBL2, Ocily10) and high expression (JEKO1, REDC1, Ocily3). In general, most of B-NHL cell lines expressed intermediate level of *ENTPD-1*.

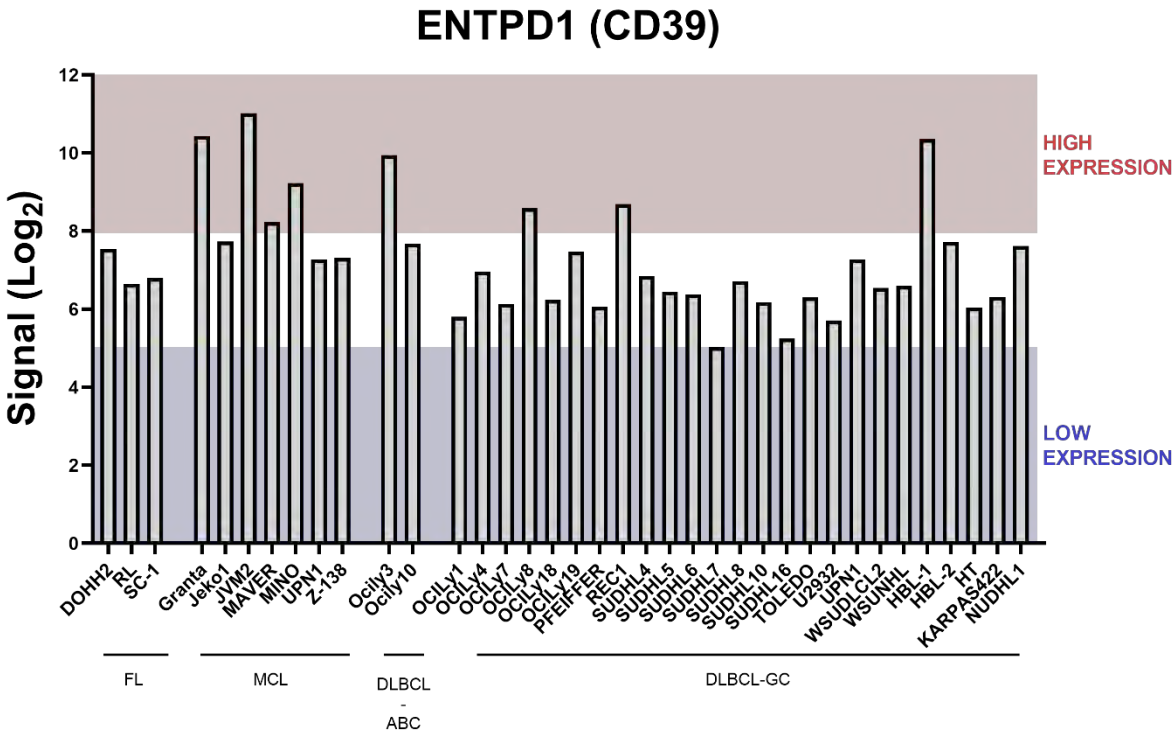

Figure 83 : *ENTPD-1* expression on several B-NHL cell lines
GEP public databases generated with Affymetrix Human Genome U133 plus 2.0. All data were normalized using the expression console software v1.4.1.46 (Affymetrix) and by using the Limma package included in transcriptome analysis console (Applied Biosystems).

Second, we characterized at the protein level, the expression profile on different B-NHL cell lines cultured in suspension (2D) and in 3D (ULA-MALC). As illustrated in figure 84, ABC-DLBCL cell lines (Ocily-3 and Ocily-10) presented a high CD39 expression level, whereas GC-DLBCL cell lines exhibited different patterns with high expression on Ocily19, intermediate expression on Ocily8 and no expression on Ocily1. For FL, low expression was found in DOHH2 and almost no expression on WSU-FSCLL and RL cell lines. No difference was observed between 2D and 3D cultures. We also monitored the 3D structuration at day 3 of 3D cultures by an inverted microscope and observed different patterns from the less to the most aggregated: WSU-FSCLL > Ocily1 > DOHH2> Ocily10> Ocily8 > Ocily3 > Ocily19 > RL.

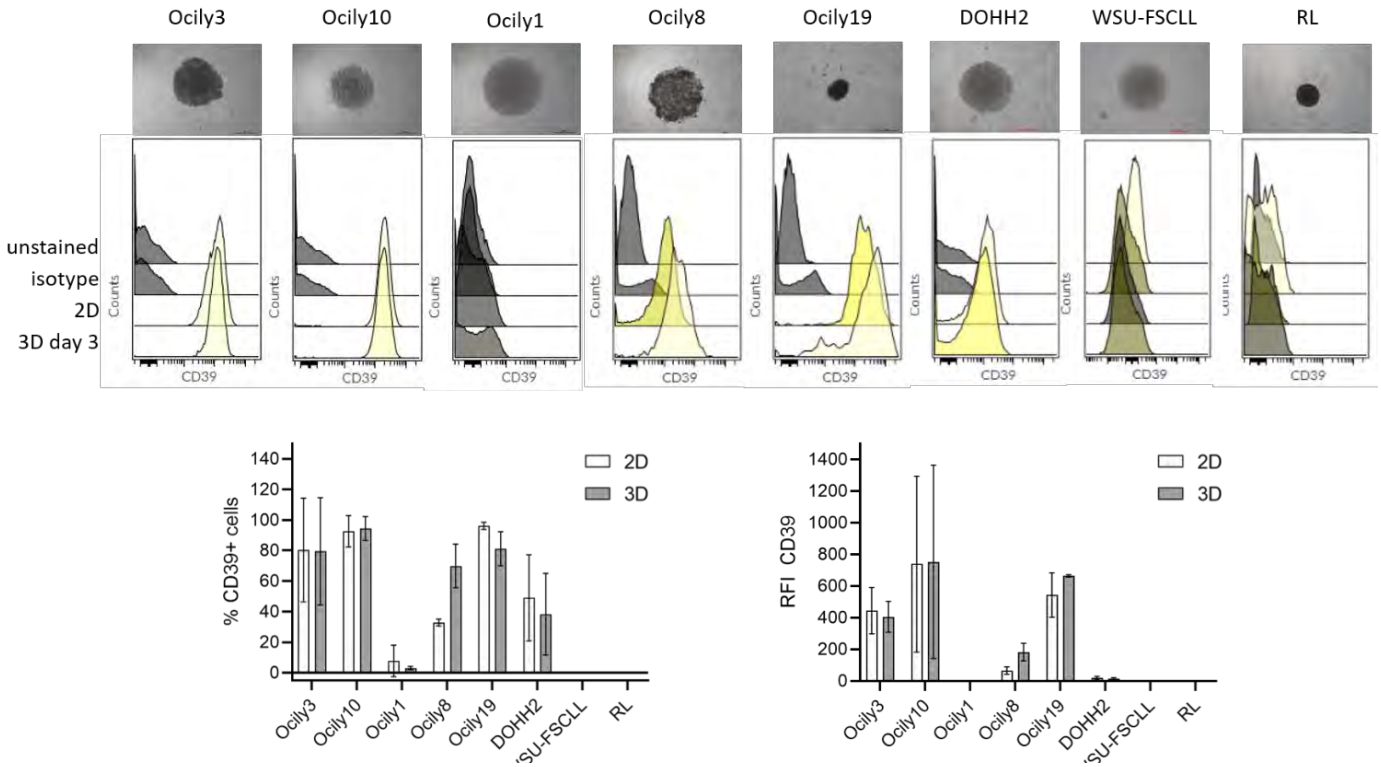

Figure 84 : CD39 expression measurement by flow cytometry on several B-NHL cell lines cultured in 2D and 3D
n=3 independent experiments / cell line was conducted on 2D cell culture and 3D cell culture at day 3.

Next, we determined the expression of CD39 on γδ T cells derived from healthy donors. Indeed, these specific lymphocytes are important effector cells in potential anti-cancer treatment as they infiltrate FL and express CD16 and PD-1. Primary γδ T cells were generated according to Capietto et al [232]. We observed that both expression and % of CD39 expressing cells were strongly increased in the first days of culture due PAgs addition as previously described in the literature [203]. Although a variability between donors was observed, this expression was maintained until 20 days of culture with around 60 % of γδ T cells expressing CD39 (Figure 85).

Altogether, these results obtained on NHL cells and γδ T cells support that CD39 appears as an interesting target.

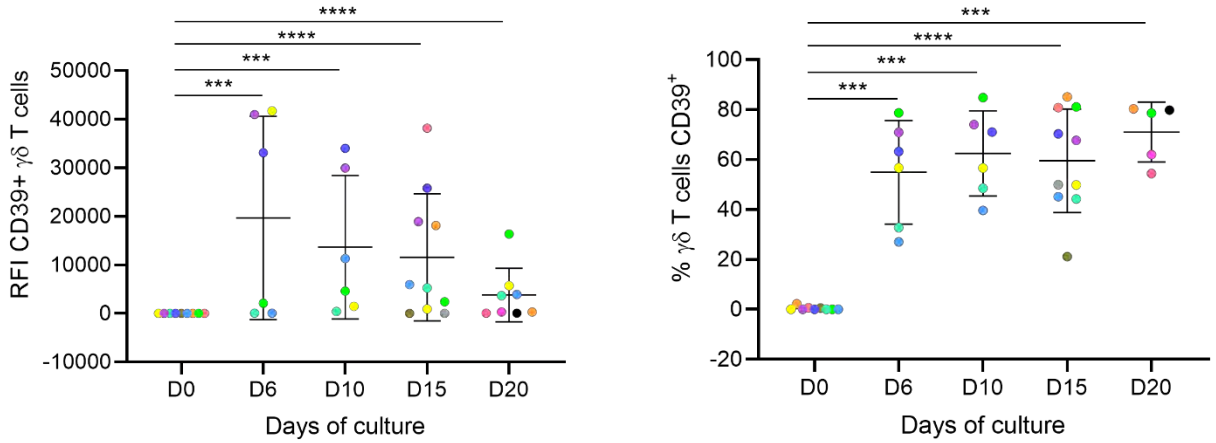

Figure 85 : CD39 expression followed by flow cytometry upon γδ T cell primary cell culture

Left panel represents ratio of mean fluorescence and right panel CD39+ percent of expressing γδ T cells.

So, to better characterize the role of CD39 expression on immune cells, we decided to co-culture RL cells, which do not express CD39and γδ T cells which does. In absence of specific anti-CD39 mAbs, we performed *in vitro* experiments with POM1 which efficient doses were determined by measuring ATP consumption in γδ T cells. As shown in figure 86, POM1 induced a dose-dependent inhibition of ATP consumption reaching a maximum at 500µM without affecting γδ T cell number. Based on these resultsand in accordance with the literature, we decided to use POM1 at 10 and 100µM for the co-culture experiments.

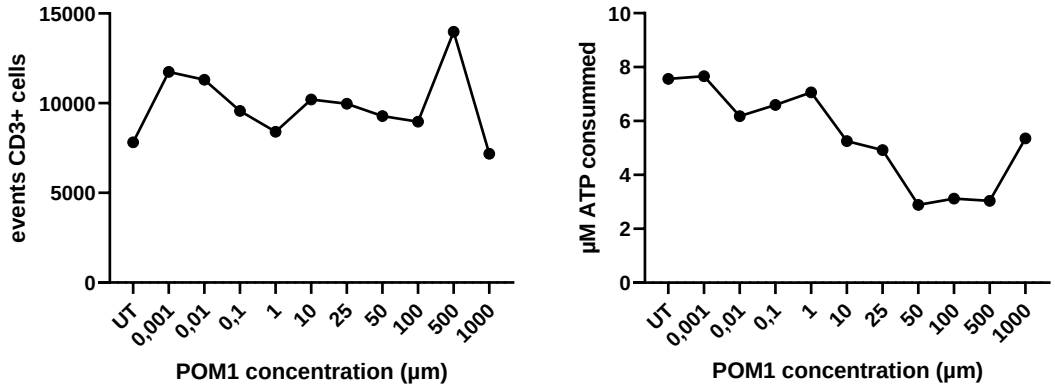

Figure 86 : Effect of POM1 in γδ T cell number and ATP consumption

The number of γδ T cells was measured by flow cytometry and ATP consumption by the ATPlight kit and analyzed with Clariostar.

In order to determine the role of CD39 in IE, we explored the effect of POM1 on ADCC induced by GA101 in γδ T cell-MALC co-culture. By monitoring morphology by Operetta® CLS™, operetta, we

observed that in co-culture, MALC were composed by monolayer surrounding the 3D part that was increased after treatment combining GA101+POM1 at 10µM. Area quantification of MALC alone showed that: (i) untreated MALC were round (roundness around 1) and presented an area of 250 000µm²; (ii) treatment by GA101 induced an area decrease of around 8% and iii) POM1 in combination or not with GA101 did not induce any changes. In co-culture, only the roundness was impacted with a decrease of 31% with GA101 alone, 15% with GA101 + POM1 10µM and 14% for GA101+POM1 100µM (Figure 87).

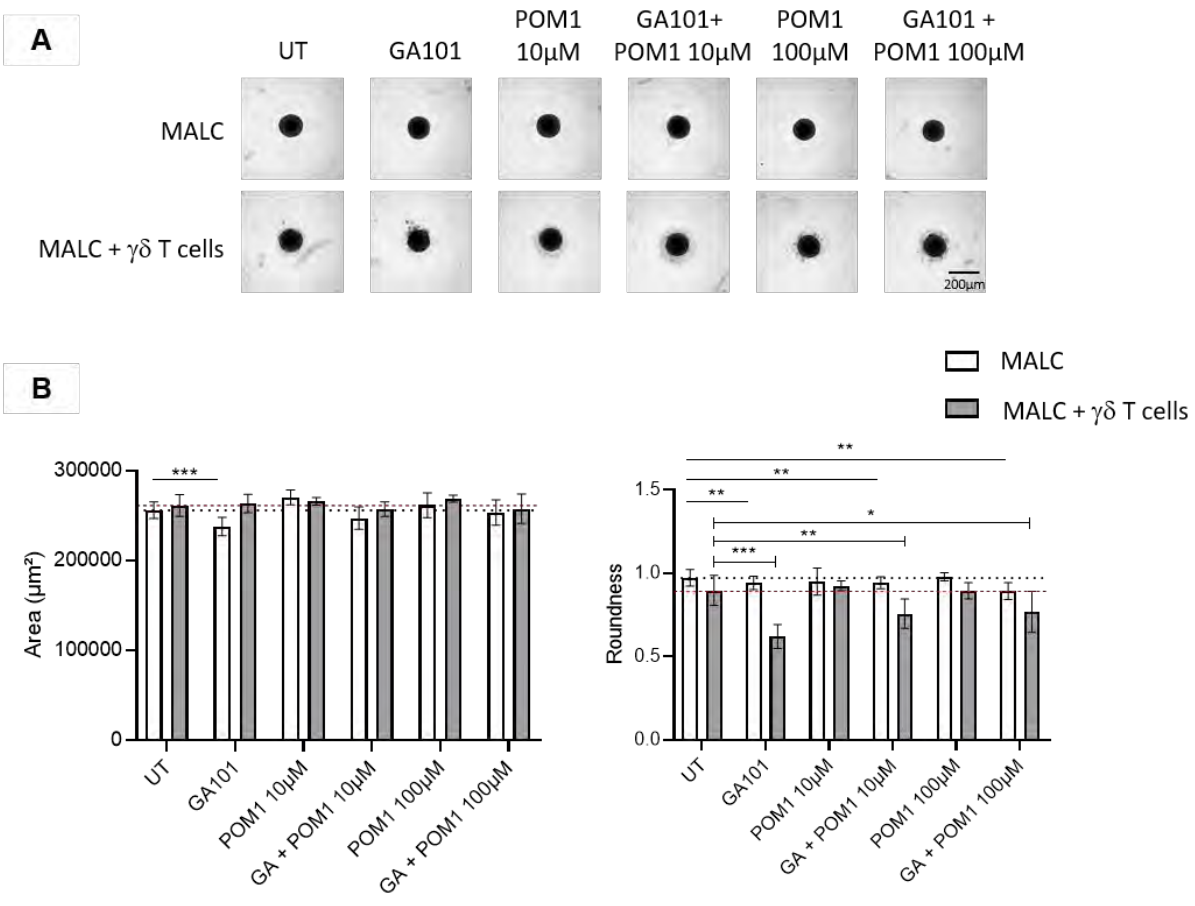

Figure 87 : Effect of POM1 on ADCC induced by GA101 in co-cultured or not with γδ T cells (0.5:1).
MALC at day 3 of culture were co-cultured with γδ T cells or not and treated with GA101 (10µg/mL) and/or POM1 (10 or 100µM) during 24h. A. Brightfield pictures obtained with operetta (scale = 200µm). B. Measurement of area and roundness with columbus software. SD of n=9 MALC independent. Black dotted lines represent MALC UT area or roundness and red dotted line represent MALC+ γδ T cells UT area or roundness

To go further in the investigation, we evaluated the effect of POM1 on ADCC induced by mAbs determined, by effector γδ T cell degranulation and by target B cell death. As shown in figure 88, GA101 did not induced effector cells degranulation compared to untreated cells when cultured without target cells.

However, when co-cultured with ULA-MALC, two different profiles were observed:

- Decrease or very weak increase of CD107a+ cells percent observed after GA101 and no enhancement when combined with POM1 (#0429B and #0429A).
- Increase of CD107a+ cells percent after GA101 which was slightly enhanced in presence of POM1 at 100µM (#0415B).

Interestingly, when compared to CD39 and CD16 expression profiles, donor responding better to GA101 and CD39 targeting in terms of γδ T cell degranulation, was the one exhibiting the highest expression of the ectonucleotidase and FcγRIIIa (Figure 88 B).

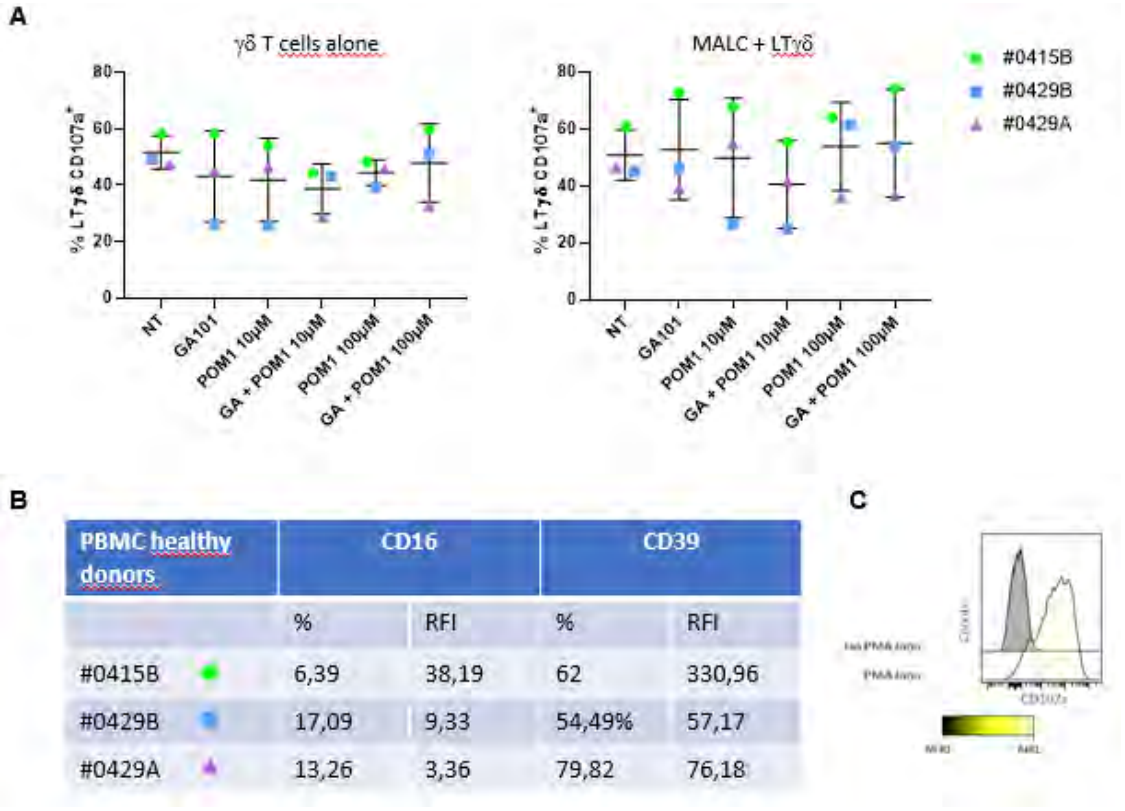

PBMC healthy donors	CD16		CD39	
	%	RFI	%	RFI
#0415B	6,39	38,19	62	330,96
#0429B	17,09	9,33	54,49%	57,17
#0429A	13,26	3,36	79,82	76,18

Figure 88 : Effect of POM1 on degranulation of γδ T cells induced by GA101
A. % of CD107a+ expressing γδ T cells analyzed by flow cytometry on γδ T cell alone (left) or after 4h of co-culture with MALC (right) and treatment with GA101 (10µg/mL) and/or POM1 (10 or 100µM). B. Evaluation of CD16 and CD39 expression (% and RFI) by flow cytometry on 3 PBMC healthy donors associated with one symbol and color. C. CD107a expression measured by flow cytometry after 4h treatment with PMA/Ionomycin for positive control. Each color and symbol represent a donor, mean and SD on 3 different donors.

We next determined if γδ T cell degranulation could induce B cell death. To do so, we evaluated by annexin V / 7AAD staining, the level of living, apoptotic and dead cells. Only GA101 induced apoptosis in MALC, and this was potentiated in presence of γδ T cells (Figure 89 A). This was not enhanced by POM1 irrespectively the used dose. To determine if this phenomenon was donor specific, we analyzed the percentage of AnV+ cells for each donor co-cultured with MALC (Figure 89 B).

Moreover, the direct effect of treatment on MALC was also evaluated (ULA-MALC). We observed that depending on experiments, MALC presented a basal cell death from 2.55 to 10%. This percent was increased in presence of GA101 and a slight potentialization was observed in combination with POM1 at 10 and 100µM in comparison to single drugs in 2/3 experiments. When MALC were in co-culture, basal cell death was increased in comparison to culture without γδ T cells and even higher in presence of GA101 in 2/3 donors (#0415B and #0429B). Nevertheless, no potentialization was observed with POM1. In panel C, we represented the ratio of cell death obtained in co-cultures reported to ULA MALC alone. We observed that 2/3 donors responded to GA101 (#0429A and #0415B) and only one responded to POM1 at 100µM (#0415B). However, no potentialization was observed with combination.

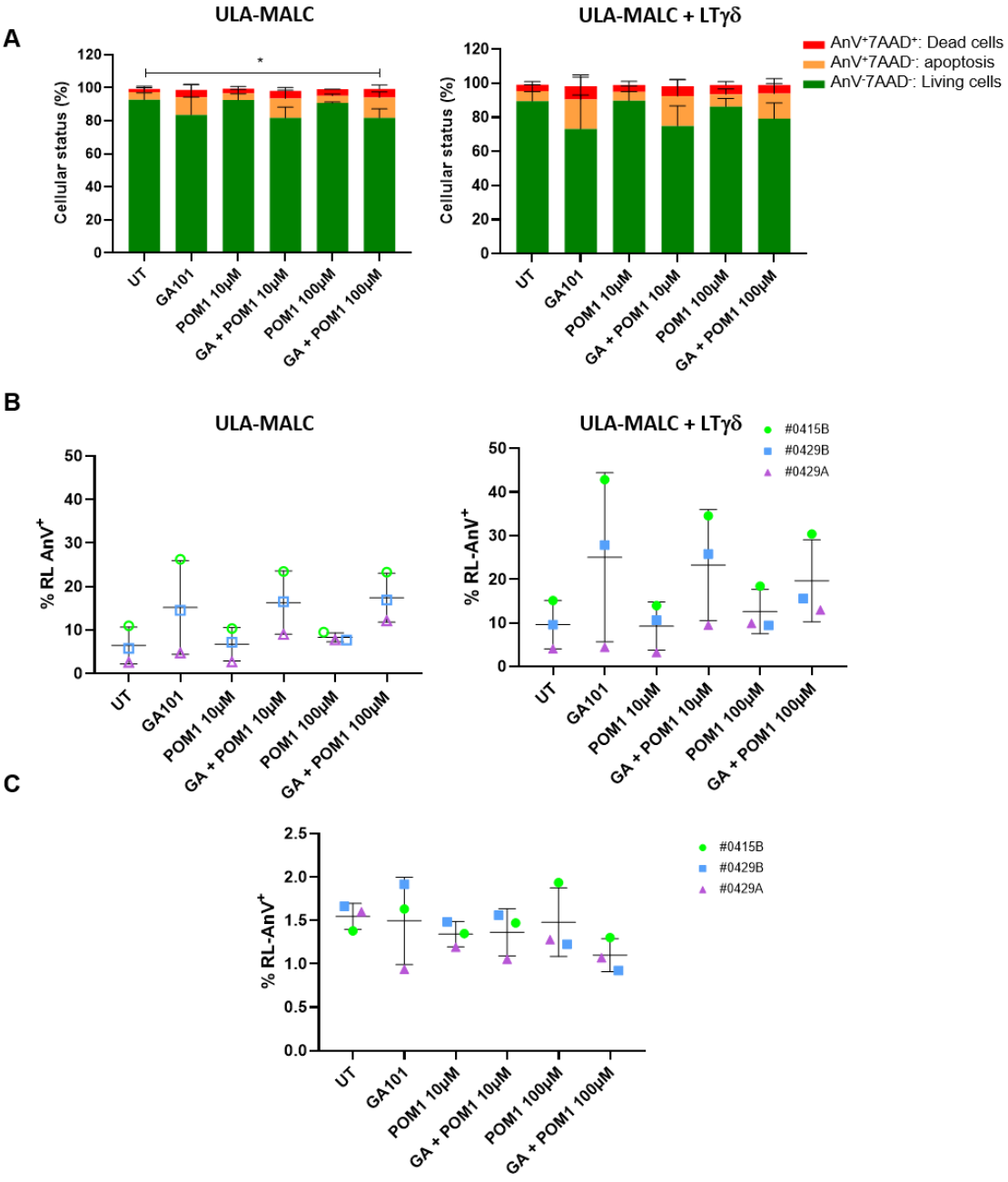

Figure 89 : Effect of POM1 effect on apoptosis of RL cells in MALC treated or not with GA101 and in co-culture or not with γδ T cells

At day 3 of culture MALC or co-cultured or not with γδ T cells (0,5/1 ratio) were treated or not with GA101 (10µg/mL) and/or POM1 (10 or 100µM) during 24h. A. Cellular status of RL cells was evaluated by flow cytometry to evaluate the percent of living cells (AnV-/7AAD-), apoptotic cells (AnV+/7AAD-) and dead cells (AnV+/7AAD+). Histogrammes represend 3 independent experiments. B. AnV+ cells % was evaluated on MALC alone or in co-culture with γδ T cells upon treatment of GA101 and/or POM1 during 24h. C. Ratio of AnV+ cells of MALC+γδ T cells over MALC alone. All graphs represent 3 independent experiments.

As we were not able to observe a correlation between γδ T cell degranulation and B cell death measured with AnV/7AAD labelling, we decided to assess the biological effect of γδ T cell activation on target cells by determining viability and B cell depletion (trypan blue assay). In figure 90 A, we observed that GA101 induced a decrease of 16% viability when MALC were cultured alone and this was not affected by POM1. When co-cultured with γδ T cells, although GA101 induced a decrease of B cell viability in the three experiments, no potentialization with POM1 was observed in terms of viability. Interestingly, B cell depletion allowed us to observe different patterns of response (Figure 90 B). First, when MALC were cultured alone, we observed that GA101 induced a direct effect in 2/3 experiments and that the depletion was increased when combined to POM1 100µM for 2/3 experiments. Second, in co-culture, except for donor #0429B, we observed a B cell depletion which was potentiated with combination of GA101 and POM1 100µM.

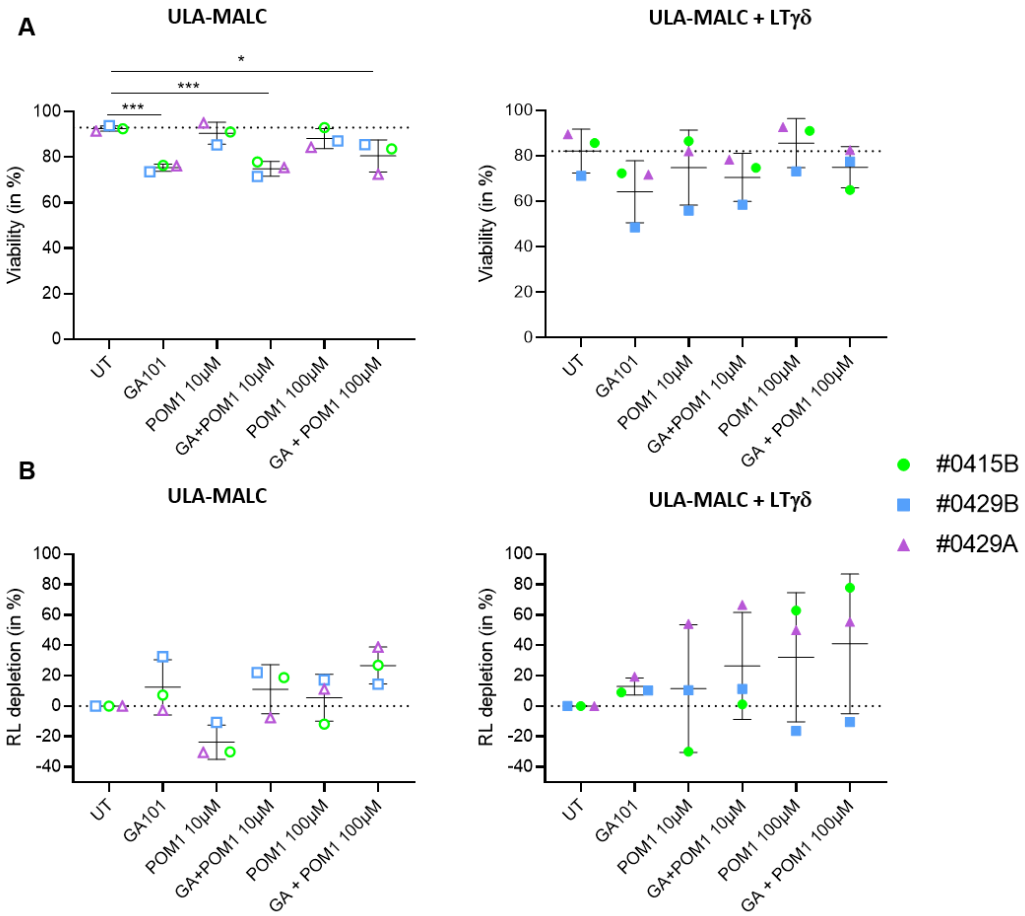

Figure 90 : Effect of POM1 on viability and depletion of RL cells in MALC co-culture or not with γδ T cell.

MALC were co-cutured or not with γδ T cells (ratio E:T 0.5:1) and treated or not at day 3 by GA101 (10µg/ml) or POM1 (10 or 100µM). A. Viability was determined by Trypan blue assay on 5 MALC dissociated and pooled. B. Depletion was determined by comparison to cell number of UT condition. Each symbol and color represents a donor and an experiment, SD represents 3 independent experiments

Altogether, we observed that CD39 targeting was able to enhance γδ T cell cytotoxic effect, concomitantly with B cell depletion in 1/3 donors. Although this result seemed to be correlated to the level of expression of CD39 and CD16, we need, to increase the number of donors in order to draw conclusions. As POM1 results were ambiguous, we decided to generate CD39 gene KO in primary γδ T cells, using CRISPR Cas9. As shown in figure 91, CD39 expression was totally abolished on γδ T cells with CRISPR-Cas9 guide targeting *ENTPD-1* (g*ENTPD-1*) in comparison to non-electroporated (No ELP) and control guide (gCtl).

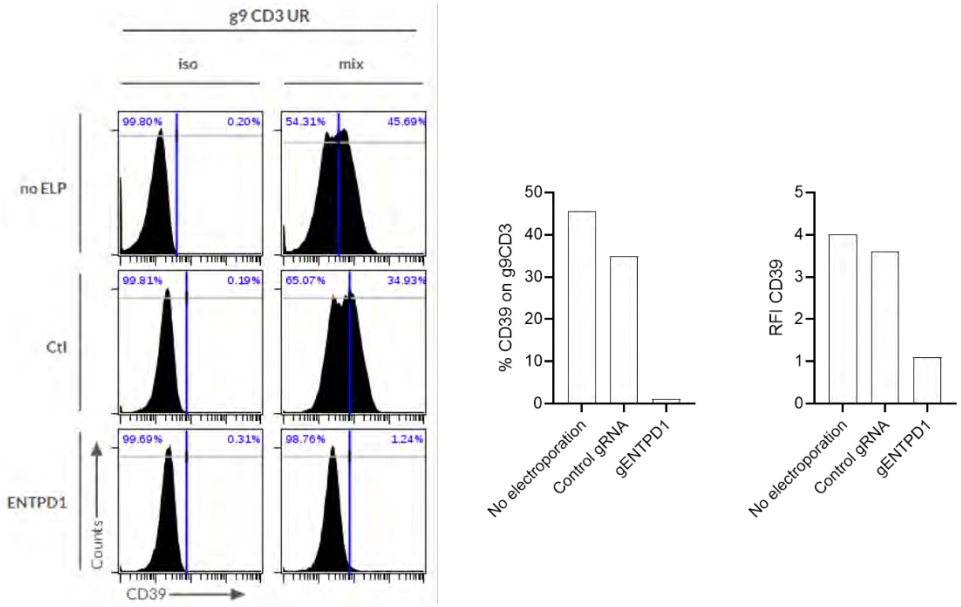

Figure 91 : Depletion of *ENTPD1* in one γδ T cells donor after CRISPR-Cas9 method

Non electroporated γδ T cells (no-ELP), electroporated and receiving a guide RNA *ENTPD-1* to deplete the gene (g*ENTPD-1*) and electroporated and receiving a guide control (gCtl) were washed and stained with CD39 to evaluate CD39 depletion by flow cytometry. Cells were transfected using Neon® Transfection System (MPK5000)

Then, we explored the effect of *ENTPD-1* gene depletion on several read out. First, on morphology, we observed that MALC area was decreased by γδ T cells addition and this was not significantly affected by after *ENTPD-1* depletion by CRISPR-Cas9 (Figure 92). Second, on ADCC induced by GA101 in presence of γδ T cells, we observed that *ENTPD-1* gene depletion did not affect the B cell

depletion but seemed to inhibit the GrB secretion. However, the control condition (gCtl) exhibited similar results. These results are inconsistent and more experiments are needed to draw conclusions.

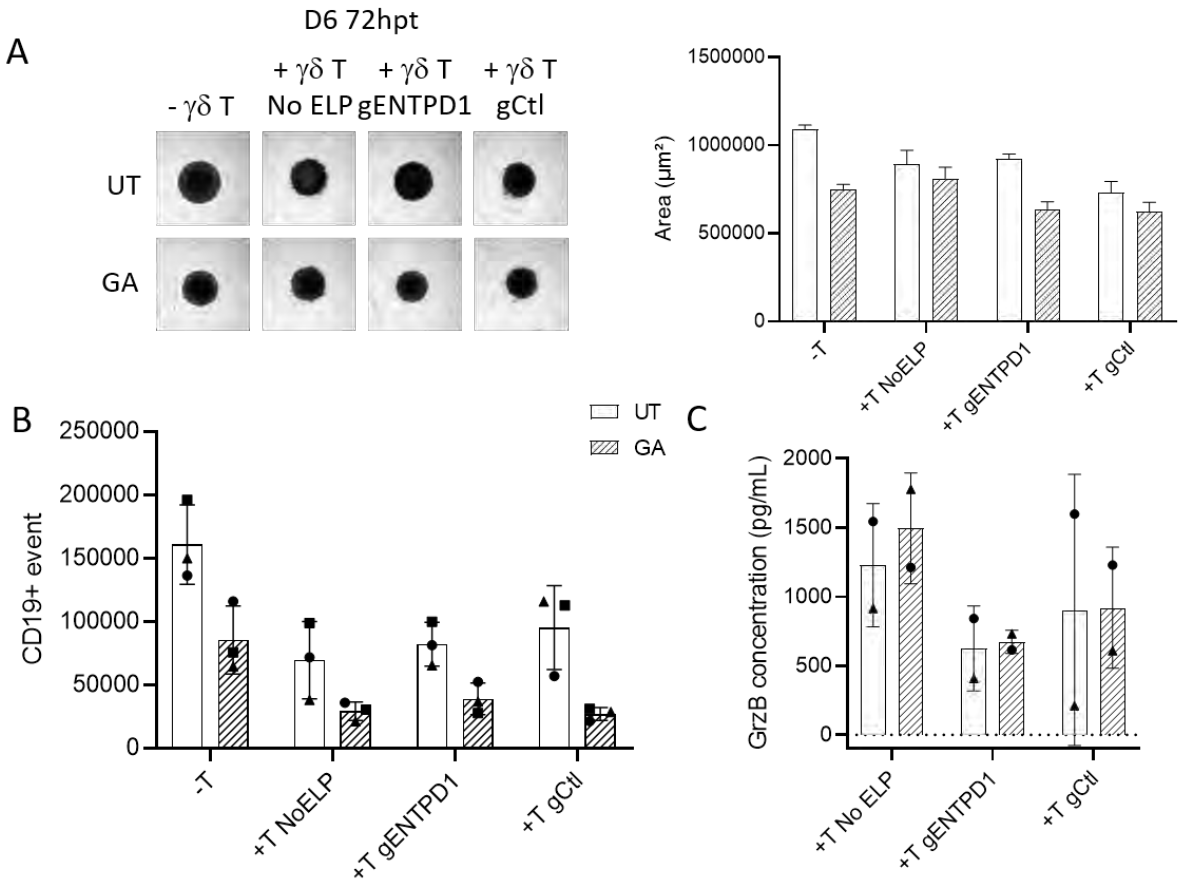

Figure 92 : Effect of *ENTPD1* depletion by CRISPR-Cas9 on γδ T cells on morphology, depletion and granzyme B release at 72h post-treatment

A. Briedfield pictures obtained with the operetta system at 4X magnification. Scale 200µm (left) and area quantification by Columbus software (right) B. CD19+ event count by MAQSquant device upon GA101 treatment on non electroporated γδ T cells, electroporated and received a guide RNA *ENTPD-1* to deplete the gene (g*ENTPD-1*) and electroporated and received a guide control (gCtl). C. Granzyme B release quantified with BD CBA beads detection by flow cytometry.

3.3 Conclusions and perspectives on CD39 targeting in FL

In conclusion, we observed that FL TILs express variable but high level of *ENTPD-1* gene and protein. The targeting with POM1 inhibitor at low doses did not induced detectable effect on MALC and PDLS in contrast to high doses that induced significant depletion that could be potentiate with GA101 in PDLS. However, POM1 is not a specific CD39 inhibitor and one could speculate that the effect observed were not related to CD39 targeting. Thus, in order to verify the role of CD39, we used CRISPR-Cas9 method. Nevertheless, CD39 depletion seemed to highly diminish γδ T cells cytokine secretion and not affected significantly GA101-induced B cell depletion. This counteracts our hypothesis that CD39 is an IE mechanism whose inhibition could potentiate effect of mAbs. However, only three

experiments were performed so far and need to be repeated to conclude. Moreover, many pending questions remains:

- Why results obtained with POM1 and CRISPR-Cas 9 are different? Although more experiments are needed to confirm these results, it should be interesting to evaluate CD39 inhibition by targeting both gene expression and activity. Moreover, it also should be interesting to determined the effect of anti-CD39 mAb combined with other mAbs such as anti-CD20 and/or anti-PD-1. Thus, further investigations and improvement are needed to understand CD39 implication in IE observed in FL. Using more specific mAbs targeting CD39 or other methods such as siRNA could be a way to better investigate this pathway. Although CD39 implication in IE was the focus of our preliminary investigations, it would also be interesting to evaluate its involvement in the metabolism. Indeed, Aroua et al, showed that in AML, CD39 was upregulated in cytarabine-resistant leukemic cells from both AML cell lines and patient samples in *vivo* and *in vitro.* Moreover, they demonstrated that this resistance was due to an enhanced mitochondrial activity and biogenesis through activation of a cAMP-mediated adaptive mitochondrial stress response. In this study they used shRNA to downregulate CD39 gene and POM1 to inhibit CD39 activity and showed that both inhibition blocked activity of the mitochondrial reprogramming triggered by cytarabine treatment and interestingly, potentiated AML cell death *in vivo* and *in vitro* upon cytarabine treatment[471]. Thus, these observations revealed CD39 as an even more interesting target that could have a potent effect on activating anti-tumoral immune response on the one side and metabolic resistance on the other.
- What is the mechanism responsible for the expression of CD39 on γδ T cells after BrHPP treatment? We could hypothyzed that in a tumoral context, cellular stress can induce secretion of PAgs that, in turns, leads to increase CD39 expression. In a physiological context, Gruenbacher et al demonstrated that CD39 could also use PAgs as substract, in addition to ATP, in order to impede γδ T cell activation [203]. Thus, this mechanism could be a process to control overactivation of γδ T cells in a normal context and be exacerbated in a tumoral context.
- Does a correlation exist between CD39, CD16 expression and the enhancement of ADCC by POM1 in presence of GA101? To verify this, it should be interesting to perform experiments with more donors. We are currently running experiments on primary cell cultured γδ T cells to determine their stage of differentiation during the culture and correlate these results with existing results on γδ T cells differentiation trajectory by transcriptomic analyses [472].
- What role does CD39 play when it is expressed on tumoral cells? Indeed, in contrast to RL cells, we observed a high expression of CD39 on DLBCL cell lines such as Ocily10. Thus, further experiments

are needed using CRISPR-Cas9 or anti-CD39 mAb in order to decipher the role of CD39 expressed on γδ T cell or on NHL cells.

- Does CD39 expression correlate with the aggressiveness of the pathology? This remains an essential issue as we observed by analyzing public transcriptomic datas that FL patient survival is inversely correlated with *ENTPD-1* expression. Indeed, patients presenting high level of *ENTPD-1* exhibit a poorer survival than patients with low *ENTPD-1* expression (Figure 93). To determine if CD39 is a factor of poor prognosis, we will use cohorts of annotated patients whose clinical data have been collected by the clinical team of the IUCT Haematology Department and included in the regional IALYMPH cohort (CNIL N°2206723v0). A collection of fixed and included paraffin DLBCL and LF lymph node samples are available at the IUCT Pathology Laboratory and stored in the Toulouse Tumor Library/CRB (BB-0033-00014; DC-2008-463; AC-2008-820) and in the CeVi/CALYM living cell collection (DC-2014-2213; AC; 2015-2554; DR-2014-582 with CNIL N°914559) under the responsibility of Pr Laurent. Thus, we will assess whether correlations exist between the level of expression of CD39 determined by IHC on paraffin block and the history of the patient's disease. In addition, cohorts of FL patients who relapsed within 24 months will allow us to determine if CD39 is a biomarker in FL and/or DLBCL.

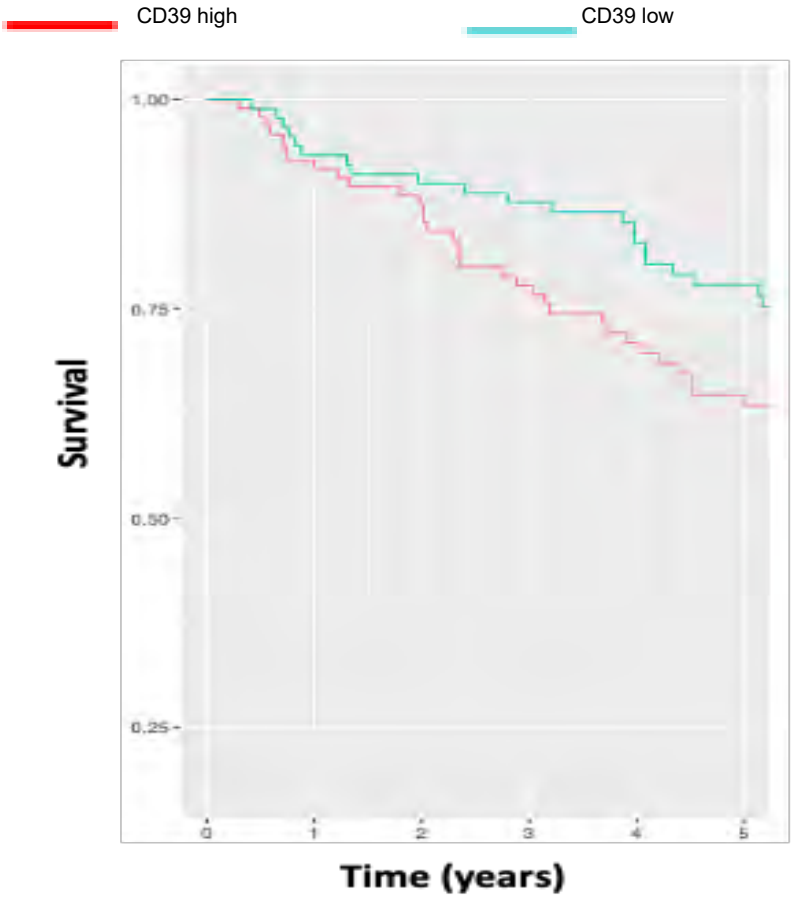

Figure 93 : FL patient survival depending on their level of CD39 expression (high or low)

In total, this preliminary work on CD39 targeting opens new perspectives in deciphering the IE mechanism in FL that could be targeted in order to propose new therapeutic strategies in this disease. Moreover, these preliminary results rencently led to a new project called CATALY (Cd39: A new Target in LYmphoma) that received a grant from CALYM-Janssen and is carried out by a PhD student, Léa Rimailho, in our group.

IV. DISCUSSION AND GENERAL PERSPECTIVES

During my PhD I have contributed to the advancement of four main research axis: (i) establishment of 3D cultures from FL cell lines (ULA-MALC) and from patient samples (PDLS), (ii) full characterization of these models by transcriptomic, phenotypic and imaging methods (immune cell population composition, ICP phenotyping, morphology etc...) (iii) IT testing on PDLS (anti-CD20 and anti-PD-1 mAbs) (iv) discovery of the new therapeutic targets such as CD39.

Over the years, three-dimensional cultures have made their way into cancer research as they allowed to more closely model cellular responses and TME structuration observed in patients, compared to classical two-dimensional cultures [473]. These features propelled them to the rank of powerful tools for studying pathology and drug efficacy. Unfortunately, this outstanding new model advancement is stugglying to enter the hematological field. In this context, my team firstly established the HD-MALC that I strongly participated to improve into a more robust, reliable and simple model with the ULA-MALC. Indeed, we demonstrated that this model could be used in a standardized and quick way for medium/high throughput screening of lymphoma therapies as described for solid cancers by others[474,475]. Nevertheless, aware of MALC model's limitations but taking into account methodological settings established, the next challenge of my PhD was the establishment of a 3D model from FL LN biopsies. Indeed, *in vitro* primary FL cell cultures are known to be difficult to maintain without TME[464]. So far, no 3D models using bulk cells coming from FL LN biopsies exist. Few teams including K. Tarte group, have started to work on patients' cells, but using only purified B cells from LN [430,440]. Thus, thanks to all the effort made during the IMLINFO's project with the group of my co-PhD director, we established a method comprising a specific enriched medium allowing the development of viable and well-structured 3D models from FL LN. Then, by using anti-CD20 and anti-PD-1 mAbs, we brought the proof of concept that PDLS could be used as a preclinical platforme to assess treatment efficacy by monitoring morphology, characterizing immune cell distribution and ICPand determining B cell depletion. Finally, with the characterization of this model we were able to identify a new potential target in FL, CD39. Unfortunately, even if from literature insight, this endonucleotidase seemed promising, we were not able to perform enough reliable experiments to conclude any potent effect upon POM1 treatment, a non-specific inhibitor. Thus, further investigations are needed with a more relevant drugs such as anti-CD39 mAbs in order to target CD39 in a more specific manner and demonstrate its role in FL IE.

One of the main limitations of PDLS is the absence of stromal cells such as macrophages and fibroblast which can produce ECM. This is certainly due to the freezing/thawing step required for the diagnosis step, before culturing cells in the appropriate enriched medium. My team is currently performing experiments to try to improve the biopsy processing procedure, in order to preserve the complete FL TME, but for now, no convincing results were obtained. Working on fresh samples would be the most appropriate but unfortunately, the feasilibily of the global workflow could not be realized and the 3D culture would likely not be optimal in a non-specific medium for FL. Thus, in order to improve 3D cultures and evolve the model towards tumoroid, my co-PhD director established co-cultures where collagen and monocytes were added to PDLS. Moreover, it would be also interesting to add other essential TME elements such as endothelial cells to recapitulate the vasculature. Another way to perform this improvement, should be to use microchannels allowing not only the migration of immune cells for example, but also allowing the perfusion of tumors with drugs. With the priviledge working environment englobing our project, we can combine the tumor modelling of each patient with medical imaging and bioinformatics tools to analyses genomic datas in order to provide a complete picture of each patient and propose an adapted therapy in a disease that remains incurable. In this perspective, PDLS represent a promising preclinical model to address biological questions of FL progression but also to propose a platform for personalized medicine (Figure 94).

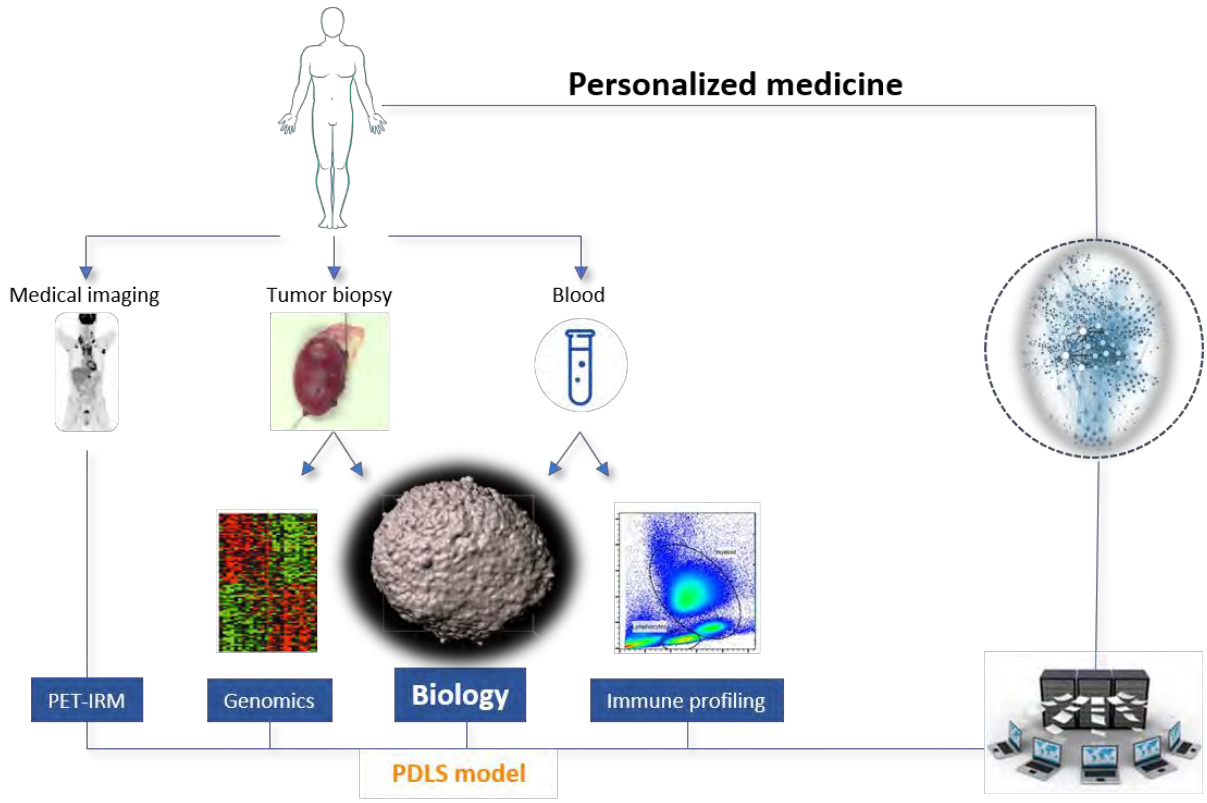

Figure 94 : Personalized medicine platform for FL patients

Personalized medicine is the fruit of cancer research evolution through time thanks to great advancement in technology and novel approaches to study and model cancer [442,443,476]. Indeed, from the first human cancer cell line culture (HeLa) to recent advances in single-cell sequencing technologies and organoids, allowing an unprecedented insight into tumor heterogeneity, cancer research has gain power to dissect and discover new therapeutic targets. Among the last century main technology breakthrough, was made possible thanks to the project of all Human Genome Atlas, allowing to suequence the whole-human genome. This huge advancement allowed scientists to believe for a time, that curing cancer was possible. Nevertheless, even if we greatly benefited from this achievement in the understanding of cancer genetic landmarks, the community quickly realized that it was not enough. Indeed, as M. Bissel introduced the concept: "context matters". This statement summarizes the fact that our cells, even if governed by DNA, are interacting with each other in a very complex way that could not be modelled only with classical *in vitro* culture, without taking into account TME. With our two feet in the single-cell eraand as we move into spatially resolved single-cell genomics, many unresolved questions on cancer development and progression are now within reach. Beyond these important biological questions, the challenge of curing FL and other cancers remains the ultimate goal. However, to obtain a new drug candidate for patients, a long process needs to be followed with, target identification by scientists, validation in preclinical and clinical studies and finally agency validation to be used in patients. To accelerate this process that could take decades, many changes can be brought and are ongoing in the discipline. These changes can be possible by collaborating and working in an interdisciplinary manner, concentrating the efforts of: hematologist, physicians, mathematicians, chemists, and bioinformaticians to address together important questions and continue to improve technological throughput. As much as COVID-19 pandemic is an unfortunate event, it is also a perfect example of how, by joining forces, scientists were able to provide a vaccine to the world in less than a year, a process that takes normally around 15 years. The vision of timeconsuming and painful progress in science is now changing thanks to this kind of collaborative work that allowed the emergence of technologies such as spactial transcriptomic, multiplexed histology, mass cytometry, high-speed fluorescence image... Indeed, with one single biopsy, we are now able to extract a huge amount of datas, to better understand pathology organization and progression.

Many challenges remain ahead for scientist to meet, including extraction of meaningfull informations from the overwhelming stream, of constanly generated big data. One of the main messages that single cell RNA seq have brought to us is: we are all different and there is no exception for cancers. Thus, medicine needs to adapt to these differences in order to provide more efficient treatment approaches for each individual. As Francis Collis, former director of the National Institutes of Health (NIH), said "*the idea that medicine would be applied in a fashion that ignores those*

differences, can't be any more correct than going to the shoe store and buying any old pair of shoes without checking the size". This concept, even if existing since over 20 years, has gain insight in preclinical and clinical studies recently, thanks to new available *in vitro* and *in vivo* platforms such as spheroids, organoids/tumoroids, or PDTX. The literature on organoids/tumoroids have exploded recently and encouraging results are ongoing in regenerative medicine and in cancer research but some technical and conceptual limitations are still to be considered. Indeed, organoids do not always recapitulate primary tissue cell types diversity which mostly include a combination of immune cells and stromal cells that are sometimes difficult to extract from biopsies. Moreover, organoid is not able to reproduce, so far, same environmental exposures as animal models such as aging processes or nutrition impact. Thus, the future challenge of organoid research will be to develop robust protocols reproducing adequate tissue organization, differentiated cells, vascularization, immune cell infiltration and even microbiome for some organs (for instance skin and intestine) [477–479]. With 3D models, new technical considerations need to be taken into account, including: penetration of dyes and drugs, differences in cell behavior depending on the layer in the model, development of imaging and bioinformatic tools to visualize them efficiently.

In this purpose of joining forces, the Human Cell Atlas organization developed a project called Organoid Cell Atlas with the goal of combining human organoids with single cell technology. This project is an open and collaborative network that follows four directions: (i) improvement in standardization of single-cell profiling of human organoids, (ii) establishment of a friendly user acess to single-cell organoid data using their infrastructure, (iii) development of computational methods and tools for comparing organoid profiles and primary tissue data and (iv) comparison of all these datas in order to create comprehensive reference maps of organoids as a basis for understanding human health and for diagnosing, monitoring and treating disease. Thus, like the human genome project, this project aims to provide substantial biomedical impact, in particular in the field of personalized medicine and regenerative biology. This very ambitious and challenging project will certainly take time. Nevertheless, as theoretically everything is impossible until it is done, science will have to sacrifice sometime so that medicine can win in the future and bring new hope for patients. By creating such inspiring projects with inclusive research environment that facilitates collaboration among a broad range of interested researchers, bridging communities and integrating expertise in organoids and single-cell technology, the translation from bench to bedside is getting real. Now more than ever, Marie Skłodowska-Curie's words make echoes for the next generation of scientists that will have to deal with new challenges in cancer research.

"Nothing in life is to be feared, it is only to be understood.

Now is the time to understand more, so that we may fear less".

V. BIBLIOGRAPHY

1. Lee, M. K. S. *et al.* Interplay between Clonal Hematopoiesis of Indeterminate Potential and Metabolism. *Trends in Endocrinology & Metabolism* **31**, 525–535 (2020).
2. Nagasawa, T. Microenvironmental niches in the bone marrow required for B-cell development. *Nat Rev Immunol* **6**, 107–116 (2006).
3. Patel, A. M. *et al.* The Role of B Cells in Adult and Paediatric Liver Injury. *Front. Immunol.* **12**, 729143 (2021).
4. Bao, Y. & Cao, X. Epigenetic Control of B Cell Development and B-Cell-Related Immune Disorders. *Clin Rev Allergy Immunol* **50**, 301–311 (2016).
5. Kondo, M., Weissman, I. L. & Akashi, K. Identification of clonogenic common lymphoid progenitors in mouse bone marrow. *Cell* **91**, 661–672 (1997).
6. Hardy, R. R., Carmack, C. E., Shinton, S. A., Kemp, J. D. & Hayakawa, K. Resolution and characterization of pro-B and pre-pro-B cell stages in normal mouse bone marrow. *J Exp Med* **173**, 1213–1225 (1991).
7. Tonegawa, S. Somatic generation of antibody diversity. *Nature* **302**, 575–581 (1983).
8. Hesse, J. E., Lieber, M. R., Mizuuchi, K. & Gellert, M. V(D)J recombination: a functional definition of the joining signals. *Genes Dev* **3**, 1053–1061 (1989).
9. Schatz, D. G., Oettinger, M. A. & Schlissel, M. S. V(D)J recombination: molecular biology and regulation. *Annu Rev Immunol* **10**, 359–383 (1992).
10. Fugmann, S. D., Lee, A. I., Shockett, P. E., Villey, I. J. & Schatz, D. G. The RAG proteins and V(D)J recombination: complexes, ends, and transposition. *Annu Rev Immunol* **18**, 495–527 (2000).
11. Bergman, Y. & Cedar, H. A stepwise epigenetic process controls immunoglobulin allelic exclusion. *Nat Rev Immunol* **4**, 753–761 (2004).
12. Kaeser, G. & Chun, J. Brain cell somatic gene recombination and its phylogenetic foundations. *J Biol Chem* **295**, 12786–12795 (2020).
13. Herzog, S., Reth, M. & Jumaa, H. Regulation of B-cell proliferation and differentiation by pre-B-cell receptor signalling. *Nat Rev Immunol* **9**, 195–205 (2009).
14. Carsetti, R., Rosado, M. M. & Wardmann, H. Peripheral development of B cells in mouse and man. *Immunol Rev* **197**, 179–191 (2004).
15. Chen, K. & Cerutti, A. New insights into the enigma of immunoglobulin D: Regulation and function of IgD. *Immunological Reviews* **237**, 160–179 (2010).
16. Vinuesa, C. G., Sanz, I. & Cook, M. C. Dysregulation of germinal centres in autoimmune disease. *Nat Rev Immunol* **9**, 845–857 (2009).
17. Allen, C. D. C., Okada, T. & Cyster, J. G. Germinal-center organization and cellular dynamics. *Immunity* **27**, 190–202 (2007).
18. Muramatsu, M. *et al.* Specific expression of activation-induced cytidine deaminase (AID), a novel member of the RNA-editing deaminase family in germinal center B cells. *J Biol Chem* **274**, 18470–18476 (1999).
19. Muramatsu, M. *et al.* Class switch recombination and hypermutation require activation-induced cytidine deaminase (AID), a potential RNA editing enzyme. *Cell* **102**, 553–563 (2000).
20. Klein, U. & Dalla-Favera, R. Germinal centres: role in B-cell physiology and malignancy. *Nat Rev Immunol* **8**, 22–33 (2008).
21. Nutt, S. L., Hodgkin, P. D., Tarlinton, D. M. & Corcoran, L. M. The generation of antibody-secreting plasma cells. *Nat Rev Immunol* **15**, 160–171 (2015).
22. Dranoff, G. Cytokines in cancer pathogenesis and cancer therapy. *Nat. Rev. Cancer* **4**, 11–22 (2004).
23. Arend, W. P., Palmer, G. & Gabay, C. IL-1, IL-18, and IL-33 families of cytokines. *Immunol Rev* **223**, 20–38 (2008).

24. Beltrame, M. H., Catarino, S. J., Goeldner, I., Boldt, A. B. W. & de Messias-Reason, I. J. The Lectin Pathway of Complement and Rheumatic Heart Disease. *Front. Pediatr.* **2**, (2015).
25. Lee, J. *et al.* The Multifaceted Role of Th1, Th9, and Th17 Cells in Immune Checkpoint Inhibition Therapy. *Front Immunol* **12**, 625667 (2021).
26. Chiossone, L., Dumas, P.-Y., Vienne, M. & Vivier, E. Natural killer cells and other innate lymphoid cells in cancer. *Nat Rev Immunol* **18**, 671–688 (2018).
27. Braza, M. S. & Klein, B. Anti-tumour immunotherapy with Vγ9Vδ2 T lymphocytes: from the bench to the bedside. *Br J Haematol* **160**, 123–132 (2013).
28. Tosolini, M., Algans, C., Pont, F., Ycart, B. & Fournié, J.-J. Large-scale microarray profiling reveals four stages of immune escape in non-Hodgkin lymphomas. *OncoImmunology* **5**, e1188246 (2016).
29. Ciofani, M. & Zúñiga-Pflücker, J. C. Determining γδ versus αß T cell development. *Nat Rev Immunol* **10**, 657–663 (2010).
30. Melichar, H. J. *et al.* Regulation of gammadelta versus alphabeta T lymphocyte differentiation by the transcription factor SOX13. *Science* **315**, 230–233 (2007).
31. Van de Walle, I. *et al.* Specific Notch receptor-ligand interactions control human TCR-αβ/γδ development by inducing differential Notch signal strength. *J Exp Med* **210**, 683–697 (2013).
32. Attaf, M., Legut, M., Cole, D. K. & Sewell, A. K. The T cell antigen receptor: the Swiss army knife of the immune system. *Clin Exp Immunol* **181**, 1–18 (2015).
33. Di Lorenzo, B., Ravens, S. & Silva-Santos, B. High-throughput analysis of the human thymic Vδ1+ T cell receptor repertoire. *Sci Data* **6**, 115 (2019).
34. Li, X. *et al.* Tim-3 suppresses the killing effect of Vγ9Vδ2 T cells on colon cancer cells by reducing perforin and granzyme B expression. *Exp Cell Res* **386**, 111719 (2020).
35. Petrasca, A., Melo, A. M., Breen, E. P. & Doherty, D. G. Human Vδ3+ γδ T cells induce maturation and IgM secretion by B cells. *Immunol Lett* **196**, 126–134 (2018).
36. Ma, R., Yuan, D., Guo, Y., Yan, R. & Li, K. Immune Effects of γδ T Cells in Colorectal Cancer: A Review. *Front Immunol* **11**, 1600 (2020).
37. Lafont, V. *et al.* Plasticity of Î³Î´ T Cells: Impact on the Anti-Tumor Response. *Frontiers in Immunology* **5**, (2014).
38. Bonneville, M., O'Brien, R. L. & Born, W. K. Gammadelta T cell effector functions: a blend of innate programming and acquired plasticity. *Nat Rev Immunol* **10**, 467–478 (2010).
39. Paul, S., Singh, A. K., Shilpi & Lal, G. Phenotypic and Functional Plasticity of Gamma–Delta (γδ) T Cells in Inflammation and Tolerance. *International Reviews of Immunology* **33**, 537–558 (2014).
40. Vantourout, P. & Hayday, A. Six-of-the-best: unique contributions of γδ T cells to immunology. *Nat Rev Immunol* **13**, 88–100 (2013).
41. Moser, B. & Eberl, M. gammadelta T cells: novel initiators of adaptive immunity. *Immunol Rev* **215**, 89–102 (2007).
42. Catros, V. *et al.* [Tgammadelta lymphocytes in oncology: unconventional killer lymphocytes]. *Med Sci (Paris)* **26**, 185–191 (2010).
43. Chien, Y. & Konigshofer, Y. Antigen recognition by gammadelta T cells. *Immunol Rev* **215**, 46–58 (2007).
44. Thedrez, A. *et al.* Self/non-self discrimination by human gammadelta T cells: simple solutions for a complex issue? *Immunol Rev* **215**, 123–135 (2007).
45. Viey, E. *et al.* Chemokine receptors expression and migration potential of tumor-infiltrating and peripheral-expanded Vgamma9Vdelta2 T cells from renal cell carcinoma patients. *J Immunother* **31**, 313–323 (2008).
46. Burjanadzé, M. *et al.* In vitro expansion of gamma delta T cells with anti-myeloma cell activity by Phosphostim and IL-2 in patients with multiple myeloma. *Br J Haematol* **139**, 206–216 (2007).
47. Saitoh, A. *et al.* Anti-tumor cytotoxicity of gammadelta T cells expanded from peripheral blood cells of patients with myeloma and lymphoma. *Med Oncol* **25**, 137–147 (2008).
48. Braza, M. S., Klein, B., Fiol, G. & Rossi, J.-F. γδ T-cell killing of primary follicular lymphoma cells is dramatically potentiated by GA101, a type II glycoengineered anti-CD20 monoclonal antibody. *Haematologica* **96**, 400–407 (2011).

49. Liu, Z., Guo, B. L., Gehrs, B. C., Nan, L. & Lopez, R. D. Ex vivo expanded human Vgamma9Vdelta2+ gammadelta-T cells mediate innate antitumor activity against human prostate cancer cells in vitro. *J Urol* **173**, 1552–1556 (2005).
50. Corvaisier, M. *et al.* V gamma 9V delta 2 T cell response to colon carcinoma cells. *J Immunol* **175**, 5481–5488 (2005).
51. Bouet-Toussaint, F. *et al.* Vgamma9Vdelta2 T cell-mediated recognition of human solid tumors. Potential for immunotherapy of hepatocellular and colorectal carcinomas. *Cancer Immunol Immunother* **57**, 531–539 (2008).
52. Fisch, P. *et al.* Gamma/delta T cell clones and natural killer cell clones mediate distinct patterns of non-major histocompatibility complex-restricted cytolysis. *J Exp Med* **171**, 1567–1579 (1990).
53. Fournié, J. J. & Bonneville, M. Stimulation of gamma delta T cells by phosphoantigens. *Res Immunol* **147**, 338–347 (1996).
54. Kabelitz, D., Wesch, D., Pitters, E. & Zöller, M. Characterization of tumor reactivity of human V gamma 9V delta 2 gamma delta T cells in vitro and in SCID mice in vivo. *J Immunol* **173**, 6767–6776 (2004).
55. Poupot, M. & Fournié, J.-J. Non-peptide antigens activating human Vgamma9/Vdelta2 T lymphocytes. *Immunol Lett* **95**, 129–138 (2004).
56. Gober, H.-J. *et al.* Human T cell receptor gammadelta cells recognize endogenous mevalonate metabolites in tumor cells. *J Exp Med* **197**, 163–168 (2003).
57. Yazdanifar, M., Barbarito, G., Bertaina, A. & Airoldi, I. γδ T Cells: The Ideal Tool for Cancer Immunotherapy. *Cells* **9**, E1305 (2020).
58. Harly, C., Peigné, C.-M. & Scotet, E. Molecules and Mechanisms Implicated in the Peculiar Antigenic Activation Process of Human Vγ9Vδ2 T Cells. *Front Immunol* **5**, 657 (2014).
59. Harly, C. *et al.* Key implication of CD277/butyrophilin-3 (BTN3A) in cellular stress sensing by a major human γδ T-cell subset. *Blood* **120**, 2269–2279 (2012).
60. Kunzmann, V. & Wilhelm, M. Anti-lymphoma effect of gammadelta T cells. *Leuk. Lymphoma* **46**, 671–680 (2005).
61. Meraviglia, S. *et al.* In vivo manipulation of Vgamma9Vdelta2 T cells with zoledronate and low-dose interleukin-2 for immunotherapy of advanced breast cancer patients. *Clin Exp Immunol* **161**, 290–297 (2010).
62. Tosolini, M. *et al.* Assessment of tumor-infiltrating TCRVγ9Vδ2 γδ lymphocyte abundance by deconvolution of human cancers microarrays. *Oncoimmunology* **6**, e1284723 (2017).
63. Chen, W.-C. *et al.* Interleukin-17-producing cell infiltration in the breast cancer tumour microenvironment is a poor prognostic factor. *Histopathology* **63**, 225–233 (2013).
64. Peng, G. *et al.* Tumor-infiltrating gammadelta T cells suppress T and dendritic cell function via mechanisms controlled by a unique toll-like receptor signaling pathway. *Immunity* **27**, 334–348 (2007).
65. Ye, J. *et al.* Tumor-derived γδ regulatory T cells suppress innate and adaptive immunity through the induction of immunosenescence. *J Immunol* **190**, 2403–2414 (2013).
66. Sebestyen, Z., Prinz, I., Déchanet-Merville, J., Silva-Santos, B. & Kuball, J. Translating gammadelta (γδ) T cells and their receptors into cancer cell therapies. *Nat Rev Drug Discov* **19**, 169–184 (2020).
67. Almeida, A. R. *et al.* Delta One T Cells for Immunotherapy of Chronic Lymphocytic Leukemia: Clinical-Grade Expansion/Differentiation and Preclinical Proof of Concept. *Clin Cancer Res* **22**, 5795–5804 (2016).
68. Capsomidis, A. *et al.* Chimeric Antigen Receptor-Engineered Human Gamma Delta T Cells: Enhanced Cytotoxicity with Retention of Cross Presentation. *Molecular Therapy* **26**, 354–365 (2018).
69. Marcu-Malina, V. *et al.* Redirecting αβT cells against cancer cells by transfer of a broadly tumor-reactive γδT-cell receptor. *Blood* **118**, 50–59 (2011).
70. Braza, M. S. *et al.* gammadelta T lymphocytes count is normal and expandable in peripheral blood of patients with follicular lymphoma, whereas it is decreased in tumor lymph nodes compared with inflammatory lymph nodes. *J Immunol* **184**, 134–140 (2010).

71. Rossi, C. *et al.* Boosting γδ T cell-mediated antibody-dependent cellular cytotoxicity by PD-1 blockade in follicular lymphoma. *OncoImmunology* **8**, 1554175 (2019).
72. Caccamo, N., Dieli, F., Meraviglia, S., Guggino, G. & Salerno, A. γ δ T Cell Modulation in Anticancer Treatment. *CCDT* **10**, 27–36 (2010).
73. Wilhelm, M. *et al.* Gammadelta T cells for immune therapy of patients with lymphoid malignancies. *Blood* **102**, 200–206 (2003).
74. Kunzmann, V. *et al.* Tumor-promoting Versus Tumor-antagonizing Roles of γδ T Cells in Cancer Immunotherapy: Results From a Prospective Phase I/II Trial. *Journal of Immunotherapy* **35**, 205–213 (2012).
75. Jaffe, E. S. The 2008 WHO classification of lymphomas: implications for clinical practice and translational research. *Hematology Am Soc Hematol Educ Program* 523–531 (2009) doi:10.1182/asheducation-2009.1.523.
76. Hodgkin, T. On the Uses of the Spleen. *Edinb Med Surg J* **18**, 83–91 (1822).
77. Sun, R., Medeiros, L. J. & Young, K. H. Diagnostic and predictive biomarkers for lymphoma diagnosis and treatment in the era of precision medicine. *Mod Pathol* **29**, 1118–1142 (2016).
78. Crombie, J. & LaCasce, A. The treatment of Burkitt lymphoma in adults. *Blood* **137**, 743–750 (2021).
79. Lenze, D. *et al.* The different epidemiologic subtypes of Burkitt lymphoma share a homogenous micro RNA profile distinct from diffuse large B-cell lymphoma. *Leukemia* **25**, 1869–1876 (2011).
80. Dave, S. S. *et al.* Molecular diagnosis of Burkitt's lymphoma. *N Engl J Med* **354**, 2431–2442 (2006).
81. Abramson, J. S. T-cell/histiocyte-rich B-cell lymphoma: biology, diagnosis, and management. *Oncologist* **11**, 384–392 (2006).
82. Alizadeh, A. A. *et al.* Distinct types of diffuse large B-cell lymphoma identified by gene expression profiling. *Nature* **403**, 503–511 (2000).
83. Müller, A. M. S., Ihorst, G., Mertelsmann, R. & Engelhardt, M. Epidemiology of non-Hodgkin's lymphoma (NHL): trends, geographic distribution, and etiology. *Ann Hematol* **84**, 1–12 (2005).
84. Lenz, G. & Staudt, L. M. Aggressive lymphomas. *N Engl J Med* **362**, 1417–1429 (2010).
85. Runge, H. F. P. *et al.* Application of the LymphGen classification tool to 928 clinically and genetically-characterised cases of diffuse large B cell lymphoma (DLBCL). *Br J Haematol* **192**, 216–220 (2021).
86. Nygren, L. *et al.* Prognostic role of SOX11 in a population-based cohort of mantle cell lymphoma. *Blood* **119**, 4215–4223 (2012).
87. Hassler, M. R., Schiefer, A.-I. & Egger, G. Combating the epigenome: epigenetic drugs against non-Hodgkin's lymphoma. *Epigenomics* **5**, 397–415 (2013).
88. Gillot, L., Baudin, L., Rouaud, L., Kridelka, F. & Noël, A. The pre-metastatic niche in lymph nodes: formation and characteristics. *Cell Mol Life Sci* **78**, 5987–6002 (2021).
89. Scott, D. W. & Gascoyne, R. D. The tumour microenvironment in B cell lymphomas. *Nat Rev Cancer* **14**, 517–534 (2014).
90. Mounier, M. *et al.* Changes in dynamics of excess mortality rates and net survival after diagnosis of follicular lymphoma or diffuse large B-cell lymphoma: comparison between European population-based data (EUROCARE-5). *The Lancet Haematology* **2**, e481–e491 (2015).
91. Dreyling, M. *et al.* Newly diagnosed and relapsed follicular lymphoma: ESMO Clinical Practice Guidelines for diagnosis, treatment and follow-up. *Annals of Oncology* **32**, 298–308 (2021).
92. Linet, M. S. *et al.* Medical history, lifestyle, family history, and occupational risk factors for follicular lymphoma: the InterLymph Non-Hodgkin Lymphoma Subtypes Project. *J Natl Cancer Inst Monogr* **2014**, 26–40 (2014).
93. Sant, M. *et al.* Incidence of hematologic malignancies in Europe by morphologic subtype: results of the HAEMACARE project. *Blood* **116**, 3724–3734 (2010).
94. Junlén, H. R. *et al.* Follicular lymphoma in Sweden: nationwide improved survival in the rituximab era, particularly in elderly women: a Swedish Lymphoma Registry study. *Leukemia* **29**, 668–676 (2015).
95. Kridel, R., Sehn, L. H. & Gascoyne, R. D. Pathogenesis of follicular lymphoma. *J. Clin. Invest.* **122**, 3424–3431 (2012).

96. Casulo, C. *et al.* Early Relapse of Follicular Lymphoma After Rituximab Plus Cyclophosphamide, Doxorubicin, Vincristine, and Prednisone Defines Patients at High Risk for Death: An Analysis From the National LymphoCare Study. *JCO* **33**, 2516–2522 (2015).
97. Casulo, C., Burack, W. R. & Friedberg, J. W. Transformed follicular non-Hodgkin lymphoma. *Blood* **125**, 40–47 (2015).
98. Schatz, J. H., Oricchio, E., Puvvada, S. D. & Wendel, H. G. Progress against follicular lymphoma: *Current Opinion in Hematology* **20**, 320–326 (2013).
99. Freedman, A. & Jacobsen, E. Follicular lymphoma: 2020 update on diagnosis and management. *Am. J. Hematol.* **95**, 316–327 (2020).
100. Das, S., Basu, D., Dubashi, B. & Jain, A. Low grade follicular lymphoma with high proliferation index; diagnostic and management issues. *Indian J Pathol Microbiol* **55**, 516–518 (2012).
101. Roulland, S. *et al.* t(14;18) Translocation: A Predictive Blood Biomarker for Follicular Lymphoma. *JCO* **32**, 1347–1355 (2014).
102. Roulland, S. *et al.* Early steps of follicular lymphoma pathogenesis. *Adv Immunol* **111**, 1–46 (2011).
103. Skibola, C. F. *et al.* Genome-wide association study identifies five susceptibility loci for follicular lymphoma outside the HLA region. *Am J Hum Genet* **95**, 462–471 (2014).
104. Huet, S., Sujobert, P. & Salles, G. From genetics to the clinic: a translational perspective on follicular lymphoma. *Nature Reviews Cancer* (2018) doi:10.1038/nrc.2017.127.
105. Kumar, E., Pickard, L. & Okosun, J. Pathogenesis of follicular lymphoma: genetics to the microenvironment to clinical translation. *Br. J. Haematol.* **194**, 810–821 (2021).
106. Zhang, J. *et al.* Disruption of KMT2D perturbs germinal center B cell development and promotes lymphomagenesis. *Nat Med* **21**, 1190–1198 (2015).
107. Zhang, J. *et al.* The CREBBP Acetyltransferase Is a Haploinsufficient Tumor Suppressor in B-cell Lymphoma. *Cancer Discov* **7**, 322–337 (2017).
108. Béguelin, W. *et al.* EZH2 is required for germinal center formation and somatic EZH2 mutations promote lymphoid transformation. *Cancer Cell* **23**, 677–692 (2013).
109. Béguelin, W. *et al.* EZH2 and BCL6 Cooperate to Assemble CBX8-BCOR Complex to Repress Bivalent Promoters, Mediate Germinal Center Formation and Lymphomagenesis. *Cancer Cell* **30**, 197–213 (2016).
110. Clozel, T. *et al.* Mechanism-based epigenetic chemosensitization therapy of diffuse large B-cell lymphoma. *Cancer Discov* **3**, 1002–1019 (2013).
111. Young, R. M. & Staudt, L. M. Targeting pathological B cell receptor signalling in lymphoid malignancies. *Nat Rev Drug Discov* **12**, 229–243 (2013).
112. Krysiak, K. *et al.* Recurrent somatic mutations affecting B-cell receptor signaling pathway genes in follicular lymphoma. *Blood* **129**, 473–483 (2017).
113. Lamason, R. L., McCully, R. R., Lew, S. M. & Pomerantz, J. L. Oncogenic CARD11 Mutations Induce Hyperactive Signaling by Disrupting Autoinhibition by the PKC-Responsive Inhibitory Domain. *Biochemistry* **49**, 8240–8250 (2010).
114. Coelho, V. *et al.* Glycosylation of surface Ig creates a functional bridge between human follicular lymphoma and microenvironmental lectins. *Proc Natl Acad Sci U S A* **107**, 18587–18592 (2010).
115. Linley, A. *et al.* Lectin binding to surface Ig variable regions provides a universal persistent activating signal for follicular lymphoma cells. *Blood* **126**, 1902–1910 (2015).
116. Yildiz, M. *et al.* Activating STAT6 mutations in follicular lymphoma. *Blood* **125**, 668–679 (2015).
117. Karube, K. *et al.* Recurrent mutations of NOTCH genes in follicular lymphoma identify a distinctive subset of tumours. *J Pathol* **234**, 423–430 (2014).
118. Rossi, D., Ciardullo, C. & Gaidano, G. Genetic aberrations of signaling pathways in lymphomagenesis: revelations from next generation sequencing studies. *Semin Cancer Biol* **23**, 422–430 (2013).
119. Okosun, J. *et al.* Recurrent mTORC1-activating RRAGC mutations in follicular lymphoma. *Nat Genet* **48**, 183–188 (2016).

120. Zoncu, R., Efeyan, A. & Sabatini, D. M. mTOR: from growth signal integration to cancer, diabetes and ageing. *Nat Rev Mol Cell Biol* **12**, 21–35 (2011).
121. Green, M. R. *et al.* Mutations in early follicular lymphoma progenitors are associated with suppressed antigen presentation. *Proc Natl Acad Sci U S A* **112**, E1116-1125 (2015).
122. Riese, R. J. *et al.* Essential role for cathepsin S in MHC class II-associated invariant chain processing and peptide loading. *Immunity* **4**, 357–366 (1996).
123. Bararia, D. *et al.* Cathepsin S Alterations Induce a Tumor-Promoting Immune Microenvironment in Follicular Lymphoma. *Cell Rep* **31**, 107522 (2020).
124. Dheilly, E. *et al.* Cathepsin S Regulates Antigen Processing and T Cell Activity in Non-Hodgkin Lymphoma. *Cancer Cell* **37**, 674-689.e12 (2020).
125. Carbone, A. *et al.* Follicular lymphoma. *Nat Rev Dis Primers* **5**, 83 (2019).
126. Huang, C. Germinal Center Reaction. *Adv Exp Med Biol* **1254**, 47–53 (2020).
127. Cui, W. *et al.* Nodal follicular lymphoma without complete follicular dendritic cell networks is related to localized clinical stage. *Pathol Int* **61**, 737–741 (2011).
128. Lamaison, C. & Tarte, K. Impact of B cell/lymphoid stromal cell crosstalk in B-cell physiology and malignancy. *Immunology Letters* **215**, 12–18 (2019).
129. Amé-Thomas, P. *et al.* Human mesenchymal stem cells isolated from bone marrow and lymphoid organs support tumor B-cell growth: role of stromal cells in follicular lymphoma pathogenesis. *Blood* **109**, 693–702 (2007).
130. Lin, Y. *et al.* Immunosuppressive CD14+HLA-DR(low)/- monocytes in B-cell non-Hodgkin lymphoma. *Blood* **117**, 872–881 (2011).
131. Pan, Y., Yu, Y., Wang, X. & Zhang, T. Tumor-Associated Macrophages in Tumor Immunity. *Front Immunol* **11**, 583084 (2020).
132. Taskinen, M., Karjalainen-Lindsberg, M.-L., Nyman, H., Eerola, L.-M. & Leppä, S. A high tumor-associated macrophage content predicts favorable outcome in follicular lymphoma patients treated with rituximab and cyclophosphamide-doxorubicin-vincristine-prednisone. *Clin Cancer Res* **13**, 5784–5789 (2007).
133. Mantovani, A., Sozzani, S., Locati, M., Allavena, P. & Sica, A. Macrophage polarization: tumor-associated macrophages as a paradigm for polarized M2 mononuclear phagocytes. *Trends Immunol* **23**, 549–555 (2002).
134. Clear, A. J. *et al.* Increased angiogenic sprouting in poor prognosis FL is associated with elevated numbers of CD163+ macrophages within the immediate sprouting microenvironment. *Blood* **115**, 5053–5056 (2010).
135. Ma, Y. *et al.* Anticancer chemotherapy-induced intratumoral recruitment and differentiation of antigen-presenting cells. *Immunity* **38**, 729–741 (2013).
136. Kridel, R. *et al.* The Prognostic Impact of CD163-Positive Macrophages in Follicular Lymphoma: A Study from the BC Cancer Agency and the Lymphoma Study Association. *Clin Cancer Res* **21**, 3428–3435 (2015).
137. Amé-Thomas, P. *et al.* Characterization of intratumoral follicular helper T cells in follicular lymphoma: role in the survival of malignant B cells. *Leukemia* **26**, 1053–1063 (2012).
138. Farinha, P. *et al.* The architectural pattern of FOXP3-positive T cells in follicular lymphoma is an independent predictor of survival and histologic transformation. *Blood* **115**, 289–295 (2010).
139. Sweetenham, J. W. *et al.* Prognostic value of regulatory T cells, lymphoma-associated macrophages, and MUM-1 expression in follicular lymphoma treated before and after the introduction of monoclonal antibody therapy: a Southwest Oncology Group Study. *Ann Oncol* **21**, 1196–1202 (2010).
140. Wahlin, B. E., Sander, B., Christensson, B. & Kimby, E. CD8+ T-Cell Content in Diagnostic Lymph Nodes Measured by Flow Cytometry Is a Predictor of Survival in Follicular Lymphoma. *Clin Cancer Res* **13**, 388–397 (2007).
141. Alvaro, T. *et al.* Immunohistochemical patterns of reactive microenvironment are associated with clinicobiologic behavior in follicular lymphoma patients. *J Clin Oncol* **24**, 5350–5357 (2006).

142. Laurent, C. *et al.* Distribution, function, and prognostic value of cytotoxic T lymphocytes in follicular lymphoma: a 3-D tissue-imaging study. *Blood* **118**, 5371–5379 (2011).
143. Ramsay, A. G. *et al.* Follicular lymphoma cells induce T-cell immunologic synapse dysfunction that can be repaired with lenalidomide: implications for the tumor microenvironment and immunotherapy. *Blood* **114**, 4713–4720 (2009).
144. Kiaii, S. *et al.* Follicular Lymphoma Cells Induce Changes in T-Cell Gene Expression and Function: Potential Impact on Survival and Risk of Transformation. *JCO* **31**, 2654–2661 (2013).
145. Gravelle, P., Jean, C., Valleron, W., Laurent, G. & Fournié, J.-J. Innate predisposition to immune escape in follicular lymphoma cells. *Oncoimmunology* **1**, 555–556 (2012).
146. Mongini, P. K. A. *et al.* Innate immunity and human B cell clonal expansion: effects on the recirculating B2 subpopulation. *J. Immunol.* **175**, 6143–6154 (2005).
147. Gibson, S. E., Swerdlow, S. H. & Felgar, R. E. Natural killer cell subsets and natural killer-like T-cell populations in benign and neoplastic B-cell proliferations vary based on clinicopathologic features. *Hum Pathol* **42**, 679–687 (2011).
148. Enqvist, M. *et al.* Systemic and Intra-Nodal Activation of NK Cells After Rituximab Monotherapy for Follicular Lymphoma. *Front. Immunol.* **10**, 2085 (2019).
149. Dave, S. S. *et al.* Prediction of Survival in Follicular Lymphoma Based on Molecular Features of Tumor-Infiltrating Immune Cells. *N Engl J Med* **351**, 2159–2169 (2004).
150. Sugimoto, T. & Watanabe, T. Follicular Lymphoma: The Role of the Tumor Microenvironment in Prognosis. *JCEH* **56**, 1–19 (2016).
151. Mourcin, F., Pangault, C., Amin-Ali, R., Amé-Thomas, P. & Tarte, K. Stromal Cell Contribution to Human Follicular Lymphoma Pathogenesis. *Frontiers in Immunology* **3**, (2012).
152. Pangault, C. *et al.* Follicular lymphoma cell niche: identification of a preeminent IL-4-dependent TFH–B cell axis. *Leukemia* **24**, 2080–2089 (2010).
153. Amé-Thomas, P. & Tarte, K. The yin and the yang of follicular lymphoma cell niches: Role of microenvironment heterogeneity and plasticity. *Seminars in Cancer Biology* **24**, 23–32 (2014).
154. Haebe, S. *et al.* Single-cell analysis can define distinct evolution of tumor sites in follicular lymphoma. *Blood* **137**, 2869–2880 (2021).
155. Brown, F. D. & Turley, S. J. Fibroblastic reticular cells: organization and regulation of the T lymphocyte life cycle. *J Immunol* **194**, 1389–1394 (2015).
156. Epron, G. *et al.* Monocytes and T cells cooperate to favor normal and follicular lymphoma B-cell growth: role of IL-15 and CD40L signaling. *Leukemia* **26**, 139–148 (2012).
157. Valero, J. G. *et al.* The receptor of the colony-stimulating factor-1 (CSF-1R) is a novel prognostic factor and therapeutic target in follicular lymphoma. *Leukemia* **35**, 2635–2649 (2021).
158. Perez Galan, P. *et al.* DECIPHERING THE CONTRIBUTION OF MACROPHAGES TO FOLLICULAR LYMPHOMA PATHOGENESIS: NEW INSIGHTS INTO THERAPY. *Hematol Oncol* **37**, 151–152 (2019).
159. Amin, R. *et al.* DC-SIGN-expressing macrophages trigger activation of mannosylated IgM B-cell receptor in follicular lymphoma. *Blood* **126**, 1911–1920 (2015).
160. Hollander, N. & Haimovich, J. Altered N-Linked Glycosylation in Follicular Lymphoma and Chronic Lymphocytic Leukemia: Involvement in Pathogenesis and Potential Therapeutic Targeting. *Front Immunol* **8**, 912 (2017).
161. van der Burg, S. H., Arens, R., Ossendorp, F., van Hall, T. & Melief, C. J. M. Vaccines for established cancer: overcoming the challenges posed by immune evasion. *Nat Rev Cancer* **16**, 219–233 (2016).
162. Pytlik, R., Polgarova, K., Karolova, J. & Klener, P. Current Immunotherapy Approaches in Non-Hodgkin Lymphomas. *Vaccines (Basel)* **8**, E708 (2020).
163. Andor, N. *et al.* Single-cell RNA-Seq of follicular lymphoma reveals malignant B-cell types and coexpression of T-cell immune checkpoints. *Blood* **133**, 1119–1129 (2019).
164. Yang, Z.-Z. *et al.* Mass Cytometry Analysis Reveals that Specific Intratumoral CD4+ T Cell Subsets Correlate with Patient Survival in Follicular Lymphoma. *Cell Rep* **26**, 2178-2193.e3 (2019).
165. Armengol, M. *et al.* Immune-Checkpoint Inhibitors in B-Cell Lymphoma. *Cancers (Basel)* **13**, E214 (2021).

166. Batlevi, C. L., Matsuki, E., Brentjens, R. J. & Younes, A. Novel immunotherapies in lymphoid malignancies. *Nat Rev Clin Oncol* **13**, 25–40 (2016).
167. Gravelle, P. *et al.* Impaired functional responses in follicular lymphoma CD8 $^{+}$ TIM-3 $^{+}$ T lymphocytes following TCR engagement. *OncoImmunology* **5**, e1224044 (2016).
168. Josefsson, S. E. *et al.* T Cells Expressing Checkpoint Receptor TIGIT Are Enriched in Follicular Lymphoma Tumors and Characterized by Reversible Suppression of T-cell Receptor Signaling. *Clin Cancer Res* **24**, 870–881 (2018).
169. Yang, Z.-Z. *et al.* IL-12 upregulates TIM-3 expression and induces T cell exhaustion in patients with follicular B cell non-Hodgkin lymphoma. *J. Clin. Invest.* **122**, 1271–1282 (2012).
170. Yang, Z.-Z. *et al.* Expression of LAG-3 defines exhaustion of intratumoral PD-1^{+} T cells and correlates with poor outcome in follicular lymphoma. *Oncotarget* **8**, (2017).
171. Yang, Z.-Z. *et al.* TIGIT Expression Is Associated with T-cell Suppression and Exhaustion and Predicts Clinical Outcome and Anti-PD-1 Response in Follicular Lymphoma. *Clin Cancer Res* **26**, 5217–5231 (2020).
172. Anderson, A. C., Joller, N. & Kuchroo, V. K. Lag-3, Tim-3, and TIGIT: Co-inhibitory Receptors with Specialized Functions in Immune Regulation. *Immunity* **44**, 989–1004 (2016).
173. Acharya, N., Sabatos-Peyton, C. & Anderson, A. C. Tim-3 finds its place in the cancer immunotherapy landscape. *J Immunother Cancer* **8**, e000911 (2020).
174. Myklebust, J. H. *et al.* High PD-1 expression and suppressed cytokine signaling distinguish T cells infiltrating follicular lymphoma tumors from peripheral T cells. *Blood* **121**, 1367–1376 (2013).
175. Laurent, C. *et al.* Several immune escape patterns in non-Hodgkin's lymphomas. *OncoImmunology* **4**, e1026530 (2015).
176. Gertner-Dardenne, J. *et al.* The co-receptor BTLA negatively regulates human Vγ9Vδ2 T-cell proliferation: a potential way of immune escape for lymphoma cells. *Blood* **122**, 922–931 (2013).
177. Germain, C. *et al.* Lectin-like transcript 1 is a marker of germinal center-derived B-cell non-Hodgkin's lymphomas dampening natural killer cell functions. *Oncoimmunology* **4**, e1026503 (2015).
178. Chao, M. P. *et al.* Anti-CD47 antibody synergizes with rituximab to promote phagocytosis and eradicate non-Hodgkin lymphoma. *Cell* **142**, 699–713 (2010).
179. Yang, Z.-Z., Novak, A. J., Ziesmer, S. C., Witzig, T. E. & Ansell, S. M. Attenuation of CD8 $^{+}$ T-Cell Function by CD4 $^{+}$ CD25 $^{+}$ Regulatory T Cells in B-Cell Non-Hodgkin's Lymphoma. *Cancer Res* **66**, 10145–10152 (2006).
180. Yang, Z.-Z., Novak, A. J., Ziesmer, S. C., Witzig, T. E. & Ansell, S. M. Malignant B cells skew the balance of regulatory T cells and TH17 cells in B-cell non-Hodgkin's lymphoma. *Cancer Res* **69**, 5522–5530 (2009).
181. Rawal, S. *et al.* Cross Talk between Follicular Th Cells and Tumor Cells in Human Follicular Lymphoma Promotes Immune Evasion in the Tumor Microenvironment. *J.I.* **190**, 6681–6693 (2013).
182. Le, K.-S. *et al.* Follicular B Lymphomas Generate Regulatory T Cells via the ICOS/ICOSL Pathway and Are Susceptible to Treatment by Anti-ICOS/ICOSL Therapy. *Cancer Res* **76**, 4648–4660 (2016).
183. Fernández, P. *et al.* Extracellular Generation of Adenosine by the Ectonucleotidases CD39 and CD73 Promotes Dermal Fibrosis. *The American Journal of Pathology* **183**, 1740–1746 (2013).
184. Eltzschig, H. K. Extracellular adenosine signaling in molecular medicine. *J Mol Med (Berl)* **91**, 141–146 (2013).
185. Eltzschig, H. K. Adenosine: An Old Drug Newly Discovered: *Anesthesiology* **111**, 904–915 (2009).
186. Di Virgilio, F., Sarti, A. C., Falzoni, S., De Marchi, E. & Adinolfi, E. Extracellular ATP and P2 purinergic signalling in the tumour microenvironment. *Nat. Rev. Cancer* **18**, 601–618 (2018).
187. Allard, B., Beavis, P. A., Darcy, P. K. & Stagg, J. Immunosuppressive activities of adenosine in cancer. *Current Opinion in Pharmacology* **29**, 7–16 (2016).
188. Li, X.-Y. *et al.* Targeting CD39 in Cancer Reveals an Extracellular ATP- and Inflammasome-Driven Tumor Immunity. *Cancer Discov* **9**, 1754–1773 (2019).

189. Moesta, A. K., Li, X.-Y. & Smyth, M. J. Targeting CD39 in cancer. *Nat Rev Immunol* **20**, 739–755 (2020).
190. Novitskiy, S. V. *et al.* Adenosine receptors in regulation of dendritic cell differentiation and function. *Blood* **112**, 1822–1831 (2008).
191. Ahlmanner, F. *et al.* CD39+ regulatory T cells accumulate in colon adenocarcinomas and display markers of increased suppressive function. *Oncotarget* **9**, 36993–37007 (2018).
192. Ohta, A. & Sitkovsky, M. Extracellular adenosine-mediated modulation of regulatory T cells. *Front Immunol* **5**, 304 (2014).
193. Figueiró, F. *et al.* Phenotypic and functional characteristics of CD39high human regulatory B cells (Breg). *Oncoimmunology* **5**, e1082703 (2016).
194. Ohta, A. *et al.* A2A adenosine receptor protects tumors from antitumor T cells. *Proceedings of the National Academy of Sciences* **103**, 13132–13137 (2006).
195. Beavis, P. A. *et al.* Targeting the adenosine 2A receptor enhances chimeric antigen receptor T cell efficacy. *Journal of Clinical Investigation* **127**, 929–941 (2017).
196. Waickman, A. T. *et al.* Enhancement of tumor immunotherapy by deletion of the A2A adenosine receptor. *Cancer Immunology, Immunotherapy* **61**, 917–926 (2012).
197. Sorrentino, C., Miele, L., Porta, A., Pinto, A. & Morello, S. Myeloid-derived suppressor cells contribute to A2B adenosine receptor-induced VEGF production and angiogenesis in a mouse melanoma model. *Oncotarget* **6**, 27478–27489 (2015).
198. Vijayan, D., Young, A., Teng, M. W. L. & Smyth, M. J. Targeting immunosuppressive adenosine in cancer. *Nature Reviews Cancer* **17**, 765–765 (2017).
199. Allard, D., Allard, B. & Stagg, J. On the mechanism of anti-CD39 immune checkpoint therapy. *J Immunother Cancer* **8**, (2020).
200. Bonnefoy, N., Bastid, J., Alberici, G., Bensussan, A. & Eliaou, J.-F. CD39: A complementary target to immune checkpoints to counteract tumor-mediated immunosuppression. *OncoImmunology* **4**, e1003015 (2015).
201. Cardoso, C. C. *et al.* The importance of CD39, CD43, CD81, and CD95 expression for differentiating B cell lymphoma by flow cytometry: CD39, CD43, CD81, AND CD95 FOR LYMPHOMA DIAGNOSIS. *Cytometry Part B: Clinical Cytometry* **94**, 451–458 (2018).
202. Hilchey, S. P. *et al.* Human Follicular Lymphoma CD39+-Infiltrating T Cells Contribute to Adenosine-Mediated T Cell Hyporesponsiveness. *The Journal of Immunology* **183**, 6157–6166 (2009).
203. Gruenbacher, G. *et al.* Ecto-ATPase CD39 Inactivates Isoprenoid-Derived Vγ9Vδ2 T Cell Phosphoantigens. *Cell Reports* **16**, 444–456 (2016).
204. Nakamura, K. *et al.* Targeting an adenosine-mediated "don't eat me signal" augments anti-lymphoma immunity by anti-CD20 monoclonal antibody. *Leukemia* (2020) doi:10.1038/s41375-020-0811-3.
205. Watanabe, T. The Tumor Microenvironment in Follicular Lymphoma: Its Pro-Malignancy Role with Therapeutic Potential. *Int J Mol Sci* **22**, 5352 (2021).
206. Solal-Céligny, P. *et al.* Watchful Waiting in Low–Tumor Burden Follicular Lymphoma in the Rituximab Era: Results of an F2-Study Database. *JCO* **30**, 3848–3853 (2012).
207. MacManus, M. *et al.* Randomized Trial of Systemic Therapy After Involved-Field Radiotherapy in Patients With Early-Stage Follicular Lymphoma: TROG 99.03. *JCO* **36**, 2918–2925 (2018).
208. Herfarth, K. *et al.* Rituximab With Involved Field Irradiation for Early-stage Nodal Follicular Lymphoma: Results of the MIR Study. *HemaSphere* **2**, e160 (2018).
209. Ardeshna, K. *et al.* Long-term effect of a watch and wait policy versus immediate systemic treatment for asymptomatic advanced-stage non-Hodgkin lymphoma: a randomised controlled trial. *The Lancet* **362**, 516–522 (2003).
210. Marcus, R. *et al.* Phase III Study of R-CVP Compared With Cyclophosphamide, Vincristine, and Prednisone Alone in Patients With Previously Untreated Advanced Follicular Lymphoma. *JCO* **26**, 4579–4586 (2008).

211. Hiddemann, W. Frontline therapy with rituximab added to the combination of cyclophosphamide, doxorubicin, vincristine, and prednisone (CHOP) significantly improves the outcome for patients with advanced-stage follicular lymphoma compared with therapy with CHOP alone: results of a prospective randomized study of the German Low-Grade Lymphoma Study Group. *Blood* **106**, 3725–3732 (2005).
212. Herold, M. *et al.* Rituximab Added to First-Line Mitoxantrone, Chlorambucil, and Prednisolone Chemotherapy Followed by Interferon Maintenance Prolongs Survival in Patients With Advanced Follicular Lymphoma: An East German Study Group Hematology and Oncology Study. *JCO* **25**, 1986–1992 (2007).
213. Bachy, E. *et al.* Long-term follow up of the FL2000 study comparing CHVP-interferon to CHVP-interferon plus rituximab in follicular lymphoma. *Haematologica* **98**, 1107–1114 (2013).
214. Schulz, H. *et al.* Immunochemotherapy With Rituximab and Overall Survival in Patients With Indolent or Mantle Cell Lymphoma: A Systematic Review and Meta-analysis. *JNCI Journal of the National Cancer Institute* **99**, 706–714 (2007).
215. Marcus, R. *et al.* Obinutuzumab for the First-Line Treatment of Follicular Lymphoma. *N Engl J Med* **377**, 1331–1344 (2017).
216. Morschhauser, F. *et al.* Rituximab plus Lenalidomide in Advanced Untreated Follicular Lymphoma. *N. Engl. J. Med.* **379**, 934–947 (2018).
217. Bachy, E. *et al.* Sustained Progression-Free Survival Benefit of Rituximab Maintenance in Patients With Follicular Lymphoma: Long-Term Results of the PRIMA Study. *J. Clin. Oncol.* **37**, 2815–2824 (2019).
218. Kumar, A., Planchais, C., Fronzes, R., Mouquet, H. & Reyes, N. Binding mechanisms of therapeutic antibodies to human CD20. *Science* **369**, 793–799 (2020).
219. Li, H., Ayer, L. M., Lytton, J. & Deans, J. P. Store-operated Cation Entry Mediated by CD20 in Membrane Rafts. *Journal of Biological Chemistry* **278**, 42427–42434 (2003).
220. Uchida, J. Mouse CD20 expression and function. *International Immunology* **16**, 119–129 (2004).
221. Parren, P. W. H. I., Carter, P. J. & Plückthun, A. Changes to International Nonproprietary Names for antibody therapeutics 2017 and beyond: of mice, men and more. *mAbs* **9**, 898–906 (2017).
222. Bezombes, C., Fournie, J.-J. & Laurent, G. Direct Effect of Rituximab in B-Cell-Derived Lymphoid Neoplasias: Mechanism, Regulation, and Perspectives. *Molecular Cancer Research* **9**, 1435–1442 (2011).
223. Klein, C., Jamois, C. & Nielsen, T. Anti-CD20 treatment for B-cell malignancies: current status and future directions. *Expert Opin Biol Ther* **21**, 161–181 (2021).
224. Bonavida, B. 'Rituximab-induced inhibition of antiapoptotic cell survival pathways: implications in chemo/immunoresistance, rituximab unresponsiveness, prognostic and novel therapeutic interventions'. *Oncogene* **26**, 3629–3636 (2007).
225. Garbán, H. J. & Bonavida, B. Nitric Oxide Inhibits the Transcription Repressor Yin-Yang 1 Binding Activity at the Silencer Region of the Fas Promoter: A Pivotal Role for Nitric Oxide in the Up-Regulation of Fas Gene Expression in Human Tumor Cells. *J Immunol* **167**, 75–81 (2001).
226. Vega, M. I. *et al.* Rituximab inhibits p38 MAPK activity in 2F7 B NHL and decreases IL-10 transcription: Pivotal role of p38 MAPK in drug resistance. *Oncogene* **23**, 3530–3540 (2004).
227. Vivier, E., Tomasello, E., Baratin, M., Walzer, T. & Ugolini, S. Functions of natural killer cells. *Nat Immunol* **9**, 503–510 (2008).
228. Cooper, M. A., Fehniger, T. A. & Caligiuri, M. A. The biology of human natural killer-cell subsets. *Trends in Immunology* **22**, 633–640 (2001).
229. Benyamine, A. *et al.* BTN3A molecules considerably improve Vγ9Vδ2T cells-based immunotherapy in acute myeloid leukemia. *Oncoimmunology* **5**, e1146843 (2016).
230. Gertner-Dardenne, J. *et al.* Bromohydrin pyrophosphate enhances antibody-dependent cell-mediated cytotoxicity induced by therapeutic antibodies. *Blood* **113**, 4875–4884 (2009).
231. Tokuyama, H. *et al.* V gamma 9 V delta 2 T cell cytotoxicity against tumor cells is enhanced by monoclonal antibody drugs--rituximab and trastuzumab. *Int J Cancer* **122**, 2526–2534 (2008).

232. Capietto, A.-H., Martinet, L. & Fournié, J.-J. Stimulated γδ T Cells Increase the In Vivo Efficacy of Trastuzumab in HER-2 $^{+}$ Breast Cancer. *J.I.* **187**, 1031–1038 (2011).
233. Decaup, E. *et al.* A Tridimensional Model for NK Cell-Mediated ADCC of Follicular Lymphoma. *Front Immunol* **10**, 1943 (2019).
234. Decaup, E. *et al.* Anti-tumor activity of obinutuzumab and rituximab in a follicular lymphoma 3D model. *Blood Cancer Journal* **3**, e131 (2013).
235. Mossner, E. *et al.* Increasing the efficacy of CD20 antibody therapy through the engineering of a new type II anti-CD20 antibody with enhanced direct and immune effector cell-mediated B-cell cytotoxicity. *Blood* **115**, 4393–4402 (2010).
236. Ivanov, A. *et al.* Monoclonal antibodies directed to CD20 and HLA-DR can elicit homotypic adhesion followed by lysosome-mediated cell death in human lymphoma and leukemia cells. *J Clin Invest* **119**, 2143–2159 (2009).
237. Beers, S. A. *et al.* Type II (tositumomab) anti-CD20 monoclonal antibody out performs type I (rituximab-like) reagents in B-cell depletion regardless of complement activation. *Blood* **112**, 4170–4177 (2008).
238. Dalle, S. *et al.* Preclinical studies on the mechanism of action and the anti-lymphoma activity of the novel anti-CD20 antibody GA101. *Mol Cancer Ther* **10**, 178–185 (2011).
239. Herter, S. *et al.* Preclinical activity of the type II CD20 antibody GA101 (obinutuzumab) compared with rituximab and ofatumumab in vitro and in xenograft models. *Mol Cancer Ther* **12**, 2031–2042 (2013).
240. Freeman, C. L. & Sehn, L. H. A tale of two antibodies: obinutuzumab versus rituximab. *Br J Haematol* **182**, 29–45 (2018).
241. Maloney, D. G. Anti-CD20 Antibody Therapy for B-Cell Lymphomas. *New England Journal of Medicine* **366**, 2008–2016 (2012).
242. Cartron, G. *et al.* Therapeutic activity of humanized anti-CD20 monoclonal antibody and polymorphism in IgG Fc receptor FcγRIIIa gene. *Blood* **99**, 754–758 (2002).
243. Murawski, N. *et al.* Optimization of rituximab for the treatment of DLBCL (I): dose-dense rituximab in the DENSE-R-CHOP-14 trial of the DSHNHL. *Ann Oncol* **25**, 1800–1806 (2014).
244. Pfreundschuh, M. *et al.* Optimization of rituximab for the treatment of DLBCL: increasing the dose for elderly male patients. *Br J Haematol* **179**, 410–420 (2017).
245. Rezvani, A. R. & Maloney, D. G. Rituximab resistance. *Best Practice & Research Clinical Haematology* **24**, 203–216 (2011).
246. Olejniczak, S. H., Hernandez-Ilizaliturri, F. J., Clements, J. L. & Czuczman, M. S. Acquired Resistance to Rituximab Is Associated with Chemotherapy Resistance Resulting from Decreased Bax and Bak Expression. *Clin Cancer Res* **14**, 1550–1560 (2008).
247. Vega, M. I. *et al.* Rituximab-Mediated Cell Signaling and Chemo/Immuno-sensitization of Drug-Resistant B-NHL Is Independent of Its Fc Functions. *Clinical Cancer Research* **15**, 6582–6594 (2009).
248. Leseux, L. *et al.* PKC ζ–mTOR pathway: a new target for rituximab therapy in follicular lymphoma. *Blood* **111**, 285–291 (2008).
249. Terui, Y. *et al.* Identification of CD20 C-Terminal Deletion Mutations Associated with Loss of CD20 Expression in Non-Hodgkin's Lymphoma. *Clin Cancer Res* **15**, 2523–2530 (2009).
250. Beum, P. V., Kennedy, A. D., Williams, M. E., Lindorfer, M. A. & Taylor, R. P. The Shaving Reaction: Rituximab/CD20 Complexes Are Removed from Mantle Cell Lymphoma and Chronic Lymphocytic Leukemia Cells by THP-1 Monocytes. *J Immunol* **176**, 2600–2609 (2006).
251. Takei, K., Yamazaki, T., Sawada, U., Ishizuka, H. & Aizawa, S. Analysis of changes in CD20, CD55, and CD59 expression on established rituximab-resistant B-lymphoma cell lines. *Leukemia Research* **30**, 625–631 (2006).
252. Di Gaetano, N. *et al.* Complement activation determines the therapeutic activity of rituximab in vivo. *J Immunol* **171**, 1581–1587 (2003).
253. Weng, W.-K. & Levy, R. Two Immunoglobulin G Fragment C Receptor Polymorphisms Independently Predict Response to Rituximab in Patients With Follicular Lymphoma. *JCO* **21**, 3940–3947 (2003).

254. Uchida, J. *et al.* The innate mononuclear phagocyte network depletes B lymphocytes through Fc receptor-dependent mechanisms during anti-CD20 antibody immunotherapy. *J Exp Med* **199**, 1659–1669 (2004).
255. Lykken, J. M. *et al.* Galectin-1 drives lymphoma CD20 immunotherapy resistance: validation of a preclinical system to identify resistance mechanisms. *Blood* **127**, 1886–1895 (2016).
256. Daydé, D. *et al.* Tumor burden influences exposure and response to rituximab: pharmacokinetic-pharmacodynamic modeling using a syngeneic bioluminescent murine model expressing human CD20. *Blood* **113**, 3765–3772 (2009).
257. Meignan, M. *et al.* Baseline Metabolic Tumor Volume Predicts Outcome in High–Tumor-Burden Follicular Lymphoma: A Pooled Analysis of Three Multicenter Studies. *JCO* **34**, 3618–3626 (2016).
258. Davids, M. S. *et al.* Phase I First-in-Human Study of Venetoclax in Patients With Relapsed or Refractory Non-Hodgkin Lymphoma. *J Clin Oncol* **35**, 826–833 (2017).
259. Davids, M. S. *et al.* Long-term Follow-up of Patients with Relapsed or Refractory Non–Hodgkin Lymphoma Treated with Venetoclax in a Phase I, First-in-Human Study. *Clinical Cancer Research* **27**, 4690–4695 (2021).
260. Ujjani, C. S. *et al.* Ibrutinib and Venetoclax in Relapsed and Refractory Follicular Lymphoma. *Blood* **136**, 46–47 (2020).
261. Zinzani, P. L. *et al.* Venetoclax-rituximab with or without bendamustine vs bendamustine-rituximab in relapsed/refractory follicular lymphoma. *Blood* **136**, 2628–2637 (2020).
262. Ysebaert, L. & Morschhauser, F. Immunomodulatory Agents in Follicular Lymphoma. *Hematol Oncol Clin North Am* **34**, 715–726 (2020).
263. Leonard, J. P. *et al.* AUGMENT: A Phase III Study of Lenalidomide Plus Rituximab Versus Placebo Plus Rituximab in Relapsed or Refractory Indolent Lymphoma. *JCO* **37**, 1188–1199 (2019).
264. Morschhauser, F. *et al.* Obinutuzumab combined with lenalidomide for relapsed or refractory follicular B-cell lymphoma (GALEN): a multicentre, single-arm, phase 2 study. *Lancet Haematol* **6**, e429–e437 (2019).
265. Ersahin, T., Tuncbag, N. & Cetin-Atalay, R. The PI3K/AKT/mTOR interactive pathway. *Mol Biosyst* **11**, 1946–1954 (2015).
266. Thorpe, L. M., Yuzugullu, H. & Zhao, J. J. PI3K in cancer: divergent roles of isoforms, modes of activation and therapeutic targeting. *Nat Rev Cancer* **15**, 7–24 (2015).
267. Burger, J. A. & Wiestner, A. Targeting B cell receptor signalling in cancer: preclinical and clinical advances. *Nat Rev Cancer* **18**, 148–167 (2018).
268. Vanhaesebroeck, B. *et al.* P110delta, a novel phosphoinositide 3-kinase in leukocytes. *Proc Natl Acad Sci U S A* **94**, 4330–4335 (1997).
269. Okkenhaug, K. *et al.* Impaired B and T cell antigen receptor signaling in p110delta PI 3-kinase mutant mice. *Science* **297**, 1031–1034 (2002).
270. Courtney, K. D., Corcoran, R. B. & Engelman, J. A. The PI3K pathway as drug target in human cancer. *J Clin Oncol* **28**, 1075–1083 (2010).
271. Gopal, A. K. *et al.* PI3Kδ inhibition by idelalisib in patients with relapsed indolent lymphoma. *N Engl J Med* **370**, 1008–1018 (2014).
272. Phillips, T. J. *et al.* Phase 1 study of the PI3Kδ inhibitor INCB040093 ± JAK1 inhibitor itacitinib in relapsed/refractory B-cell lymphoma. *Blood* **132**, 293–306 (2018).
273. Gopal, A. K. *et al.* Ibrutinib as Treatment for Patients With Relapsed/Refractory Follicular Lymphoma: Results From the Open-Label, Multicenter, Phase II DAWN Study. *JCO* **36**, 2405–2412 (2018).
274. Fowler, N. H. *et al.* The combination of ibrutinib and rituximab demonstrates activity in first-line follicular lymphoma. *Br J Haematol* **189**, 650–660 (2020).
275. Kuo, H.-P. *et al.* Combination of Ibrutinib and ABT-199 in Diffuse Large B-Cell Lymphoma and Follicular Lymphoma. *Mol Cancer Ther* **16**, 1246–1256 (2017).

276. Italiano, A. *et al.* Tazemetostat, an EZH2 inhibitor, in relapsed or refractory B-cell non-Hodgkin lymphoma and advanced solid tumours: a first-in-human, open-label, phase 1 study. *Lancet Oncol* **19**, 649–659 (2018).
277. Ogura, M. *et al.* A multicentre phase II study of vorinostat in patients with relapsed or refractory indolent B-cell non-Hodgkin lymphoma and mantle cell lymphoma. *Br J Haematol* **165**, 768–776 (2014).
278. Chen, R. *et al.* A phase II study of vorinostat and rituximab for treatment of newly diagnosed and relapsed/refractory indolent non-Hodgkin lymphoma. *Haematologica* **100**, 357–362 (2015).
279. Fayad, L. *et al.* Safety and Clinical Activity of a Combination Therapy Comprising Two Antibody-Based Targeting Agents for the Treatment of Non-Hodgkin Lymphoma: Results of a Phase I/II Study Evaluating the Immunoconjugate Inotuzumab Ozogamicin With Rituximab. *JCO* **31**, 573–583 (2013).
280. Preliminary results of a phase II randomized study (ROMULUS) of polatuzumab vedotin or pinatuzumab vedotin plus rituximab in patients with relapsed/refractory non-Hodgkin lymphoma (NHL). *Clin Adv Hematol Oncol* **12**, 15–18 (2014).
281. Diefenbach, C. *et al.* Polatuzumab vedotin plus obinutuzumab and lenalidomide in patients with relapsed or refractory follicular lymphoma: a cohort of a multicentre, single-arm, phase 1b/2 study. *The Lancet Haematology* **8**, e891–e901 (2021).
282. Kline, J., Godfrey, J. & Ansell, S. M. The immune landscape and response to immune checkpoint blockade therapy in lymphoma. *Blood* **135**, 523–533 (2020).
283. Manson, G. *et al.* Long-term efficacy of anti-PD1 therapy in Hodgkin lymphoma with and without allogenic stem cell transplantation. *Eur J Cancer* **115**, 47–56 (2019).
284. Simeone, E., Grimaldi, A. M. & Ascierto, P. A. Anti-PD1 and anti-PD-L1 in the treatment of metastatic melanoma. *Melanoma Manag* **2**, 41–50 (2015).
285. Mazieres, J. *et al.* Immune checkpoint inhibitors for patients with advanced lung cancer and oncogenic driver alterations: results from the IMMUNOTARGET registry. *Ann Oncol* **30**, 1321–1328 (2019).
286. Bertucci, F., Finetti, P., Birnbaum, D. & Mamessier, E. The PD1/PDL1 axis, a promising therapeutic target in aggressive breast cancers. *Oncoimmunology* **5**, e1085148 (2016).
287. Richendollar, B. G., Pohlman, B., Elson, P. & Hsi, E. D. Follicular programmed death 1–positive lymphocytes in the tumor microenvironment are an independent prognostic factor in follicular lymphoma. *Human Pathology* **42**, 552–557 (2011).
288. Armand, P. *et al.* Efficacy and safety results from CheckMate 140, a phase 2 study of nivolumab for relapsed/refractory follicular lymphoma. *Blood* **137**, 637–645 (2021).
289. Nastoupil, L. J. *et al.* HIGH RESPONSE RATES WITH PEMBROLIZUMAB IN COMBINATION WITH RITUXIMAB IN PATIENTS WITH RELAPSED FOLLICULAR LYMPHOMA: INTERIM RESULTS OF AN ON OPEN-LABEL, PHASE II STUDY. *Hematological Oncology* **35**, 120–121 (2017).
290. Armand, P. *et al.* A phase 1b study of dual PD-1 and CTLA-4 or KIR blockade in patients with relapsed/refractory lymphoid malignancies. *Leukemia* **35**, 777–786 (2021).
291. Advani, R. *et al.* CD47 Blockade by Hu5F9-G4 and Rituximab in Non-Hodgkin's Lymphoma. *N Engl J Med* **379**, 1711–1721 (2018).
292. Cahill, K. E. & Smith, S. M. Follicular Lymphoma: a Focus on Current and Emerging Therapies. *Oncology (Williston Park)* **36**, 97–106 (2022).
293. Dobaño-López, C., Araujo-Ayala, F., Serrat, N., Valero, J. G. & Pérez-Galán, P. Follicular Lymphoma Microenvironment: An Intricate Network Ready for Therapeutic Intervention. *Cancers (Basel)* **13**, 641 (2021).
294. Anastasia, A. & Rossi, G. Novel Drugs in Follicular Lymphoma. *Mediterr J Hematol Infect Dis* **8**, e2016061 (2016).
295. Barbosa, M. A. G., Xavier, C. P. R., Pereira, R. F., Petrikaitė, V. & Vasconcelos, M. H. 3D Cell Culture Models as Recapitulators of the Tumor Microenvironment for the Screening of Anti-Cancer Drugs. *Cancers (Basel)* **14**, 190 (2021).

296. Scherer, W. F., Syverton, J. T. & Gey, G. O. STUDIES ON THE PROPAGATION IN VITRO OF POLIOMYELITIS VIRUSES. *Journal of Experimental Medicine* **97**, 695–710 (1953).
297. Drexler, H. G. & Matsuo, Y. Guidelines for the characterization and publication of human malignant hematopoietic cell lines. *Leukemia* **13**, 835–842 (1999).
298. Drexler, H. G. & Minowada, J. History and classification of human leukemia-lymphoma cell lines. *Leuk Lymphoma* **31**, 305–316 (1998).
299. O'Dwyer, M. E. & Druker, B. J. STI571: an inhibitor of the BCR-ABL tyrosine kinase for the treatment of chronic myelogenous leukaemia. *The Lancet Oncology* **1**, 207–211 (2000).
300. Shoemaker, R. H. The NCI60 human tumour cell line anticancer drug screen. *Nat Rev Cancer* **6**, 813–823 (2006).
301. Mirabelli, Coppola, & Salvatore. Cancer Cell Lines Are Useful Model Systems for Medical Research. *Cancers* **11**, 1098 (2019).
302. Eray, M. *et al.* Follicular Lymphoma Cell Lines, an In Vitro Model for Antigenic Selection and Cytokine-Mediated Growth Regulation of Germinal Centre B Cells. *Scand J Immunol* **57**, 545–555 (2003).
303. Semac, I. *et al.* Anti-CD20 therapeutic antibody rituximab modifies the functional organization of rafts/microdomains of B lymphoma cells. *Cancer Res* **63**, 534–540 (2003).
304. Sandberg, R. & Ernberg, I. Assessment of tumor characteristic gene expression in cell lines using a tissue similarity index (TSI). *Proc. Natl. Acad. Sci. U.S.A.* **102**, 2052–2057 (2005).
305. Roider, T. *et al.* Dissecting intratumour heterogeneity of nodal B-cell lymphomas at the transcriptional, genetic and drug-response levels. *Nat Cell Biol* **22**, 896–906 (2020).
306. Zanoni, M. *et al.* Modeling neoplastic disease with spheroids and organoids. *J Hematol Oncol* **13**, 97 (2020).
307. Donnou, S. *et al.* Murine models of B-cell lymphomas: promising tools for designing cancer therapies. *Adv Hematol* **2012**, 701704 (2012).
308. Lampreht Tratar, U., Horvat, S. & Cemazar, M. Transgenic Mouse Models in Cancer Research. *Front. Oncol.* **8**, 268 (2018).
309. Mahmoudian, R. A., Farshchian, M. & Abbaszadegan, M. R. Genetically engineered mouse models of esophageal cancer. *Experimental Cell Research* **406**, 112757 (2021).
310. Oricchio, E., Wolfe, A. L., Schatz, J. H., Mavrakis, K. J. & Wendel, H.-G. Mouse models of cancer as biological filters for complex genomic data. *Disease Models & Mechanisms* **3**, 701–704 (2010).
311. Berg, T. *et al.* A transgenic mouse model demonstrating the oncogenic role of mutations in the polycomb-group gene EZH2 in lymphomagenesis. *Blood* **123**, 3914–3924 (2014).
312. McDonnell, T. J. *et al.* bcl-2-immunoglobulin transgenic mice demonstrate extended B cell survival and follicular lymphoproliferation. *Cell* **57**, 79–88 (1989).
313. Ortega-Molina, A. *et al.* Oncogenic Rag GTPase signalling enhances B cell activation and drives follicular lymphoma sensitive to pharmacological inhibition of mTOR. *Nat Metab* **1**, 775–789 (2019).
314. Brescia, P. *et al.* MEF2B Instructs Germinal Center Development and Acts as an Oncogene in B Cell Lymphomagenesis. *Cancer Cell* **34**, 453-465.e9 (2018).
315. Pasqualucci, L. & Klein, U. Mouse Models in the Study of Mature B-Cell Malignancies. *Cold Spring Harb Perspect Med* **11**, a034827 (2021).
316. Cacciapuoti, M. T. *et al.* In Vivo and Ex Vivo Patient-Derived Tumor Xenograft Models of Lymphoma for Drug Discovery. *Current Protocols* **1**, (2021).
317. Byrne, A. T. *et al.* Interrogating open issues in cancer precision medicine with patient-derived xenografts. *Nat Rev Cancer* **17**, 254–268 (2017).
318. Pizzi, M. & Inghirami, G. Patient-derived tumor xenografts of lymphoproliferative disorders: are they surrogates for the human disease? *Current Opinion in Hematology* **24**, 384–392 (2017).
319. Guenot, D. *et al.* Primary tumour genetic alterations and intra-tumoral heterogeneity are maintained in xenografts of human colon cancers showing chromosome instability. *J. Pathol.* **208**, 643–652 (2006).

320. Fichtner, I. *et al.* Anticancer drug response and expression of molecular markers in early-passage xenotransplanted colon carcinomas. *European Journal of Cancer* **40**, 298–307 (2004).
321. Burack, W. R. *et al.* Patient-derived xenografts of low-grade B-cell lymphomas demonstrate roles of the tumor microenvironment. *Blood Advances* **1**, 1263–1273 (2017).
322. Gerstein, R. *et al.* Patient-Derived Xenografts (PDX) of B Cell Lymphoma in NSG Mice: A Mouse Avatar for Developing Personalized Medicine. *Blood* **126**, 5408–5408 (2015).
323. Zhang, L. *et al.* B-Cell Lymphoma Patient-Derived Xenograft Models Enable Drug Discovery and Are a Platform for Personalized Therapy. *Clin Cancer Res* **23**, 4212–4223 (2017).
324. Townsend, E. C. *et al.* The Public Repository of Xenografts Enables Discovery and Randomized Phase II-like Trials in Mice. *Cancer Cell* **29**, 574–586 (2016).
325. Landgraf, M., McGovern, J. A., Friedl, P. & Hutmacher, D. W. Rational Design of Mouse Models for Cancer Research. *Trends in Biotechnology* **36**, 242–251 (2018).
326. Sutherland, R. M., McCredie, J. A. & Inch, W. R. Growth of multicell spheroids in tissue culture as a model of nodular carcinomas. *J Natl Cancer Inst* **46**, 113–120 (1971).
327. Sutherland, R. M., Inch, W. R., McCredie, J. A. & Kruuv, J. A Multi-component Radiation Survival Curve Using an *in Vitro* Tumour Model. *International Journal of Radiation Biology and Related Studies in Physics, Chemistry and Medicine* **18**, 491–495 (1970).
328. Bissell, M. J., Kenny, P. A. & Radisky, D. C. Microenvironmental Regulators of Tissue Structure and Function Also Regulate Tumor Induction and Progression: The Role of Extracellular Matrix and Its Degrading Enzymes. *Cold Spring Harbor Symposia on Quantitative Biology* **70**, 343–356 (2005).
329. Nelson, C. M. & Bissell, M. J. Of extracellular matrix, scaffolds, and signaling: tissue architecture regulates development, homeostasis, and cancer. *Annu Rev Cell Dev Biol* **22**, 287–309 (2006).
330. Bissell, M. J. Architecture Is the Message: The role of extracellular matrix and 3-D structure in tissue-specific gene expression and breast cancer. *Pezcoller Found J* **16**, 2–17 (2007).
331. Spencer, V. A., Xu, R. & Bissell, M. J. Extracellular Matrix, Nuclear and Chromatin Structure, and Gene Expression in Normal Tissues and Malignant Tumors: A Work in Progress. in *Advances in Cancer Research* vol. 97 275–294 (Elsevier, 2007).
332. Lochter, A. & Bissell, M. J. Involvement of extracellular matrix constituents in breast cancer. *Seminars in Cancer Biology* **6**, 165–173 (1995).
333. Petersen, O. W., Rønnov-Jessen, L., Weaver, V. M. & Bissell, M. J. Differentiation and cancer in the mammary gland: shedding light on an old dichotomy. *Adv Cancer Res* **75**, 135–161 (1998).
334. Martinez-Pacheco, S. & O'Driscoll, L. Pre-Clinical In Vitro Models Used in Cancer Research: Results of a Worldwide Survey. *Cancers* **13**, 6033 (2021).
335. Nath, S. & Devi, G. R. Three-dimensional culture systems in cancer research: Focus on tumor spheroid model. *Pharmacology & Therapeutics* **163**, 94–108 (2016).
336. Li, N. T., L. Co, I., Landon-Brace, N., Latour, S. & McGuigan, A. P. Tissue-engineered 3D cancer microenvironment for screening therapeutics. in *Biomaterials for 3D Tumor Modeling* 453–479 (Elsevier, 2020). doi:10.1016/B978-0-12-818128-7.00019-8.
337. Marsee, A. *et al.* Building consensus on definition and nomenclature of hepatic, pancreatic, and biliary organoids. *Cell Stem Cell* **28**, 816–832 (2021).
338. Mazzocchi, A. R., Rajan, S. A. P., Votanopoulos, K. I., Hall, A. R. & Skardal, A. In vitro patient-derived 3D mesothelioma tumor organoids facilitate patient-centric therapeutic screening. *Sci Rep* **8**, 2886 (2018).
339. Esch, E. W., Bahinski, A. & Huh, D. Organs-on-chips at the frontiers of drug discovery. *Nat Rev Drug Discov* **14**, 248–260 (2015).
340. Shanti, A., Teo, J. & Stefanini, C. In Vitro Immune Organs-on-Chip for Drug Development: A Review. *Pharmaceutics* **10**, 278 (2018).
341. Song, J. W. *et al.* Microfluidic Endothelium for Studying the Intravascular Adhesion of Metastatic Breast Cancer Cells. *PLoS ONE* **4**, e5756 (2009).
342. Cui, X. *et al.* Dissecting the immunosuppressive tumor microenvironments in Glioblastoma-on-a-Chip for optimized PD-1 immunotherapy. *eLife* **9**, e52253 (2020).

343. Zervantonakis, I. K. *et al.* Three-dimensional microfluidic model for tumor cell intravasation and endothelial barrier function. *Proc. Natl. Acad. Sci. U.S.A.* **109**, 13515–13520 (2012).
344. Jeon, J. S. *et al.* Human 3D vascularized organotypic microfluidic assays to study breast cancer cell extravasation. *Proc. Natl. Acad. Sci. U.S.A.* **112**, 214–219 (2015).
345. Vickerman, V. & Kamm, R. D. Mechanism of a flow-gated angiogenesis switch: early signaling events at cell–matrix and cell–cell junctions. *Integr. Biol.* **4**, 863 (2012).
346. Sung, K. E. *et al.* Transition to invasion in breast cancer: a microfluidic in vitro model enables examination of spatial and temporal effects. *Integr. Biol.* **3**, 439–450 (2011).
347. Polacheck, W. J., Charest, J. L. & Kamm, R. D. Interstitial flow influences direction of tumor cell migration through competing mechanisms. *Proc. Natl. Acad. Sci. U.S.A.* **108**, 11115–11120 (2011).
348. Zhang, Y. S. *et al.* Multisensor-integrated organs-on-chips platform for automated and continual in situ monitoring of organoid behaviors. *Proc. Natl. Acad. Sci. U.S.A.* **114**, (2017).
349. Berthier, E., Young, E. W. K. & Beebe, D. Engineers are from PDMS-land, Biologists are from Polystyrenia. *Lab Chip* **12**, 1224 (2012).
350. van Midwoud, P. M., Janse, A., Merema, M. T., Groothuis, G. M. M. & Verpoorte, E. Comparison of Biocompatibility and Adsorption Properties of Different Plastics for Advanced Microfluidic Cell and Tissue Culture Models. *Anal. Chem.* **84**, 3938–3944 (2012).
351. Capulli, A. K. *et al.* Approaching the in vitro clinical trial: engineering organs on chips. *Lab Chip* **14**, 3181 (2014).
352. Tibbitt, M. W. & Anseth, K. S. Hydrogels as extracellular matrix mimics for 3D cell culture. *Biotechnol. Bioeng.* **103**, 655–663 (2009).
353. Ingeson-Carlsson, C., Martinez-Monleon, A. & Nilsson, M. Differential effects of MAPK pathway inhibitors on migration and invasiveness of BRAFV600E mutant thyroid cancer cells in 2D and 3D culture. *Experimental Cell Research* **338**, 127–135 (2015).
354. Alessandri, K. *et al.* Cellular capsules as a tool for multicellular spheroid production and for investigating the mechanics of tumor progression in vitro. *Proceedings of the National Academy of Sciences* **110**, 14843–14848 (2013).
355. Kunz-Schughart, L. A., Kreutz, M. & Knuechel, R. Multicellular spheroids: a three-dimensional *in vitro* culture system to study tumour biology. *International Journal of Experimental Pathology* **79**, 1–23 (1998).
356. Singh, M., Close, D. A., Mukundan, S., Johnston, P. A. & Sant, S. Production of Uniform 3D Microtumors in Hydrogel Microwell Arrays for Measurement of Viability, Morphology, and Signaling Pathway Activation. *ASSAY and Drug Development Technologies* **13**, 570–583 (2015).
357. Goodarzi, S. *et al.* Quantifying nanotherapeutic penetration using a hydrogel-based microsystem as a new 3D *in vitro* platform. *Lab Chip* **21**, 2495–2510 (2021).
358. Zhang, Y. S. *et al.* Bioprinting the Cancer Microenvironment. *ACS Biomater. Sci. Eng.* **2**, 1710–1721 (2016).
359. Du, F., Zhao, X. & Fan, D. Soft Agar Colony Formation Assay as a Hallmark of Carcinogenesis. *BIO-PROTOCOL* **7**, (2017).
360. Foty, R. A Simple Hanging Drop Cell Culture Protocol for Generation of 3D Spheroids. *JoVE* 2720 (2011) doi:10.3791/2720.
361. Hirschhaeuser, F. *et al.* Multicellular tumor spheroids: An underestimated tool is catching up again. *Journal of Biotechnology* **148**, 3–15 (2010).
362. Zanoni, M. *et al.* 3D tumor spheroid models for in vitro therapeutic screening: a systematic approach to enhance the biological relevance of data obtained. *Sci Rep* **6**, 19103 (2016).
363. Riffle, S., Pandey, R. N., Albert, M. & Hegde, R. S. Linking hypoxia, DNA damage and proliferation in multicellular tumor spheroids. *BMC Cancer* **17**, 338 (2017).
364. Nunes, A. S., Barros, A. S., Costa, E. C., Moreira, A. F. & Correia, I. J. 3D tumor spheroids as in vitro models to mimic in vivo human solid tumors resistance to therapeutic drugs: NUNES ET AL. *Biotechnology and Bioengineering* **116**, 206–226 (2019).
365. Lesher-Pérez, S. C. *et al.* Dispersible oxygen microsensors map oxygen gradients in three-dimensional cell cultures. *Biomater. Sci.* **5**, 2106–2113 (2017).

366. Carlsson, J. & Acker, H. Relations between ph, oxygen partial pressure and growth in cultured cell spheroids. *Int. J. Cancer* **42**, 715–720 (1988).
367. Huber, V. *et al.* Cancer acidity: An ultimate frontier of tumor immune escape and a novel target of immunomodulation. *Seminars in Cancer Biology* **43**, 74–89 (2017).
368. Oloumi, A., MacPhail, S. H., Johnston, P. J., Banáth, J. P. & Olive, P. L. Changes in subcellular distribution of topoisomerase IIalpha correlate with etoposide resistance in multicell spheroids and xenograft tumors. *Cancer Res* **60**, 5747–5753 (2000).
369. Imamura, Y. *et al.* Comparison of 2D- and 3D-culture models as drug-testing platforms in breast cancer. *Oncology Reports* **33**, 1837–1843 (2015).
370. Jensen, C. & Teng, Y. Is It Time to Start Transitioning From 2D to 3D Cell Culture? *Front. Mol. Biosci.* **7**, 33 (2020).
371. Jeanes, A., Gottardi, C. J. & Yap, A. S. Cadherins and cancer: how does cadherin dysfunction promote tumor progression? *Oncogene* **27**, 6920–6929 (2008).
372. Bonnans, C., Chou, J. & Werb, Z. Remodelling the extracellular matrix in development and disease. *Nat Rev Mol Cell Biol* **15**, 786–801 (2014).
373. Tannock, I. F., Lee, C. M., Tunggal, J. K., Cowan, D. S. M. & Egorin, M. J. Limited penetration of anticancer drugs through tumor tissue: a potential cause of resistance of solid tumors to chemotherapy. *Clin Cancer Res* **8**, 878–884 (2002).
374. Minchinton, A. I. & Tannock, I. F. Drug penetration in solid tumours. *Nat Rev Cancer* **6**, 583–592 (2006).
375. Huanwen, W. *et al.* Intrinsic chemoresistance to gemcitabine is associated with constitutive and laminin-induced phosphorylation of FAK in pancreatic cancer cell lines. *Mol Cancer* **8**, 125 (2009).
376. Longati, P. *et al.* 3D pancreatic carcinoma spheroids induce a matrix-rich, chemoresistant phenotype offering a better model for drug testing. *BMC Cancer* **13**, 95 (2013).
377. Aoudjit, F. & Vuori, K. Integrin signaling inhibits paclitaxel-induced apoptosis in breast cancer cells. *Oncogene* **20**, 4995–5004 (2001).
378. Weigelt, B., Lo, A. T., Park, C. C., Gray, J. W. & Bissell, M. J. HER2 signaling pathway activation and response of breast cancer cells to HER2-targeting agents is dependent strongly on the 3D microenvironment. *Breast Cancer Res Treat* **122**, 35–43 (2010).
379. Zietarska, M. *et al.* Molecular description of a 3D in vitro model for the study of epithelial ovarian cancer (EOC). *Mol. Carcinog.* **46**, 872–885 (2007).
380. Cody, N. A. *et al.* Influence of monolayer, spheroid, and tumor growth conditions on chromosome 3 gene expression in tumorigenic epithelial ovarian cancer cell lines. *BMC Med Genomics* **1**, 34 (2008).
381. Gravelle, P. *et al.* Cell growth in aggregates determines gene expression, proliferation, survival, chemoresistance, and sensitivity to immune effectors in follicular lymphoma. *The American journal of pathology* **184**, 282–295 (2014).
382. Lazzari, G. *et al.* Light sheet fluorescence microscopy versus confocal microscopy: in quest of a suitable tool to assess drug and nanomedicine penetration into multicellular tumor spheroids. *Eur J Pharm Biopharm* **142**, 195–203 (2019).
383. Cavaco, A. C. M. *et al.* The Interaction between Laminin-332 and α3β1 Integrin Determines Differentiation and Maintenance of CAFs, and Supports Invasion of Pancreatic Duct Adenocarcinoma Cells. *Cancers (Basel)* **11**, E14 (2018).
384. Jeong, S.-Y., Lee, J.-H., Shin, Y., Chung, S. & Kuh, H.-J. Co-Culture of Tumor Spheroids and Fibroblasts in a Collagen Matrix-Incorporated Microfluidic Chip Mimics Reciprocal Activation in Solid Tumor Microenvironment. *PLoS ONE* **11**, e0159013 (2016).
385. Courau, T. *et al.* Cocultures of human colorectal tumor spheroids with immune cells reveal the therapeutic potential of MICA/B and NKG2A targeting for cancer treatment. *j. immunotherapy cancer* **7**, 74 (2019).
386. Boucherit, N., Gorvel, L. & Olive, D. 3D Tumor Models and Their Use for the Testing of Immunotherapies. *Front Immunol* **11**, 603640 (2020).

387. O'Donnell, J. S., Teng, M. W. L. & Smyth, M. J. Cancer immunoediting and resistance to T cell-based immunotherapy. *Nat Rev Clin Oncol* **16**, 151–167 (2019).
388. Peranzoni, E. *et al.* Macrophages impede CD8 T cells from reaching tumor cells and limit the efficacy of anti-PD-1 treatment. *Proc Natl Acad Sci U S A* **115**, E4041–E4050 (2018).
389. Wallstabe, L. *et al.* ROR1-CAR T cells are effective against lung and breast cancer in advanced microphysiologic 3D tumor models. *JCI Insight* **4**, 126345 (2019).
390. Tuveson, D. & Clevers, H. Cancer modeling meets human organoid technology. *Science* **364**, 952–955 (2019).
391. Kretzschmar, K. & Clevers, H. Organoids: Modeling Development and the Stem Cell Niche in a Dish. *Developmental Cell* **38**, 590–600 (2016).
392. Barker, N. *et al.* Identification of stem cells in small intestine and colon by marker gene Lgr5. *Nature* **449**, 1003–1007 (2007).
393. Sato, T. *et al.* Long-term Expansion of Epithelial Organoids From Human Colon, Adenoma, Adenocarcinoma, and Barrett's Epithelium. *Gastroenterology* **141**, 1762–1772 (2011).
394. Bleijs, M., Wetering, M., Clevers, H. & Drost, J. Xenograft and organoid model systems in cancer research. *EMBO J* **38**, (2019).
395. Dijkstra, K. K. *et al.* Generation of Tumor-Reactive T Cells by Co-culture of Peripheral Blood Lymphocytes and Tumor Organoids. *Cell* **174**, 1586-1598.e12 (2018).
396. Smith, R. C. & Tabar, V. Constructing and Deconstructing Cancers using Human Pluripotent Stem Cells and Organoids. *Cell Stem Cell* **24**, 12–24 (2019).
397. Finnberg, N. K. *et al.* Application of 3D tumoroid systems to define immune and cytotoxic therapeutic responses based on tumoroid and tissue slice culture molecular signatures. *Oncotarget* **8**, 66747–66757 (2017).
398. d'Aldebert, E. *et al.* Characterization of Human Colon Organoids From Inflammatory Bowel Disease Patients. *Front Cell Dev Biol* **8**, 363 (2020).
399. Múnera, J. O. *et al.* Differentiation of Human Pluripotent Stem Cells into Colonic Organoids via Transient Activation of BMP Signaling. *Cell Stem Cell* **21**, 51-64.e6 (2017).
400. Sachs, N. *et al.* A Living Biobank of Breast Cancer Organoids Captures Disease Heterogeneity. *Cell* **172**, 373-386.e10 (2018).
401. Broutier, L. *et al.* Human primary liver cancer–derived organoid cultures for disease modeling and drug screening. *Nat Med* **23**, 1424–1435 (2017).
402. Miller, A. J. *et al.* Generation of lung organoids from human pluripotent stem cells in vitro. *Nat Protoc* **14**, 518–540 (2019).
403. Hohwieler, M. *et al.* Human pluripotent stem cell-derived acinar/ductal organoids generate human pancreas upon orthotopic transplantation and allow disease modelling. *Gut* **66**, 473–486 (2017).
404. Kopper, O. *et al.* An organoid platform for ovarian cancer captures intra- and interpatient heterogeneity. *Nat Med* **25**, 838–849 (2019).
405. Horsley, H., Dharmasena, D., Malone-Lee, J. & Rohn, J. L. A urine-dependent human urothelial organoid offers a potential alternative to rodent models of infection. *Sci Rep* **8**, 1238 (2018).
406. Bar-Ephraim, Y. E., Kretzschmar, K. & Clevers, H. Organoids in immunological research. *Nat Rev Immunol* **20**, 279–293 (2020).
407. Neal, J. T. *et al.* Organoid Modeling of the Tumor Immune Microenvironment. *Cell* **175**, 1972-1988.e16 (2018).
408. Goldfracht, I. *et al.* Engineered heart tissue models from hiPSC-derived cardiomyocytes and cardiac ECM for disease modeling and drug testing applications. *Acta Biomater* **92**, 145–159 (2019).
409. Takasato, M. *et al.* Kidney organoids from human iPS cells contain multiple lineages and model human nephrogenesis. *Nature* **526**, 564–568 (2015).
410. Xu, Z. *et al.* Design and Construction of a Multi-Organ Microfluidic Chip Mimicking the in vivo Microenvironment of Lung Cancer Metastasis. *ACS Appl. Mater. Interfaces* **8**, 25840–25847 (2016).

411. Berthiaume, F., Maguire, T. J. & Yarmush, M. L. Tissue engineering and regenerative medicine: history, progress, and challenges. *Annu Rev Chem Biomol Eng* **2**, 403–430 (2011).
412. Donners, R., Yiin, R. S. Z., Blackledge, M. & Koh, D.-M. Whole-body diffusion-weighted MRI of normal lymph nodes: prospective apparent diffusion coefficient histogram and nodal distribution analysis in a healthy cohort. *Cancer Imaging* **21**, 64 (2021).
413. O'Neill, N. A., Eppler, H. B., Jewell, C. M. & Bromberg, J. S. Harnessing the lymph node microenvironment. *Curr Opin Organ Transplant* **23**, 73–82 (2018).
414. Wiig, H., Keskin, D. & Kalluri, R. Interaction between the extracellular matrix and lymphatics: consequences for lymphangiogenesis and lymphatic function. *Matrix Biol* **29**, 645–656 (2010).
415. Suematsu, S. & Watanabe, T. Generation of a synthetic lymphoid tissue–like organoid in mice. *Nat Biotechnol* **22**, 1539–1545 (2004).
416. Irvine, D. J., Stachowiak, A. N. & Hori, Y. Lymphoid tissue engineering: invoking lymphoid tissue neogenesis in immunotherapy and models of immunity. *Semin. Immunol.* **20**, 137–146 (2008).
417. Seifert, M. *et al.* Crosstalk between immune cells and mesenchymal stromal cells in a 3D bioreactor system. *IJAO* **35**, 986–995 (2012).
418. Giese, C. *et al.* Immunological substance testing on human lymphatic micro-organoids in vitro. *Journal of Biotechnology* **148**, 38–45 (2010).
419. Radke, L. *et al.* In Vitro Evaluation of Glycoengineered RSV-F in the Human Artificial Lymph Node Reactor. *Bioengineering* **4**, 70 (2017).
420. Purwada, A. *et al.* Ex vivo engineered immune organoids for controlled germinal center reactions. *Biomaterials* **63**, 24–34 (2015).
421. Purwada, A. & Singh, A. Immuno-engineered organoids for regulating the kinetics of B-cell development and antibody production. *Nature Protocols* **12**, 168–182 (2016).
422. Purwada, A., Shah, S. B., Beguelin, W., Melnick, A. M. & Singh, A. Modular Immune Organoids with Integrin Ligand Specificity Differentially Regulate Ex Vivo B Cell Activation. *ACS Biomater. Sci. Eng.* **3**, 214–225 (2017).
423. Purwada, A. *et al.* Ex vivo synthetic immune tissues with T cell signals for differentiating antigen-specific, high affinity germinal center B cells. *Biomaterials* **198**, 27–36 (2019).
424. Ross, A. E., Belanger, M. C., Woodroof, J. F. & Pompano, R. R. Spatially resolved microfluidic stimulation of lymphoid tissue ex vivo. *Analyst* **142**, 649–659 (2017).
425. Moura Rosa, P., Gopalakrishnan, N., Ibrahim, H., Haug, M. & Halaas, Ø. The intercell dynamics of T cells and dendritic cells in a lymph node-on-a-chip flow device. *Lab Chip* **16**, 3728–3740 (2016).
426. Mitra, B. *et al.* Microdevice integrating innate and adaptive immune responses associated with antigen presentation by dendritic cells. *RSC Adv.* **3**, 16002 (2013).
427. Lenti, E. *et al.* Therapeutic Regeneration of Lymphatic and Immune Cell Functions upon Lympho-organoid Transplantation. *Stem Cell Reports* **12**, 1260–1268 (2019).
428. Decaup, E. *et al.* A Tridimensional Model for NK Cell-Mediated ADCC of Follicular Lymphoma. *Front. Immunol.* **10**, 1943 (2019).
429. Vidal-Crespo, A. *et al.* Daratumumab displays in vitro and in vivo anti-tumor activity in models of B-cell non-Hodgkin lymphoma and improves responses to standard chemo-immunotherapy regimens. *Haematologica* **105**, 1032–1041 (2020).
430. Lamaison, C. *et al.* A novel 3D culture model recapitulates primary FL B cell features and promotes their survival. *Blood Advances* bloodadvances.2020003949 (2021) doi:10.1182/bloodadvances.2020003949.
431. Goy, A. & Feldman, T. Expanding Therapeutic Options in Mantle Cell Lymphoma. *Clinical Lymphoma and Myeloma* **7**, S184–S191 (2007).
432. Kurtova, A. V., Tamayo, A. T., Ford, R. J. & Burger, J. A. Mantle cell lymphoma cells express high levels of CXCR4, CXCR5, and VLA-4 (CD49d): importance for interactions with the stromal microenvironment and specific targeting. *Blood* **113**, 4604–4613 (2009).
433. Caicedo-Carvajal, C. E., Liu, Q., Remache, Y., Goy, A. & Suh, K. S. Cancer Tissue Engineering: A Novel 3D Polystyrene Scaffold for In Vitro Isolation and Amplification of Lymphoma Cancer Cells from Heterogeneous Cell Mixtures. *J Tissue Eng* **2011**, 362326 (2011).

434. Tang, J. *et al.* Identification and characterization of the cellular subclones that contribute to the pathogenesis of mantle cell lymphoma. *Genes Dis* **6**, 407–418 (2019).
435. Tian, Y. F. *et al.* Integrin-specific hydrogels as adaptable tumor organoids for malignant B and T cells. *Biomaterials* **73**, 110–119 (2015).
436. Moreno-Layseca, P. & Streuli, C. H. Signalling pathways linking integrins with cell cycle progression. *Matrix Biol* **34**, 144–153 (2014).
437. Cioroianu, A. I. *et al.* Tumor Microenvironment in Diffuse Large B-Cell Lymphoma: Role and Prognosis. *Anal Cell Pathol (Amst)* **2019**, 8586354 (2019).
438. Mannino, R. G. *et al.* 3D microvascular model recapitulates the diffuse large B-cell lymphoma tumor microenvironment in vitro. *Lab Chip* **17**, 407–414 (2017).
439. Sabhachandani, P. *et al.* Microfluidic assembly of hydrogel-based immunogenic tumor spheroids for evaluation of anticancer therapies and biomarker release. *Journal of Controlled Release* **295**, 21–30 (2019).
440. Foxall, R. *et al.* Developing a 3D B Cell Lymphoma Culture System to Model Antibody Therapy. *Front Immunol* **11**, 605231 (2020).
441. Gava, F. *et al.* 3D Model Characterization by 2D and 3D Imaging in t(14;18)-Positive B-NHL: Perspectives for In Vitro Drug Screens in Follicular Lymphoma. *Cancers* **13**, 1490 (2021).
442. Diamandis, M., White, N. M. A. & Yousef, G. M. Personalized medicine: marking a new epoch in cancer patient management. *Mol Cancer Res* **8**, 1175–1187 (2010).
443. Pokorska-Bocci, A. *et al.* 'Personalized medicine': what's in a name? *Per Med* **11**, 197–210 (2014).
444. Bullinger, L. & Valk, P. J. M. Gene expression profiling in acute myeloid leukemia. *J Clin Oncol* **23**, 6296–6305 (2005).
445. Wiechmann, L. *et al.* Presenting features of breast cancer differ by molecular subtype. *Ann Surg Oncol* **16**, 2705–2710 (2009).
446. Druker, B. J. *et al.* Efficacy and safety of a specific inhibitor of the BCR-ABL tyrosine kinase in chronic myeloid leukemia. *N Engl J Med* **344**, 1031–1037 (2001).
447. Baselga, J., Norton, L., Albanell, J., Kim, Y. M. & Mendelsohn, J. Recombinant humanized anti-HER2 antibody (Herceptin) enhances the antitumor activity of paclitaxel and doxorubicin against HER2/neu overexpressing human breast cancer xenografts. *Cancer Res* **58**, 2825–2831 (1998).
448. Jurinovic, V. *et al.* Evaluation of the m7-FLIPI in Patients with Follicular Lymphoma Treated within the Gallium Trial: EZH2 mutation Status May be a Predictive Marker for Differential Efficacy of Chemotherapy. *Blood* **134**, 122–122 (2019).
449. Barrington, S. F. & Johnson, P. W. M. 18F-FDG PET/CT in Lymphoma: Has Imaging-Directed Personalized Medicine Become a Reality? *J Nucl Med* **58**, 1539–1544 (2017).
450. Radford, J. *et al.* Results of a trial of PET-directed therapy for early-stage Hodgkin's lymphoma. *N Engl J Med* **372**, 1598–1607 (2015).
451. Rodriguez-Antona, C., Gomez, A., Karlgren, M., Sim, S. C. & Ingelman-Sundberg, M. Molecular genetics and epigenetics of the cytochrome P450 gene family and its relevance for cancer risk and treatment. *Hum Genet* **127**, 1–17 (2010).
452. Roukos, D. H. & Briasoulis, E. Individualized preventive and therapeutic management of hereditary breast ovarian cancer syndrome. *Nat Clin Pract Oncol* **4**, 578–590 (2007).
453. Byrski, T. *et al.* Pathologic complete response to neoadjuvant cisplatin in BRCA1-positive breast cancer patients. *Breast Cancer Res Treat* **147**, 401–405 (2014).
454. Valle, L. *et al.* Update on genetic predisposition to colorectal cancer and polyposis. *Mol Aspects Med* **69**, 10–26 (2019).
455. Pauli, C. *et al.* Personalized *In Vitro* and *In Vivo* Cancer Models to Guide Precision Medicine. *Cancer Discov* **7**, 462–477 (2017).
456. Tiriac, H. *et al.* Organoid Profiling Identifies Common Responders to Chemotherapy in Pancreatic Cancer. *Cancer Discov* **8**, 1112–1129 (2018).
457. Driehuis, E., Kretzschmar, K. & Clevers, H. Establishment of patient-derived cancer organoids for drug-screening applications. *Nat Protoc* **15**, 3380–3409 (2020).

458. Jacob, F., Ming, G. & Song, H. Generation and biobanking of patient-derived glioblastoma organoids and their application in CAR T cell testing. *Nat Protoc* **15**, 4000–4033 (2020).
459. Schnalzger, T. E. *et al.* 3D model for CAR -mediated cytotoxicity using patient-derived colorectal cancer organoids. *EMBO J* **38**, (2019).
460. Mongini, P. K. A. *et al.* Innate Immunity and Human B Cell Clonal Expansion: Effects on the Recirculating B2 Subpopulation. *J Immunol* **175**, 6143–6154 (2005).
461. Mongini, P. K. A. *et al.* TLR-9 and IL-15 Synergy Promotes the In Vitro Clonal Expansion of Chronic Lymphocytic Leukemia B Cells. *J.I.* **195**, 901–923 (2015).
462. Ross, S. H. & Cantrell, D. A. Signaling and Function of Interleukin-2 in T Lymphocytes. *Annu Rev Immunol* **36**, 411–433 (2018).
463. Chraa, D., Naim, A., Olive, D. & Badou, A. T lymphocyte subsets in cancer immunity: Friends or foes. *J Leukoc Biol* **105**, 243–255 (2019).
464. Goval, J.-J. *et al.* The prevention of spontaneous apoptosis of follicular lymphoma B cells by a follicular dendritic cell line: involvement of caspase-3, caspase-8 and c-FLIP. *Haematologica* **93**, 1169–1177 (2008).
465. Yang, Z.-Z. *et al.* TGF-β upregulates CD70 expression and induces exhaustion of effector memory T cells in B-cell non-Hodgkin's lymphoma. *Leukemia* **28**, 1872–1884 (2014).
466. Chapuy, B. *et al.* Diffuse large B-cell lymphoma patient-derived xenograft models capture the molecular and biological heterogeneity of the disease. *Blood* **127**, 2203–2213 (2016).
467. Quan, L. *et al.* PD-1 Blockade Can Restore Functions of T-Cells in Epstein-Barr Virus-Positive Diffuse Large B-Cell Lymphoma In Vitro. *PLoS ONE* **10**, e0136476 (2015).
468. Gravelle, P. *et al.* Mechanisms of PD-1/PD-L1 expression and prognostic relevance in non-Hodgkin lymphoma: a summary of immunohistochemical studies. *Oncotarget* **8**, (2017).
469. Josefsson, S. E. *et al.* TIGIT and PD-1 Mark Intratumoral T Cells with Reduced Effector Function in B-cell Non-Hodgkin Lymphoma. *Cancer Immunol Res* **7**, 355–362 (2019).
470. Yang, Z.-Z. *et al.* PD-1 expression defines two distinct T-cell sub-populations in follicular lymphoma that differentially impact patient survival. *Blood Cancer Journal* **5**, e281–e281 (2015).
471. Aroua, N. *et al.* Extracellular ATP and CD39 Activate cAMP-Mediated Mitochondrial Stress Response to Promote Cytarabine Resistance in Acute Myeloid Leukemia. *Cancer Discov* **10**, 1544–1565 (2020).
472. Cerapio, J. P. *et al.* Single-Cell RNAseq Profiling of Human γδ T Lymphocytes in Virus-Related Cancers and COVID-19 Disease. *Viruses* **13**, 2212 (2021).
473. Pampaloni, F., Reynaud, E. G. & Stelzer, E. H. K. The third dimension bridges the gap between cell culture and live tissue. *Nat. Rev. Mol. Cell Biol.* **8**, 839–845 (2007).
474. Horvath, P. *et al.* Screening out irrelevant cell-based models of disease. *Nature Reviews Drug Discovery* **15**, 751–769 (2016).
475. Friedrich, J., Seidel, C., Ebner, R. & Kunz-Schughart, L. A. Spheroid-based drug screen: considerations and practical approach. *Nat Protoc* **4**, 309–324 (2009).
476. Elemento, O. The future of precision medicine: towards a more predictive personalized medicine. *Emerging Topics in Life Sciences* **4**, 175–177 (2020).
477. LeSavage, B. L., Suhar, R. A., Broguiere, N., Lutolf, M. P. & Heilshorn, S. C. Next-generation cancer organoids. *Nat Mater* **21**, 143–159 (2022).
478. Foo, M. A. *et al.* Clinical translation of patient-derived tumour organoids- bottlenecks and strategies. *Biomark Res* **10**, 10 (2022).
479. Letai, A., Bhola, P. & Welm, A. L. Functional precision oncology: Testing tumors with drugs to identify vulnerabilities and novel combinations. *Cancer Cell* **40**, 26–35 (2022).

VI. ANNEXES

Poster presentation

- June 29-30th 2021: EACR Imaging Cancer (Virtual congress)

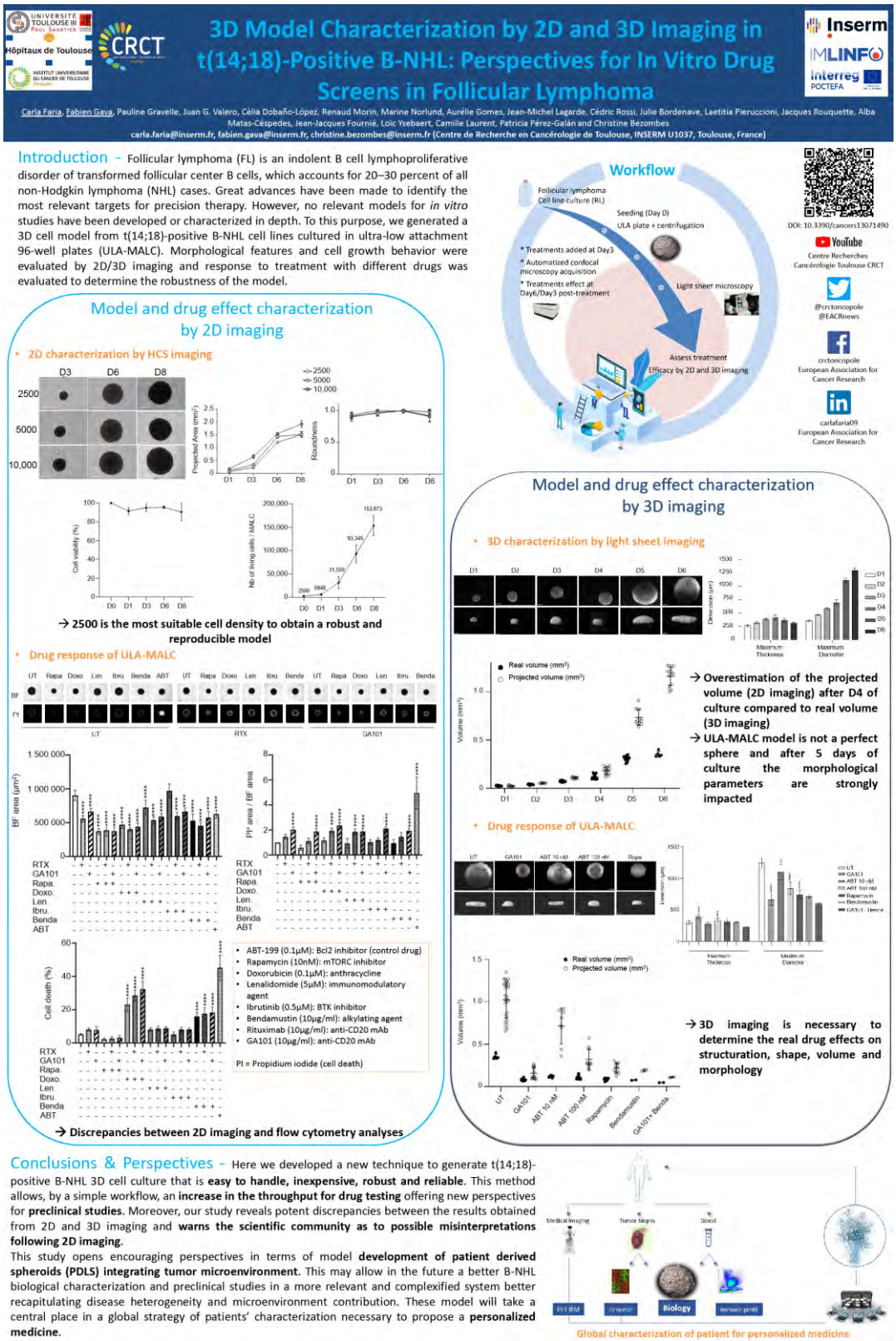

- October 05-06th 2021: EACR Goodbye flat biology (Virtual congress)

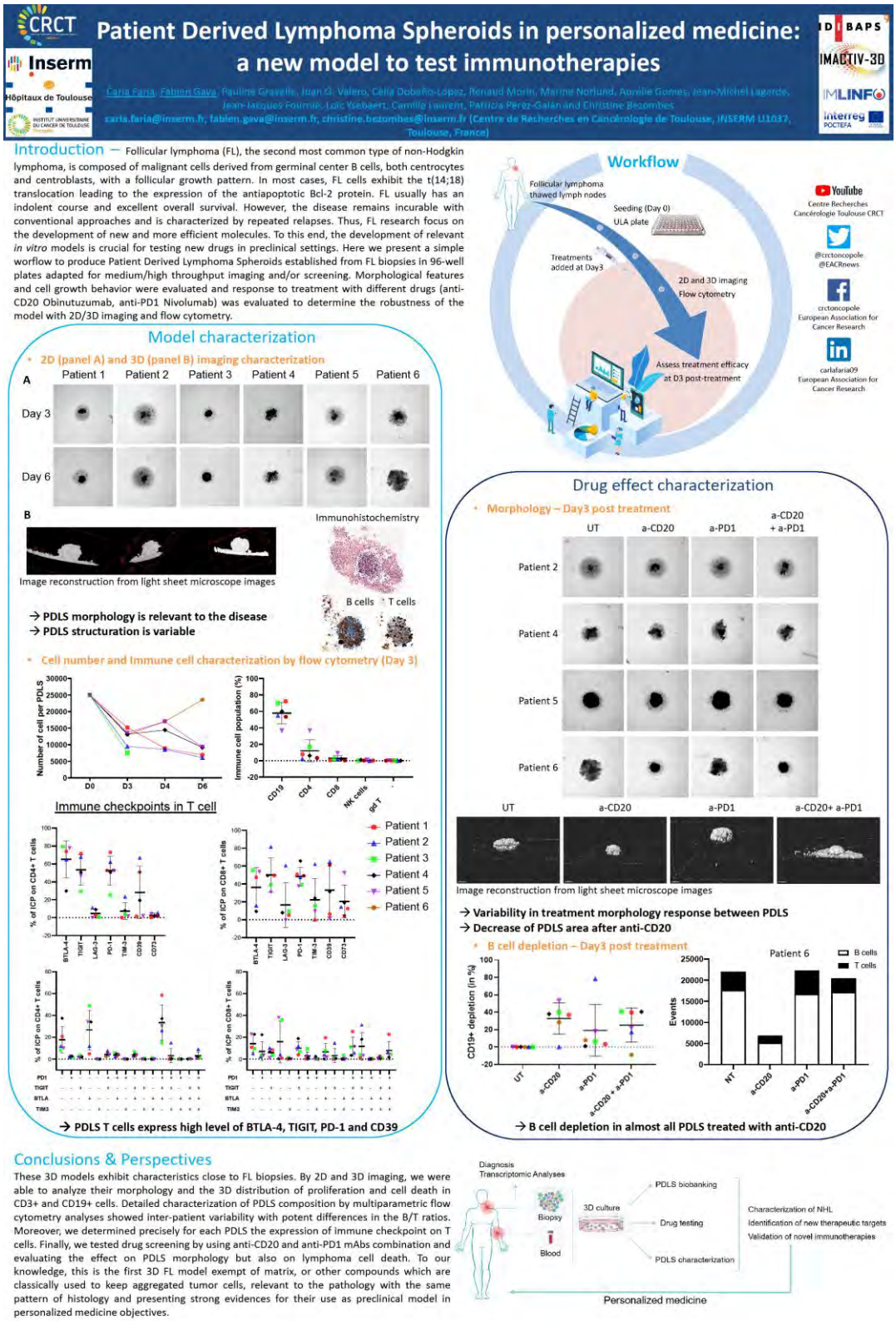

Oral communications :

- September 23-24th 2019: 3ème édition du workshop « Biofabrication & cancer », Montpellier
- October 21st 2021 : FITC (Société Française d'Immuno-Thérapie du Cancer) annual meeting, Paris

Workshop organization

- June 7-11th 2021: Highlight your 3D samples. In collaboration with Laetitia Ligat from CRCT pole technologique